

Structural studies of dynein's interaction with microtubules and herpesvirus

Samuel Edward Lacey

MRC Laboratory of Molecular Biology
Darwin College - University of Cambridge
October 2019

This thesis is submitted for the degree of Doctor of Philosophy

Declaration

This dissertation is the result of my own work and includes nothing which is the outcome of work done in collaboration except as declared in the Preface and specified in the text. It is not substantially the same as any that I have submitted, or, is being concurrently submitted for a degree or diploma or other qualification at the University of Cambridge or any other University or similar institution except as declared in the Preface and specified in the text. I further state that no substantial part of my dissertation has already been submitted, or, is being concurrently submitted for any such degree, diploma or other qualification at the University of Cambridge or any other University or similar institution except as declared in the Preface and specified in the text. It does not exceed the prescribed word of 60000 prescribed by the Biology Degree Committee

Samuel Lacey

October 2019

Abstract

The dynein family is a group of minus-end directed microtubule motor proteins vital for long-range cytoplasmic cargo transport and ciliary beating. The dynein heavy chain consists of an N-terminal tail domain responsible for cargo binding and dimerization, and a C-terminal motor domain. In order to move, the dynein motor cyclically binds and releases from the microtubule by changing the conformation of its microtubule-binding domain (MTBD). In chapter 3, I solve the structure of cytoplasmic and axonemal dynein MTBDs bound to microtubules by cryo-EM. From this, I present a new model of how dynein interacts with the microtubule, and a novel role of axonemal dyneins in physically distorting the microtubule. In my chapter 4, I use cryo-electron microscopy to demonstrate why dynein moves towards the minus-end and not the plus-end of microtubules. To do this, I image the structural difference between wild-type dynein and an engineered dynein that walks in reverse. Along with the work of collaborators, these results demonstrate that movement of a flexible element within the dynein motor domain called the linker is the key determinant of dynein directionality. In chapter 5, I investigate how herpes viruses hijack dynein. During cell entry, these viruses are transported by dynein over long distances from the cell periphery to the nucleus. The basis of the interaction between dynein and herpes is unknown. I use a combination of cell biology and mass-spectrometry to identify host proteins that are potentially recruited to the virus and in turn recruit dynein.

Acknowledgements

I would like to thank Dr Andrew Carter for supervision and advice throughout my PhD; everyone in the Carter lab past and present, especially Linas Urnavicius, Kai Zhang and Helen Foster for training at the start of my PhD; my second supervisor Dr Sjors Scheres and his PhD student Shaoda He for their software developments contributing to my project; my university supervisor Dr Colin Crump for advice on viral issues and time spent performing experiments with me; Dr Ahmet Yildiz and his PhD student Sinan Can for their collaborations.

Table of Contents

Abstract	4
Acknowledgements	5
Table of Contents	6
Table of figures	11
List of tables	14
Abbreviations	15
Chapter 1. Introduction	17
1.1 Microtubules	17
1.1.1 Organisation of microtubules in cells.....	18
1.1.2 Structure of the tubulin dimer	20
1.1.3 Lateral interactions between adjacent tubulin subunits in microtubules	20
1.1.4 Dynamic Instability.....	21
1.1.5 GTP hydrolysis at the longitudinal interface is linked to dynamic instability..	21
1.1.6 Interactions between microtubules and microtubule associated proteins	25
1.1.7 Microtubule dynamics are controlled at multiple levels.....	25
1.1.8 Doublet microtubules form the axoneme.....	26
1.2 Single-particle cryo-electron microscopy	28
1.2.1 Biological samples are vitrified for cryo-EM.....	28
1.2.2 Image Formation in Cryo-Electron Microscopy.....	29
1.2.3 Recent advances in resolution are due to direct electron detectors	30
1.2.4 Single-particle cryo-EM workflow	31
1.2.5 Microtubule structures by cryo-EM	32
1.3 Microtubule motors	35
1.3.1 Humans encode 45 different kinesin family members	35
1.3.2 Structure of the kinesin motor domain and its interaction with microtubules	36
1.3.3 Kinesin step in a directional hand-over-hand mechanism	37
1.3.4 The dynein family are all minus-end directed microtubule motors.....	38
1.3.5 Cytoplasmic dyneins are processive, long-distance motors.....	39
1.3.6 Axonemal dyneins power the ciliary beat	41
1.3.7 Dynein stepping is irregular	43
1.3.8 The conserved dynein motor domain belongs to the AAA+ superfamily	44
1.3.9 The nucleotide cycle of AAA1 controls dynein stepping	46
1.3.10 The nucleotide state of AAA1 is transmitted to the MTBD and linker domains.....	47
1.3.11 Mammalian dynein motility is dependent on dynactin and a cargo adaptor	51
1.3.12 Dynein, dynactin and cargo adaptors form multiple separate interactions.	54
1.4 Herpesvirus and dynein	57

1.4.1 Structure and organisation of α -herpesviruses	57
1.4.2 Herpes viruses enter cells through membrane fusion	59
1.4.3 Dynein-dependent retrograde transport delivers the capsid to the nucleus. 61	
1.4.4 The viral genome is ejected through the nuclear pore	64
1.4.5 Procapsids are assembled in the nucleus.....	64
1.4.6 Nuclear egress of new capsids occurs through primary envelopment.....	65
1.4.7 Egress occurs following anterograde transport.....	66
1.5 Aims	67
Chapter 2. Materials & Methods.....	68
2.1 Cloning and Protein Purifications	68
2.1.1 Touchdown PCR and Gibson Cloning.....	68
2.1.2 Purification of SRS Fusion proteins.....	68
2.1.3 Insect Cell Expression	69
2.1.4 Purification of ZZ-tagged proteins	70
2.1.5 Purification of Strep-tagged pUL36 and pUL37 constructs	70
2.1.6 SEC-MALS.....	71
2.1.7 Fluorescent labelling of SNAP tags	71
2.1.8 Purification of Dynactin	71
2.2 Electron Microscopy	72
2.2.1 13-protofilament microtubule polymerisation for EM.....	72
2.2.2 Preparation of grids with microtubules fully decorated by SRS constructs or monomeric motor domain	72
2.2.3 Data collection for fully decorated microtubule samples	73
2.2.4 Microtubule reconstruction in Chuff	74
2.2.5 Microtubule reconstruction in Relion	74
2.2.6 Subtraction and Symmetry expansion.....	76
2.2.7 Model Refinement.....	77
2.2.8 Analysis of microtubule distortion	77
2.2.9 Preparation of sparsely decorated Cyt1 and Cyt1 ^{RK+7hep} Grids	77
2.2.10 Imaging microtubules decorated with Cyt1 and Cyt1 ^{RK+7hep}	78
2.2.11 2D classification of Cyt1 and Cyt1 ^{RK+7hep} motor domains	78
2.3 Total Internal Reflection Microscopy	79
2.3.1 Polymerisation of labelled microtubules.....	79
2.3.2 Preparation of TIRF Chambers.....	79
2.4 Studies in Mammalian Cells	80
2.4.1 Mammalian Cell Transfections	80
2.4.2 Spinning disk microscopy	81
2.4.3 Pull-downs	81
2.4.4 Western Blots	82
2.4.5 Mass-spectrometry	83

2.4.6 Immunofluorescence	83
2.4.7 Virus	85
Chapter 3. Structural studies of dynein binding to microtubules.....	86
3.1 Background	86
3.2 Results	91
3.2.1 Dynein MTBD constructs used for structural determination by cryo-EM	91
3.2.2 Purification of Cyt1-SRS.....	92
3.2.3 Polymerisation of microtubules for Cryo-EM.....	92
3.2.4 Preparation of decorated microtubules for cryo-EM.....	93
3.2.5 Reconstructing microtubules in Chuff.....	94
3.2.6 Cyt1-SRS reconstruction from Chuff	95
3.2.7 Reconstruction of pseudosymmetrical microtubules in Relion	97
3.2.8 Reconstruction of Cyt1-SRS in Relion	98
3.2.9 Maximising resolution through particle expansion and subtraction	102
3.2.10 Refining a new model	104
3.2.11 Structure of the cytoplasmic dynein-1 microtubule-binding domain bound to microtubules	107
3.2.12 Validating the Cyt1-SRS structure with a dynein motor domain structure	110
3.2.13 Testing the microtubule processing workflow on other data	112
3.2.14 DNAH7 construct binding to microtubules.....	115
3.2.15 Structure of the DNAH7 MTBD bound to microtubules	117
3.2.16 The DNAH7 flap interacts with a second protofilament.....	119
3.2.17 A potential link between the DNAH7 MTBD and the β -tubulin E-hook.....	120
3.2.18 The DNAH7 MTBD changes the cross-sectional curvature of microtubules	121
3.2.19 DNAH7 binding to microtubules is cooperative	125
3.3 Discussion	126
3.3.1 How does dynein bind to microtubules?	126
3.3.2 The structure of the MTBD flap.....	127
3.3.3 Roles of distortion	129
3.3.4 Processing microtubules in Relion	130
Chapter 4. Using cryo-EM to investigate why an engineered dynein walks backwards	133
4.1 Background	133
4.2 Results	138
4.2.1 Purification of SRS-Cyt1 ^{RK} for cryo-EM	138
4.2.2 SRS-Cyt1 ^{RK} weakly decorates microtubules in cryo-EM	138
4.2.3 Cross-linking MTBD to the microtubule resulted in further protein aggregation	139
4.2.4 The stalk is not visible in a 3D reconstruction of microtubules partially decorated with Cyt1 ^{RK} -SRS	140

4.2.5 Engineered monomeric dynein motors stably bind to microtubules in cryo-EM	141
4.2.6 The polarity of non-13 protofilament microtubules can be determined by cryo-EM	144
4.2.7 The stalk angle of Cyt1 ^{RK+7hep} -MD has been flipped compared to wild-type	147
4.2.8 The AAA+ ring of Cyt1 ^{RK+7hep} -MD is rotated 180° compared to wild-type....	150
4.2.9 A crescent shaped AAA+ ring in Cyt1 ^{RK+7hep} -MD can be explained by a separate rotation.....	151
4.3 Discussion.....	153
4.3.1 Models for directionality	153
4.3.2 Motor movement	155
Chapter 5. Investigating the recruitment of Dynein to Herpesviruses.....	157
5.1 Background.....	157
5.2 Results.....	160
5.2.1 Full-length pUL36 is insoluble.....	160
5.2.2 A modified PCR protocol used to clone UL36.....	162
5.2.3 UL36 ^{ΔCBD} is soluble during affinity purification.....	164
5.2.4 N- and C-terminal truncations improve the stability of pUL36	166
5.2.5 pUL36 ⁷⁴³⁻²⁹⁸⁵ is monomeric	168
5.2.6 <i>TIRF Microscopy of pUL36</i>	169
5.2.7 Colocalisation of pUL36 and activated dynein complexes	171
5.2.8 pUL36 ^{ΔCBD} motility can be recapitulated in Vero cells.....	173
5.2.9 GFP-pUL36 ^{ΔCBD} is only motile in a subset of cells	174
5.2.10 Exploring methods to increase pUL36 motility in cells	176
5.2.11 pUL36 constructs used for pull-downs	180
5.2.12 Optimisation of GFP-trap pull-downs to reduce background binding	180
5.2.13 pUL36 ^{ΔCBD_MTS} pull-down and mass-spectrometry.....	182
5.2.14 pUL36 ^{ΔCBD} pull-down and mass-spectrometry.....	184
5.2.15 Validation of mass-spectrometry hits with immunofluorescence colocalisation.....	186
5.2.16 pUL36 ^{ΔCBD} colocalises with Cyclin B1	190
5.2.17 Testing the importance of RanBP2 for pUL36 motility with knock-downs	191
5.2.18 pUL36 interacts more strongly with Dynactin in the presence of RanBP2	194
5.2.19 HSV1 capsids colocalise with RanBP2 in the cytoplasm.....	196
5.3 Discussion.....	198
5.3.1 What conformation does pUL36 adopt?	198
5.3.2 Variability in pUL36 motility	198
5.3.3 A model for RanBP2-dependent motility of pUL36 in cells	199
5.3.4 Separate models for pUL36 transport	201
Chapter 6. References.....	204

Table of Figures

Figure 1.1 - Schematic of a microtubule	17
Figure 1.2 - Crystal structure of the tubulin dimer	19
Figure 1.3 - Lateral interactions between tubulin.....	21
Figure 1.4 - The tubulin active site is shared between two subunits.....	22
Figure 1.5 - Interactions of microtubule associated proteins with the microtubule	24
Figure 1.6 - Organisation of microtubules in axoneme	27
Figure 1.7 - Image formation in the electron microscope	29
Figure 1.8 - Reference matching in the super-particle seam-finding step.....	33
Figure 1.9 - Schematic of a kinesin-1	35
Figure 1.10 - Structure and microtubule binding of the kinesin motor domain.....	37
Figure 1.11 - Kinesin steps hand-over-hand	38
Figure 1.12 - Schematic of Cytoplasmic dynein-1	39
Figure 1.13 - Organisation of dyneins in the axoneme	42
Figure 1.14 - Dynein stepping is stochastic.....	44
Figure 1.15 - Structure of a dynein motor	45
Figure 1.16 - The AAA1 active site is flexible around a hinge	46
Figure 1.17 - The nucleotide state of AAA1 is transmitted through the AAA+ ring.....	47
Figure 1.18 - Nucleotide-dependent change in linker conformation	48
Figure 1.19 - Nucleotide dependent changes in stalk registry.....	49
Figure 1.20 - A conformational change in the MTBD controls microtubule binding and release	50
Figure 1.21 - Structural changes in the dynein motor controlled by AAA1	51
Figure 1.22 - Behaviour of Dynein in single-molecule motility assays.....	52
Figure 1.23 - Schematic of the dynactin complex.....	52
Figure 1.24 - Mode of interaction between dynein, dynactin and BICD2N	54
Figure 1.25 - Structural organisation of the HSV-1 capsid and inner tegument	58
Figure 1.26 - Viral entry occurs through membrane fusion.....	60
Figure 1.27 - Dynein-dependent retrograde transport delivers capsids to the nucleus.....	62
Figure 1.28 - Viral egress requires kinesin transport	65
Figure 2.1 -Data collection parameters for large cryo-EM datasets	74
Figure 3.1 - Stalk and buttress movements that result in a low-microtubule affinity state.....	86
Figure 3.2 - Established structures of cytoplasmic dynein-1 MTBD	87
Figure 3.3 - Sequence alignment of human dynein MTBDs	89
Figure 3.4 - Schematic of a dynein MTBD/SRS fusion construct	91
Figure 3.5 - Purification of Cyt1-SRS	92
Figure 3.6 - Decoration of microtubules by Cyt1-SRS.....	93
Figure 3.7 - Workflow for reconstructing decorated microtubules in Chuff.....	95
Figure 3.8 - Assessment of map quality from Chuff refinement of Cyt1-SRS	96
Figure 3.9 - Operators of non-crystallographic symmetry	97

<i>Figure 3.10 - Workflow for reconstructing microtubules in Relion</i>	99
Figure 3.11 - The effect of initial sampling rate and application of local symmetry on seam finding in Relion	101
Figure 3.12 - FSC curves for C1 and symmetrised Cyt1-SRS map in Relion	102
Figure 3.13 - Strategies to specifically improve the resolution of the Cyt1-SRS MTBD.....	103
Figure 3.14 - Final Cyt1-SRS map and assessment of local map quality.....	105
Figure 3.15 - Comparison between newly refined and reference tubulin models.....	106
Figure 3.16 - Comparison of the newly refined high-affinity Cyt1-SRS model with previous models.....	108
Figure 3.17 - Potential interactions between the MTBD and the microtubule.....	109
Figure 3.18 - Processing pipeline for Cyt1-MD bound to microtubules	110
Figure 3.19 - Structure of a dynein motor domain MTBD bound to microtubules	111
Figure 3.20 - Comparison between symmetrised EB3 maps.....	113
Figure 3.22 - Comparison between Cytoplasmic Dynein-1 and DNAH7 sequences.....	115
Figure 3.23 - Purification of DNAH7-85:82-SRS.....	116
Figure 3.24 - Microtubule decoration of DNAH7 constructs in cryo-EM	116
Figure 3.25 - Processing pipeline for DNAH7-SRS	117
Figure 3.26 - The DNAH7 MTBD structure and refined model.....	118
Figure 3.27 - Interaction between the DNAH7 flap and a second protofilament	120
Figure 3.28 - A second link between DNAH7 and the adjacent protofilament	121
Figure 3.29 - The effect of symmetry on the refined DNAH7 map using regular and refined operators.....	122
Figure 3.30 - Analysis of protofilament angles in the Cyt1-SRS and DNAH7-SRS maps	123
Figure 3.31 - Distortion of microtubules induced by DNAH7-SRS.....	124
Figure 3.32 - TIRF microscopy measurements of MTBD binding to microtubules	125
Figure 3.33 - A steric clash prevents dynein binding in the low-affinity state	126
Figure 3.34 - MTBD sequence alignment in regions that interact with the microtubule.....	127
Figure 3.35 - Location of flap containing dyneins within the axoneme	128
Figure 3.36 - Three Euler angles describe a particles orientation	131
<i>Figure 4.1 - The linker swing during the dynein power stroke points towards the minus-end.</i>	133
Figure 4.2 - Reversing dyneins stalk angle is predicted to change the LSV	135
Figure 4.3 gliding activity of Dyn ^{RK}	136
Figure 4.4 - Cyt1 ^{RK} -SRS preparation.....	138
Figure 4.5 - Cyt1 ^{RK} -SRS microtubule decoration.....	139
Figure 4.6 - Chemical cross-linking of SRS-Cyt1 ^{RK} to microtubules.....	140
Figure 4.7 - The Cyt1 ^{RK} -SRS stalk is not resolved in a 3D reconstruction	141
Figure 4.8 - The Cyt1 ^{RK+7hep} modifications are predicted to reverse the LSV direction.....	142
Figure 4.9 - Dynein motors decorating microtubules in cryo-EM	144
Figure 4.10 - Determining microtubule polarity in cryo-EM images	145
Figure 4.11 - Data processing strategy to determine orientation of motor domains bound to microtubules	147
Figure 4.12 - Focussed sub-classification of Cyt1 and Cyt1 ^{RK+7hep}	148
Figure 4.13 - Quantification of motor domain stalk angles and stalk lengths.....	149

Figure 4.14 - 2D classification of the Cyt1 and Cyt1 ^{RK+7hep} AAA+ ring	150
Figure 4.15 - Crescent shaped appearance of Cyt1 ^{RK+7hep} can be explained by a 32° rotation .	152
Figure 4.16 - Dyn ^{RK+7hep} walks towards the microtubule plus-end	153
Figure 4.17 - Directionality introduced in the priming stroke	155
Figure 5.1 - Subdomains of pUL36	158
Figure 5.2 - pUL36 ^{FL} is almost completely insoluble following Sf9 expression	161
Figure 5.3 - Schematic of Gibson Cloning Protocol	162
Figure 5.4 - A modified PCR protocol for UL36	163
Figure 5.5 - Affinity purification and gel filtration of pUL36 ^{ΔCBD}	165
Figure 5.6 - Purification of N- and C-terminal truncations of pUL36	166
Figure 5.7 - SEC-MALS of pUL36 ⁷⁴³⁻²⁹⁸⁵	168
Figure 5.8 - Single Molecule motility assay of pUL36 constructs	170
Figure 5.9 - pUL36 ⁷⁴³⁻²⁹⁸⁵ binds to and diffuses on microtubules	171
Figure 5.10 - Two-colour motility assay of TMR-Dynein and Alexa647-UL36 ⁷⁴³⁻²⁹⁸⁵	172
Figure 5.11 - Motility of pUL36 in Vero cells	173
Figure 5.12 - Variability of GFP-UL36 ^{ΔCBD} motility in Vero cells	176
Figure 5.13 - Effect of K442 ubiquitination on pUL36 motility	177
Figure 5.14 - pUL36 ^{ΔCBD} is not motile when co-expressed with pUL37	178
Figure 5.15 - pUL36 ^{ΔCBD_MTS} clusters mitochondria	179
Figure 5.16 - pUL36 ^{ΔCBD} is immotile in human cell lines	180
Figure 5.17 - Optimisation of pUL36 ^{ΔCBD_MTS} pull-down assau	181
Figure 5.18 - Triplicate pull-down of pUL36 ^{ΔCBD_MTS} in HeLa cells	182
Figure 5.19 - Proteins enriched in pUL36 ^{ΔCBD_MTS} pull-down mass-spectrometry	183
Figure 5.20 - Triplicate pull-down of pUL36 ^{ΔCBD} in Vero cells	185
Figure 5.21 - Proteins enriched in pUL36 ^{ΔCBD} pull-down mass-spectrometry from Vero cells..	186
Figure 5.22 - Assessing colocalisation between pUL36 and pull-down hits with immunofluorescence	188
Figure 5.23 - Nuclear pore associated proteins colocalise with pUL36 in the cytoplasm	189
Figure 5.24 - Colocalisation between pUL36 and Cyclin B1	191
Figure 5.25 - Cyclin B1 expression is associated with pUL36 ^{ΔCBD} activity	191
Figure 5.26 - Two different knockdown strategies for RanBP2	192
Figure 5.27 - Colocalisation between RanBP2 and pUL36 ^{ΔCBD_MTS} after RanBP2 knockdown	194
Figure 5.28 - pUL36 ^{ΔCBD} interacts more strongly with dynein when RanBP2 is present	196
Figure 5.29 - Colocalisation between HSV1 and RanBP2	197

List of tables

Table 1 - Model refinement validation statistics for Cyt1-SRS.....	107
Table 2 - Model refinement validation statistics for DNAH7-SRS	119

Abbreviations

aa	amino acids
AAA+	ATPases associated with diverse cellular activities
ADP	adenosine diphosphate
ATP	adenosine triphosphate
<i>C. reinhardtii</i>	<i>Chlamydomonas reinhardtii</i>
CBD	capsid binding domain
CC1/2	Coiled coil 1/2 (in reference to the dynein stalk)
Cryo-EM	cryo electron microscopy
Cryo-ET	cryo electron tomography
CTF	contrast transfer function
CV	column Volume
Da	Dalton
DLIC	dynein light intermediate chain
DNA	deoxyribonucleic acid
DTT	dithiothreitol
DUB	deubiquitinase domain
<i>E. coli</i>	<i>Escherichia coli</i>
EDTA	ethylene diamine tetraacetic acid
EGTA	ethylene glycol tetraacetic acid
FSC	Fourier shell correlation
GFP	green fluorescent protein
GDP	guanosine diphosphate
GTP	guanosine triphosphate
HSV1/2	Herpes Simplex Virus Type 1/2
IDA	inner dynein arm
IF	immunofluorescence
IFT	intraflagellar transport
MAP	microtubule associated protein
MOI	multiplicity of infection
MS	mass spectrometry
MT	microtubule
MTBD	microtubule binding domain

MTOC	microtubule organizing center
MTS	mitochondrial targeting sequence
NCS	non crystallographic symmetry
NSAF	normalised spectral abundance factor
ODA	outer dynein arms
ORF	open reading frame
PCR	polymerase chain reaction
PDB	Protein Data Bank
PEI	polyethylenimine
PF	protofilament
PMSF	phenylmethylsulfonyl fluoride
PrV	Pseudorabies Virus
pUL36	Protein product of UL36 (see UL36 below)
<i>S. cerevisiae</i>	<i>Saccharomyces cerevisiae</i>
SDS-PAGE	sodium dodecyl sulfate polyacrylamide gel electrophoresis
SEC-MALS	size-exclusion chromatography multi-angle light scattering
SRS	seryl tRNA-synthetase
TIRF	total internal fluorescence
UL36	36 th gene in the unique long (UL) segment of the HSV1 genome (aka VP1/2)

Chapter 1. Introduction

1.1 Microtubules

Microtubules are polymeric protein filaments that form an extended, organized cytoskeletal network in eukaryotic cells. They are formed of individual protofilaments that interact laterally to form a closed circular tube 25 nm in diameter (**Figure 1.1A-D**, (Desai and Mitchison, 1997)). Each protofilament is a polymer of constitutive α - and β -tubulin heterodimers organized head-to-tail (**Figure 1.1C**). Microtubules are therefore polar, with β -tubulin exposed at the 'plus-end' and α -tubulin at the 'minus-end'. Microtubules polymerise up to 3-fold faster from the plus-end compared to the minus end (Mitchison and Kirschner, 1984; Ti et al., 2016).

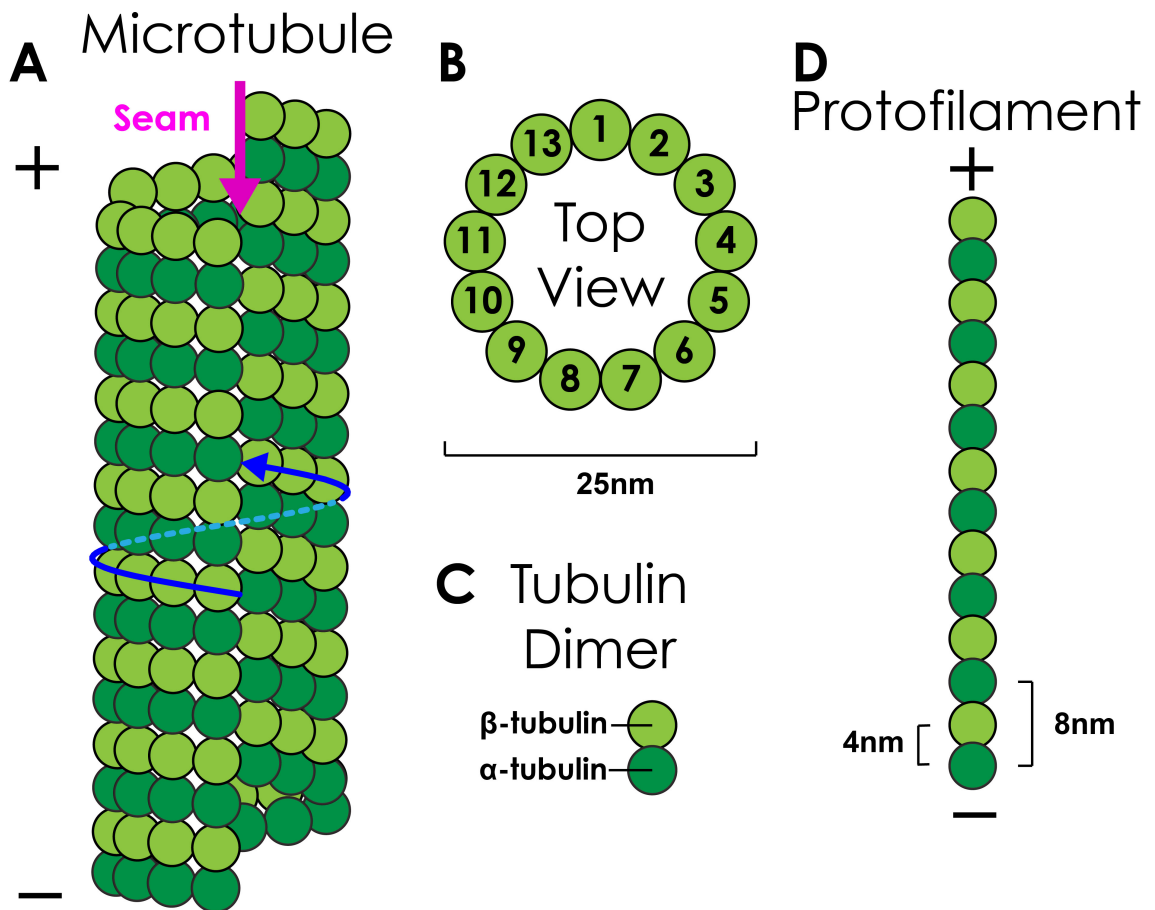


Figure 1.1 - Schematic of a microtubule

*Cartoon representations of a microtubule. α - and β -tubulin dark and light green respectively **A** - A full 13-protofilament microtubule viewed from the side. Position of the seam, where α - and β -tubulin interact laterally, indicated with magenta arrow. Lateral interactions traced through 360° (blue arrow) results in a total rise of 3 tubulin monomers. **B** - Top view of microtubule. **C** - Side view of a single tubulin dimer. **D** - A single protofilament. Plus (+) and minus (-) ends indicated*

α - and β -tubulin are closely related, containing 40% sequence identity and 60% sequence similarity (Burns, 1991). They both contain a GTP-binding site, although hydrolysis only occurs in β -tubulin (Weisenberg et al., 1968; Desai and Mitchison, 1997). In vitro polymerized tubulin creates microtubules with different numbers of protofilaments, highlighting the flexible lateral interactions between protofilaments (Pierson et al., 1978). However, in mammalian cells microtubules all possess 13-profilaments (Tilney et al., 1973), with homotypic lateral interactions between protofilaments (i.e. α -tubulin to α -tubulin or β -tubulin to β -tubulin). Microtubules in the cell are 3-start helices, meaning that there is a rise of 3-tubulin monomers as lateral lattice interactions are traced 360° (blue arrow, **Figure 1.1A**, (Amos and Klug, 1974)). This results in a single continuous line of asymmetry, referred to as the seam, where heterotypic (α -to- β) lateral interactions occur (magenta arrow, **Figure 1.1**).

Microtubules perform both structural and organizational roles within the cell. The mitotic spindle consists of two opposing microtubule arrays, and microtubules are fundamentally important at every step of mitosis (Meunier and Vernos, 2012). Microtubules form the basis for the axoneme (Amos and Klug, 1974), and are therefore essential for processes such as motility of sperm cells, removal of mucus from the trachea, and transport of oocytes out of the ovary (Mitchison and Valente, 2017). In the cytoplasm of interphase cells, microtubules form a network of tracks for cytoskeletal motors to transport diverse cargoes throughout the cell (Franker and Hoogenraad, 2013).

1.1.1 Organisation of microtubules in cells

In vitro, tubulin spontaneously polymerises into microtubules above a threshold concentration (~10 μ M, depending on conditions) (Fyngson et al., 1994; Mitchison and Kirschner, 1984). However the key energetic barrier for polymerization is initial nucleation, and polymerization from pre-existing microtubules can occur at lower concentrations (Fyngson et al., 1994). Accordingly, the cell controls microtubule organisation by controlling the location and level of microtubule nucleation. The primary microtubule nucleator of the cell is the γ -tubulin Ring Complex (γ TuRC) (Roostalu and Surrey, 2017), a ring shaped scaffold topped with the tubulin isoform γ -tubulin (Kollman et al., 2015). The scaffold arranges γ -tubulin in a 13-fold ring with the same rise as mature microtubules, making it an effective template for polymerisation.

Microtubules grow plus-end out from the γ TuRC with up to 600-fold greater efficiency than tubulin alone (Kollman et al., 2015).

γ TuRC complexes are primarily recruited to the peri-centrosomal matrix, making the centrosome the main microtubule-organising centre (MTOC) in most cells (Teixidó-Travesa et al., 2012). This leads to a radial array of microtubules with the plus-end at the cell periphery. However, many differentiated cells have specialized sites of microtubule nucleation independent from a centrosomal MTOC. For example, in the axon of neurons microtubules are all oriented with the plus-end pointing away from the cell body (Tas et al., 2017; Yau et al., 2016). In polar epithelial cells, the microtubule minus-ends are anchored at the luminal surface, and point down towards the basal surface (Meads and Schroer, 1995). Organisation of the microtubule cytoskeleton is fundamental to the activities of unidirectional microtubule motors.

To achieve acentrosomal microtubule organization, γ TuRC complexes can be localized to different subcellular locations, such as axons (Sánchez-Huertas et al., 2016). However, nucleation can also occur independently of the γ TuRC. Two proteins, Tpx2 and XMAP215, are thought to aid polymerization by bringing two tubulin dimers together longitudinally (Nithianantham et al., 2018; Zhang et al., 2017b). These two proteins and a centrosomal protein (SPD-5) are potent microtubule nucleators *in vitro* (Woodruff et al., 2017).

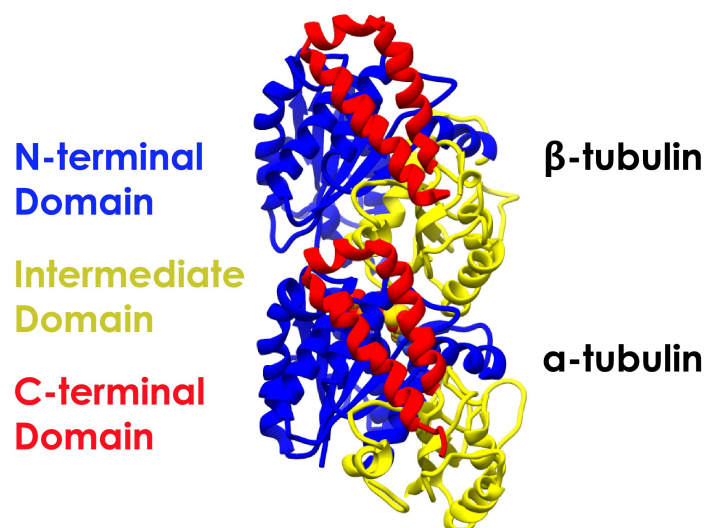


Figure 1.2 - Crystal structure of the tubulin dimer

The crystal structure of tubulin dimers from zinc sheets (PDB 1JFF, (Löwe et al., 2001)), coloured according to its subdomain and viewed as from the exterior of the microtubule.

1.1.2 Structure of the tubulin dimer

A high-resolution structure of the tubulin dimer was initially difficult to obtain due to the propensity of the sample to polymerise rather than crystallise. However, upon addition of zinc ions tubulin forms 2D crystallographic sheets of antiparallel protofilaments packed together (Baker and Amos, 1978). These sheets were subjected to 2D electron crystallography, resulting in a 3.7Å structure (Nogales et al., 1998a) and later a more complete 3.5Å structure (Löwe et al., 2001).

These structures showed that α - and β -tubulin adopt essentially identical folds, with only small divergences in some loops. Three structural subdomains were established (**Figure 1.2**). The N-terminal domain (Blue, **Figure 1.2**) forms a fold similar to the classic nucleotide-binding Rossmann motif, consisting of two tandem BABAB motifs (where B is a β -strand and A is an α -helix), and contains the core of a nucleotide binding pocket. The intermediate domain is made up of a mixed four-stranded sheet with accompanying helices (yellow, **Figure 1.2**). The C-terminal domain consists of the two helices that form the outer surface of the microtubule (Nogales et al., 1999), as well as the unstructured, highly acidic C-terminus (red, **Figure 1.2**).

1.1.3 Lateral interactions between adjacent tubulin subunits in microtubules

The lateral interactions in the crystal structure were not native, as the adjacent protofilaments in zinc sheets are antiparallel. Initial low-resolution and subsequent high-resolution cryo-EM has since identified the structural elements involved in lateral interactions in microtubules (Nogales et al., 1999; Zhang et al., 2015a). The only lateral interactions are formed by an aromatic residue in the “M-loop” (S7-H9 loop) of one subunit fitting in a pocket formed by the H2-S3 and H1'-S2 loops of the adjacent subunit (**Figure 1.3A/B**). These loops are well conserved in α - and β -tubulin, and so can form across the seam as well (Zhang et al., 2015b). The three loops are all flexible relative to the core of the tubulin dimer, allowing the microtubule to accommodate various protofilament numbers.

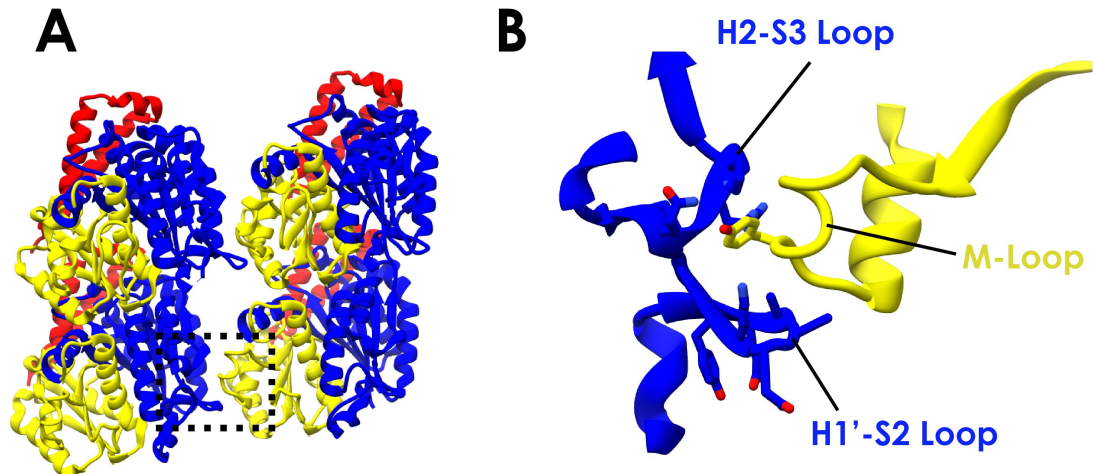


Figure 1.3 - Lateral interactions between tubulin

A - A pair of tubulin dimers built into a high resolution cryo-EM map (PDB 3JAR), viewed from the inside of the microtubule. Coloured by subdomains as in Figure 1.2. B - The only lateral interactions between tubulins is from the M-loop fitting into a hydrophobic pocket formed by H2-S3 and H1'-S2 loops

1.1.4 Dynamic Instability

Microtubules polymerization is subject to dynamic instability (Horio and Hotani, 1986; Mitchison and Kirschner, 1984). This means that even above the critical tubulin concentration at which polymerization can occur, some of the microtubules in a population will rapidly depolymerize. Mitchison and Kirschner predicted that the switch from polymerisation to depolymerisation (“catastrophe”) is controlled by a GTP-cap. If hydrolysis of the exchangeable GTP occurred in enough of the subunits near the cap, the lattice destabilises and falls apart. Hydrolysis further away from the cap had already occurred, so the weakened lattice continues to fall apart like dominoes. Snapshots from recent cryo-EM studies, presented below, have lead to a mechanistic model for dynamic instability in microtubules.

1.1.5 GTP hydrolysis at the longitudinal interface is linked to dynamic instability

The nucleotide pocket is shared at the longitudinal interface between two tubulin subunits (Figure 1.4A). The β -tubulin nucleotide site is exposed at the plus-end of the microtubule (Figure 1.4A, (Nogales et al., 1999)), and is only completed by the α -tubulin residue E254 (Figure 1.4C). As such, nucleotide hydrolysis is only catalyzed following addition of another

tubulin dimer. The residue corresponding to E254 that β -tubulin contributes to the α -tubulin active site is a lysine (**Figure 1.4C**), which stabilizes rather than hydrolyses GTP.

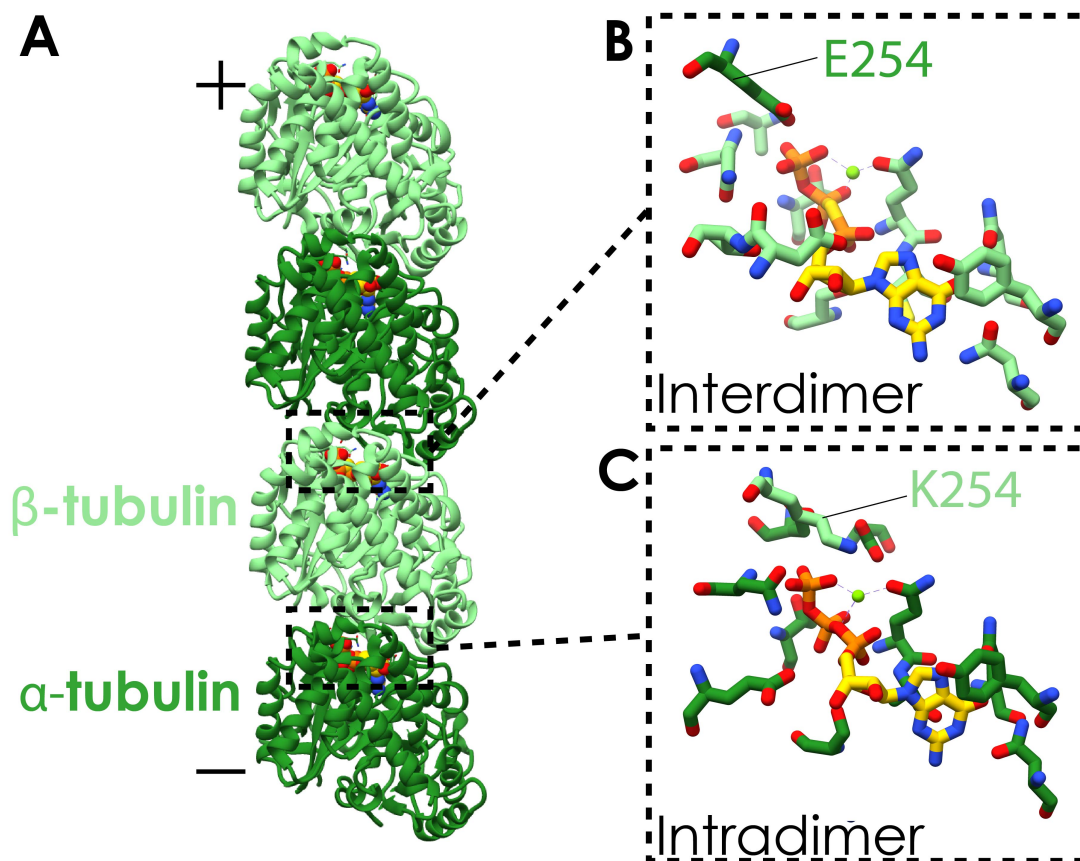


Figure 1.4 - The tubulin active site is shared between two subunits

A - Two longitudinally interacting tubulin dimers stabilised with GMPCPP (PDB 6EVW, (Manka and Moores, 2018)). **B** - The β -tubulin active site coordinates most of the GMPCPP with β -tubulin residues, but α -tubulin from the next dimer contributes a glutamate residue (E254) that coordinates a water molecule during catalysis. **C** - The equivalent residue that β -tubulin contributes to the α -tubulin active site is lysine (K254), which stabilises the gamma phosphate in the active site.

Cryo-EM shows that the nucleotide state at the exchangeable interdimer site (i.e. the active site of β -tubulin) controls the structure of the microtubule lattice (Manka and Moores, 2018; Zhang et al., 2015a, 2018c). The key structural difference following GTP hydrolysis is a compression of the longitudinal (axial) repeat from 83Å to 81Å. Dissociation of the gamma-phosphate creates a void that pulls the α -tubulin above the interdimer interface towards the β -tubulin below. However, the N-terminal and intermediate domains move unevenly (2Å vs 1Å respectively). The N-terminal domain contains the H1'-S2 and H2-S3 loop, and the intermediate domain contains the M-loop (**Figure 1.3B**). As such, the elements involved in the

lateral interactions become more distant, making their interactions weaker (Manka and Moores, 2018). The microtubule lattice is under constant strain since the tubulin dimer is naturally curved at the intradimer interface (Brouhard and Rice, 2014), but is forced to be straight by the lateral interactions. When the lateral interactions become weaker in the GDP-bound state the strain overcomes the strength of the lattice and the microtubule depolymerizes. The absence of lateral contacts allows the dimers to return to a native curved state, weakening longitudinal interactions and resulting in depolymerisation (Brouhard and Rice, 2014).

The GTP cap model states that microtubules polymerise when the plus-end is capped by a layer (or multiple layers) of GTP-tubulin. If the GTP hydrolysis occurs faster than the addition of new subunits, the weaker GDP lattice peels away from the ends (Brouhard and Rice, 2018; Mitchison and Kirschner, 1984). Longitudinal constraints prevent GDP-tubulin away from the tip from dissociating. High resolution TIRF microscopy of growing microtubules diluted into tubulin-free buffer showed that the faster the microtubule is polymerizing at the point of dilution, the longer delay before catastrophe (Duellberg et al., 2016). This suggests that the GTPase activity is essentially constant, and faster polymerization leads to a longer and more stable cap. The GTP cap is therefore a dynamic structure, with catastrophe occurring if polymerization can not keep up with hydrolysis.

The microtubule stabilizing agent paclitaxel (taxol) prevents microtubules from depolymerising (Arnal and Wade, 1995). It binds in a wedge between the N-terminal and intermediate domains of β -tubulin (Nogales et al., 1998b). Taxol is thought to stabilize microtubules by preventing the dimer from adopting a curved conformation (Elie-Caille et al., 2007; Kellogg et al., 2017). Therefore, when the lateral interactions are weakened, the strain that would normally drive depolymerization is relaxed, and the microtubule stays intact.

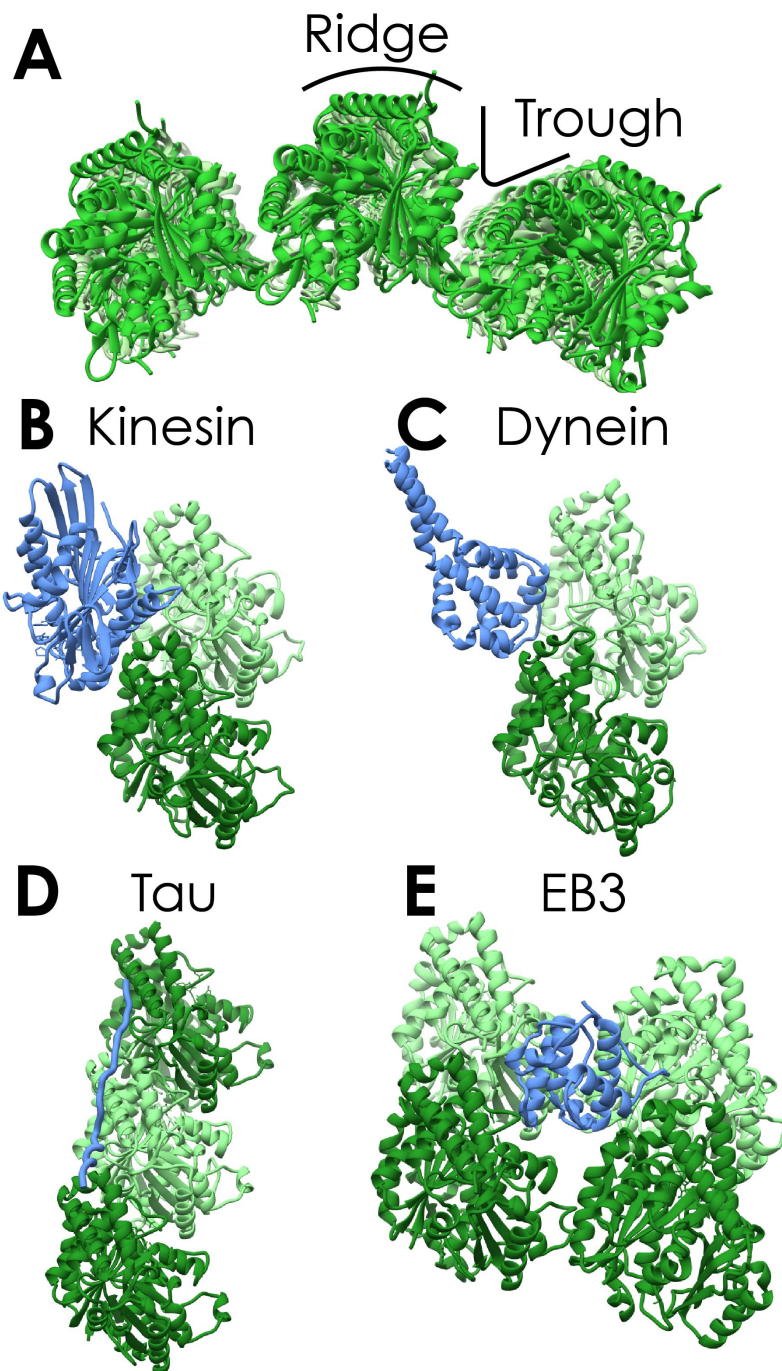


Figure 1.5 - Interactions of microtubule associated proteins with the microtubule

A - Atomic models for tubulin (PDB 5syf) arranged as in the microtubule and viewed down the microtubule long axis, showing a ridge on each protofilament and a trough separating adjacent protofilaments. **B** - Cryo-EM model of a kinesin-1 motor domain bound to microtubules (now as viewed from the exterior of the microtubule (PDB 3j8Y). **C** - Cryo-EM model of cytoplasmic dynein-1 MTBD bound to microtubules (PDB 3J1T). **D** - Cryo-EM model of tau bound to microtubules (PDB 6CVN). **E** - Cryo-EM model of EB3 bound to microtubules (PDB 3JAR)

1.1.6 Interactions between microtubules and microtubule associated proteins

In microtubules, each protofilament forms a ridge, separated from the adjacent protofilament by a trough (**Figure 1.5A**). Cryo-EM structures show that microtubule-associated proteins (MAPs) explore the full-extent of the microtubule lattice. The two families of microtubule motors, kinesin and dynein, both bind to the microtubule on top of the ridge, at the intradimer interface (**Figure 1.5B-C**) (Redwine et al., 2012; Shang et al., 2014). Tau stretches over three tubulin monomers, meaning that it samples both the intradimer and interdimer interfaces (**Figure 1.5D**) (Kellogg et al., 2018). Finally, a group of MAPs including EB3, Doublecortin and CAMSAP (Calmodulin-regulated spectrin-associated protein) straddle two ridges and bind in the trough, where they can contact four tubulin monomers simultaneously (**Figure 1.5E**) (Zhang et al., 2015a; Moores et al., 2006; Atherton et al., 2017).

Proteins can also make transient or unstructured interactions with the microtubule. The C-termini of α - and β -tubulin are disordered stretches of ~ 20 (depending on the isoform) mostly acidic residues (Ludueña, 1993). These C-terminal tails create a strong negatively charged surface on the microtubule. The dynactin complex subunit p150 has C-terminal basic and CAP-Gly domains that recruit the complex to the microtubule (Schroer, 2004). They form a strong but disordered electrostatic interaction with the C-terminal tails of tubulin (Wang et al., 2014a).

1.1.7 Microtubule dynamics are controlled at multiple levels

The organization of the microtubule cytoskeleton and the way it associates with microtubule-associated proteins (MAPs) can be fine-tuned at multiple levels. Expression of different tubulin isoforms, which mostly differ in the C-terminal tail (Ludueña, 1993) is controlled throughout development (Lewis et al., 1985). Tubulin dimers with a specific combination of tubulin isoforms ($\alpha 1B \beta I/IVb$) polymerise and depolymerise at quicker rates to mixed isoform brain tubulin, and undergo catastrophe less frequently (Vemu et al., 2017). Controlling these dynamics allows the cell to control the balance between dynamic microtubules rapidly exploring the cytoplasm, and stable microtubules maintaining a longer-term organisation. Furthermore, there are multiple reports of microtubule-associated proteins (MAPs) preferentially binding to different tubulin isoforms (Bonnet et al., 2001; Law et al., 2014; Raff et al., 2008)

Tubulin is also subject to a wide range of post-translational modifications. Acetylation of K40 on the luminal surface of the α -tubulin makes only subtle structural differences, nominally strengthening lateral interactions (Eshun-Wilson et al., 2019). However, microtubules with K40 acetylation are much more stable and resistant to mechanical strain (Xu et al., 2017). Tubulin in the axoneme is highly enriched for acetylation (L'Hernault, 1983).

Other post-translational modifications are used to modulate the interaction of MAPs with the microtubule. For example, the removal of the C-terminal tyrosine residue of α -tubulin (detyrosination) almost completely abolishes the initiation of dynein motility (McKenney et al., 2016). Furthermore, kinesin-1 and kinesin-3 family members have preferential attachment to acetylated and tyrosinated microtubules respectively (Tas et al., 2017).

Some microtubule-associated proteins are used to control the organization of the microtubule cytoskeleton. End-binding (EB) proteins specifically bind to the plus-ends of microtubules, and promote a lattice compaction that leads to higher catastrophe rates (Duellberg et al., 2016; Zhang et al., 2018c). Many microtubule interacting proteins (e.g. tau, doublecortin) stabilize the lattice and protect against catastrophe (Kadavath et al., 2015; Moores et al., 2004). Two microtubule severing proteins, katanin and spastin create partial breakages in the microtubule lattice (Vemu et al., 2018). However, this is thought to stabilize the microtubule in the long-term by allowing GTP-tubulin to be incorporated into the side of the microtubule (Aumeier et al., 2016).

1.1.8 Doublet microtubules form the axoneme

Cilia are sub-cellular structures that project up to 10 μm out of a cell. Primary cilia are present in most mammalian cells, and are thought to be important for organizing the reception of extracellular signals (Lee and Gleeson, 2010; Satir et al., 2010). In motile cilia, the entire structure beats in a regular oscillation, powering movement of the motile cells, or creating liquid flow on epithelial cells (Mitchison and Valente, 2017). The axoneme is the organized microtubule core that forms the structural basis of cilia. Microtubules in the axoneme have a second 10-protofilament tubule appended to the side of a regular 13-protofilament microtubule, and so are called microtubule doublets (**Figure 1.6A**, (Amos and Klug, 1974b)).

The axoneme typically contains a ring of 9 microtubule doublets, and in motile cilia a central pair of regular microtubules (**Figure 1.6B**, (Ishikawa, 2016)). A centriole at the base of the axoneme forms the template for this nine-fold organization, with microtubules growing plus-end out (Werner et al., 2017).

In motile cilia, the beat is powered by the interaction of the microtubule doublets with axonemal dyneins. These are microtubule motors that are immobilised on the A-tubule of one microtubule doublet, but able to move on the other (**Figure 1.6B**). When only a subset of doublets have active dyneins at once, this creates relative movement between adjacent doublets, resulting in a beating motion in the cilium (Lin and Nicastro, 2018; Satir et al., 2014).

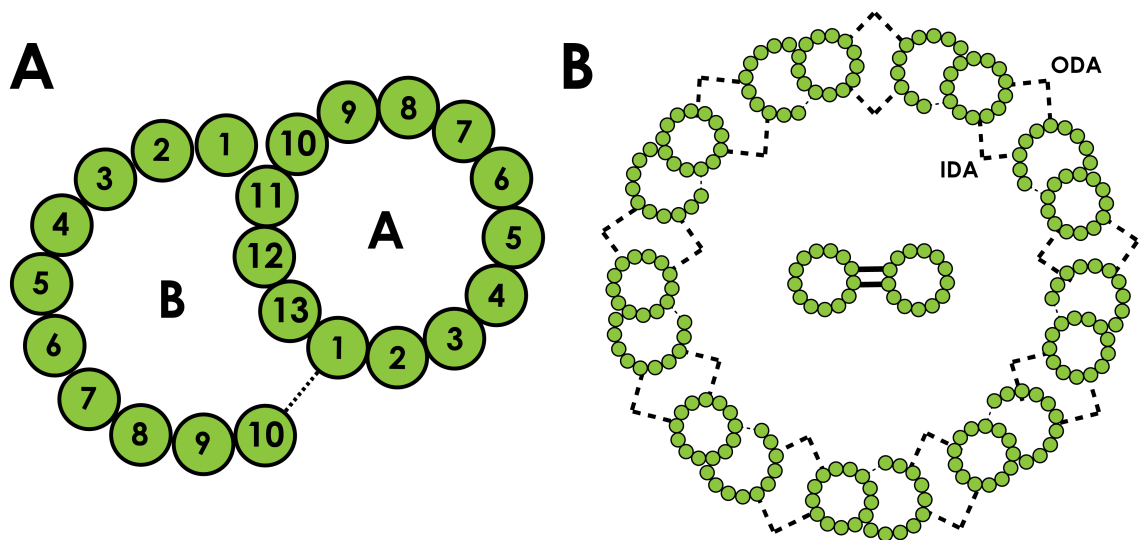


Figure 1.6 - Organisation of microtubules in axoneme

A - Doublet microtubules in the axoneme consist of a regular 13-protofilament microtubule (A-tubule) with a second 10-protofilament B-tubule appended. B - Nine microtubule doublet arrange in a ring to form the axoneme. In motile cilia, a central pair of two 13-protofilament microtubules is present, as are outer dynein arms (ODA) and inner dynein arms (IDA) that cross-link adjacent doublets.

1.2 Single-particle cryo-electron microscopy

Cryo-electron microscopy (cryo-EM) of frozen hydrated biological specimens was developed in 1984 (Adrian et al., 1984), but has only recently been developed into a technique capable of routinely determining structures at atomic resolution. It involves a biological macromolecule being rapidly vitrified in its native state and imaged in the electron microscope at cryogenic temperature. From the resulting images, particles in different orientations are aligned and averaged in three-dimensional space to form a reconstruction.

1.2.1 Biological samples are vitrified for cryo-EM

Imaging biological samples by cryo-EM needs to be performed on frozen hydrated samples to prevent desiccation in the microscope vacuum. Cryogenic temperatures also reduce the amount of radiation damage to the sample. Freezing is routinely performed by applying a drop of sample to an EM grid, blotting it to form a thin film and rapidly plunging it into liquid ethane (Adrian et al., 1984). Liquid ethane has a thermal conductivity up to 400 times greater than liquid nitrogen (Dobro et al., 2010), and thus vitreously freezes the water before it can order into a crystalline state. Crystalline water is unsuitable for imaging as it strongly scatters electrons and thus obscures the biological sample. Furthermore, the shear forces formed during the formation of crystalline ice can destroy or damage the sample.

Cryo-electron tomography (cryo-ET) shows that the majority of samples adsorb to the air-water interface during freezing (Noble et al., 2018). The surface tension at the air-water interface can cause particles to adopt a preferred orientation, or even denature them (Glaeser and Han, 2017). This can be offset by the addition of detergents to reduce the surface tension, or adsorbing the sample to a thin film of hydrophilic carbon or graphene to keep it away from the air-water interface (Glaeser, 2018). Nevertheless, surface effects still represent a common hurdle for many samples. Interestingly, cryo-ET suggests that microtubules generally stay away from the air-water interface without the need for detergent or carbon supports (Atherton et al., 2018)

1.2.2 Image Formation in Cryo-Electron Microscopy

The electron beam of the electron microscope is produced by an electron gun. This is typically a tungsten or LaB₆ filament, or a field-emission gun (FEG). The FEG is the electron source of choice in higher-end microscopes due to its higher brightness and coherence. It consists of a sharpened tungsten crystal coated in ZrO₂, with electrons extracted by an external electric field (Orlova and Saibil, 2011). The electrons are subsequently accelerated into the main column of the microscope by attraction to an anode below the electron source (Egerton, 2005)

The divergent accelerated electrons are focused onto the sample with the condenser lenses. A TEM lens is an electromagnet surrounding the beam, creating an electric field that converges the electrons in the beam (Egerton, 2005; Reimer, 2013). The majority of the incident electrons pass through the sample without interaction (**Figure 1.7A**) (Orlova and Saibil, 2011). However, they experience a deflective force if they interact with the electric field of an atom in the sample (elastic scattering) (**Figure 1.7A**).

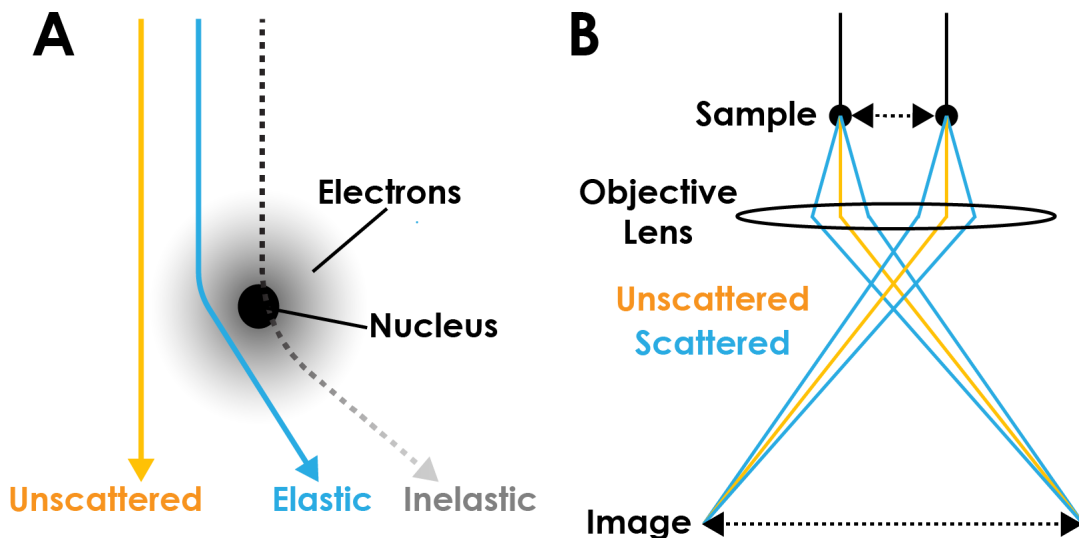


Figure 1.7 - Image formation in the electron microscope

A - Interaction between atoms in the sample and the electron beam. Most electrons pass through the sample without scattering (unscattered, orange). Elastic scattering occurs when an incident electron is deflected by the electric field of an atom (elastic, blue). Inelastic scattering occurs when an incident electron collides with an atomic nucleus, transferring energy to the sample (inelastic, black to grey). **B** - A simplified diagram of image formation in the electron microscope. Scattered and unscattered electrons are focussed to the same point in the image plane. The path difference in the scattered beam compared to the unscattered beam produces a phase difference that leads to interference. In reality, between the objective lens and image plane, there are a series of intermediate and projector lenses that increase the magnification.

The unscattered electrons and elastically scattered electrons are focused by the objective and projector lenses to the same point in the image plane (**Figure 1.7B**). The path of the scattered electrons is longer than that of the unscattered electrons, creating a phase difference when they converge in the image (Dubochet et al., 1988; Egerton, 2005). This creates interference between the scattered and unscattered electrons, which manifests as positional amplitude differences proportional to the scattering potential in the specimen.

One of the biggest limitations in cryo-electron microscopy is that biological macromolecules are made up of small atoms. This means that elastic scattering events only deflect the electrons by a small angle, resulting in a small phase-difference and low contrast. Recently, attempts have been made to increase the phase difference between the scattered and unscattered beam with the phase plate (Danev and Baumeister, 2016). This is a thin layer of amorphous carbon placed in the back focal plane that further increases the path length of the scattered beam compared to the unscattered beam. However, contrast is typically enhanced by imaging under focus, which increases the path length differential at the expense of precise spatial resolution (Erickson and Klug, 1971). A further phase shift is introduced by the small spherical aberration inherent to electromagnetic lenses, meaning that the focal strength in the centre of the lens is different to that at the edge (Erickson and Klug, 1971).

A second key limitation to the amount of contrast achieved in biological cryo-EM is radiation damage (Henderson, 1995). As well as elastic scattering events, collision between an incoming electron and an atomic nucleus causes energy transfer to the sample (inelastic scattering, **Figure 1.7A**). This energy can break the covalent bonds in the sample, producing free-radicals and destroying the structure being imaged (Baker and Rubinstein, 2010). As such, only a low dose (typically $\sim 50e^-/\text{\AA}^2$) can be applied to the sample, limiting the signal-to-noise ratio.

1.2.3 Recent advances in resolution are due to direct electron detectors

Prior to 2012, high-resolution cryo-EM structures were typically obtained from images recorded on film (Orlova and Saibil, 2011). The introduction of direct electron detectors was the major step in cryo-EM becoming a mainstream technique to routinely determine atomic-resolution structures. Direct electron detectors are based on complementary metal-oxide-

semiconductor (CMOS) chips. The silicon wells that detect electrons have been made particularly thin in order to prevent scattering events in the detector, which resulted in image blurring in the older generation models (McMullan et al., 2014). The current generation of detectors have a superior detective quantum efficiency (DQE) compared to film (McMullan et al., 2014). DQE is the ratio of the output to input signal to noise ratios, and is a measure for how faithfully the wave is represented by the detector (McMullan et al., 2014). The readout of the detectors is also very fast, meaning multiple frames can be recorded over the course of an illumination. This allows beam-induced motion in the sample to be corrected by aligning and averaging each frame, thus minimizing the blurring that is captured on film (Brilot et al., 2012).

1.2.4 Single-particle cryo-EM workflow

A typical single-particle cryo-EM workflow starts with collection of hundreds or thousands of images. Motion correction is performed, resulting in a single averaged micrograph per image. Next, the contrast transfer function (CTF) is determined. This is the expression of the microscopes point-spread function (i.e. the blurring applied to the image due to systematic aberrations of the EM lenses) in Fourier space. The CTF oscillates between positive and negative values at increasing resolution in Fourier space (Orlova and Saibil, 2011). The observed image is a convolution of the real image and the CTF, and so therefore has frequencies with negative contrast that are not representative of the real image. By determining the oscillations in the CTF and correcting for them an approximation of the real image can be restored. The frequency and amplitude of CTF oscillations varies as a function of defocus, so the CTF should be determined for each image. Recently per-particle CTF measurement and correction has been introduced, in order to account for particles that are in different focal planes in the specimen (Zivanov et al., 2018).

Particles from the micrographs are picked manually, or with automated algorithms that use cross-correlation to a reference particle. 2D classification is used to group and average particles in the same orientation and separately to group “bad” particles (Sigworth, 2016). These bad particles generally appear fuzzy or featureless, and include partially denatured sample, contaminating ice or biological samples, and particles from thick ice or experiencing excessive drift. Particles from “good” 2D classes are then used for 3D classification or refinement.

Cryo-EM produces an approximation of the 2D projection of a 3D object. The approximation becomes less accurate for larger objects where the depth of focus is smaller than the particle (DeRosier, 2000). The Fourier transform of 2D projections represents a central slice of the 3D Fourier transform of the 3D object (De Rosier and Klug, 1968). For 3D refinement, the Fourier transform of each 2D particle is tested against a 3D reference in 3D Fourier space to find the optimal orientations. Refinement is iterative, with each iteration gaining resolution and accuracy. Different refinement packages use different algorithms to determine the orientation of each particle that best matches the reference in 3D space (Grant et al., 2018; Punjani et al., 2017; Scheres, 2012), although the end results are generally the same (Grant et al., 2018). The 3D refinement strategies can also be performed against multiple 3D references for 3D classification.

Most modern refinement software uses the “gold-standard” protocol to prevent overfitting of noise (Scheres and Chen, 2012). The particles are split into two equal lots and refined against a reference model independently of each other. After each iteration, the Fourier Shell Correlation (FSC) over all frequencies is determined. The FSC is the cross-correlation coefficient between the three-dimensional Fourier transforms of the two reconstructions, but broken down into bands (shells) of increasing resolution. Since the two maps are from the same data, they should have the same features and have high FSC values. However, the FSC drops at high frequencies when noise starts to dominate. The point at which the FSC drops below 0.143 is taken to be the resolution of the whole reconstruction (Rosenthal and Henderson, 2003).

1.2.5 Microtubule structures by cryo-EM

Initial cryo-EM reconstructions of microtubules used 15 protofilament 2-start microtubules (Nogales et al., 1999; Sosa et al., 1997). Microtubules with even start numbers do not possess a seam, and as such can be subjected to conventional helical alignment and averaging. However, the seam in 13-protofilament 3-start microtubules (**Figure1.1A**) makes them asymmetric. This represents a challenge for conventional single-particle cryo-EM, as there are 13 peaks in cross-correlation as the microtubule is rotated around the long axis but only one true orientation. In this sense, 13-protofilament 3-start microtubules are considered

“pseudosymmetric”. Regular single-particle techniques fail to reliably align the seam in the raw particles with the reference, resulting in incoherent averaging between particles with different seam orientations. As such, bespoke processing pipelines were developed in order to determine the position of the seam.

Cryo-EM structures of seam-containing microtubules are all based around the same basic technique developed by Sindelar and Downing (Sindelar and Downing, 2007). Synthetic 2D projections of a decorated microtubule with a seam are made with a fine angular sampling. Every projection is then compared to each particle by cross-correlation, with the orientation of the reference in the best match taken to be the orientation of the particle. Only local orientations are refined in 3D refinement in order to keep the seam position fixed. This process of matching and refinement is repeated iteratively at increasingly high resolutions.

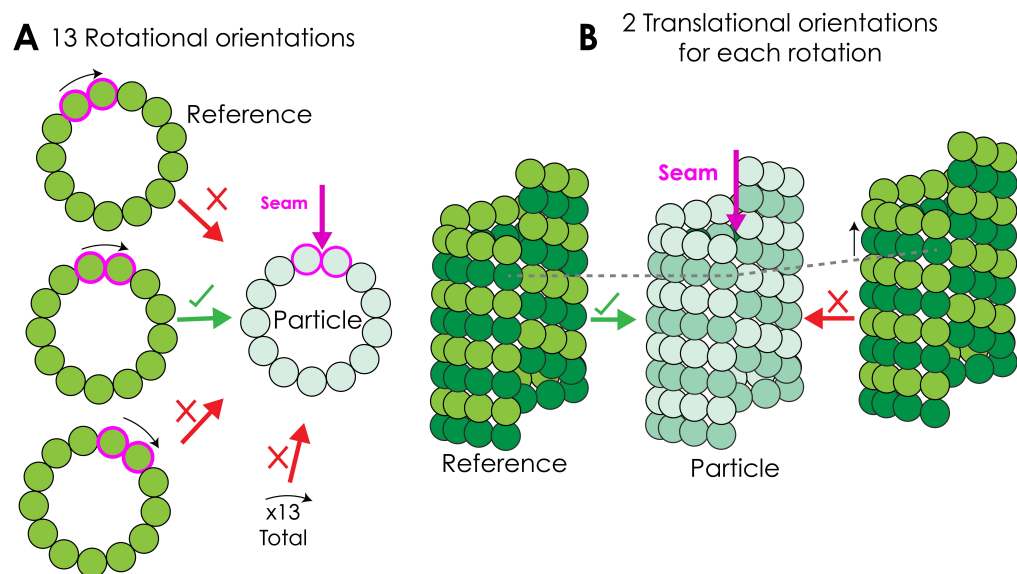


Figure 1.8 - Reference matching in the super-particle seam-finding step

The super-particle approach tests each particle against projections of a reference microtubule sourced from previous structural work or generated in-silico from PDB coordinates in 26 different orientations. The reference is rotated 13 times around the MT long axis (A) to find the position of the seam. Each of these 13 orientations is re-tested with a 4 nm translation along the MT long axis (B) to ensure that α - and β -tubulin are in the correct register.

This basic protocol was modified for the recent high resolution structures of decorated and undecorated microtubules (Kellogg et al., 2018; Zhang et al., 2015b, 2018d). Consecutive segments from the same microtubule have similar orientations in three-dimensions due to the restraints imposed by the helical lattice (i.e. they are all aligned head-to-tail in a straight line

with the seam in the same position). As such multiple neighbouring segments can be coherently averaged together to increase the signal to noise ratio compared to individual particles. These averaged “super-particles” can then be used for more accurate refinements against a reference. Zhang *et al.* found that averaging 7 consecutive segments gave the best results (Zhang and Nogales, 2015a). For a 13-protofilament (PF) microtubule, the reference is sampled and locally refined against the super-particle around 26 orientations. This corresponds to the microtubule being rotated 13 times so that the seam is sampled at each protofilament (**Figure 1.8A**). Each of these orientations is also shifted by one tubulin monomer axially, to test the initial registry between α - and β -tubulin (**Figure 1.8B**). The refined orientation with the best cross-correlation with the reference is then taken to be the correct orientation for all 7 particles in the super-particle. These orientations are then used as the starting point for a full three-dimensional local refinement of all the data to reach the final structure.

1.3 Microtubule motors

There are two families of microtubule motors. The kinesin family is related to the myosin family, which act on the actin cytoskeleton (Hartman and Spudich, 2012; Rayment, 1996). The dynein family is unrelated, and belongs to AAA+ ATPase superfamily (Neuwald et al., 1999). They both convert chemical energy from ATP into a directional stepping motion on the microtubule. Stepping from individual motors can produce up to 6 pN of force (Belyy et al., 2016), sufficient to move cargoes as large as the nucleus, albeit often in ensembles.

1.3.1 Humans encode 45 different kinesin family members

The kinesin family contains 17 subfamilies, with potentially many members in each subfamily (Lawrence et al., 2004; Wickstead and Gull, 2006). Humans encode 45 different kinesins (Miki et al., 2001), most of which are plus-end directed. The kinesin heavy chain consists of a motor domain and a tail domain. The tail is involved in cargo attachments and self-association. The tail and the motor domains are linked by a flexible element called the neck-linker. Kinesins that travel long distance are typically dimeric, but monomeric, trimeric and tetrameric kinesins all exist (Scholey et al., 2014; Verhey et al., 2011). The main long-distance transport kinesin family, kinesin-1, consists of a dimer of heavy chains in combination with a pair of light chains bound to the tail (Endow et al., 2010; Gindhart et al., 1998) (Figure 1.9).

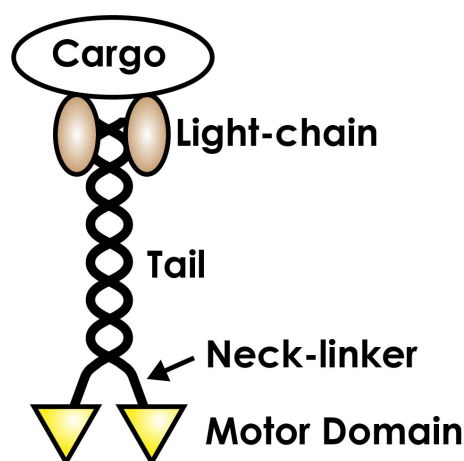


Figure 1.9 - Schematic of a kinesin-1

A dimeric kinesin contains two heavy chains, each with a coiled coil tail, a globular motor domain (yellow), a neck-linker connecting the two. Kinesin 1 family members have a dimeric light chain. The tail connects to cargo.

In metazoans, minus-end directed kinesins contribute to the balance of forces that organize the mitotic spindle (Fink et al., 2009). In plants (which do not encode the dynein motors), minus-end directed kinesins are the primary source of long-range retrograde transport (Yamada et al., 2017). The processive minus-end directed kinesin family is expanded in plants as a result. Separately, non-processive minus-end kinesins depolymerize microtubules by bending protofilaments from the plus-end (Desai et al., 1999; Hunter et al., 2003)

The kinesin-1, -2 and -3 families are all processive, and involved in long-range cytoplasmic transport (Endow et al., 2010). As plus-end motors, this typically transports cargoes from the cell body to the periphery. Cargoes for kinesin-1 and -3 often overlap, and include endosomes, mitochondria, presynaptic vesicles, Golgi-derived vesicles and mRNP complexes (Hirokawa et al., 2009). The kinesin-2 family is responsible for anterograde intraflagellar transport in the cilia, transporting IFT cargo from the base to the tip (Scholey, 2013). However, kinesin-2 family members also operate in the cytoplasm and overlap to some degree with kinesin-1 and -3 (Hirokawa et al., 2009; Scholey, 2013).

Mitotic kinesins are involved in formation and maintenance of the mitotic (and meiotic) spindle. Kinesin-5 family members are homotetramers of heavy chains arranged into a bipolar structure (Kashina et al., 1996). Each end has a pair of motor domains that can bind to and walk on a microtubule. When cross-linking antiparallel microtubules from two halves of the spindle, the two heads walk in opposite directions, pushing the two microtubules apart (Kapitein et al., 2005). This is the basis on which separation of the two centrosomes occurs during spindle formation (Kapoor et al., 2000). Other kinesin family members contribute to spindle formation and organization during mitosis, as well as microtubule attachment at the kinetochore (Endow et al., 2010)

1.3.2 Structure of the kinesin motor domain and its interaction with microtubules

The conserved kinesin motor is a ~40kDa globular P-loop ATPase domain containing a core β -sheet surrounded by helices (Kull et al., 1996). The motor domain binds to the microtubule at the intradimer interface of tubulin (**Figure 1.10A**, (Amos and Hirose, 1997; Rice et al., 1999)). The nucleotide-binding site is directly linked to helix 4, which forms the main interface with the microtubule. In the ADP-bound state, partial uncoiling of helix 4 weakens the interaction

with the microtubule and causes detachment (**Figure 1.10B/C**) (Atherton et al., 2014; Shang et al., 2014). Reversal of these effects upon nucleotide release results in microtubule rebinding. As such, the motor domain cyclically binds and releases once per nucleotide cycle.

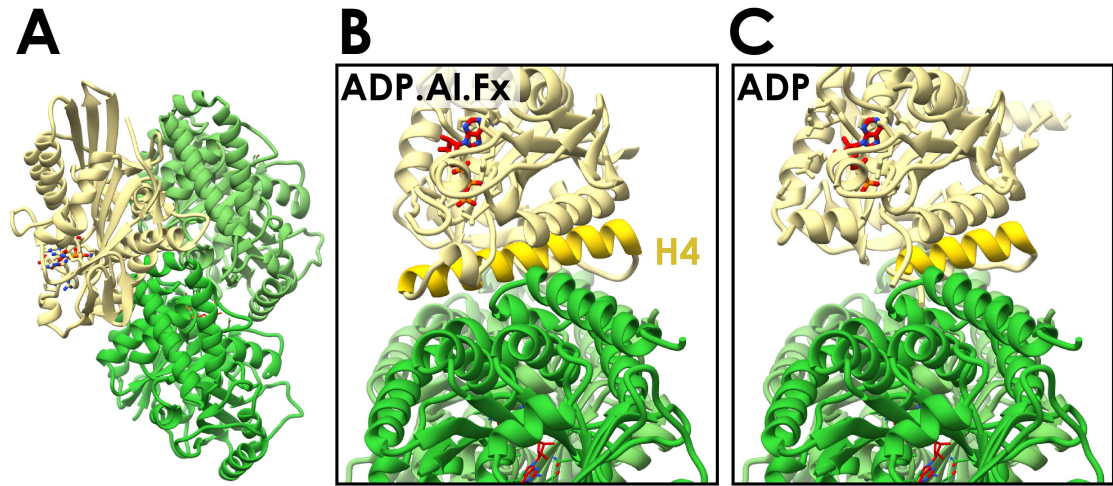


Figure 1.10 - Structure and microtubule binding of the kinesin motor domain

A - Cryo-EM model of kinesin-1 motor domain (yellow) bound to a microtubule (α - and β -tubulin dark and light green) - PDB 3J8Y. **B** - Looking along a protofilament towards the plus end, H4 of the kinesin motor (gold) straddles the interdimer interface in the high-affinity ADP.Ai.Fx state and forms the main interaction with the microtubule. **C** - Docking a crystal structure of low-affinity ADP-bound kinesin (1mkj) to the high-affinity motor shows that H4 has uncoiled, therefore weakening the interaction with the microtubule.

1.3.3 Kinesin step in a directional hand-over-hand mechanism

Kinesin walks straight along a single protofilament (Ray et al., 1993). Tracking labeled kinesin heads in an optical trap showed that kinesin dimers walk in a hand-over-hand motion (**Figure 1.11**) (Yildiz et al., 2004; Asbury et al., 2003). From a two-head-bound state the trailing head releases, and moves in front of the attached head and reattaches. The head that was previously leading is now trailing, starting the cycle again. This tightly regulated, cyclical step is controlled by the nucleotide cycle of the motors active site. The motor dissociates from the microtubule in the ADP-bound state (**Figure 1.10C**). However, further allosteric changes in the attached motor domain allow its neck-linker to transition from an unstructured state to an ordered structure docked to the plus-end of the motor (Rice et al., 1999). Since the neck linker connects the two heads together, this biased docking positions the unattached head in front of the leading head (**Figure 1.11**).

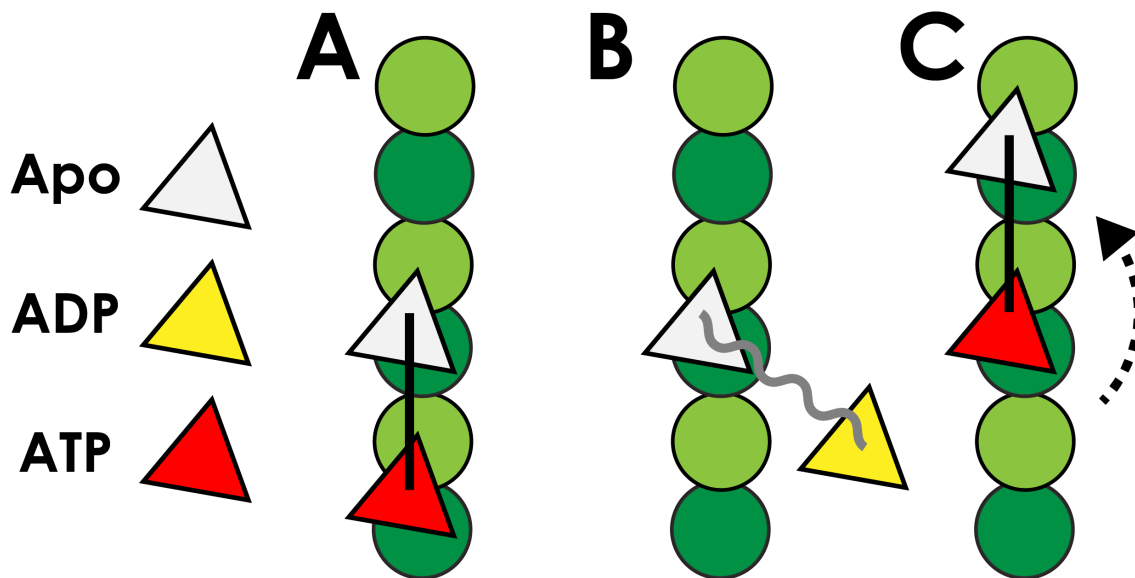


Figure 1.11 - Kinesin steps hand-over-hand

A - Cartoon representation of kinesin dimer in the two-head bound state. The rear head can bind ATP but the leading head cannot due to asymmetric tension gating by the neck-linker. B - The trailing head hydrolyses ATP, leading to the low-affinity GDP state that detaches from microtubules. C - The microtubule attached head binds ATP, causing a disordered-to-ordered transition of the neck linker, positioning the unattached head at the next binding site. It rebinds and releases ADP.

Coordination between the two heads ensures that the trailing head releases from the microtubule first. The two-head bound state creates intramolecular strain in the two neck linkers, with one being pulled forwards and the other backwards. This creates structural asymmetry in the two heads, which is transmitted to the two nucleotide sites. Backwards tension in the neck-linker prevents the active site binding ATP and reaching the low-affinity ADP-bound state (Andreasson et al., 2015; Liu et al., 2017). As such, the stepping mechanism of kinesin motors is tightly regulated and highly regular.

1.3.4 The dynein family are all minus-end directed microtubule motors

The dynein family is a group of minus-end directed microtubule motors. Like kinesin, they use ATP hydrolysis to produce force relative to the microtubule. However, they are unrelated to the kinesin/myosin superfamily, instead belonging to the AAA+ ATPase superfamily (Neuwald et al., 1999). Most AAA+ proteins typically assemble into functional hexameric rings, however dynein is atypical in that the six subunits are linked in its primary structure. Only two other proteins, Rhea1/Midasin and P7BP2, are known to follow this architecture, although neither

possess motor activity or bind microtubules (Chen et al., 2018; Niwa et al., 2018). Dynein family members are found in the basal protozoan eukaryotes through to fungi and metazoans (Wickstead and Gull, 2007). However many plant species, including all flowering plants, have lost the entire dynein family from their genome (Kollmar, 2016; Lawrence et al., 2001).

The dynein family is split into the cytoplasmic and axonemal subfamilies (Wickstead and Gull, 2007). There are two related cytoplasmic dyneins, both of which are dimeric. Cytoplasmic dynein-1 functions throughout the cytoplasm, whereas cytoplasmic dynein-2 functions primarily in the cilium for intraflagellar transport (Roberts et al., 2013). There are 8 classes of axonemal dyneins, but the number of axonemal dyneins in the genome varies from species to species (Wickstead and Gull, 2007). Axonemal dyneins can be monomeric, dimeric or trimeric, and are only expressed in cells with motile cilia (Roberts et al., 2013; Satir et al., 2014). The force produced by axonemal dyneins powers the beating motion of cilia.

1.3.5 Cytoplasmic dyneins are processive, long-distance motors

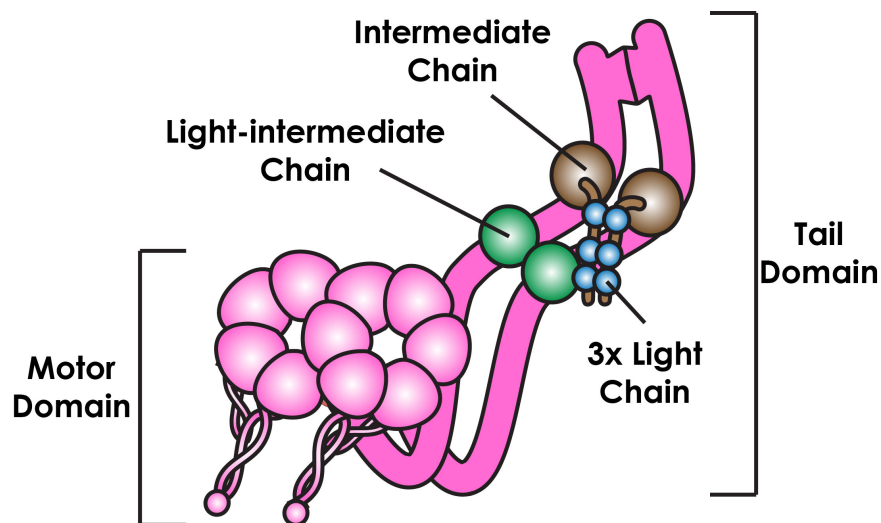


Figure 1.12 - Schematic of Cytoplasmic dynein-1

Cytoplasmic dynein-1 is a dimer of heavy chains (magenta). The N-terminal tail domain dimerises and forms the binding site for the intermediate chain (brown) and light intermediate chain (green). Three pairs of light chains (blue) bind to the intermediate chain dimer. (Reck-Peterson et al., 2018)

The two cytoplasmic dynein family members belong to the same outgroup of the dynein family (Wickstead and Gull, 2007), and are related by 27% sequence identity and 47% sequence similarity. Each forms a complex of two heavy chains associated with a pair of intermediate

and light intermediate chains, and three (cytoplasmic dynein-1) or four (cytoplasmic dynein-2) pairs of light chains (**Figure 1.12**) (Asante et al., 2014; Pfister et al., 2006). Both are processive motors, capable of moving their cargoes over long distances in the cell.

Cytoplasmic dynein-1 operates in the bulk cytoplasm of the cell, transporting cargoes to the minus-end of microtubules. It organizes both the endosomal and autophagocytic pathways to maintain cellular homeostasis. Endosomes are internalized from the cell exterior and transported to the center of the cell (Aniento et al., 1993; Harada et al., 1998). Autophagosomes, containing host proteins or organelles directed for degradation, are also taken to the centre of the cell by dynein (Kimura et al., 2008). In both cases, the vesicles are fused with a lysosome to degrade their contents. Cytoplasmic dynein-1 also transports internalized vesicles of activated surface receptors (“signaling endosomes”) from axon terminals to the nucleus to enact a transcriptional response (Heerssen et al., 2004). Furthermore, dynein transport is vital to control the cellular localization of the nucleus (Splinter et al., 2010a), the clustering of the Golgi apparatus (Harada et al., 1998), and the morphology of the endoplasmic reticulum (Woźniak et al., 2009).

Cytoplasmic dynein-1 also transports cargoes that are not surrounded by a membrane. It transports aggregated proteins to the centre of the cell where they accumulate as the aggresome (Calderilla-Barbosa et al., 2014; Kawaguchi et al., 2003). Transcription factors are transported from the sites of axonal damage to the nucleus to elicit an appropriate cellular response (Hanz et al., 2003). During mitosis cytoplasmic dynein-1 is recruited to the minus-end of microtubules and walks towards the minus-end of an adjacent microtubule (Hueschen et al., 2017). This clusters the minus-ends of microtubules in the spindle, and dynein depletion causes severe defects in spindle morphology (Merdes et al., 1996). Furthermore, dynein transports spindle assembly checkpoint proteins to the spindle poles following kinetochore attachment (Howell et al., 2001). This is thought to remove their suppressive effects and allow mitosis to continue. Finally, dynein anchored to the cell cortex exerts force on astral spindle microtubules to control the position of the spindle throughout mitosis (McNally, 2013)

Cytoplasmic dynein-2 is responsible for retrograde transport inside primary and motile cilia. Intra-flagellar transport (IFT) controls the movement of structural components and signaling molecules required for establishment, maintenance and function of cilia (Hao and Scholey,

2009; Ishikawa and Marshall, 2017). In the axoneme, microtubules are organized with their plus-ends out. Cytoplasmic dynein-2 is transported to the tip of the cilium in an inactive conformation by a kinesin-2 family member, along with other IFT cargoes (Jordan et al., 2018; Roberts et al., 2014; Toropova et al., 2017). By an unknown mechanism, it is then activated at the tip, where it initiates retrograde transport back to the cell body. IFT cargoes include tubulin (Bhogaraju et al., 2013) and axonemal dyneins (Qin et al., 2004) which are incorporated into the axoneme at the tip. Retrograde IFT transport takes kinesin motors, the IFT transport scaffold, and waste products from the tip back to the base (Hao and Scholey, 2009; Prevo et al., 2017). As a result, cytoplasmic dynein-2 null mutants are unable to grow cilia, due to the inability to recycle the components at the tip (Engel et al., 2012). Furthermore, in tandem with an anterograde IFT kinesin, cytoplasmic dynein-2 controls the localization of various signaling molecules involved in multiple signaling cascades, such that they are only transported to the cell body when a membrane receptor is activated (Prevo et al., 2017). Inhibition of cytoplasmic dynein-2 disrupts hedgehog signaling, preventing tumour cell differentiation in culture (Höing et al., 2018).

1.3.6 Axonemal dyneins power the ciliary beat

Axonemal dyneins generate the force for ciliary beating. Adjacent microtubule doublets in the 9-fold ring of the axoneme are cross-linked at regular intervals by axonemal dyneins (**Figure 1.6B**, (Kamiya and Yagi, 2014)). The N-terminal tail is fixed on the A-tubule of one doublet, allowing the motor to move on the B-tubule of the adjacent doublet.

Two categories of axonemal dyneins form both functional and phylogenetic groups. Outer dynein arms (ODAs) form the exterior links between adjacent microtubule doublets, while inner dynein arms (IDAs) form the interior links (**Figure 1.6B**, **Figure 1.13A/B**). Studies on *C. reinhardtii* mutants lacking ODA form normal beating waveforms but swim much slower (Kamiya and Okamoto, 1985; Mitchell and Rosenbaum, 1985). This suggests that the ODAs produce the majority of the force in the axoneme. In contrast, loss of one or more inner arm dyneins results in irregular beating waveforms, or a complete loss of the ciliary beat (Brokaw and Kamiya, 1987; Kamiya et al., 1991). Furthermore, gliding assays performed with a purified IDA showed that it rotates the microtubule around the long axis (Vale and Toyoshima, 1988).

Taken together, these results suggest that the role of the IDAs is to initiate and regulate the ciliary waveform, potentially through the application of torque.

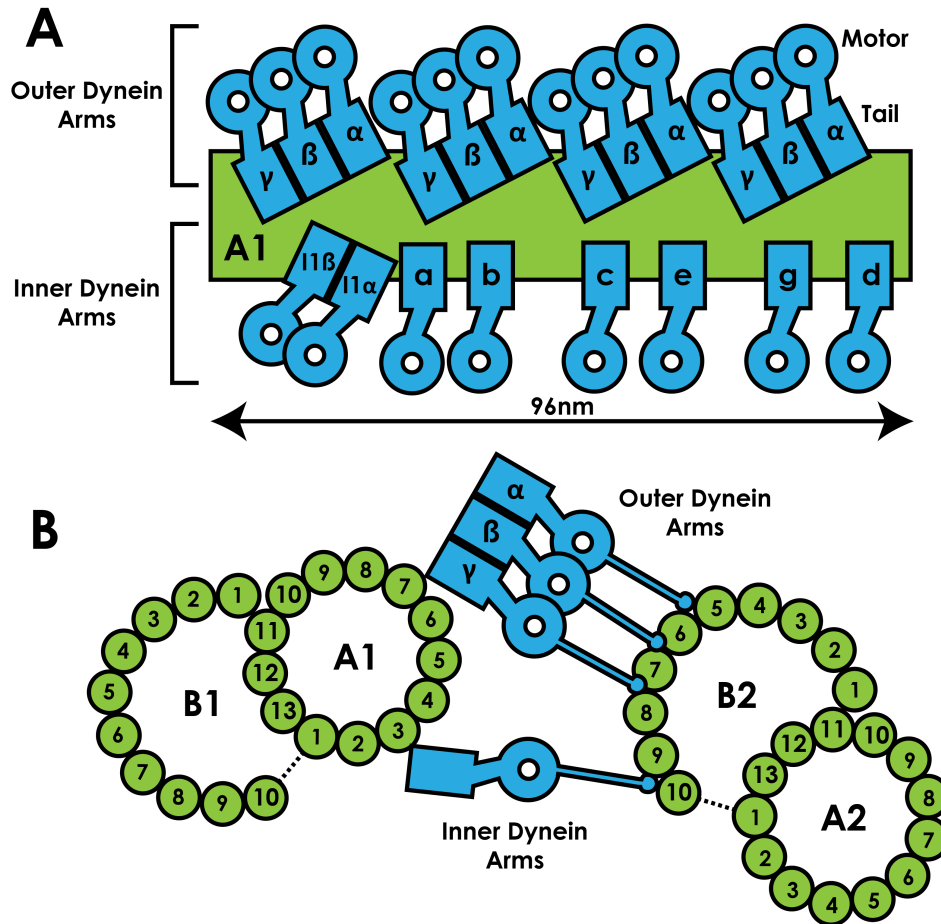


Figure 1.13 - Organisation of dyneins in the axoneme

A - Cryo-ET from *C. reinhardtii* has determined the location of each axonemal dynein (blue) in the 96 nm axonemal repeat. The tails of the heavy chains are docked onto the A tubule (green), viewed in profile. **B** - Orthogonal view of A, now looking down the microtubule long-axis. The motor domains are positioned on the B tubule of the adjacent microtubule doublet.

The localization of axonemal dyneins is regulated by docking complexes into a regular 96 nm repeat (**Figure 1.13A**) (Ishikawa et al., 2007; Nicastro et al., 2006; Song et al., 2018). There are four identical ODA complexes and six separate IDA complexes per 96nm. Protozoa and algae have trimeric outer arm dyneins (α , β and γ chains), where metazoans only have dimeric outer arm complexes (β and γ chains) (King, 2016). Most of the inner dynein arms are monomeric, with the exception of the dimeric IDA11/f group (**Figure 1.13A**) (Hom et al., 2011; Wickstead and Gull, 2007). Different ODA and IDA gene products localize to different regions of the cilium to fine-tune the specific waveform (Dougherty et al., 2016; Yagi et al., 2009).

Axonemal dynein activity is coordinated to ensure only a subset of motors are active at once (Satir et al., 2014). Specifically, cilia beat in an oscillatory waveform, and cryo-EM shows that axonemal dyneins are only ever active on the outside of a bend (Lin and Nicastro, 2018). This creates an imbalance in the forces acting on each of the nine doublets, creating an overall force that reverses the bend. In this way, the oscillation is propagated cyclically through the axoneme, creating a repetitive defined waveform. However, the mechanism underlying coordination between different dyneins is unknown.

1.3.7 Dynein stepping is irregular

The processive kinesins are highly regular, with cyclical hand-over-hand steps along a single protofilament. In contrast, dynein stepping is irregular and stochastic. High-resolution single-molecule fluorescence tracking of yeast cytoplasmic dynein showed that frequent backwards or sideways steps occur (**Figure 1.14A/B**, (Reck-Peterson et al., 2006)). Furthermore, differential labelling of the two motor domains in a dimer showed that the stepping of one head is poorly correlated with the other (DeWitt et al., 2012; Qiu et al., 2012). Dynein therefore only walks towards the minus end of microtubules due to an overall bias of a stochastic stepping mechanism. Less work has been done on axonemal dyneins stepping, but some evidence suggests that they are less processive than cytoplasmic dyneins (i.e. they take fewer steps before dissociating) (Sakakibara et al., 1999; Shimizu et al., 2014). However, because they exclusively work in ensembles, processivity of individual motors is less important.

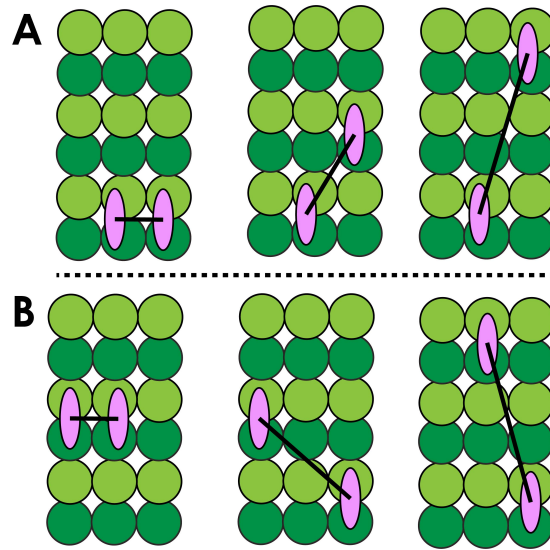


Figure 1.14 - Dynein stepping is stochastic

A - One head of a dimeric dynein motor (pink) can take multiple forward steps before the other head releases from the microtubule (green). **B** - Dynein takes frequent backwards and sideways steps.

1.3.8 The conserved dynein motor domain belongs to the AAA+ superfamily

The primary structure of the dynein motor domain is highly conserved throughout different dynein family members and different organisms (Wickstead and Gull, 2007). The dynein motor domain consists of a N-terminal linker domain, a ring of 6 tandem AAA+ ATPase domains (AAA1-6) and an unrelated C-terminal domain that is missing in some fungi (King, 2000; Neuwald et al., 1999). The linker domain is the flexible element whose movements create the dynein power stroke (Burgess et al., 2003; Lin et al., 2014; Roberts et al., 2009). The role of the C-terminal domain is not fully understood, but its removal has been reported to make dimeric dynein motors able to withstand more force (Nicholas et al., 2015a). Consistent with a role in the mechanics of the motor, structural results suggest it helps transmit conformational changes across the AAA+ ring (Niekamp et al., 2019).

Encoding the AAA+ domains in a continuous strand allows each domain to contain unique characteristics. For instance, AAA5 and AAA4 have additional coiled coil extensions called the buttress and stalk respectively (Gee et al., 1997). The end of the stalk contains dynein's microtubule-binding domain (MTBD) (Koonce et al., 2000). Furthermore, the nucleotide binding elements in AAA5 and AAA6 have been lost (Neuwald et al., 1999), and the AAA2 Walker B motif, which is usually responsible for coordinating the γ -phosphate for hydrolysis,

lacks the catalytic glutamate residue. As such, it constitutively binds ATP without hydrolysing it. Finally, AAA1-5 each have different combinations of three inserts (pre-sensor I, H2 or H2-B3) (Gleave et al., 2014), promoting differential interactions with the linker domain in different nucleotide states.

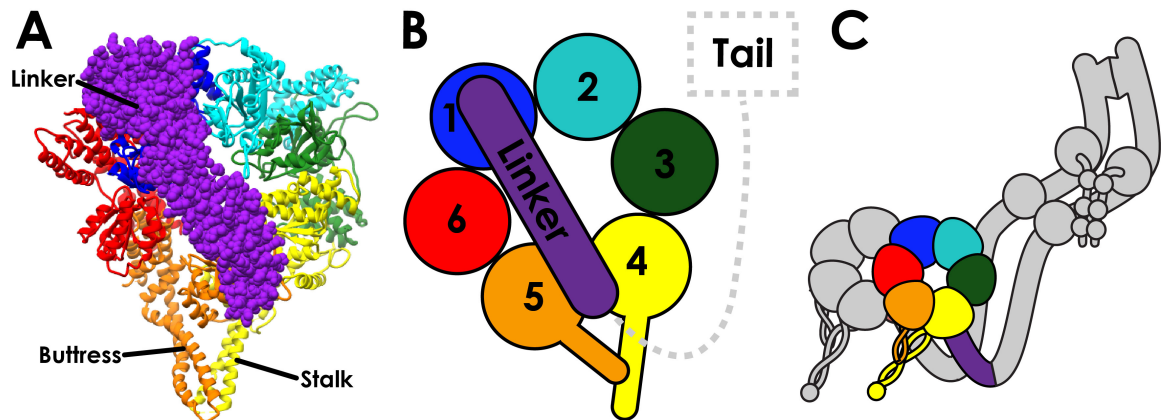


Figure 1.15 - Structure of a dynein motor

*A - Crystal structure of *Saccharomyces cerevisiae* cytoplasmic dynein-1 motor domain, coloured according to the cartoons. B - Cartoon of the motor domain as shown in A, with individual AAA+ subdomains labelled. C - Cartoon representation of A in the context of a full dynein dimer (regions not represented in structure coloured grey).*

The first three-dimensional structural information of the motor domain came from a low resolution crystal structure (**Figure 1.15**, (Carter et al., 2011; Kon et al., 2011)). Each of the AAA+ subdomains adopts the conserved AAA+ fold of a large and small subdomain (**Figure 1.16, left**). The large subdomain (AAAL) consists of a 5-strand parallel β sheet surrounded by 5 helices, and the small subdomain (AAAs) consists of 5 helices (one more than most AAA+ proteins (Neuwald et al., 1999)). The AAAL and AAAs subdomains from neighbouring AAA domains (e.g. AAA1s and AAA2L) pack together as a rigid unit, whereas the interaction between AAAL and AAAs within the same subdomain is flexible around a hinge. The linker domain consists of 4 linked helical bundles that, in these structures, sits straight over the center of the ring. These initial crystal structures were later added to with high-resolution structures in the presence of ADP (Kon et al., 2012), no nucleotide (Schmidt et al., 2012), and ADP Vanadate (ADP.Vi, mimicking the ATP hydrolysis state) (Schmidt et al., 2015).

1.3.9 The nucleotide cycle of AAA1 controls dynein stepping

The key active site of dynein is the nucleotide-binding site of AAA1 (Kon et al., 2004). Allosteric communication propagates from this site through the entire AAA+ ring, controlling the conformation of the linker domain and microtubule-binding domains. These structural changes create the dynein power stroke, and control the microtubule affinity of the MTBD, causing it to cyclically bind and release from microtubules.

The AAA1 active site is conserved from other AAA+ proteins (Miller and Enemark, 2016; Neuwald et al., 1999). The nucleotide base occupies a hydrophobic pocket in the flexible wedge between AAA1L and AAA1s (Kon et al., 2012; Schmidt et al., 2015). AAA1L contains the Walker A motif (responsible for nucleotide phosphate binding), Walker B motif (involved in magnesium coordination and catalysis) and sensor 1 residue (also coordinating catalysis) (Miller and Enemark, 2016). The active site is completed by an arginine finger from AAA2L, which coordinates the gamma-phosphate (Schmidt et al., 2015).

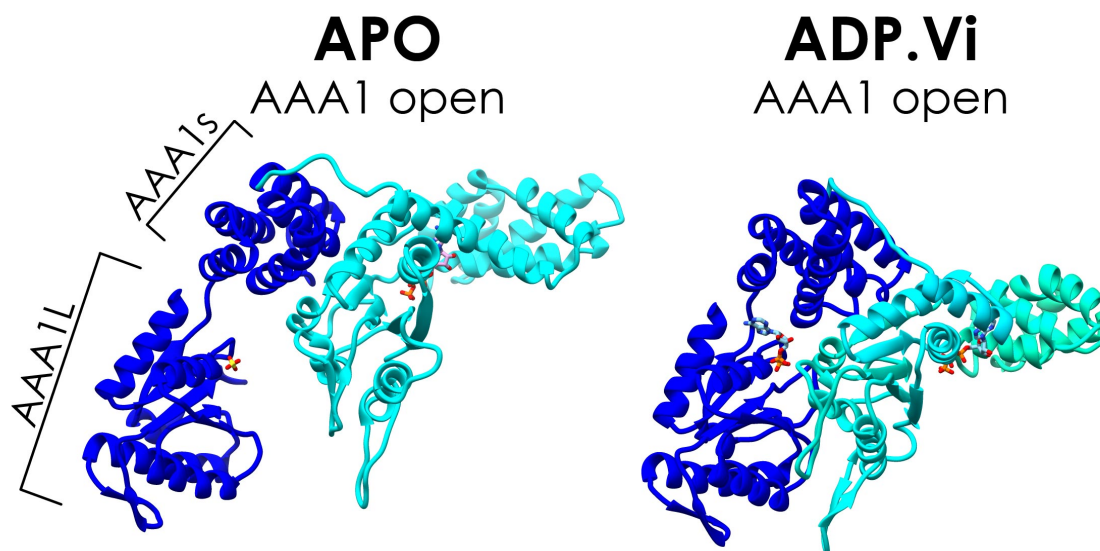


Figure 1.16 - The AAA1 active site is flexible around a hinge

Comparison between the AAA1 active site in two nucleotide states. In the apo (nucleotide-free) state, the large and small subdomains of AAA1 (dark blue) are open around their connecting hinge. In the ADP.Vi state, the nucleotide causes closure of the active site, which is completed by AAA2L (blue).

Crystal structures show that the hinge between AAA1L and AAA1s swings depending on its nucleotide state (**Figure 1.16**). When no nucleotide is present (“Apo”) the hinge is open (Carter et al., 2011; Schmidt et al., 2012). In the ATP hydrolysis state, mimicked by ADP Vanadate

(ADP.Vi), hydrophobic interactions with the base, and coordination of phosphates by the Walker motifs bring AAA1L and AAA1s together (**Figure 1.16**) (Schmidt et al., 2015). This is reinforced by the AAA2L arginine finger extending into the active site, creating a fully closed AAA1 site. An ADP-bound structure shows that removal of the gamma-phosphate causes the AAA1 active site to partially open up again (Kon et al., 2012), with a full opening seen when nucleotide is lost and the cycle starts again (Schmidt et al., 2012).

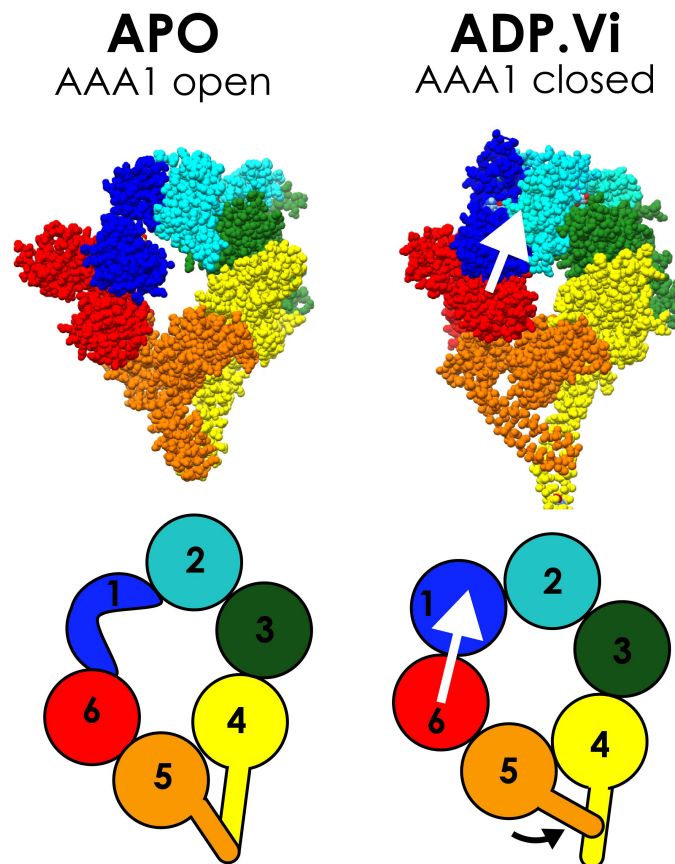


Figure 1.17 - The nucleotide state of AAA1 is transmitted through the AAA+ ring
Crystal structures of dynein ring show how the nucleotide state of AAA1 is transmitted through the ring. In the Apo state, the AAA1 active site is open, pushing AAA6 and AAA5 out from a true circle. Closure of the nucleotide site in the ADP.Vi pulls AAA6 and AAA5 up towards AAA1s, resulting in a closed, symmetric ring.

1.3.10 The nucleotide state of AAA1 is transmitted to the MTBD and linker domains

Since the interface between the large and small subdomains of neighbouring AAA+ domains is rigid, closure of the AAA1 active site in the ATP hydrolysis state pulls on both AAA2 (through the AAA1s/2L block) and AAA6 (through AAA1L/6s) (**Figure 1.17**, (Carter et al., 2011; Schmidt

and Carter, 2016). These in turn pull on their neighboring domains to transmit the state of AAA1 throughout the ring, to the linker and the MTBD.

In the nucleotide-free state the linker is straight and docks onto AAA5L and AAA1L either side of the central pore (**Figure 1.18**, (Schmidt et al., 2012)). In the ADP.Vi state, closure of the ring pushes AAA4L up into the linker, causing it to kink 90° and dock onto AAA2/3 (**Figure 1.18**, (Schmidt and Carter, 2016; Schmidt et al., 2015)). The power stroke occurs when the gamma-phosphate at AAA1 is released, making the ring asymmetric again and allowing the linker to return to its straight conformation (**Figure 1.18**, (Kon et al., 2012; Schmidt et al., 2015; Schmidt and Carter, 2016)).

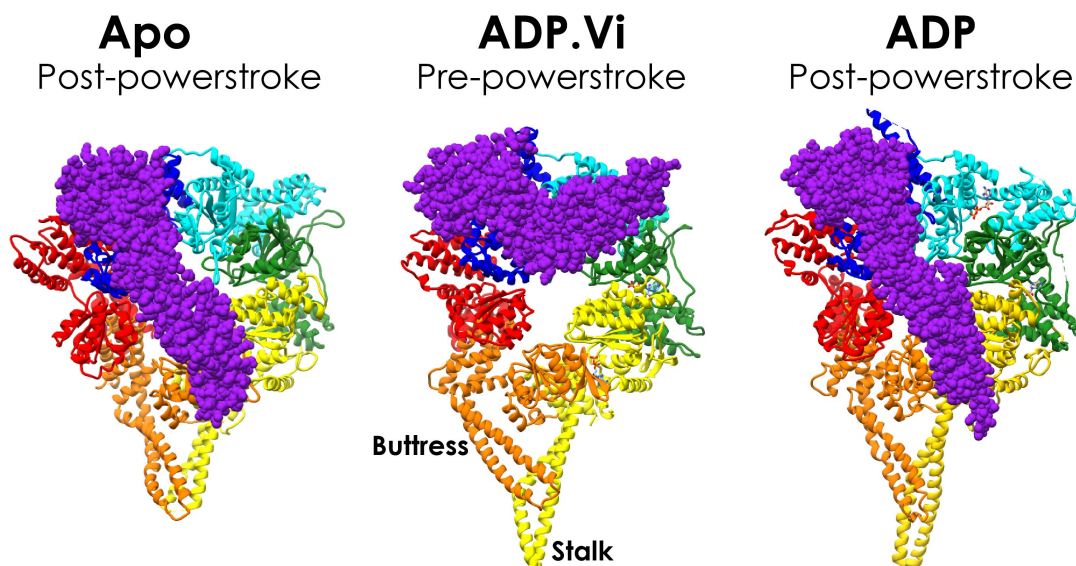


Figure 1.18 - Nucleotide-dependent change in linker conformation

The conformation of the ring, dependent on the nucleotide state of AAA1 (Figure 1.14), controls the conformation of the linker. In the apo state, the linker is straight, and docks onto AAA4/5. In the ADP.Vi state, AAA4 is pushed up relative to the linker, causing it to undock and redock at AAA2/3 with a 90° kink. In the ADP state, the block has been released and the linker returns to its starting position. This movement is the dynein power stroke.

Similarly, opening and closure of AAA1 controls the affinity of the motor for microtubules. The closure of AAA1 is transmitted to AAA5, causing it to rotate relative to AAA4 (Schmidt et al., 2015). This means that the buttness, the short coiled coil projection from AAA5, rotates towards the ring (**Figure 1.19**). The buttness forms hydrophobic interactions with helix CC2 (coiled coil 2) of the stalk, which cause CC2 to be pulled up towards the ring as well. Since helix CC1 (coiled coil 1) of the stalk is not contacted, this creates relative movement between the

two stalk helices. This manifests as a change in the packing registry between the two helices, made possible by CC1 lacking some hydrophobic residues in the heptad repeat that would be solvent exposed if a canonical coiled coil were to change registry (Gibbons et al., 2005a). The MTBD is in the high-affinity state when the stalk is in the α -registry, and the low affinity state when the stalk is in the β + registry.

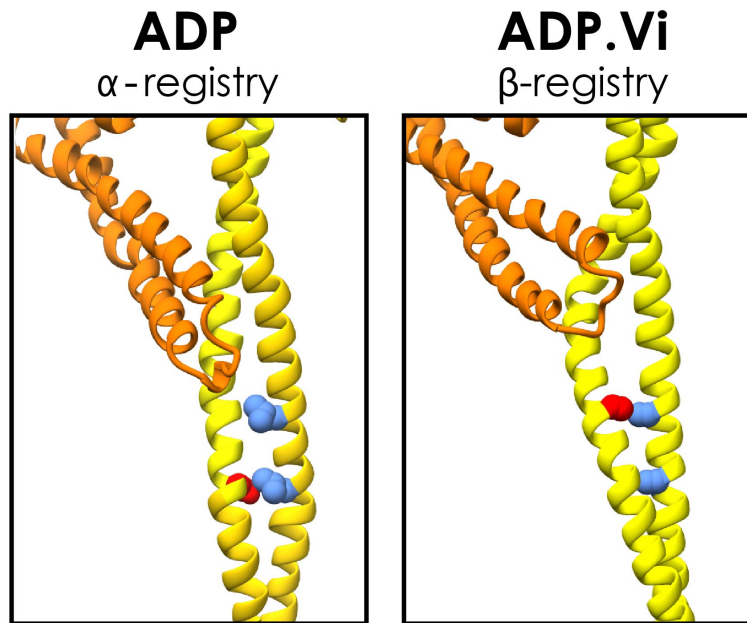


Figure 1.19 - Nucleotide dependent changes in stalk registry

The buttress of AAA5 (orange) contacts the stalk of AAA4 (yellow). Conformational changes transmitted through the ring in the transition from a high-affinity state (ADP here, as the apo-state structure does not contain a fully resolved stalk) to a low-affinity state (ADP.Vi) cause the buttress to rotate towards the ring. This pulls CC2 (red residue) of the stalk towards the ring relative to CC1 (blue residues).

This structural change is transmitted down to the MTBD, changing its affinity for microtubules (**Figure 1.20**) (Carter et al., 2008; Gibbons et al., 2005a; Kon et al., 2009). The MTBD is formed by six short helices (H1-H6) and the ends of CC1 and CC2 (**Figure 1.20A**) (Carter et al., 2008). Changing the stalk registry therefore leads to a conformational change in the MTBD. A 9.7Å cryo-EM structure of cytoplasmic dynein-1 bound to microtubules suggested that moving into the high-affinity α registry causes CC1 and H1 move up $\sim 12\text{\AA}$ together over the intradimer interface in the high-affinity state (**Figure 1.20B**) (Redwine et al., 2012). This removes a steric block between H1 and the microtubule surface that prevents a strong interaction in the low-affinity β + registry. By controlling the registry of the stalk, the nucleotide state of AAA1 therefore controls the affinity of dynein for microtubules.

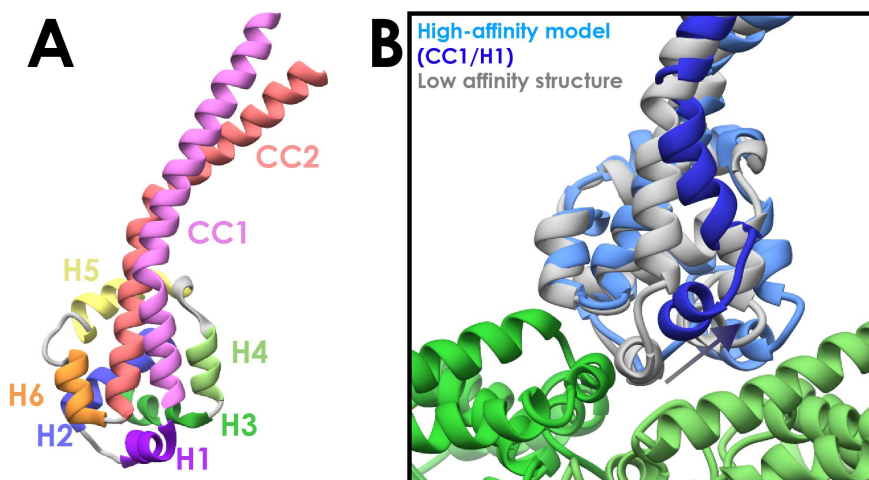


Figure 1.20 - A conformational change in the MTBD controls microtubule binding and release
A - Low-affinity state crystal structure of cytoplasmic dynein-1 MTBD (PDB 3ERR, (Carter et al., 2008). It consists of 6 helices (H1-H6) and the base of the two stalk coiled coil helices (CC1 and CC2). **B** - A comparison between the cryo-EM model of the MTBD in the high microtubule affinity state (Blue, PDB 3J1T, (Redwine et al., 2012)) and the low-affinity state in A (grey, PDB 3ERR, microtubule in green). CC1 and H1 (dark blue) undergo a 12Å translocation to form the high-affinity state.

The above structural data, together with biochemical studies, led to a structural model for the dynein mechanochemical cycle as follows. When AAA1 is in the nucleotide-free apo state the linker sits straight across the ring and the MTBD is in the high-affinity state attached to microtubules (**Figure 1.21A**). Binding and hydrolyzing ATP results in the motor dissociating from the microtubule and the linker forming a 90° kink (the priming stroke) (**Figure 1.21B**). The stalk probably exists in an equilibrium of the different registries (Kon et al., 2009), which means that the motor can rebind and the MTBD returns to the high-affinity α registry (**Figure 1.21C**) (Redwine et al., 2012). This presumably favours phosphate release, which in turn triggers the bent-to-straight conformational change in the linker (the power stroke), and fully stabilises the high-affinity state of the stalk and MTBD (**Figure 1.21D**).

The nucleotide state of AAA3 supplements this basic mechanism controlling the power stroke and microtubule affinity of dynein. AAA3 Walker A and Walker B mutants (preventing ATP binding and hydrolysis respectively) result in a much stronger attachment to the microtubule, and can override low mt-affinity states of AAA1 (DeWitt et al., 2015; Nicholas et al., 2015b). The exact structural basis for this is yet to be determined.

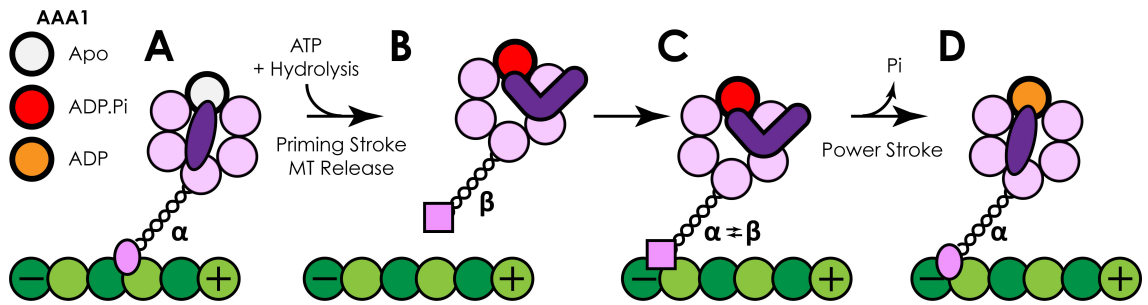


Figure 1.21 - Structural changes in the dynein motor controlled by AAA1

A - A dynein motor with AAA1 in the apo state (white), with a straight linker domain (purple) and the MTBD in the high-affinity state (circular). B - Binding and hydrolyzing ATP leads to the ADP.Pi state (red), in which the linker is bent and the MTBD is in the low affinity state (square). C - A weak interaction between the MTBD and the microtubule partially stabilizes the α registry of the stalk. D - This is communicated to AAA1, which releases the phosphate, leading to the power stroke in the linker (bent-to-straight) and the fully stabilised high-affinity state in the MTBD.

1.3.11 Mammalian dynein motility is dependent on dynein and a cargo adaptor

Fluorescent-labeled dimeric dynein motility can be assessed in a single-molecule TIRF motility assay. For this assay, microtubules are surface immobilized, and the position of single dynein molecules is tracked through time. However, on its own mammalian dynein binds microtubules but does not move for long distances upon them (**Figure 1.22A**) (Schlager et al., 2014a; Trokter et al., 2012). In the cell, dynein activity is absolutely dependent on its interaction with the 23 subunit, 1.0 MDa dynein complex (Schroer, 2004). In dynein, 8 copies of Arp1 and 1 copy of β -actin form a ~ 40 nm actin-like filament, complete with actin-capping complexes at the pointed and barbed ends (**Figure 1.23**) (Eckley et al., 1999; Urnavicius et al., 2015). Sitting on top of the filament is a “shoulder” complex, containing copies of dynein-specific proteins p150, p50 and p24 (Urnavicius et al., 2015). Despite a direct interaction between the dynein intermediate chain and the dynein subunit p150 (King et al., 2003; Vaughan and Vallee, 1995), dynein alone is not sufficient to turn dynein into an active, motile complex (**Figure 1.22B**) (Schlager et al., 2014a).

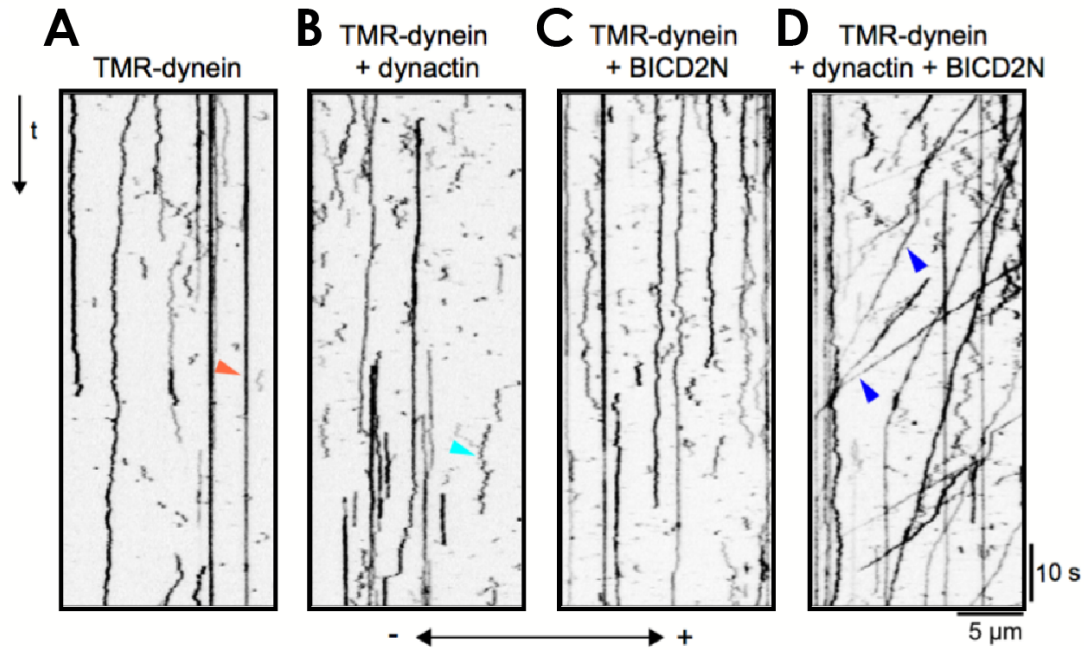


Figure 1.22 - Behaviour of Dynein in single-molecule motility assays

Adapted from (Schlager et al., 2014a). A - Kymograph of fluorescently labeled mammalian dynein, with the minus-end oriented to the left. Dynein is mostly static (orange arrow) or diffusive. B - Adding dynactin does not activate dynein, which stays static or diffusive (cyan arrow). C - Dynein is still inactive with BICD2N only. D - Dynein, dynactin and BICD2N together make a processive minus-end directed complex, as shown by diagonal lines in the kymograph (blue arrows).

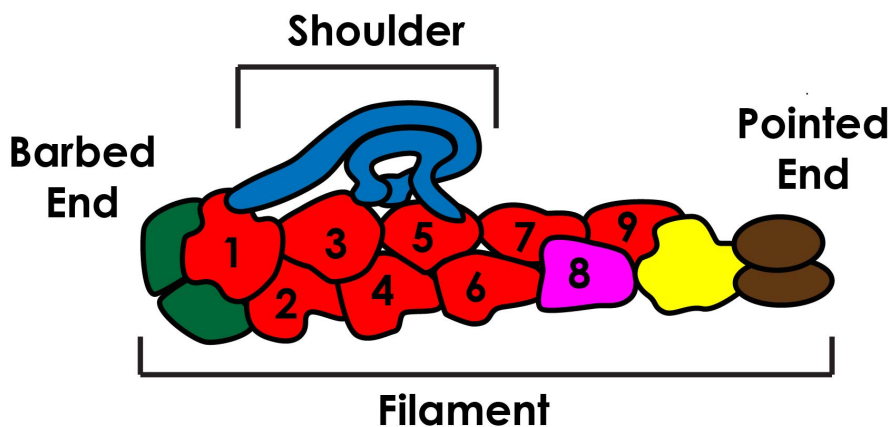


Figure 1.23 - Schematic of the dynactin complex

Dynactin consists of a actin-like filament containing 8 copies of Arp1 (red) and 1 copy of β -actin (magenta, position 8). The barbed end is capped by CapZ (green), and the pointed end is capped by Arp11 (yellow), p62 and p25/27 (brown). The shoulder (blue) consists of p150, p50 and p24 (Schmidt et al., 2015)

As such, Schlager *et al.* concluded that there must be another cellular protein that activates dynein, and focused on BICD2. Previous studies demonstrated the importance of BICD2 for recruitment of dynein to trans-Golgi network derived vesicles. BICD2 is a homodimer that arranges into three coiled coil domains (Hoogenraad *et al.*, 2001; Liu *et al.*, 2013). The two N-terminal coiled coils pull out both dynein and dynactin from cell lysates (Hoogenraad *et al.*, 2001). This construct is often referred to as BICD2N. Mitochondria cluster at the MTOC when they are tethered to BICD2N, indicating this interaction recruits active dynein in the cellular environment (Hoogenraad *et al.*, 2003). Importantly, sucrose gradients showed that dynein and dynactin combine into a larger molecular weight species in the presence of BICD2N, showing that BICD2 strengthens the interaction between dynein and dynactin (Splinter *et al.*, 2012).

A mixture of purified dynein, dynactin and BICD2N (DDB) results in long distance unidirectional motility (**Figure 1.20D**) (Schlager *et al.*, 2014a). Similarly, DDB complexes formed following affinity purification from pig brain lysate with purified BICD2N as bait form a motile complex (McKenney *et al.*, 2014). Three other predicted dynein cargo adaptors (Rab11-FIP3, Spindly and HOOK3) all replicated this result (McKenney *et al.*, 2014). This has now led to the activating cargo adaptor model, in which dynein and dynactin are brought together in a triple complex with a cargo adaptor, simultaneously recruiting dynein to a cargo and activating it.

In order for the activation of dynein by the BICD2 N-terminus to result in cargo transport, it follows that the BICD2 C-terminus binds to cargo. A truncation containing just the C-terminus of BICD2 retained its native localization on Golgi-derived vesicles (Hoogenraad *et al.*, 2001), confirming that it is responsible for cargo binding. It binds to Rab6a (Matanis *et al.*, 2002), which is directly inserted into the membrane of the vesicles through two hydrophobic prenyl groups added to its C-terminus (Beranger *et al.*, 1994; Calero *et al.*, 2003).

A small number of activating cargo adaptors have been identified and validated in the last 5 years. The initial experiments identified BICD2, Spindly, Rab11FIP3 and HOOK3 as activating cargo adaptors (McKenney *et al.*, 2014; Schlager *et al.*, 2014a). Relatives of BICD2 and HOOK3, BICD-related protein 1 (BICDR1) and HOOK1, are also confirmed activating adaptors (Urnavicius *et al.*, 2018; Olenick *et al.*, 2019). BioID tagging of dynein intermediate chain and p62 (part of the dynactin pointed-end complex) identified Ninein and Ninein-like as two coiled

coil proteins that interact with the dynein complex (Redwine et al., 2017). These were both validated as activating cargo adaptors in the single molecule motility assay. CRACR2a and Rab45 are the latest activating adaptors to be verified (Wang et al., 2018b). These both contain N-terminal EF-hands, central coiled coils and a C-terminal Rab GTPase domain, suggesting that they bind to their cargoes directly. Multiple other proteins have been predicted to be activating cargo adaptors, but are yet to be validated (Reck-Peterson et al., 2018)

1.3.12 Dynein, dynactin and cargo adaptors form multiple separate interactions

All activating cargo adaptors identified to date contain a stretch of coiled coil over 200 amino acids in length. The structure of three different activating adaptors (BICD2, BICDR1, HOOK3) in complex with dynein and dynactin have now been solved by single-particle cryo-EM (Urnavicius et al., 2015, 2018). In each case, the interaction between dynein and dynactin is stabilized by the coiled coil coil of the cargo adaptor in an extended three-way interface (**Figure 1.24**). This is thought to keep the tail in a rigid conformation that is transmitted to the motor domains, orienting them parallel to the microtubule (Zhang et al., 2017a). The two motor domains are therefore oriented to match their binding sites on the microtubule, resulting in long distance, directional motility.

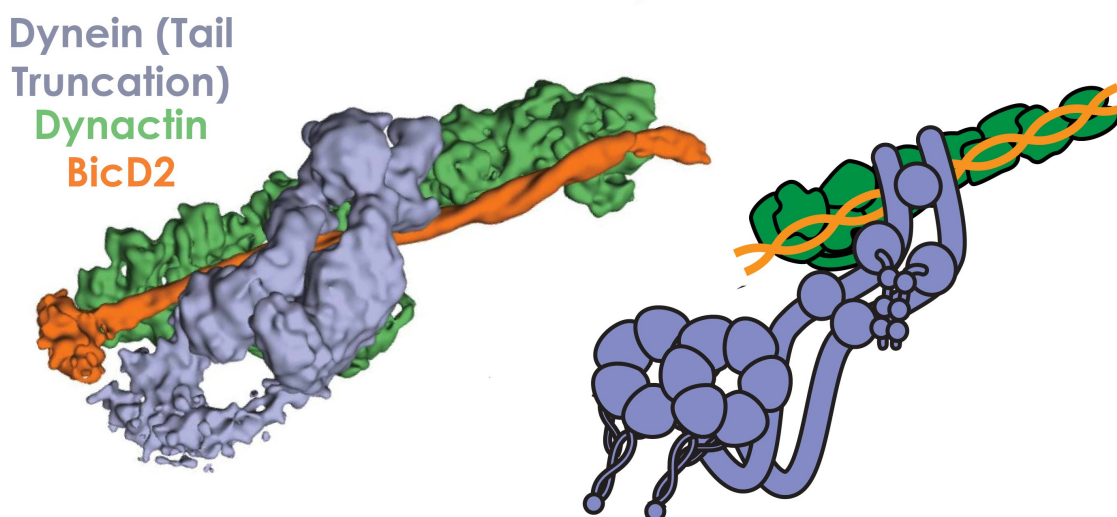


Figure 1.24 - Mode of interaction between dynein, dynactin and BICD2N

Adapted from (Urnavicius et al., 2015). Cryo-EM of a complex consisting of a dynein tail truncation (blue), dynactin (green), and BICD2N (orange) shows that dynein binds to the filament of dynactin, with the interface between the two completed by BICD2N.

BICDR1 and HOOK3 both recruit two dynein dimers to a single dynactin complex (Urnavicius et al., 2018; Grotjahn et al., 2018). However, the density for the cargo adaptor coiled coils is relatively low resolution, indicative of flexibility. As such, it is unclear what residues mediate the interactions at the interface. Underlining this, there does not appear to be a conserved motif within the coiled coil of cargo adaptors (Reck-Peterson et al., 2018)

However, there are conserved sequences between cargo adaptors away from the coiled coils. In the BICD and Spindly families, the CC1-box is a ~20 residue patch of conserved residues including a universal AAxxG motif. Mutations of conserved residues in the CC1-box abolish the interaction between BICD2 and dynein/dynactin (Schlager et al., 2014b). *In vitro* pull-down assays showed that the CC1-box interacts directly with the dynein light-intermediate chain (DLIC) C-terminus (Gama et al., 2017). The CC1-box is present in some predicted activating cargo adaptors that have yet to be verified, such as TRAK1 and HAP1 (Reck-Peterson et al., 2018)

The Hook family form a separate interaction with the DLIC C-terminus mediated by the N-terminal Hook domain (Lee et al., 2018). Rab11FIP3 binds to the DLIC with via an EF hand motif, also vital for function (Horgan et al., 2010). Each of these adaptors binds to the same short helix in the mostly disordered C-terminus of the DLIC (Celestino et al., 2019). As such, most identified activating adaptors contain an interaction site for the DLIC C-terminus. This interaction is thought to mediate the initial contact between dynein and cargo adaptor, and stabilize the coiled coil interaction.

A second motif conserved between different cargo adaptors is called the 'spindly box' (Barisic and Geley, 2011). It is found in Spindly, BicD-family, Hook-family and Rab11FIP3 and some predicted activators (Gama et al., 2017; Reck-Peterson et al., 2018). It is thought to interact with the pointed-end of dynactin, and a mutation of a conserved hydrophobic residue prevented it pulling dynein/dynactin out of pig brain lysate (Gama et al., 2017). Like the DLIC interactions, it is unclear why this is necessary to supplement the interface formed by the coiled coils.

Mammalian cytoplasmic dynein-2 is not dependent on dynactin or a cargo adaptor for activity (Asante et al., 2014). Similarly, *Saccharomyces cerevisiae* cytoplasmic dynein-1 can undergo processive motility in the absence of dynactin (Reck-Peterson et al., 2006). The differential dependence of different cytoplasmic dyneins on dynactin is not presently understood (Toropova et al., 2017).

1.4 Herpesvirus and dynein

Herpesviruses are a family of enveloped double-stranded DNA viruses that infect various metazoans. 8 herpesvirus species infect humans, causing diseases ranging from chickenpox and cold sores to herpes keratitis (leading to blindness) and cancer. Different sub-families of herpesviruses are capable of infecting different host cell types, but all share the ability to switch from lytic to latent infections (Knipe and Howley, 2007). In latent infections the viral genome is maintained as a repressed episome in the nucleus, with sporadic reactivation occurring for the remainder of the host lifetime (Knipe and Howley, 2007; Lieberman, 2016).

The group of alpha-herpesviruses, which include the human pathogens Herpes Simplex Virus 1 and 2 (HSV1/2) and the closely related porcine pathogen Pseudorabies virus (PrV), typically start an infection by lytic replication in host epithelial cells. This allows the virus to breach the epithelium and infect the axon termini of innervating peripheral neurons below (Miranda-Saksena et al., 2018; Smith, 2012). The viral capsids undergo dynein-dependent retrograde transport through the axon to the soma (Lyman and Enquist, 2009). It is not clear why the virus then tends to enter latency in neurons but not epithelial cells. One theory suggests that VP16, the viral tegument protein that triggers expression of immediate-early genes, is only inefficiently transported with the capsid. This means that it is lost following long-distance transport in axons but still present following short-distance transport in epithelial cells (Hafezi et al., 2012; Thellman and Triezenberg, 2017). Consistent with this, VP16 expression is an absolute requirement for viral reactivation from latency (Thompson et al., 2009). During latency, the viral genome is maintained as repressed episomal DNA, from which only a non-coding RNA is produced (Hafezi et al., 2012; Lieberman, 2016; Nicoll et al., 2012). Reactivation is often correlated to cell damage or stress, or weakening of the immune system (Koyuncu et al., 2018).

1.4.1 Structure and organisation of α -herpesviruses

Herpesviruses possess an icosahedral capsid, separated from the spiked envelope by a layer of amorphous tegument proteins (Dai and Zhou, 2018; Grünewald et al., 2003; Owen et al., 2015). The diameter of a mature virus is 175-200nm, with the capsid only occupying around 1/3 of the total internal volume (Grünewald et al., 2003). The loose, unstructured network of

tegument proteins fills the remaining space. There are at least 23 different viral proteins that compose the tegument (Loret et al., 2008), fulfilling multiple roles in viral egress and entry (Owen et al., 2015).

The major capsid protein, VP5, arranges into pentameric and hexameric capsomer complexes (pentons and hexons respectively) that form the basic structural unit of the icosahedral capsid (**Figure 1.25A**) (Brown and Newcomb, 2011; Yuan et al., 2018). 150 hexons cover the face and edges of the capsid and a penton forms all but one of the 12 vertices. The remaining vertex contains the DNA packaging portal vertex complex (McElwee et al., 2018; Wang et al., 2018a). Cryo-EM shows that the majority of VP5 forms a column projecting away from the capsid, but separate loops and subdomains make extensive intra- and inter-capsomer contacts to cover the capsid floor (Yuan et al., 2018). Triplex complexes, made up of one VP19 and two VP23 proteins, provide further links between different capsomers, and fill in the remaining gaps on the surface to create a strong, impermeable structure (**Figure 1.25A**) (Huet et al., 2016; Yuan et al., 2018).

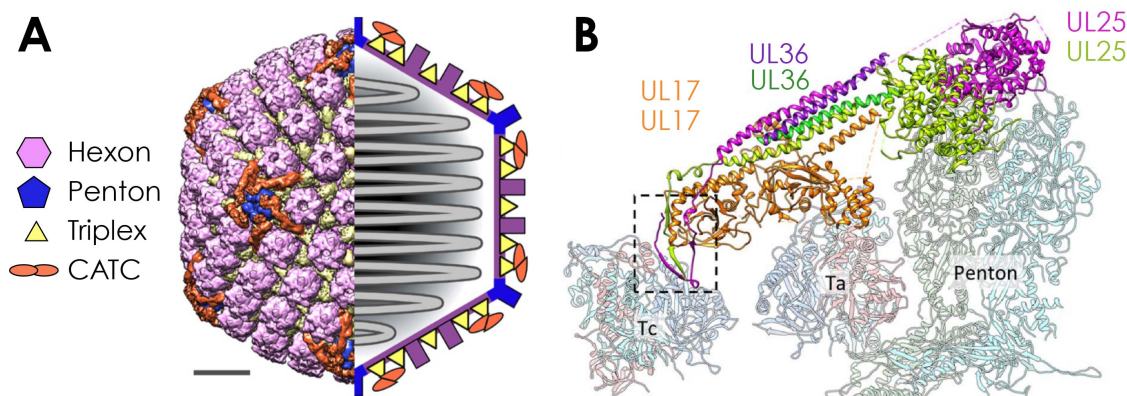


Figure 1.25 - Structural organisation of the HSV-1 capsid and inner tegument

A - Adapted from (Huet et al., 2016). Cryo-EM structure and schematic of the HSV-1 capsid organisation. Hexon capsomer (pink)s of VP5 make up the faces and edges of the capsid, and penton capsomers (blue) form the vertices. Triplex complexes of VP19 and VP23 (yellow) fill in the floor of the capsid between hexons and pentons. The Capsid-associated tegument complex (CATC, orange) forms a bridge between triplexes and the top of the pentons. **B - Adapted from (Dai and Zhou, 2018).** Cryo-EM model of the CATC. A dimer of UL17 (orange) sits on top of two triplex complexes (Ta and Tc). A four-helix bundle containing two copies each of pUL36 (purple/dark green) and UL25 (magenta/light green) sit on top of the UL17 dimer and project to the top of the penton. One such CATC forms on top of each corner of the penton

The only structurally ordered interaction between the capsid and the tegument occurs between a non-structural capsid complex called the Capsid-associated tegument complex (CATC) and the tegument protein pUL36 (**Figure 1.25A/B**) (Dai and Zhou, 2018; Huet et al., 2016). UL17 of the CATC bridges the top of two triplex complexes, and forms a platform from which a four-helical bundle containing two copies of UL25 (the other CATC protein) and two copies of pUL36 project up to the top of a penton (**Figure 1.25B**) (Dai and Zhou, 2018). An extended short helix of UL17 means that the capsid-proximal section contains 5-helices. The section of pUL36 contributing to the helical bundle, attributed to residues 3092 to 3139 (HSV1 numbering), is its only structurally resolved domain. Therefore the majority of pUL36, and by extension the rest of the tegument, is not constrained by the icosahedral symmetry of the capsid.

However, despite lacking a defined ordered structure, the tegument is still highly organized. Interaction studies have demonstrated extended links between different tegument proteins from the capsid to the envelope (Jambunathan et al., 2014; Lee et al., 2008; Vittone et al., 2005). For example, pUL36 interacts with the capsid, and directly interacts with pUL37 and UL48. pUL37 in turn interacts with the interior domain of the membrane proteins gK and UL20. UL48 interacts with the interior domain of glycoprotein gH. Super-resolution microscopy showed that three tegument proteins, pUL36, pUL37 and UL48, are localized to specific stratified shells within the virus (Laine et al., 2015). All three proteins engage in further interactions with other tegument proteins, creating an extended interaction network (Diefenbach, 2015; Owen et al., 2015).

1.4.2 Herpes viruses enter cells through membrane fusion

The viral life cycle starts when an extracellular enveloped virus binds to a host cell membrane (**Figure 1.26**). The four HSV-1 membrane proteins essential for cell entry are gB, gD, gH and gL, though others can also play a role (Cooper and Heldwein, 2015; Eisenberg et al., 2012; Spear and Longnecker, 2003). An initial loose attachment occurs through an interaction between gB and the host surface glycoprotein heparin sulfate (**Figure 1.26A**) (Shieh et al., 1992). When this interaction occurs on filopodia, the virus can 'surf' towards the cell body (Oh et al., 2010), potentially mediated by non-muscle myosin IIA (Arii et al., 2010).

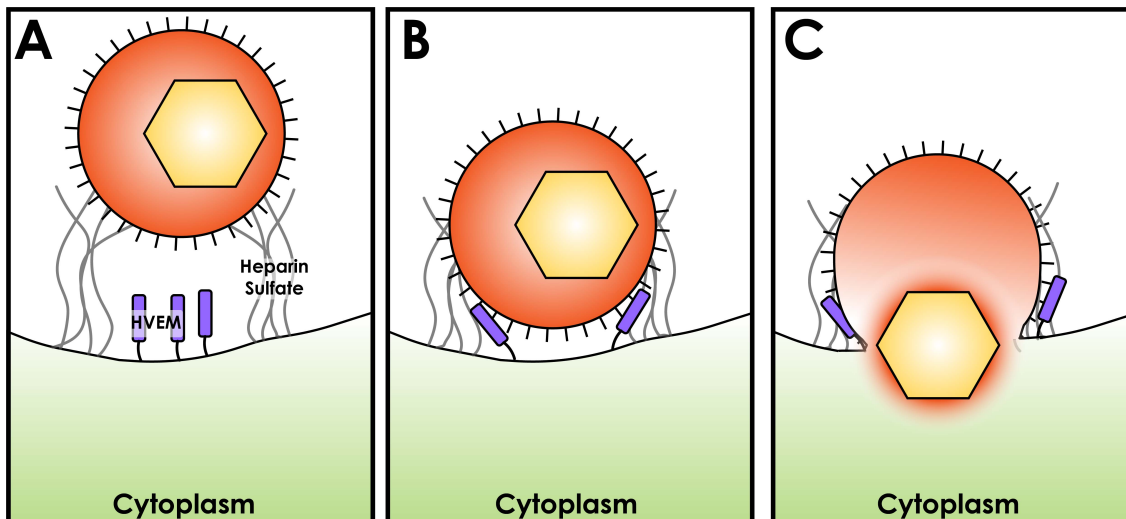


Figure 1.26 - Viral entry occurs through membrane fusion

A - Initial attachment between an enveloped virus (capsid yellow, tegument orange) is mediated between viral glycoprotein gB and Heparin sulphate. B - A tight interaction is formed between gD and one of three viral receptors (HVEM here, purple). C - Once the membrane has fused, the capsid and the inner tegument is released into the cytoplasm

Cryo-ET has showed that these initial interactions bring the virus within 20 nm of the cell membrane (Maurer et al., 2008). A tight interaction is achieved when gD binds to one of nectin-1 (Geraghty et al., 1998), Herpesvirus entry mediator (HVEM, a TNF/NGF family member) (Montgomery et al., 1996) or 3-O-sulfated heparin sulfate (Shukla et al., 1999) (**Figure 1.26B**). Following tight attachment a cascade of conformational changes in the viral membrane receptors occurs ending in the activation of the final “fusogen” gB, which brings the two membranes close enough to fuse (Cooper and Heldwein, 2015) (**Figure 1.26C**).

Separate from this method of internalisation, Herpes viruses can be endocytosed into internal vesicles (Nicola and Straus, 2004; Nicola et al., 2003) in a clathrin-independent phagocytic process (Clement et al., 2006; Devadas et al., 2014) In Chinese Hamster Ovary (CHO) cells, which do not express any of the three gD receptors, the virus is internalized but eventually degraded in the lysosomal pathway (Nicola and Straus, 2004). This suggests that for productive infection the virus still needs to fuse with host membrane and releases its capsid into the cytoplasm.

1.4.3 Dynein-dependent retrograde transport delivers the capsid to the nucleus

The cytoplasmic capsid next needs to move to the nucleus for expression of its DNA genome (**Figure 1.27A-C**). It has been estimated that an object the size of the HSV1 capsid would take 231 years to diffuse through 1cm bulk cytoplasm (Sodeik, 2000), a distance shorter than some of the neuronal axons HSV1 must traverse. As such, the capsid engages microtubule motors for intracellular transport (Sodeik et al., 1997). Given that minus-end transport is needed to move from the cell periphery to the nucleus in herpesvirus target cells, cytoplasmic dynein-1 is responsible for viral movement (Döhner et al., 2002a; Dodding and Way, 2011).

Efficient microtubule-dependent retrograde transport of HSV1 was initially observed in both epithelial cells (Sodeik, 2000; Sodeik et al., 1997) and neuronal axons (Bearer et al., 2000). However, a direct role for dynein in HSV1 transport was first shown when fewer capsids reached the nuclei of epithelial cells following overexpression of the dynactin subunit p50 (a common technique to disrupt dynein/dynactin based transport (Burkhardt et al., 1997)) (Döhner et al., 2002a). HSV1 and PrV transport is equivalent in neurons, with incoming capsids of both species moving at $\sim 2\mu\text{m/s}$. (Antinone and Smith, 2010). Recently, high-resolution tracking of retrograde transport showed that there were frequent short anterograde phases during viral entry, indicating that kinesin is recruited to the virus as well (Scherer et al., 2016).

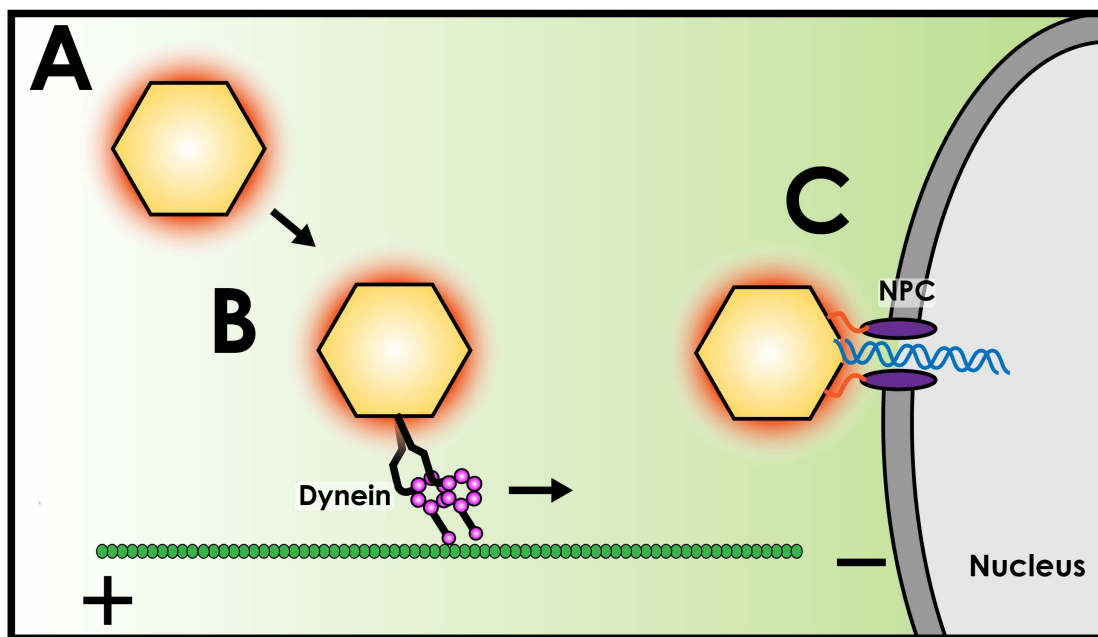


Figure 1.27 - Dynein-dependent retrograde transport delivers capsids to the nucleus

A - The capsid and inner tegument are free in the cytoplasm, and recruit active dynein complexes. B - Cytoplasmic dynein-1 (magenta) walks on microtubules (green filament) to take capsids to the center of the cell. C - Capsids dock at the nuclear pore and inject their DNA into the nucleus

Retrograde transport initiates rapidly, with capsids moving into neuronal axons within 30 minutes of infection (Aggarwal et al., 2012). RNA silencing shows that initiation is dependent on the microtubule plus-end tracking protein CLIP-170 (Jovasevic et al., 2015), however the mechanism of this dependence is unknown. Intriguingly, retrograde transport of PrV appears to depend on the simultaneous invasion of a single cell with multiple viruses (Koyuncu et al., 2015). This is potentially linked to an increase protein synthesis localized to PrV infected axons (Koyuncu et al., 2013). These results suggest that retrograde viral transport is dependent on wide-ranging modulation of the host by viral tegument proteins.

Despite these advancements in the understanding of herpesvirus transport, it is still not known *how* dynein transports viral capsids. Most fundamentally, it is unknown what viral or host proteins recruit motile dynein complexes to the capsid. Cryo-electron microscopy of HSV-1 entering synaptosomes showed that the vast majority of tegument density remains associated with the cell membrane after fusion (Maurer et al., 2008). Fluorescence microscopy shows that the only components of the tegument that stay with the capsid during transport are pUL36, pUL37 and US3 (Aggarwal et al., 2012; Antinone and Smith, 2010). Immuno-EM showed that

the tegument is required to interact with dynein, and tegument-free capsids purified from the nucleus (“C-capsids”) do not interact with dynein (Radtke et al., 2010). Furthermore, mass spectrometry showed that no microtubule motors are present in the mature virus prior to infection (Kramer et al., 2011). Therefore, it follows that upon cell entry dynein is recruited by one of these three inner tegument proteins.

Most evidence points towards pUL36 being responsible for dynein recruitment. Viruses with UL36 knocked-out do not produce progeny, meaning that subsequent infection without UL36 can not be studied (Desai, 2000; Fuchs et al., 2004a). However, pUL36 pulls-down dynein and dynactin when ectopically expressed in the absence of other viral proteins (Zaichick et al., 2013). Furthermore, Zaichick et al. demonstrated that mitochondria tethered to pUL36 form a tight cluster at the centre of the cell, showing that pUL36 is sufficient to initiate retrograde transport. Different post-translational modifications of pUL36 result in different viral motility phenotypes. Specifically, stable retrograde transport only occurs when K442 is ubiquitinated in PrV (Huffmaster et al., 2015). Taken together, these results strongly suggest that pUL36 is responsible for recruiting dynein and controlling retrograde transport.

However, despite the importance of pUL36, wild-type retrograde transport also depends on pUL37. Deletion of pUL37 slows down viruses from reaching the nucleus in epithelial cells, but does not abolish this movement (Krautwald et al., 2009). Mutations in pUL37 can result in a large increase in the amount of anterograde phases during viral entry, reducing the amount of capsid delivered to the nucleus (Richards et al., 2017). pUL36 and pUL37 directly interact (Klupp et al., 2002), and so could potentially both contribute to the same interaction with dynein.

A complication in the life cycle of herpesviruses is the require to switch transport behaviours during entry. Retrograde transport delivers the virus to the MTOC, which means that a plus-end directed motor must then transport the capsid out again, towards a nuclear pore. Mutating a nuclear localisation signal (NLS) in pUL36 results in capsid accumulation at the MTOC (Abaitua et al., 2012), suggesting that pUL36 is responsible for recruitment of plus-end directed motors as well as minus-end. This behaviour is controlled by dystonin (McElwee et al., 2013), which is in turn recruited by pUL37 (Pasdeloup et al., 2013), further highlighting the role of pUL37 in tuning viral transport during entry.

1.4.4 The viral genome is ejected through the nuclear pore

Retrograde transport delivers the capsids to the centre of the cell, where they dock to a nuclear pore complex (NPC, (Sodeik et al., 1997) **Figure 1.27C**). Recruitment of kinesin, potentially dependent on the NLS of UL36, is probably required to transport the virus from the MTOC to the nuclear pore (Abaitua et al., 2012; McElwee et al., 2013). Nuclear pore components RanBP2 (Nup358) and Nup214 interact with pUL36 and UL25 respectively (Copeland et al., 2009; Padeloup et al., 2009). TEM of capsids engaged with the NPC show that there is always one vertex pointing towards the NPC pore (Ojala et al., 2000; Sodeik et al., 1997), presumably corresponding to the portal-vertex complex. The precise trigger for the release of the viral DNA is unknown. Two candidates are pUL36 (Jovasevic et al., 2008), and the portal protein UL6 (Newcomb et al., 2007), both of which undergo proteolytic cleavage at the nuclear pore. Furthermore, immediate-early viral proteins such as ICP0 and ICP4 are imported into the nucleus, dependent on importin α 1, in order for viral gene expression to commence (Döhner et al., 2018).

Viral DNA can be stimulated to release from purified capsids by either heat or trypsin digestion (Newcomb et al., 2007). Subsequent negative stain EM showed that the DNA was ejected from a single vertex as an isolated double helix. The mechanism of ejection is ATP-independent, and probably pressure-driven in a mechanism akin to bacteriophages (Bauer et al., 2013). The DNA is injected through the nuclear pore and into the nucleus, where it can be transcribed (**Figure 1.27C**).

1.4.5 Procapsids are assembled in the nucleus

Following transcription and translation of the viral genome, new capsids are produced in the nucleus. An immature procapsid is made up of VP5 capsomers, VP19 and VP23 triplexes, the portal, and a viral scaffolding protein (UL26.5) that directs assembly (Newcomb et al., 1996). The fully formed procapsid has T=16 icosahedral symmetry, but is more circular than the mature capsid (**Figure 1.28A**, (Newcomb et al., 2000). Development into the mature capsid involves a multi-step conformational change associated with cleavage and dissociation of the scaffold protein (Heymann et al., 2003). DNA is packaged into a mature capsid through the

portal by the DNA translocase UL15 (**Figure 1.28B**, (Heming et al., 2017). pUL36 and pUL37 are both added to the capsid in the nucleus (Bucks et al., 2007), however this is not necessary for capsid maturation and nuclear egress (Fuchs et al., 2004b), and has not been observed in all studies (Radtke et al., 2010; Crump, 2018)

1.4.6 Nuclear egress of new capsids occurs through primary envelopment

The Herpesvirus capsid buds across the inner nuclear membrane and into the perinuclear space in a process known as primary envelopment (**Figure 1.28C**). This is mediated by UL31 and UL34, which form a membrane bound complex facing the interior of the nucleus able to recruit and bud off the capsids (Bigalke and Heldwein, 2015; Hagen et al., 2015; Johnson and Baines, 2011). The enveloped capsids then bud into the cytoplasm by fusion with the outer nuclear membrane by an unknown mechanism (**Figure 1.28D**) (Mettenleiter et al., 2013). Simultaneous deletion of the viral glycoproteins proteins gB and gH resulted in accumulation of HSV-1 in the perinuclear space (Farnsworth et al., 2007), suggesting they are required for fusion with the nuclear envelope. However, their deletion had no effect for nuclear egress in PrV (Klupp et al., 2008), suggesting these viruses may escape the perinuclear space by different mechanisms (potentially dependent on different systems being studied).

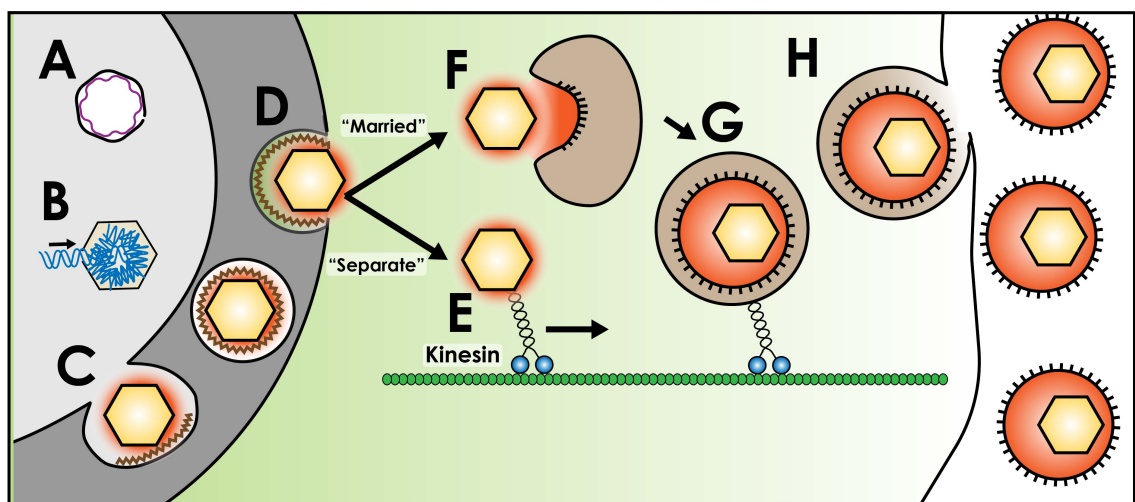


Figure 1.28 - Viral egress requires kinesin transport

A - New procapsids are formed in the nucleus with an internal UL26.5 scaffold (purple), and develop into mature capsids with packaged DNA (**B**). **C** - The mature capsid gains some inner tegument components in the nucleus and buds into the perinuclear space with the UL31/UL34 complex (brown) (primary envelopment). **D** - The perinuclear vesicle fuses with the outer nuclear membrane, releasing the capsid

into the cytoplasm. **E** - Some evidence suggests that the capsid and inner tegument directly recruits kinesin motors to travel to the cell periphery, where it would undergo secondary envelopment. **F** - Other evidence suggests that secondary envelopment occurs in the center of the cell. Outer tegument and glycoproteins are directed to TGN derived vesicles, and recruit the capsid. **G** - The capsid buds into the vesicle, which is transported by kinesin to the periphery. **H** - Following secondary envelopment, the virus is exocytosed, leaving mature virus in the cytoplasm.

1.4.7 Egress occurs following anterograde transport

To exit the cell the cytoplasmic capsid buds into a vesicle derived from the trans-Golgi network that has recruited all the tegument and glycoproteins found in the mature virus, and leaves the cell by anterograde transport and exocytosis (Owen et al., 2015; Smith, 2012). However, the precise order of events is subject to debate. Some studies have observed naked HSV1 capsids being transported on their own, in the absence of membranes or the outer tegument (**Figure 1.28D-E**, (Ibiricu et al., 2011; Miranda-Saksena et al., 2009). The inner tegument proteins have been added to the capsid at this stage (Ibiricu et al., 2011), so they should be able recruit kinesin-1 and kinesin-2 (Radtke et al., 2010). This mechanism of egress has been called the “separate model”.

However, other results support the “married model”, in which the capsids undergo secondary envelopment into post-Golgi vesicles loaded with viral membrane and tegument proteins at the centre of the cell and are then transported within their envelope to the periphery (**Figure 1.28F-G**). Fluorescence microscopy studies show co-transport of capsid components and the membrane protein gD (Antinone and Smith, 2010; Antinone et al., 2010; Wisner et al., 2011). In this model, kinesin is recruited to the enveloped cytoplasmic virus by the viral membrane proteins US9 and gE. Deletion of these components in HSV1 abrogates the anterograde spread of progeny virus in neurons (Howard et al., 2013). Furthermore, HSV1 US9 has been shown to interact directly with Kinesin 1 in *in vitro* pulldown assays (Diefenbach et al., 2016). However, cell lysate pulldowns with PrV US9 identified Kif1a, a kinesin-3 family member, as the most abundant motor (Kramer et al., 2012). These contrasting results, including those regarding naked capsid, suggest that there is considerable redundancy in the anterograde transport of herpesviruses. The mature virus is released into surroundings by exocytosis of the vesicle (**Figure 1.28H**)

1.5 Aims

My PhD contained three projects with separate aims:

- The first project, corresponding to Chapter 3, was aimed towards understanding the interaction between dynein and the microtubule more clearly. The conformational changes in the ring resulting in a change in stalk registry had been well established by high-resolution X-ray crystallography. However, the interpretation of the conformational changes that occur in the MTBD as a result of AAA1 nucleotide site were tempered by the limited resolution of the microtubule-bound MTBD cryo-EM structure. I therefore wanted to use the modern generation of direct electron detectors to solve a higher-resolution structure of the cytoplasmic dynein-1 MTBD bound to microtubules, and understand this interaction more clearly. Furthermore, divergences in sequence between cytoplasmic and axonemal dynein MTBDs made it unclear whether the mode of interaction is conserved. I therefore investigated the structure of a distantly related axonemal dynein MTBD bound to microtubules for comparison to cytoplasmic dynein-1.
- The second project, corresponding to Chapter 4, was aimed towards understanding dynein stepping behaviour and directionality. High-resolution structures had shown the mechanics underlying the dynein power stroke, but optical trap and fluorescence tracking showed that dynein stepping is irregular. It was therefore not well understood what makes dynein walk towards the microtubule minus-end. I collaborated with Dr Ahmet Yildiz and his PhD student Sinan Can to address this question.
- The third project, corresponding to Chapter 5, was aimed towards understanding how herpesviruses are transported by dynein. A large body of evidence had demonstrated that the virus is dependent on dynein transport to reach the nucleus during cell entry, but how this interaction occurs is poorly understood. Of particular interest in light of the activating cargo-adaptor model was whether a viral protein (i.e. pUL36) is able to active dynein activity as a cargo adaptor.

Chapter 2. Materials & Methods

2.1 Cloning and Protein Purifications

2.1.1 Touchdown PCR and Gibson Cloning

For cloning, primers were designed to include 30-40 bases overlap with the partner fragment. PCR was performed with Q5 DNA polymerase (NEB) with GC-rich optimised buffer according to manufacturers instructions. The only modification was the use of a touchdown PCR protocol. The annealing temperature at the first cycle was 75°C, and was decreased by 1°C each iteration. After 10 cycles, the annealing temperature was kept at 65°C until the end of the run. A Gibson reaction was performed according to the manufacturers instructions (NEB). Following incubation at 50°C for 60 minutes, the mixture was transformed into TOP10 cells. The plasmid DNA was recovered in a Miniprep (Qiagen) and its sequence was verified by Sanger sequencing (Source Bioscience)

2.1.2 Purification of SRS Fusion proteins

All SRS fusion constructs were expressed and purified according to the same protocol. Proteins were expressed in SoluBL21 *Escherichia coli* cells (Invitrogen) from a pet42a vector. Cells were grown in LB media with 50 ug/mL kanamycin at 37°C until their OD₆₀₀ measured 0.4-0.6, at which point they were supplemented with 1 mM IPTG and grown for 16 hours at 16°C. Cultures were spun at 4000 rcf for 15 minutes, and used directly for purification.

A cell pellet from 1 L of culture was resuspended in 50 mL Lysis buffer (50 mM Tris pH 8.0, 100 mM NaCl, 1 mM MgCl₂, 10% Glycerol, 10 mM Imidazole pH 8.0, 1 mM DTT, 2 mM PMSF) and lysed by sonication. The lysate was centrifuged at 30000 rcf in a Ti70 rotor (Beckman) for 30 minutes and at 4°C. The supernatant was loaded onto a 5 mL NiNTA HisTrap HP Column (GE), washed with 10 column volumes of 10% elution buffer (50 mM Tris pH 8.0, 100 mM NaCl, 1 mM MgCl₂, 10% Glycerol, 500 mM Imidazole pH 8.0, 1 mM DTT) and eluted with a step gradient to 40% elution buffer. Peak fractions were pooled and concentrated in a 15 mL 30k MWCO centrifugal concentrator (Amicon) to a concentration of ~5 mg/mL. Aliquots were snap frozen in liquid nitrogen.

Size-exclusion chromatography was run prior to grid preparation. Thawed aliquots were spun through a 0.22 μm spin filter (Amicon) to remove aggregates and loaded onto a Superose 6 10/300 column (GE) equilibrated in GF50 buffer (25 mM Tris pH 8.0, 50 mM NaCl, 1 mM MgCl_2 , 1 mM DTT). Peak fractions (as judged by InstantBlue coomassie staining (Expedeon) of an SDS-PAGE gel) were pooled and concentrated in a 4 mL 30MWCO centrifugal concentrator (Amicon) to 1/10th of the original volume. The sample was then diluted 5-fold in no-salt GF buffer (25 mM Tris pH 8.0, 1 mM MgCl_2 , 1 mM DTT) and reconcentrated. This was repeated twice, and then the sample was further diluted to a final concentration of 2 mg/mL for grid freezing.

2.1.3 Insect Cell Expression

The human cytoplasmic dynein-1 motor domain (pACEBac1 plasmid, (Steinman et al., 2017)), human full-length dimeric dynein complex (pDyn3, (Schlager et al., 2014a)), BicD2N (pACEBac1, (Schlager et al., 2014a)), and all purified pUL36 and pUL37 constructs (pACEBac1) were all expressed in the *Sf9* insect cell expression system. Both pUL36 and pUL37 sequences were obtained as a synthetic gene product (Epoch Gene, both PrV Becker strain sequences, UL36 UniProt #G3G960, UL37 UniProt #T2FKR8)

Expression followed the established protocols for the MultiBac system (Bieniossek et al., 2012). Plasmids were transformed into EmBacY cells by heat shock at 42°C for 30 seconds. These cells exchange the pACEBac1 expression cassette (including the insert ORF) into a bacmid via Tn7 transposition. Successful transposition is revealed in each colony by blue/white selection on X-Gal plates, as the insertion site disrupts a β -galactosidase gene. For bacmid preps, 8 mL of LB media was supplemented with 7 $\mu\text{g}/\text{mL}$ gentamycin, 10 $\mu\text{g}/\text{mL}$ tetracycline and 50 $\mu\text{g}/\text{mL}$ kanamycin and inoculated with a white colony. Following overnight incubation, cells were pelleted at 4000 rcf for 10 minutes, and lysed using the Qiagen miniprep buffer P1 to N3 as standard. The lysate was spun at 16000 rcf for 10 minutes, and the supernatant was added to 0.8 mL cold isopropanol. After 30 minutes incubation on ice, the precipitated bacmid DNA was pelleted at 16000 rcf for 10 minutes. The supernatant was removed and the pellet was washed by the addition of 1 mL 70% ethanol. The sample was re-spun, and the ethanol wash was repeated two more times. Following removal of the supernatant from the last wash, the bacmid pellet was resuspended in 200 μL EB buffer (Qiagen).

To transfect the bacmid into *Sf9* cells, a mixture of 2 μL 1 $\mu\text{g}/\mu\text{L}$ bacmid DNA, 5 μL FuGene HD (Promega) transfection reagent and 193 μL Insect-XPRESS media (Lonza) was incubated for 15 minutes at room temperature. This mixture was dropped onto a 6-well plate well containing 2 mL *Sf9* cells at a density of 0.5×10^6 cells/mL. Following 72 hours incubation at 27°C, the media from these wells (P1 virus) was used to infect a 50mL culture of cells at a density of 1×10^6 cells/mL. This culture was incubated at 27°C with shaking for 72 hours, after which the cells were pelleted by centrifugation at 4000 rcf for 10 minutes and the supernatant was retained as the P2 viral stock. 5 mL of P2 viral stock was used to infect a 500 mL culture of cells at 2×10^6 cells/mL for the final expression stage. Following 72 hours of incubation, the culture was spun at 4000 rcf for 15 minutes, and the cell pellet was recovered and snap-frozen in liquid nitrogen.

2.1.4 Purification of ZZ-tagged proteins

All ZZ-tagged proteins (dynein motor domain, full-length dimeric dynein, BICD2N) were purified according to the same protocol. A pellet from 1 L of cells was resuspended in 50 mL ZZ-Lysis buffer (50 mM HEPES pH 7.4, 100 mM NaCl, 1 mM MgCl_2 , 10% Glycerol, 1 mM DTT, 2 mM PMSF) and dounce homogenised with 30 strokes. The lysate was centrifuged at 500,000 rcf in a Ti70 rotor (Beckman) for 60 minutes and at 4°C. The supernatant was mixed with 2 mL IgG Sepharose 6 Fast Flow resin (GE, equilibrated in ZZ-lysis buffer) on a horizontal roller for 2 hours at 4°C. The mixture was applied to a gravity flow column, and the resin was washed with 150 mL ZZ-Lysis buffer and 150 mL TEV buffer (50 mM Tris pH 7.4, 150 mM KOAc, 2 mM MgAc, 1 mM EGTA, 10% Glycerol, 1 mM DTT). The resin was resuspended in 5 mL TEV buffer, supplemented with TEV protease to a final concentration of 0.1 mg/mL and incubated on a horizontal roller at 25°C for 80 minutes. The sample was reapplied to a gravity flow column, the eluate was collected and concentrated with a 15 mL 100kMWCO centrifugal concentrator (Amicon). Size-exclusion chromatography was performed with a Superose 6 10/300 column for the monomeric dynein motor domain and BICD2N, and with a G4000_{SWXL} column (Tosoh) for full-length dimeric dynein.

2.1.5 Purification of Strep-tagged pUL36 and pUL37 constructs

A 500 mL cell pellet was resuspended in 25 mL lysis buffer (50 mM HEPES pH7.2, 100 mM NaCl, 10% Glycerol, 1 mM DTT, 0.2 mM PMSF, 1 protease inhibitor tablet (Roche) per 50 mL). Cells

were lysed by with 30 strokes in a dounce homogeniser, and centrifuged at 30000 rcf for 30 minutes, 4°C. The supernatant was retained, and applied to 1 mL Strep-tactin resin (bed volume, IBA Life Sciences) pre-equilibrated in lysis buffer. Following 1 hour incubation on an orbital roller at 4°C, the mixture was applied to a gravity flow column and washed with 150 mL lysis buffer. The tagged protein was eluted in 1 mL fractions by the addition of lysis buffer supplemented with 2.5 mM desthiobiotin. The elution was concentrated with a 100 MWCO centrifugal concentrator (Amicon) to 1-2 mg/mL.

Where indicated, concentrated affinity elutions were run on size exclusion chromatography using a Superose 6 10/300 column (GE) equilibrated in GF150 (25 mM Hepes pH 7.2, 150 mM KCl, 1 mM MgCl₂, 1 mM DTT). The peak elution fractions were concentrated in a 100 MWCO centrifugal concentrator (Amicon) to 1-2 mg/mL

2.1.6 SEC-MALS

For SEC-MALS, pUL36⁷⁴³⁻²⁹⁸⁵ was run on a Superose 6 10/300 size-exclusion chromatography connected to a Wyatt Heleos II 18-angle light-scattering instrument, with the help of Dr Chris Johnson.

2.1.7 Fluorescent labelling of SNAP tags

UL36 and dimeric dynein SNAP tags were both fluorescently labelled using the following protocol. Following washes in the gravity flow column, the IgG or Strep-tactin beads were recovered and incubated with 10 uM fluorescent SNAP-substrate dye (NEB) for 1 hour at room temperature. The beads were then reapplied to a gravity flow column, rewashed to remove excess dye and eluted as before.

2.1.8 Purification of Dynactin

For TIRF assays, purification of dynactin was performed as previously described (Urnavicius et al., 2015). 3 Pig brains were homogenised in homogenisation buffer (HB) (35 mM PIPES-KOH pH 7.2, 1 mM MgSO₄, 0.2 mM EGTA, 0.1 mM EDTA, 1 mM DTT, 1.6 mM PMSF) using a Waring

blender. The lysate was cleared by centrifugation at 38000 rcf (15 minutes, TLA16.250, Beckman) and then 235000 rcf (50 minutes, Ti45, Beckman). The supernatant was filtered through a 0.45 μm syringe filter (Elkay) and loaded onto a self-packed 300 mL SP-Sepharose Fast Flow (GE) column. Unbound sample was washed out with 4 column volumes (CV) of buffer A (HB + 0.1mM ATP). Sample was eluted with a 0% to 25% gradient of buffer B (Buffer A + 0.5M KCl) over 4 column volumes. Peak fractions (centered around ~12% buffer B) were pooled, filtered through a 0.22 μm syringe filter, and loaded on a MonoQ HR 16/10 column (GE). The column was washed with 95% HB and 5% HB-K (HB + 1M KCl) for 10 CV. Sample was eluted with a 5% to 15% HB-K gradient over 1 CV and then a 15% to 35% HB-K gradient over 10 CV. The dynactin peak typically eluted at 29% HB-K, and was concentrated in a 100MWCO Amicon centrifugal concentrator. The concentrated sample was loaded on a G4000_{SWXL} size-exclusion chromatography column equilibrated in GF150 buffer (25 mM Hepes pH 7.2, 150 mM KCl, 1 mM MgCl₂, 1 mM DTT). The eluted peak was then reconcentrated to ~2 mg/mL and snap-frozen in aliquots.

2.2 Electron Microscopy

2.2.1 13-protofilament microtubule polymerisation for EM

Commercial lyophilised pig brain tubulin (Cytoskeleton) was resuspended in MES-NaCl buffer (25 mM MES pH 6.5, 70 mM NaCl, 1 mM MgCl₂, 1mM DTT) to a concentration of 10 mg/mL and snap frozen in aliquots. For polymerisation, an aliquot was thawed and mixed 1:1 with MES-NaCl buffer supplemented with 6 mM GTP (final GTP concentration 3 mM), and incubated at 37°C for 2 hours. 100 μL MES-NaCl buffer supplemented with 20 μM Taxol and pre-warmed to 37°C was then added, and the sample was left at room temperature overnight. Before use, the microtubules were spun at 20000x rcf for 10 minutes, and resuspended in MES-NaCl buffer with taxol to remove unpolymerised tubulin.

2.2.2 Preparation of grids with microtubules fully decorated by SRS constructs or monomeric motor domain

Quantifoil R1.2/1.3 Au300 grids were glow-discharged in an Edwards Sputter Coater for 40 seconds. 4 μL 0.4mg/mL microtubules was added to the grid and incubated at room

temperature for 1 minute. This was removed by side blotting with Whatman filter paper, then 4 μL of SRS-MTBD or motor domain was added and the grid was incubated for a further 2 minutes. Manual side blotting was repeated, another 4 μL of dynein was applied, and the grid was placed in the humidity chamber of a Vitrobot Mark II set to 100% humidity and 22°C. After 2 minutes incubation, the grid was double-side blotted for 4 seconds and plunged into liquid ethane. This method of on-grid incubation resulted in an even distribution of microtubules on the grid, with high decoration levels.

For glutaraldehyde fixation of SRS-Cyt1^{RK} to microtubules, I performed on-grid decoration of microtubules with SRS-Cyt1^{RK} as described above. Following the final incubation with SRS-MTBD, I side-blotted the sample away and replaced with 4 μL of 0.025% glutaraldehyde in GF buffer without NaCl. The grid was then placed in the Vitrobot and blotted as described above.

2.2.3 Data collection for fully decorated microtubule samples

Cyt1-SRS grids were imaged on the in-house Titan Krios microscope, and DNAH7-SRS grids were imaged on Krios III at Diamond eBIC. For the Cyt1-SRS, 1995 1.5 s exposures were collected with a pixel size of 1.04 \AA^2 and a fluence of 40 $\text{e}^-/\text{\AA}^2\text{s}$ on a Falcon III detector in linear mode. For DNAH7-SRS, 4641 1.5 s exposures were collected with a pixel size of 1.085 \AA^2 and a fluence of 45 $\text{e}^-/\text{\AA}^2\text{s}$. Microtubules saturated with dynein motor domain were imaged on a Polara microscope, with 2455 1.5 s exposures collected with a pixel size of 1.34 \AA^2 and a fluence of 37 $\text{e}^-/\text{\AA}^2\text{s}$ on a Falcon III detector in linear mode. In each case, images were acquired with a defocus ranging between -1.5 μm and -4.5 μm semi-automatically in EPU.

	Cyt1		
	Cyt1-SRS	Motor domain	DNAH7-SRS
Microscope	Krios	Polara	Krios
Detector	Falcon III	Falcon III	Falcon III
Voltage (kV)	300	300	300
Exposure time (s)	1.5	1.5	1.5
Total dose (e ⁻ /Å ²)	60	67.5	55.5
Pixel Size (Å)	1.04	1.34	1.1
Defocus Range (um)	-1.5 to -4.5	-1.5 to -4.5	-1.5 to -4.5
Sessions	1	1	1
Micrographs	1995	2455	1995
Symmetry	13*	13*	13*
Final particles	59100	38142	41984
Resolution (Å)	4.1	5.5	4.8

Figure 2.1 -Data collection parameters for large cryo-EM datasets

2.2.4 Microtubule reconstruction in Chuff

To reconstruct Cyt1-SRS images in Chuff, motion correction was performed in MotionCor2 (Zheng et al., 2017) and particles were manually picked as microtubule segments in E2Boxer (Tang et al., 2007). These images and coordinates were used as the input for Chuff, using the implementation most recently used in (Shang et al., 2014). Chuff performs all steps from this point automatically. The output reconstruction is averaged but unfiltered. For visualisation, the map was B factor sharpened and lowpass filter with *relion_image_handler* as indicated in the images. The FSC curve output from Chuff is not gold-standard. Instead, all the data are refined to a single model, and the FSC is measured by splitting the particles from this single refinement into two groups. This has been known to result in overfitting (Scheres and Chen, 2012), and is a potential reason for the overestimation of resolution compared to the features of the map.

2.2.5 Microtubule reconstruction in Relion

All processing was performed inside the Relion 3.0 pipeline (Zivanov et al., 2018). Details are given for processing the Cyt1-SRS dataset, followed by modifications to this workflow used for the other datasets. The unaligned raw movies were aligned and dose weighted in Relion's implementation of MotionCorr2, with images split into 4x4 patches (Zheng et al., 2017). CTF

determination was performed with Gctf on dose-weighted micrographs (Zhang, 2016). The start and end coordinates for 30 microtubules were manually picked from 5 images, and extracted as a helix with a helical rise of 82 Å between consecutive particles. These particles were classified into 5 2D classes, with the resulting classes used as references for autopicking over all micrographs. Autopicking resulted in 192,314 particles, which were extracted and classified into 100 2D classes. I rejected classes if they were obviously not microtubules (carbon, ice etc), if they appeared blurred or poorly aligned, if they had low levels of decoration, or if they showed signs of non-13-PF architectures (see **Figure 3.10**). Following two rounds of 2D classification, the good particles were taken forward for 3D classification. A 3D reference was made by docking a model of dynein decorated tubulin into EM density for a 13- protofilament microtubule (PDB 3J1T and EMD 6351 respectively), and converting the PDB coordinates to electron density in EMAN2 *pdb2mrc*. This model was lowpass filtered to 20 Å. Helical 3D classification (*de novo* orientations, no local symmetry) of the unbinned particles into 3 classes resulted in a single good class containing 59,100 particles.

The class was then used for 3D refinement. The final refinement used a 0.9° initial angular sampling interval, with an initial step size of 0.5°. A tight 3D solvent mask was made of the 3D reference with *relion_mask_create* and applied during the refinement, and 13-fold non-crystallographic symmetry was also applied. For the local symmetry mask, copies of PDB 3J1T were docked into the protofilament to the left of the seam (if the MT is viewed plus-end up). The PDB protofilament was then converted to electron density with EMAN, and subsequently a mask with *relion_mask_create*. *relion_local_symmetry* requires a STAR file containing the translational and rotational operators needed to move the original mask onto each successive protofilament. The psi angle, rotating around the microtubule long axis, was given as multiples of 27.69° (360°/13). The center of rotation is the center of the microtubule lumen, so the only translation needed is the rise between adjacent protofilaments. For a 3-start helix, there is a rise of 1.5 dimers through 360°. The refined helical rise between dimers in the same protofilament as measured by Relion was 82.29 Å. As such, the *_lnOriginZ* parameter increases by multiples of 9.495 Å (82.293 * 1.5 / 13). Local symmetry was applied during refinement with the additional argument *--local_symmetry*. Following completion of refinement, local symmetry was applied to both unfiltered half maps with *relion_localsym*. Postprocessing and resolution assessment was performed with three tubulin dimers docked along a single protofilament as previously described (Zhang et al., 2015a, 2018c).

The only modification made to this process for the dynein motor domain and Cyt1^{RK}-SRS datasets was four instead of three classes were used for 3D classification. For the DNAH7-SRS structure, initial 3D classification did not result in a coherent class. Instead 3D refinement on all particles from 2D classification was run, resulting in a map with blurred features. Following this, 3D classification into 8 classes using the orientations used in the refinement (i.e. with no image alignment) was performed. Following refinement of the good subclass, local symmetry operators were found with the search command in *relion_localsym*. Classes A and B were identified in another classification job, this time with Tau=20 and using 0.9° local angular searches.

The EB3 dataset was downloaded from EMPIAR (ID 10030). 3D classification was skipped since the microtubules in this dataset almost exclusively have 13 protofilaments (Zhang et al., 2015b). EB3 does not bind across the seam, which means that applying regular 13-fold symmetry was not appropriate. A separate mask was created for the tubulin and EB3 densities using the separated models from PDB 3JAR. The tubulin mask and EB3 masks were applied with 13- and 12-fold symmetry respectively.

Local resolution estimation was performed in *relion_postprocess*.

2.2.6 Subtraction and Symmetry expansion

To subtract the tubulin density from the decorated microtubule, a model for the dynein MTBD (3J1T) was docked into the MTBD density of each protofilament. This was converted into electron density in EMAN2 *pdb2mrc* and then a 3D mask in *relion_mask_create*. This was used as the mask in the “Particle Subtraction” module of Relion. The particles were then 2D classified and 3D refined as standard.

For particle symmetry expansion, the helical parameters obtained for the refinement were used to expand the particles with 13-fold symmetry using *relion_particle_symmetry_expand*. Everything but one tubulin dimer and MTBD was then subtracted, 3D classification without orientation refinement and with a tau value of 20 was performed.

2.2.7 Model Refinement

For cytoplasmic dynein-1 a low-affinity crystal structure (PDB 3ERR) was used as the starting model for refinement. For DNAH7, the starting model was a homology model made by threading the DNAH7 MTBD sequence onto the low microtubule affinity *C. reinhardtii* flagellar dynein c NMR structure (PDB 2RR7) in Modeller (Sali and Blundell, 1993). The models were fit in their respective maps using Chimera (Pettersen et al., 2004). A tubulin dimer was docked into the density using PDB 5SYF (for DNAH7-SRS the tubulin dimer contacted by the flap was added as well). Coot Real Space refine zone (Emsley and Cowtan, 2004) was used to manually fit the model to the density, followed by whole model refinement using Phenix real space refine (Adams et al., 2010). These two steps were performed iteratively until the model to map measures were maximised. For model to map FSC curves phenix.mtriage was used. All model visualisation was performed in Chimera (Pettersen et al., 2004).

2.2.8 Analysis of microtubule distortion

Protofilament angles were measured by docking a tubulin dimer pdb model (5SYF) into two adjacent protofilaments of the relevant reconstruction in Chimera. The relative rotation was measured with the “measure rotation” command. Ellipticity was measured with the Matlab fit_ellipse script deposited in the Mathworks file exchange (https://www.mathworks.com/matlabcentral/fileexchange/3215-fit_ellipse). x,y coordinates for each protofilament were obtained from maximum intensity projections of each class, binarised with the same threshold in FIJI (Schindelin et al., 2012). The center of mass of each protofilament was used as the coordinate.

2.2.9 Preparation of sparsely decorated Cyt1 and Cyt1^{RK+7hep} Grids

Our collaborator Sinan Can (in Ahmet Yildiz's group) expressed and purified the wild-type Cyt1 and engineered Cyt1^{RK+7hep} monomeric motor domain constructs from *S. cerevisiae*. To exchange these into a low-salt buffer suitable for complex formation in cryo-EM, I thawed aliquots of purified protein, diluted them five-fold in BRB10 (10 mM PIPES pH 7.0, 1 mM EGTA, 1 mM MgCl₂, 1 mM DTT, supplemented with 0.1% Tween-20) and concentrated back to the original volume. This was repeated two more times, to give a total dilution factor of 125.

Buffer exchange was performed in the absence of nucleotide to achieve the high-affinity apo state. Three minutes before freezing grids I made a mixture of 1 μM microtubules (prepared as in 2.2.1) and 150 nM dynein in BRB10. I applied 4 μL to glow-discharged Quantifoil Au300 R1.2/1.3 grids and froze using an FEI Vitrobot III using a 4.5 s blot (100% humidity, 22°C).

2.2.10 Imaging microtubules decorated with Cyt1 and Cyt1^{RK+7hep}

Grids of microtubules sparsely decorated with these motor domain constructs were imaged in an FEI F20 microscope operating at 200kV, mounted with a side-entry holder (Gatan 626). I recorded images with FEI EPU software with a defocus of -4 μm , a flux of 50 $\text{e}^- \text{\AA}^{-2} \text{s}^{-1}$, an exposure of 1.5 s and a pixel size of 2.06 \AA^2 . ~ 150 images were collected for each sample

2.2.11 2D classification of Cyt1 and Cyt1^{RK+7hep} motor domains

CTF determination was carried out with Gctf (Zhang, 2016), and frequencies with negative contrast were phase-flipped in Relion. To determine microtubule polarity, each microtubule was cropped out in Fiji (Schindelin et al., 2012) and examined its power spectrum in FIJI. Fourier filtering microtubules to only include the equatorial reflections was performed in Fiji (“paint” areas to retain in the Fourier transform and perform inverse FFT). The microtubule was manually oriented with the plus-end to the right of the image. Motor domain particles were manually picked at the junction between the stalk and microtubule. For each dataset (Cyt1 and Cyt1^{RK+7hep}) particles were aligned by 2D classification of all the particles into one class in Relion.

Focussed sub-classification of this class was used to find sub-classes of the motor domain in discrete conformations. A 2D mask to include only the regions corresponding to the AAA+ ring was made for each class (i.e. Cyt1 and Cyt1^{RK+7hep}) in Fiji. Masked 2D classification into 10 classes without orientation refinement was then performed in Relion (for **Figure 4.12**). To align the ring in each class (**Figure 4.14**), the particles were re-extracted the particles with new coordinates centered on the region corresponding to the AAA+ ring. The particles were then reclassified into a single class with a tight circular mask so that the microtubule density is ignored and the motor domain ring is aligned.

To simulate projections of the motor on a microtubule a chimeric PDB model was made, as there is no crystal structure containing the full stalk and MTBD in the nucleotide-free state. PDB models 3VKG (for the stalk (Nishikawa et al., 2016)), 3J1T (for the MTBD (Redwine et al., 2012) and 4AI6 (for the AAA+ ring (Kon et al., 2012)) were combined in Chimera. This model was converted to electron density with EMAN2 (Tang et al., 2007), lowpass filtered it to 30Å in Relion (Scheres, 2012), and synthetic projections were made in different orientations in Relion.

2.3 Total Internal Reflection Microscopy

2.3.1 Polymerisation of labelled microtubules

For fluorescent and biotin labelled microtubules, 1 µL Alexa-647 tubulin, 2 µL biotinylated tubulin (both 2 mg/mL, Cytoskeleton), 2 µL unlabelled tubulin (11 mg/mL) and 5 µL BRB80 (80 mM PIPES pH 6.9, 1 mM MgCl₂, 1 mM EGTA) was mixed with with 10 µL 2x polymerisation buffer (1x BRB80 with 20% DMSO and 2 mM MgGTP). This mixture was incubated at 37°C for 1 hour and stabilised by the addition of 100 µL BRB80 supplemented with 10 µM Taxol.

2.3.2 Preparation of TIRF Chambers

Home-made TIRF assay chambers were prepared by laying two parallel strips of double-sided tape on a microscope slide around ~0.5 cm apart. A cover slip was pressed on top, creating a channel through which liquids can be flowed by capillary action.

15 µL 0.5 mg/mL Poly-L-Lysine Polyethylene Glycol Biotin (PLL-PEG-Biotin, SuSoS) was flowed into homemade TIRF assay chambers, and washed with 15 µL TIRF Assay Buffer (TAB) (25 mM HEPES pH 7.2, 5 mM MgSO₄, 1 mM EGTA, 1 mM DTT, 10 µM taxol). 1 mg/mL Streptavidin (NEB) was then flowed in, and the chamber was washed again with 15 µL TAB. The labelled microtubules were then added at a concentration of 0.3 mg/mL, incubated for 1 minute, and washed with TAB-Casein (TAB supplemented with 1.25 mg/mL α-casein (Sigma)). The assay mixture was then added and the chamber was imaged.

For binding curves of GFP-labelled SRS-MTBD constructs, the assay mixture consisted of MTBD at the stated concentration 20 µL of TAB buffer supplemented with 1.25 mg/mL α-casein

(Sigma), 60 mM 2-mercaptoethanol, 0.45% glucose, 1.5 mg/mL Glucose oxidase (Sigma) and 0.2 mg/mL Catalase (Merck). Glucose and the two enzymes comprise an oxygen scavenging system that reduces photobleaching of fluorophores (Aitken et al., 2008).

For the single-molecule motility assay, Dynein-Dynactin-adaptor complexes were pre-incubated by mixing 1 μ L of 200 nM TMR-Dynein, 2 μ L of 200 nM Dynactin and 1 μ L of 1 μ M cargo adaptor in 10 μ L TAB (total volume). Following 15 minutes incubation on ice, 1 μ L of this mixture was added to 19 μ L TAB supplemented with 1 mM MgATP, 1.25 mg/mL α -casein (Sigma), 60 mM 2-mercaptoethanol, 0.45% glucose, 1.5 mg/mL Glucose oxidase (Sigma), 0.2 mg/mL Catalase (Merck).

In each case, the assay mixture was flowed into the chamber directly after mixing. The slides were imaged on a Nikon total internal reflection fluorescence microscope, with a 100x objective lens (Nikon, 1.49 NA Oil, APO TIRF). For intensity measurements, three 20 ms exposures were taken in independent areas per slide (without pre-exposing the areas first). In the single-molecule motility assay, movies were typically recorded in 200 ms intervals.

Fluorescence intensity measurements for binding curves were recorded with Fiji (Schindelin et al., 2012). The average intensity of 10 non-overlapping microtubules in each image was recorded, as was the intensity of background fluorescence. The background intensity was subtracted from each microtubule. Two images from three independent slides were quantified in this way. Mean intensity per image \pm standard deviation was fit to a Hill curve in GraphPad Prism 7.

2.4 Studies in Mammalian Cells

2.4.1 Mammalian Cell Transfections

pcDNA4 plasmids containing UL36 constructs were transformed into TOP10 cells by heat shock at 42°C for 30 seconds, and plated on LB agar with 100 μ g/mL ampicillin. Colonies were inoculated into 50 mL cultures of LB with 100 μ g/mL ampicillin and grown overnight at 37°C with 220rpm shaking. The culture was centrifuged at 4000rcf for 15 minutes, and the cell pellet was used for a miraprep plasmid DNA purification (Pronobis et al., 2016). The pellet was

resuspended in 2 mL Qiagen miniprep buffer P1, lysed with the addition of 2 mL buffer P2, and neutralised with the addition of 2 mL N3. The lysate was spun at 20000 rcf for 10 minutes and the supernatant was collected. An equal volume of 96% ethanol was added, and the mixed sample was spun divided between 5 Qiagen spin columns. The columns were washed with Qiagen PE buffer as for a normal miniprep, and eluted with 50 μ L EB buffer. This typically yielded 200 μ L at \sim 5 mg/mL plasmid DNA with a 260/280 ratio greater than 1.9.

Vero and HeLa cells were maintained in Dulbecco's modified Eagle Medium (DMEM, GibCo) supplemented with 10% fetal calf serum (Gibco). The day prior to transfections they were split into new dishes to give a confluency of \sim 80% at the point of transfection. DNA was transfected with polyethylenimine (PEI). For a 6-well plate, 10 μ g plasmid DNA and 20 μ L PEI was added to 100 μ L DMEM and incubated for 15 minutes. This transfection ratio was scaled up or down depending on the amount of cells being transfected. The mixture was added to the well dropwise, and the plate was incubated at 37°C, 5% CO₂ for 3 hours, after which the medium was replaced for fresh DMEM/10%FCS. The cells were imaged or assayed after 18 hours incubation.

2.4.2 Spinning disk microscopy

For imaging mammalian cells, transfections were performed in Nunc Lab-Tek 4-well glass bottomed chamber slides (Thermo). These were mounted on an Andor Revolution Spinning Disk inverted microscope, equipped with an incubation chamber heated to 37°C. Typically, movies were recorded using the oil-immersion 40x objective lens, with 1 s interval between frames.

2.4.3 Pull-downs

For pull-downs from HeLa cells, T75 plates were transfected with the relevant plasmid using the PEI method above. For pulldowns from Vero cells, the transfection efficiency with PEI was very low. Instead, electroporation using the Neon system (ThermoFisher) was used. A confluent T175 plate of Vero cells was trypsinised, and the cells were pelleted at 300 rcf and resuspended in DMEM. 700 μ L cells at a density of 1×10^7 cells/mL were pelleted, washed in PBS, pelleted, and resuspended in 700 μ L Neon Buffer R. 150 μ g plasmid DNA was added, and

the cells were electroporated in groups of 100 μ L. I found that the best transfection efficiency was from three 10 ms 1300 V pulses, after which the cells were plated T75 plates. The cells were incubated overnight and used for pulldowns as for HeLa.

When indicated, 1 hour prior to starting the pulldown 25 μ L of magnetic GFP-trap resin slurry (Chromotek) per plate was washed twice in TAP lysis buffer (50 mM Tris pH 7.4, 50 mM KCl, 1 mM $MgCl_2$, 0.1% NP-40, 1 mM DTT, 0.2 mM PMSF, 1 protease inhibitor tablet (Roche) per 50 mL), and resuspended in 1 mL TAP lysis buffer supplemented with 1% Bovine serum albumin (BSA, Sigma). To start the pull-down, each T75 plate was washed with cold PBS once, and scraped into fresh PBS using a cell scraper. The cells were pelleted at 300 rcf for 5 minutes, and resuspended in 300 μ L ice-cold TAP lysis buffer. The cells were incubated on ice for 30 minutes, with resuspension every 10 minutes. The lysate was spun at 16000 rcf, 15 minutes, 4°C, and the supernatant was collected. The concentration of supernatant from each plate was measured by Bradford assay, and each sample was normalised to the sample with the lowest concentration by dilution with TAP lysis buffer. The GFP-trap resin (if unblocked, 25 μ L slurry per plate) was washed twice in TAP lysis buffer and added to the supernatant. This mixture was incubated on an orbital roller at 4°C for 180 or 60 minutes (as indicated in the text). The GFP-trap resin was then magnetically separated, the supernatant was removed, and 1 mL TAP lysis buffer was added. The resin was washed again as indicated in the text. Following removal of the liquid in the last wash, 15 μ L 2X NuPAGE LDS-Loading buffer (Invitrogen) was added. The beads were boiled, and the buffer was loaded on a NuPAGE 4-12% BisTris 15-well 1.0 mm gel (Thermo).

For the final pulldown/mass-spec experiments, three plates were transfected and purified independently for both pUL36 and the negative control.

2.4.4 Western Blots

Following SDS-PAGE, the samples were transferred to a Nitrocellulose membrane using the Trans-Blot Turbo Transfer system (Bio-Rad). When blotting for p150 (150 kDa) or tubulin (50 kDa) the gel was transferred for 10 minutes (2.5A, 25V). For RanBP2 (358 kDa), the time was doubled to 20 minutes to account for the larger size of the protein. The membrane was blocked by incubation in blocking buffer (5% milk protein (Marvel) in TBST (50 mM Tris pH 8.0,

150 mM NaCl, 0.1% Tween-20)) for 1 hour on a rocker. The membrane was exchanged into fresh blocking buffer with the diluted primary antibody. This was incubated in a 50 mL Falcon tube on an orbital roller with 5 mL of diluted antibody. After 1 hour incubation at room temperature (or 16 hour incubation overnight at 4°C), the membrane was washed for 3x 5 minutes in TBST, and then incubated with secondary antibody diluted in blocking buffer. After 1 hour incubation at room temperature, the membrane was washed as before. The blot was developed with Amersham ECL Prime Western blotting detection reagent (GE) according to manufacturers instructions, and imaged on film.

Primary antibodies were used as follows: anti-p150 (BD Transduction Laboratories, 610473, mouse, 1/1000); anti-RanBP2 (abcam, ab64276, rabbit, 1/2000); anti-alpha-tubulin (abcam, ab4074, rabbit, 1/5000). Secondary antibodies were used as follows: HRP-conjugated goat anti-Rabbit IgG (abcam, ab6721, 1/5000); HRP-conjugated goat anti-Mouse IgG (Thermo, 62-6250, 1/1000).

2.4.5 Mass-spectrometry

The gels from the pull-downs were stained with InstantBlue Coomassie (Expedeon) and imaged. Lanes were excised in 20 even bands using a scalpel, cleaned in ethanol after each cut. These gel samples were then given to Dr Farida Begum in the LMB mass-spectrometry facility. The BisTris in the gel was solubilised and the protein samples were trypsin digested. The fragments were run on an Orbitrap mass spectrometer for peptide identification by tandem mass-spectrometry (MS/MS).

The identified fragments were viewed in Scaffold4, and ranked according to normalised spectral abundance factor (NSAF). The average NSAF value for each protein over the three repeats was compared in the pUL36 and GFP control experiments.

2.4.6 Immunofluorescence

Cells plated in imaging chambers were transfected with pUL36 constructs as above. After 18 hours, the media was removed and the wells were fixed by incubation with 4% formaldehyde in PBS for 10 minutes. The wells were washed with TBS twice, permeabilised by incubation

with TBS-T for 10 minutes, and blocked with TBST-BSA (TBS-T supplemented with 1% Bovine Serum Albumin) for 1 hour at room temperature, with gentle rocking. Wells were then incubated with primary antibody diluted in TBST-BSA for 1 hour at room temperature, washed in TBST-BSA for 3x5minutes, and incubated with secondary antibody diluted in TBST-BSA for 1 hour at room temperature. The TBST-BSA washes were repeated, and the wells were mounted in VectaShield with DAPI (Vector Labs).

Primary antibodies were used as follows: anti-MAP1B (Santa Cruz Biotechnology, 365668, mouse, 1/1000); anti-Importin alpha-7 (Santa Cruz Biotechnology, 365231, mouse, 1/1000); anti-Importin β 1 (Santa Cruz Biotechnology, 137016, mouse, 1/1000); anti-RanBP2 (abcam, ab64276, rabbit, 1/2000); anti-cyclin B1 (abcam, ab32053, rabbit, 1/100); p62/SQSTM1 (Santa Cruz Biotechnology, 28359, mouse, 1/500); anti-Rab21 (Santa Cruz Biotechnology, 81917, mouse, 1/500). Secondary antibodies were used as follows: goat anti-Rabbit IgG Alexa Fluor 568 (abcam, 175471, 1/2000); goat anti-Mouse IgG Alexa Fluor 546 (Thermo, 11030, 1/2000)

The intensity of Cyclin B1 in cells was measured in FIJI by drawing a region of interest around the cell boundary as determined by GFP-UL36 ^{Δ CBD-MTS} fluorescence.

For TRIM-away, 1 μ L of anti-RanBP2 (ab64276) and 1 μ L 6 mg/mL TRIM21 (provided by Dr Dean Clift) were mixed with 10 μ L Vero cells at a density 8×10^7 cells/mL and electroporated with 3 10 ms 1300V pulses using the Neon electroporation system (Thermo). The cells were plated in 6-well plate wells. After 5 hours the cells were lysed by the addition of 2x LDS-PAGE loading buffer and blotted for RanBP2. Band intensities were measured in FIJI.

For siRNA, ON-TARGETplus Human RanBP2 SMARTpool siRNA (L-004746-00-0010, Dharmacon) was diluted to 5 μ M. For a 6-well plate, 10 μ L siRNA solution was combined with 10 μ L Lipofectmine RNAiMax (Thermo) and 100 μ L OptiMEM (Thermo) and incubated for 30 minutes at room temperature. The mixture was added dropwise onto cells at ~50% confluency. The cells were incubated for 72 hours at 37°C/5% CO₂. When indicated, UL36 transfections were performed after 72 hours and incubated for another 18 hours.

For electroporation of anti-RanBP2 into Vero cells, I made a mixture of 1 μ L anti-RanBP2, 1 μ L UL36 plasmid (5 μ g/ μ L) and 10 μ L Vero cells at a density of 1×10^7 cells/mL. The mixture was

electroporated in a 10 μ L Neon tip (Thermo) as before. The cells were imaged after 18 hours incubation.

2.4.7 Virus

For infection of Vero cells by HSV1, Vero cells were plated in 4-well imaging chambers at a confluency of ~80%. Dr Colin Crump had previously purified a stock of YFP-VP26 HSV1 (KOS strain, by gradient fractionation as in (Albecka et al., 2016; Hutchinson et al., 2002)), and performed all virus handling. We infected the cells with a multiplicity of infection of 20, and incubated them at 37°C for 1 hour. The media was removed and the cells were washed five times with PBS to remove virus that did not enter the cells. Fresh media was added and the cells were incubated for a further two hours, at which point they were fixed in 4% formaldehyde for 20 minutes. From this point, IF for RanBP2 continued as normal however blocking was performed with 1% donkey serum (Sigma) rather than BSA.

Chapter 3. Structural studies of dynein binding to microtubules

3.1 Background

In order to walk along the microtubule, a dynein motor needs to cyclically release from the microtubule, move forwards and then rebind. Dynein stepping is ultimately controlled by the nucleotide state of the AAA1 subdomain active site (Schmidt and Carter, 2016). In most AAA1 nucleotide states the motor stays strongly attached to the microtubule. However, when AAA1 is in the ATP hydrolysis transition state a low-affinity state is formed (Imamula et al., 2007). This chapter addresses the structural basis for binding and release from the microtubule by the dynein microtubule-binding domain (MTBD).

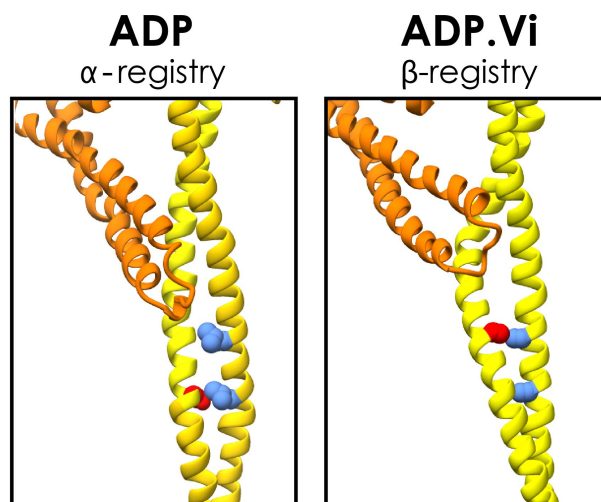


Figure 3.1 - Stalk and buttress movements that result in a low-microtubule affinity state

Rotation of the buttress (orange) moving from a high to low microtubule affinity state pulls CC2 of the stalk (yellow, CC2 has red residue indicated) up relative to CC1 (with blue residues). ADP state from PDB 3VKH, ADP.Vi from PDB 4RH7

X-ray crystallography structures and other studies showed how dynein communicates the nucleotide state of the AAA1 subdomain to the MTBD over 20nm away (Kon et al., 2009; Schmidt and Carter, 2016; Schmidt et al., 2015). Conformational changes in AAA1 are transmitted through the ring resulting in a rotation of AAA5. AAA5 contains a coiled coil extension called the buttress. Moving from the nucleotide free to ATP hydrolysis state, rotation in AAA5 causes the end of the buttress move towards the ring (**Figure 3.1**). The buttress contacts the stalk, a coiled coil extension of AAA4 that links the ring to the MTBD. The movement in the buttress pulls stalk helix CC2 towards the ring relative to CC1 (**Figure 3.1**).

The stalk coiled coil is able to change registry (i.e. the alignment between two helices in a coiled coil), in this case from the “ α ” to “ β^+ ” registry. This is due to CC1 lacking some hydrophobic residues in the heptad repeat that would be solvent exposed if a canonical coiled coil were to change registry (Gibbons et al., 2005a). The ends of CC1 and CC2 are an integral part of the MTBD (Carter et al., 2008), which means that the change in stalk registry changes the conformation of the MTBD. The α -registry stalk keeps the MTBD in a high-affinity state, whereas the β^+ registry results in a ~ 10 -fold reduction in affinity (Gibbons et al., 2005a; Kon et al., 2009; Carter et al., 2008). The ATP hydrolysis state, which favours the β^+ registry, therefore results in microtubule release. The MTBD forms a high-affinity state again when phosphate is released and the α -registry is restored.

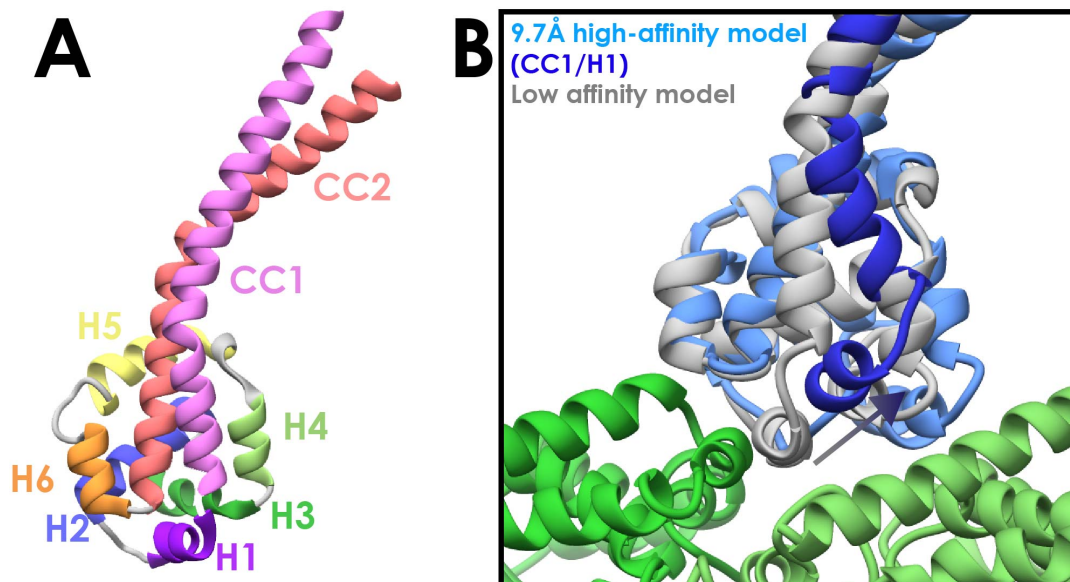


Figure 3.2 - Established structures of cytoplasmic dynein-1 MTBD

A - Low-microtubule affinity MTBD structure (stalk in β^+ registry, PDB 3ERR, (Carter et al., 2008)), coloured by helix. **B** - A comparison between the low affinity state in A (now grey) and the 9.7 Å high affinity state MTBD structure (light blue, CC1 and MTBD H1 in dark blue) bound to tubulin (α -tubulin dark green, β -tubulin light green). CC1 and H1 both move up towards β -tubulin by ~ 12 Å (arrow).

The structure of MTBD in the low affinity state has been resolved by X-ray structures (Nishikawa et al. 2016; Schmidt et al. 2015; Carter et al. 2008). It consists of 6 short helices (H1 to H6) as well as the two stalk helices CC1 and CC2 (**Figure 3.2A**). The MTBD was not resolved in structures of the motor in a high microtubule affinity state (Kon et al., 2012; Schmidt et al., 2012). This deficit was addressed in a 9.7 Å cryo-electron microscopy structure of the

cytoplasmic dynein-1 MTBD bound to microtubules (Redwine et al., 2012). A pseudoatomic model was fit into the cryo-EM map using molecular dynamic simulations from a low-affinity structure. H1, H3 and H6 form the interface with the microtubule, making salt bridges with specific α - and β -tubulin residues. Compared to the low affinity state, H1 was reported to be displaced $\sim 12\text{\AA}$ up and towards β -tubulin (**Figure 3.2B**). H2, H3 and H4 were also displaced by H1, and all variably moved towards β -tubulin to form a high-affinity state. The movement in H1 was consistent with CC1 moving up relative to CC2 and forming the α -registry.

The micrographs for the Redwine 2012 study were collected on film, before the introduction of direct-electron detectors. This limited the resolution such that secondary structure is not completely resolved in the structure. In this chapter, I make use of the recent technological advances in cryo-EM to solve an updated structure of the cytoplasmic dynein-1 MTBD bound to microtubules. Based on this structure, I present a modified model for the dynein MTBD in the high-affinity state accommodated by movement of H1 only.

Beyond cytoplasmic dynein, little is known about how the MTBDs of axonemal dyneins bind microtubules. Sequence alignment shows that the MTBD is well conserved between different dynein family members (**Figure 3.3**). However, many axonemal dyneins have an insertion between H2 and H3 called the flap, the function of which is unknown (**Figure 3.3**, starred sequences, (Kato et al., 2014)). Furthermore, some of the residues predicted to interact with the microtubule in the 9.7\AA cryo-EM model are poorly conserved (**Figure 3.3**, blue arrows, (Redwine et al., 2012)).

To address how axonemal dyneins bind microtubules, I also determine the structure of an axonemal dynein MTBD bound to microtubules. A previous NMR study determined the low-affinity structure of flagellar dynein c (a monomeric inner arm dynein) from *Chlamydomonas reinhardtii* (Kato et al., 2014). The MTBD adopts the same overall fold as cytoplasmic dynein, however the flap extends out and was predicted to form a steric clash with the microtubule. The closest relation in humans is DNAH7, which also contains the MTBD flap. I solve the structure of the DNAH7 MTBD bound to microtubules, and observe the flap remodelling to directly bind to an adjacent protofilament. I use TIRF microscopy to investigate a potential role for the flap in microtubule distortion.

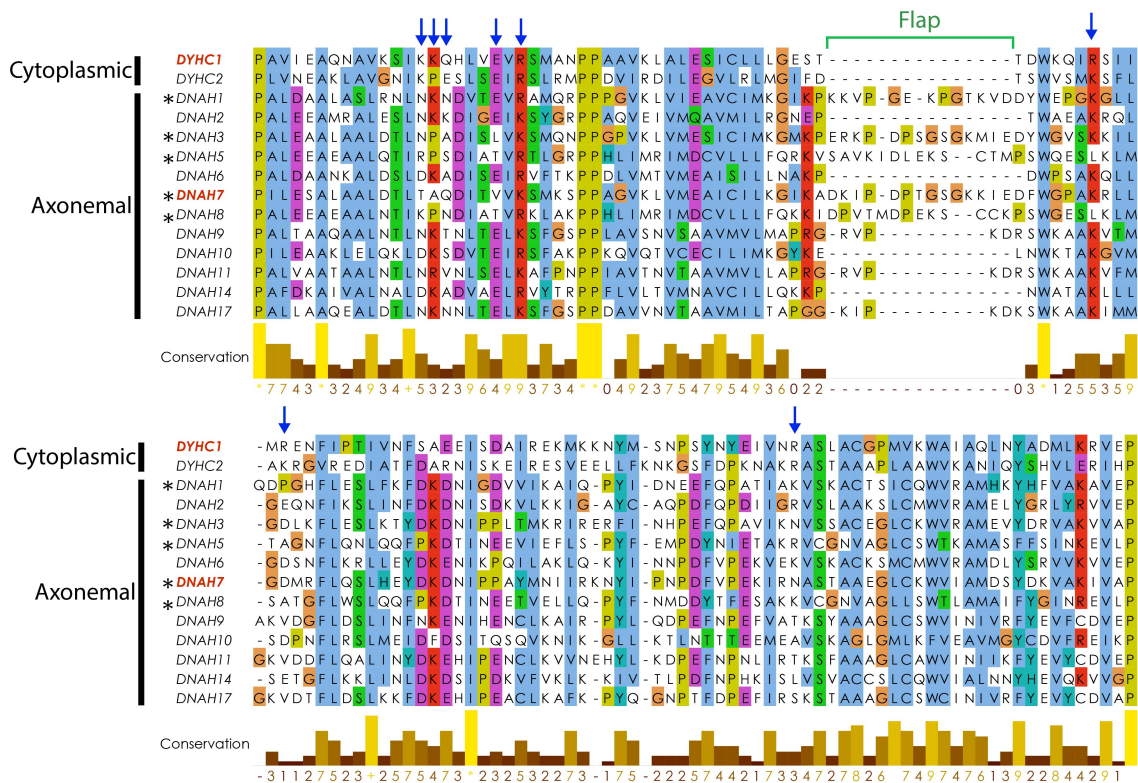


Figure 3.3 - Sequence alignment of human dynein MTBDs

Human cytoplasmic and axonemal dynein MTBD sequences between the conserved proline residues in each stalk helix. Starred (*) sequences contain a flap between H2 and H3 (green lines). Blue arrows indicate residues that are thought to form salt bridges with the microtubule in (Redwine et al., 2012). Cytoplasmic dynein-1 (DYHC1) and DNAH7 MTBDs (both bold red) were the subject of my structures.

To solve these structures, I use a new method to determine the structure of pseudohelical microtubules. Lateral interactions between tubulin in adjacent protofilaments are normally homotypic (α -tubulin to α -tubulin and β -tubulin to β -tubulin). However, most microtubule architectures, including 13-protofilament microtubules, have a seam of heterotypic interactions (α -to- β). This means that traditional helical averaging is unsuitable, and any reconstruction method needs to differentiate the seam from the other 12 protofilament junctions.

Previous microtubule structures were solved using methods that are based around reference-matching to synthetic 2D projections in order to find the seam (Figure 1.8) (Sindelar and Downing, 2007; Zhang and Nogales, 2015b). The protocol used by the Nogales lab (Zhang and Nogales, 2015a) has yielded reconstructions at 3.2Å resolution (Kellogg et al., 2018). The method I use is based on the helical Relion pipeline (He and Scheres, 2017), utilizing the new implementation of non-crystallographic symmetry. I show that this method can be used to

attain a map equivalent in quality to the previous methods. The advantage of Relion is in its ease-of-use, and its ability to sort sample heterogeneity through 2D and 3D classification.

3.2 Results

3.2.1 Dynein MTBD constructs used for structural determination by cryo-EM

When the MTBD and stalk are expressed in isolation from the remainder of the motor domain, the stalk adopts the low-affinity β^+ registry (Nishikawa et al., 2016b). Therefore, in order to decorate microtubules in cryo-EM I used a construct where the stalk helices are fused to a bacterial seryl-tRNA synthetase (SRS), as was done in previous studies (Gibbons et al., 2005b; Carter et al., 2008; Redwine et al., 2012). SRS is a globular protein with a coiled coil projecting from its core (**Figure 3.4A**). Joining the stalk helices to the SRS coiled coil fixes the stalk in a controllable registry, depending on the relative length of the CC1 and CC2 sequences (**Figure 3.4B**, (Gibbons et al., 2005b)). The α -registry is achieved by encoding three more residues in CC1 than CC2. The mouse cytoplasmic dynein-1 85:82 construct (hereafter Cyt1-SRS) I use was previously reported by (Carter et al., 2008). 85:82 refers to the number of residues in CC1 and CC2 respectively (**Figure 3.4C**). This construct is directly equivalent to that used by Redwine *et al*, but with an extra 9 heptads of coiled coil. An NMR solution study suggested that the α -registry is more stable when all of the stalk (and not just the MTBD proximal region) is present (McNaughton et al., 2010).

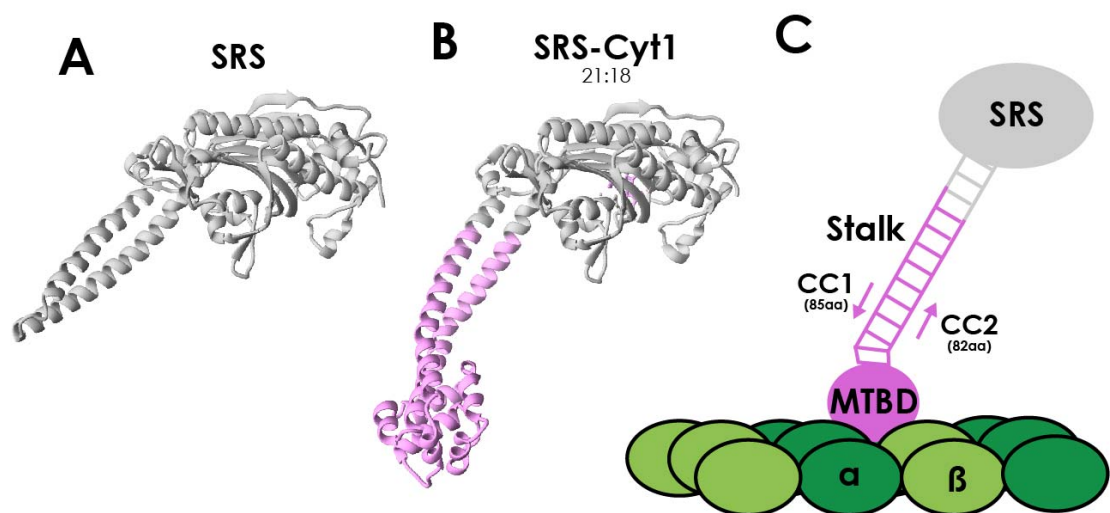


Figure 3.4 - Schematic of a dynein MTBD/SRS fusion construct

A - Crystal structure of *Thermus thermophilus* Seryl-tRNA synthetase (PDB 1SRY), showing its inherent coiled coil extension. **B** - The SRS-Cytoplasmic dynein-1 stalk fusion construct used for X-ray crystallography (PDB 3ERR) (dynein residues pink, SRS grey). Note a low affinity state 26:19 β^+ stalk registry was crystallised. **C** - Schematic detailing the SRS fusion construct I used for cryo-EM

3.2.2 Purification of Cyt1-SRS

The SRS-MTBD constructs have a C-terminal 6xHis-tag, and were purified with a single Ni-NTA affinity step (**Figure 3.5A**). On the same day as grid preparation, I would thaw an aliquot and run it in size-exclusion chromatography (**Figure 3.5B/C**). This removes most impurities and ensures the sample is monodisperse, and as such suitable for cryo-EM. I did not cleave the affinity tag, as it is distant from the MTBD and unlikely to interfere with binding.

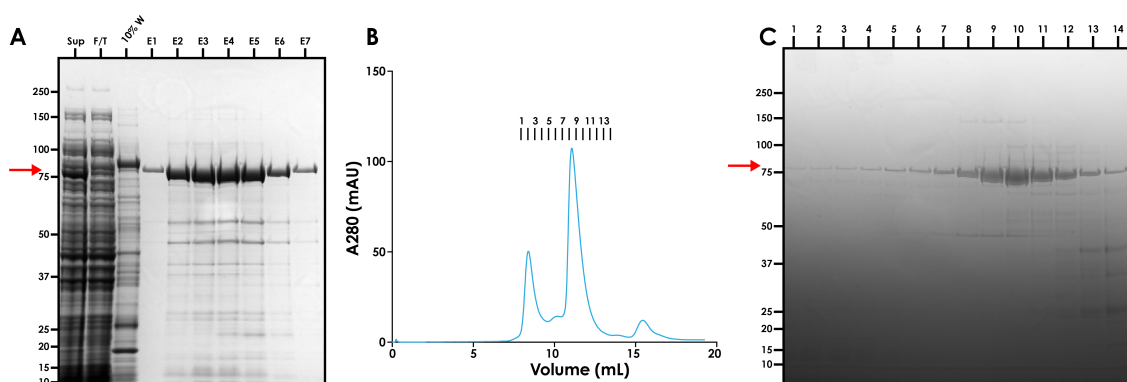


Figure 3.5 - Purification of Cyt1-SRS

A - SDS-PAGE gel of NiNTA affinity steps of Cyt1-SRS purification. Sup=Supernatant, F/T=Flowthrough, 10% W=eluate when column washed with 10% elution buffer (to remove weakly bound contaminants), E1-7=elutions. A band is clearly visible for Cyt1-SRS at ~75kDa in the elutions (red arrow) **B** - Gel filtration trace of NiNTA purified Cyt1-SRS. **C** - SDS-PAGE of the indicated fractions from B.

3.2.3 Polymerisation of microtubules for Cryo-EM

We chose to use 13 protofilament microtubules for cryo-EM, since these are representative of microtubule architectures in vivo. Typically, microtubules polymerized in vitro result mostly in 14 protofilament architectures, although anything from 10 to 15 protofilament architectures are commonly observed (Desai and Mitchison, 1997). A previous study reported that microtubules polymerized in vitro can be biased towards certain architectures with specific buffer conditions (Pierson et al., 1978). Following the protocol from this paper, I polymerized commercial lyophilized tubulin (Cytoskeleton) reconstituted in 20 mM MES pH 6.5 and 70 mM NaCl. The mixture was incubated for 90 minutes at 37°C in the presence of 3mM GTP, after which I added 1 mM taxol for long-term stabilization.

3.2.4 Preparation of decorated microtubules for cryo-EM

I prepared Cyt1-SRS decorated microtubules for cryo-EM with on-grid incubations. Microtubules adsorb to the carbon around the grid holes, so remain attached following multiple rounds of side-blotting and reapplication. I applied the microtubules to the grid, incubated, blotted away the drop and applied MTBD. The concentration of MTBD (20 μ M) was in excess of the tubulin concentration (1 μ M). To achieve highest decoration levels I performed two or three application/blot cycles with the MTBD. The grid was vitreously frozen and screened for the blotting conditions that achieve the best decoration.

The decoration levels of microtubules can be assessed quickly in two ways. The longitudinal spacing between α and β tubulin in the same protofilament is 4nm. Due to the similarity between the two, the first order longitudinal reflections of the microtubule power spectrum occur on the 4nm layer line (**Figure 3.6A**). At full decoration, dynein forms a regular 8nm repeat on the microtubule, creating new reflections on the 8nm layer line. As such, the presence and strength of reflections on the 8nm layer line can be used to assess the level of decoration. In the case of Cyt1-SRS a strong 8nm layer line was visible (**Figure 3.6B**). Small-scale 2D classification clearly showed a regular decorating density on the side of the microtubule (**Figure 3.6B** compared to **Figure 3.6A**). These results were robust and reproducible, however areas with thinner ice tended to have less decoration.

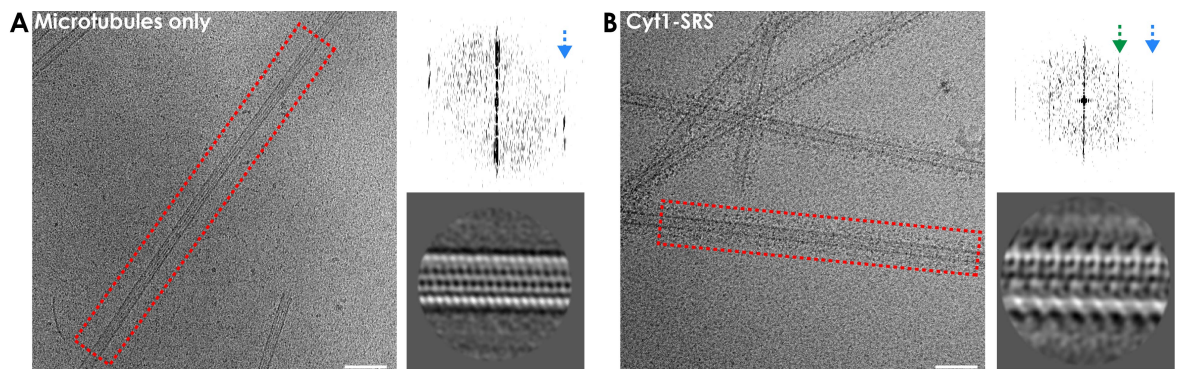


Figure 3.6 - Decoration of microtubules by Cyt1-SRS

A - Cryo-electron micrograph of a microtubule (left), and the power spectrum of the boxed microtubule (top right, blue arrow indicates 4nm layer line). 2D classification of boxed microtubule (bottom right). **B** - Corresponding images of microtubules frozen after incubation with Cyt1-SRS (green arrow indicates 8nm layer line).

3.2.5 Reconstructing microtubules in Chuff

I collected a dataset of 1563 images on a 300kV FEI Polara microscope equipped with a Falcon II detector. I chose to process these images using an established workflow for microtubules with a seam (Sindelar and Downing, 2007). This is implemented through a series of scripts written by Chuck Sindelar, who kindly shared them with us.

The scripts, referred to as “Chuff” (“CHUck’s Fancy Frealign”), require two preprocessing steps to be performed manually (**Figure 3.7A, blue box**). I ran motion correction on the images with MotionCorr2 in order to recover high-resolution signal lost due to beam-induced motion. I then manually picked the start and end point of suitable microtubules (visible decoration, not overlapping with other microtubules). The micrographs, these coordinates and a small number of physical parameters (e.g. pixel size, operating voltage) are the only user-generated input to the scripts. The refinement proceeds automatically, however supervision is required at various stages to achieve the best quality reconstruction.

The first step in Chuff is CTF estimation, followed by particle extraction (**Figure 3.7A**). The position of the seam is found in each particle by measuring its cross-correlation against 33800 synthetic projections of a decorated reference microtubule in a full sampling of orientations (reference matching, **Figure 3.7A**). The key parameter relating to the position of the seam is the axial rotation (i.e. rotation around the long axis). As the microtubule reference is axially rotated through 360° the cross-correlation sees 13 peaks and troughs as the protofilaments become aligned and unaligned (Sindelar and Downing, 2007). The highest peak should correspond to when the seam is correctly aligned between the projection and the particle. In reality, the low signal to noise ratio in raw particles means that this is not 100% successful. However, neighbouring particles in the same microtubule should have almost identical orientations due to the restraints imposed by the helical lattice. Chuff finds the consensus orientation in successive segments of the same microtubule in order to reduce the effect of noise (**Figure 3.7B**). This projection matching occurs once in a global search, followed by two increasingly fine local searches at higher resolution (**Figure 3.7B**). These orientations undergo one more smoothing step for all orientation parameters and are used to bootstrap a local 3D refinement in Frealign (**Figure 3.7A**). Following the refinement, each of the 13 protofilaments in the final map is averaged together to increase the resolution of the final map.

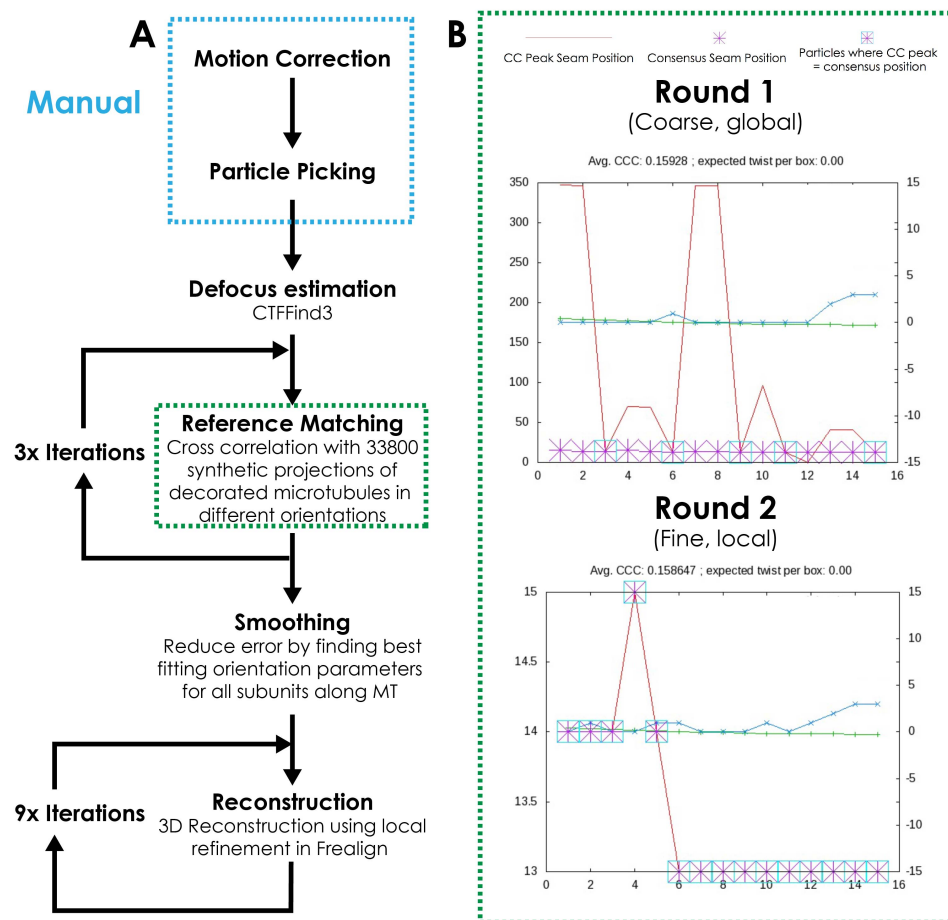


Figure 3.7 - Workflow for reconstructing decorated microtubules in Chuff

A - Two manual preprocessing steps (blue box) are performed by the user. The reference matching step (green boxes) involves three iterations. In the first, the predicted seam position for each particle is found, and the consensus seam position across an entire microtubule is applied to all particles (**B**). The next iteration only performs local optimisation around this position. These orientations are then smoothed and used for automated local 3D refinement

3.2.6 Cyt1-SRS reconstruction from Chuff

The Cyt1-SRS refinement reached a nominal resolution of 4.01Å (FSC_{0.143} cutoff, **Figure 3.8A**). However, the highest resolution features of the map started to be dominated by noise below 4.5Å (**Figure 3.8B**). At the optimal threshold to display the tubulin density at this resolution the MTBD density is not visible (**Figure 3.8B**). Lowering the surface threshold of this map to visualize the areas with weaker density shows that the MTBD region is dominated by noise (**Figure 3.8C**). This indicates that the MTBD density is at lower resolution due to flexibility, low occupancy, or both. The MTBD is clearly resolved when the map is lowpass filtered to 5.5Å

(Figure 3.8D), representing an improvement over the previous 9.7Å structure (Redwine et al., 2012).

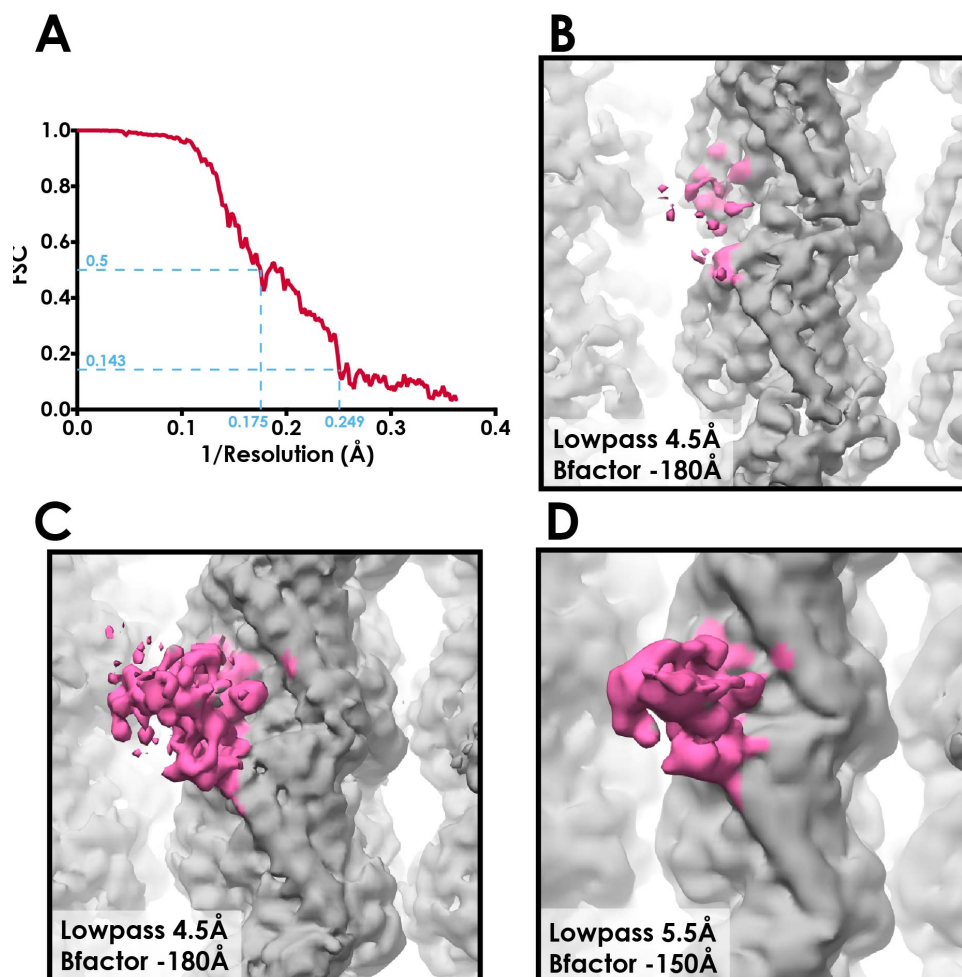


Figure 3.8 - Assessment of map quality from Chuff refinement of Cyt1-SRS

A - FSC curve of final map generated by Chuff. B - Surface representation of the resulting map optimally filtered, sharpened and thresholded for the tubulin density. Density corresponding to MTBD coloured magenta C - The same density at a lower surface threshold showing the MTBD density, which is dominated by noise. D - The same view lowpass filtered to a lower resolution to visualize the MTBD

Despite the improvement, I judged that the resolution of this reconstruction could still be improved further. This assessment is based on the limited resolution of the tubulin and the large drop-off in quality between the tubulin and MTBD density. Furthermore, there are limitations to processing microtubules in Chuff. The first is practical; processes can only be parallelized over one node, making the refinements very slow (up to one week per job). Manual picking large datasets is also time-consuming and subject to error. The second

limitation is the inability to perform classification. 2D or 3D classification would make it possible to distinguish sample heterogeneity so that, for example, highly decorated particles can be selected for. As such, I opted to shift to a different refinement strategy.

3.2.7 Reconstruction of pseudosymmetrical microtubules in Relion

Relion is a widely used single-particle cryo-EM refinement package. Helical processing was recently introduced into the Relion pipeline (He and Scheres, 2017). Microtubules can be processed as an asymmetric (C1) helix in this scheme, but this would not use the available 13-fold pseudosymmetry. To utilize this extra information, Shaoda He and Sjors Scheres implemented non-crystallographic symmetry in Relion. This allows averaging to occur between multiple user-defined points, independent of any symmetrical axis. I decided to investigate whether helical Relion in combination with the application of non-crystallographic symmetry could be used to reconstruct pseudosymmetric microtubules.

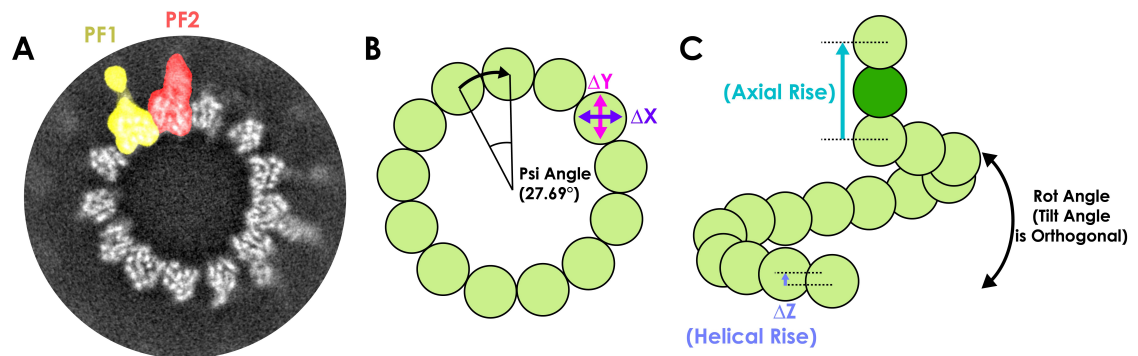


Figure 3.9 - Operators of non-crystallographic symmetry

A - Cross-sectional view of a microtubule, showing the position masks over two adjacent protofilaments (yellow, red). Such a mask is placed on each protofilament and the density within is averaged together. **B/C** - Schematics showing the operators relating adjacent protofilaments. **B** - The center of each PF lies on a circle, and one PF can be moved onto the next by a 27.69° rotation around the MT long axis. **C** - Side view of one helical turn of the microtubule. Helical rise (ΔZ) is the rise between laterally adjacent protofilaments, and axial rise is the rise between longitudinally adjacent tubulin dimers.

To apply non-crystallographic symmetry, the user needs to create a mask encompassing one unit to be averaged. In the case of the microtubule, this is a single protofilament (**Figure 3.9A, yellow**). The user provides the operations needed to move this mask onto the adjacent protofilament, and each successive protofilament. In practice, the microtubule can be assumed to be perfectly circular, and the mask can simply be rotated around the central (Psi)

axis (**Figure 3.9A, red**). Each protofilament is related to its neighbor with a 27.69° ($360^\circ/13$ protofilaments) rotation around this axis (**Figure 3.9B**). To bring the two protofilaments into register, the helical rise (the rise between laterally interacting subunits, ΔZ , **Figure 3.9C**) must be provided. For 3-start microtubules, the cumulative helical rise through 360° corresponds to 1.5x the axial rise, where the axial rise is the distance between dimers in the same protofilament (**Figure 3.9C**). The helical rise is therefore $1.5 * \text{axial rise} / 13$. During refinement Relion measures the axial rise, which will vary for different microtubule conditions. The seam is taken into account by applying an extra 1/2 helical rise to the first protofilament across from it. Relion then averages the density within the mask after each operation and applies it back to the map.

3.2.8 Reconstruction of Cyt1-SRS in Relion

I collected a new Cyt1-SRS dataset, aiming to push the resolution by using a smaller pixel size compared to the previous dataset (1.04 \AA vs 1.34 \AA). 1995 images were collected on a Krios microscope with a Falcon III camera in linear mode. I implemented a new processing regime on these images (**Figure 3.10**).

Motion correction and contrast transfer function (CTF) determination were performed in MotionCorr2 and Gctf respectively (Zheng et al., 2017; Zhang, 2016) (**Figure 3.10A**). I manually picked a small number of particles (~ 1000 , from ~ 50 microtubules) and performed 2D classification to generate references for autopicking. On a single microtubule, consecutive particles are boxes $\sim 500 \text{ \AA}$ in diameter separated by 82 \AA (i.e. one tubulin dimer) along the microtubule long axis. I was unable to optimize autopicking parameters to specifically pick 13-PF microtubules. Instead, I set the picking threshold relatively low and trusted the subsequent classification steps to sort microtubules with different protofilament numbers (**Figure 3.10B**). I entered the autopicked particles for two rounds of 2D classification and removed classes that were poorly decorated or possessed identifiable non-13 protofilament architectures (**Figure 3.10C**). In 13-PF microtubules, the protofilaments run directly parallel to the long axis. Protofilament skew in non-13-PF microtubules creates progressively changing projection patterns along the microtubule (Chrétien et al., 1996). I therefore removed any classes exhibiting protofilament skew (**Figure 3.10D**). Following 2D classification, more bad particles were removed by 3D classification (**Figure 3.10E**). The bad classes had one good side

resembling a well-aligned microtubule and a bad side with only incoherent features. These bad classes are likely to contain different non-13-PF microtubules aligning to one side but averaging incoherently on the other. They may also contain some 13-protofilament particles with lower resolution (e.g. due to bad local CTF, thick ice, drift, denaturing sample). The single good class from 3D classification was taken forward for 3D refinement (**Figure 3.10F**).

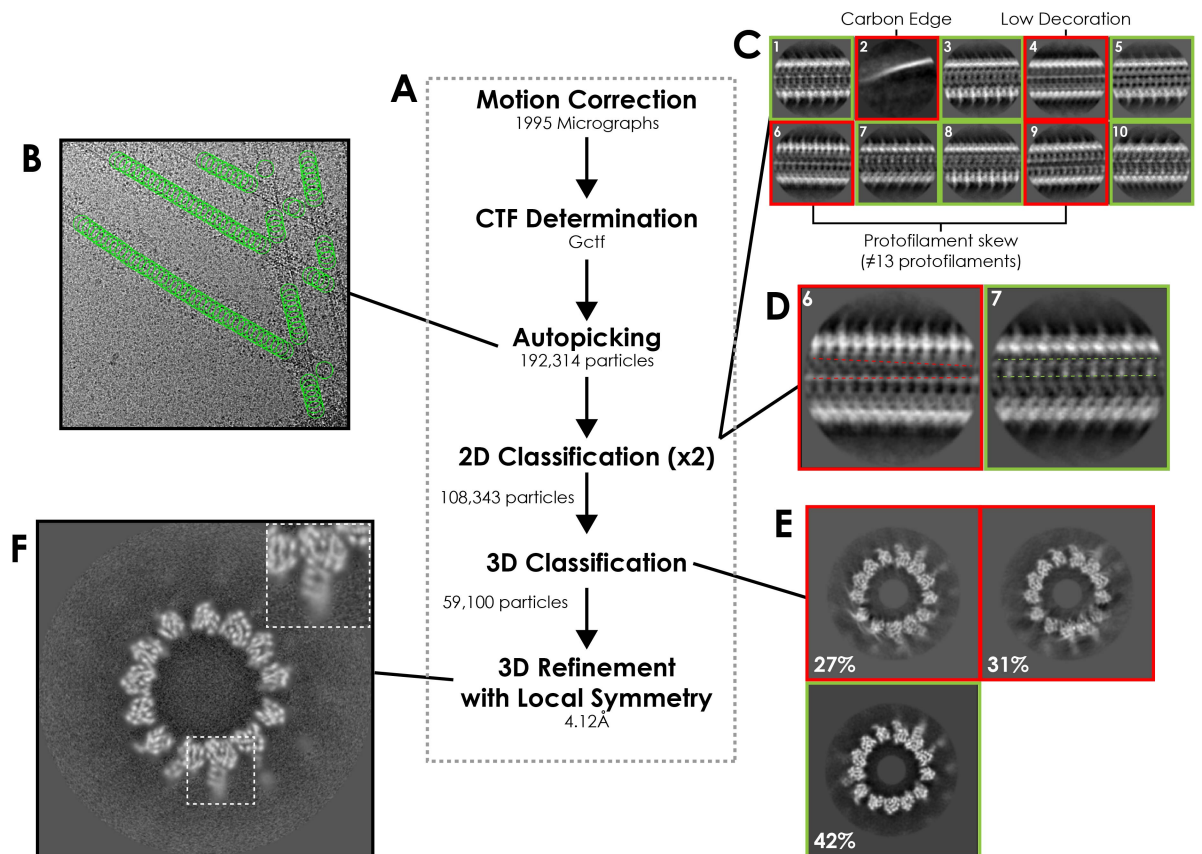


Figure 3.10 - Workflow for reconstructing microtubules in Relion

A - The steps performed in the Relion pipeline to reconstruct Cyt1-SRS. **B** - A representative electron micrograph and the particle coordinates picked for it (green circles). **C** - A selection of 2D classes showing classes that were accepted for further processing (green box) or rejected for the specified reasons (red box). **D** - Comparison of between a class with (red) and without (green) obvious protofilament skew. Not all classes without skew over this distance have 13 protofilaments, but all classes with skew certainly are not 13-PF. **E** - Good (green) and bad (red) classes from 3D classification. **F** - The final refined map in cross section, with an MTBD shown inset.

The most important consideration for 3D refinement was ensuring that the seam was found correctly. In Relion, this role is performed in the early stages of refinement when each particle

is undergoing global orientation searches to optimize cross-correlation to the 3D reference. The seam makes microtubules unusual, in that the cross-correlation has 13 local peaks (when each PF is aligned) but only one correct solution. I found that this meant the most important parameter to control for refinement is the initial angular sampling interval. For refinement, the cross-correlation of each particle against the reference model is measured in different orientations, and the cross-correlation peak is taken to be the orientation of the particle. The initial angular sampling interval controls how fine this orientational sampling is in the first iterations. An initial sampling rate of 3.7° or 1.8° resulted in a misaligned seam, in which extra density is seen between where the MTBDs were in the reference at the seam (**Figure 3.11A-B**, sampled orientations in first iteration represented by blue columns). This extra density disappears when the sampling interval is decreased to 0.9° (**Figure 3.11C**). In Relion it is recommended for most refinements to start at 7.5° initial sampling, or 3.7° for particles with symmetry. As such, the particularly fine angular sampling needed for microtubules makes them a special case.

I also found that the application of symmetry during refinement was vital to achieve the best definition at the seam (**Figure 3.11D**). The reconstruction after each iteration is used as the reference for the next. By applying symmetry, cumulative errors from poorly aligned particles are prevented and a well-defined seam is enforced on the reconstruction. Comparing refinements with and without symmetrisation at 1.8° initial sampling show that the application of symmetry greatly improved the quality of the final map (**Figure 3.11B/D**)

The highest quality map was achieved by applying the 13-fold NCS to the resulting half-maps from refinement and post-processing in Relion. This increased the overall resolution from 4.40Å to 4.12Å (**Figure 3.12**), according to the gold-standard $FSC_{0.143}$ threshold (Rosenthal and Henderson, 2003; Scheres and Chen, 2012).

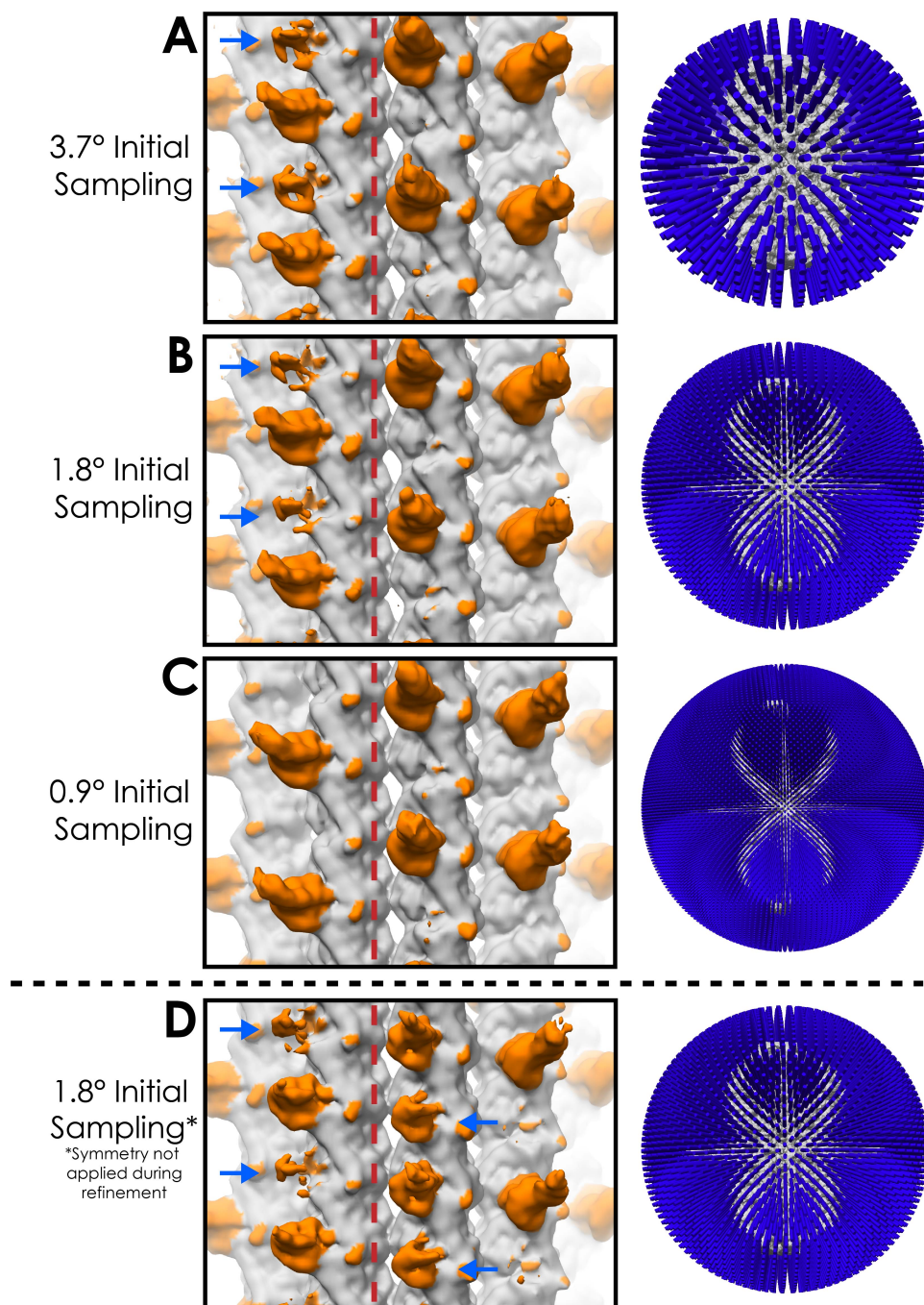


Figure 3.11 - The effect of initial sampling rate and application of local symmetry on seam finding in Relion

A-D - Cyt1-SRS maps produced from the initial sampling rate as indicated. **Left** - Surface representation of refined maps. Red line indicates the position of the seam in the reference. Orange regions represent density not attributable to tubulin. Blue arrows indicate the position of extra MTBD density formed due to misalignment of the seam in some particles. **Right** - Representation of the distribution of initial sampling positions under the indicated regimes.

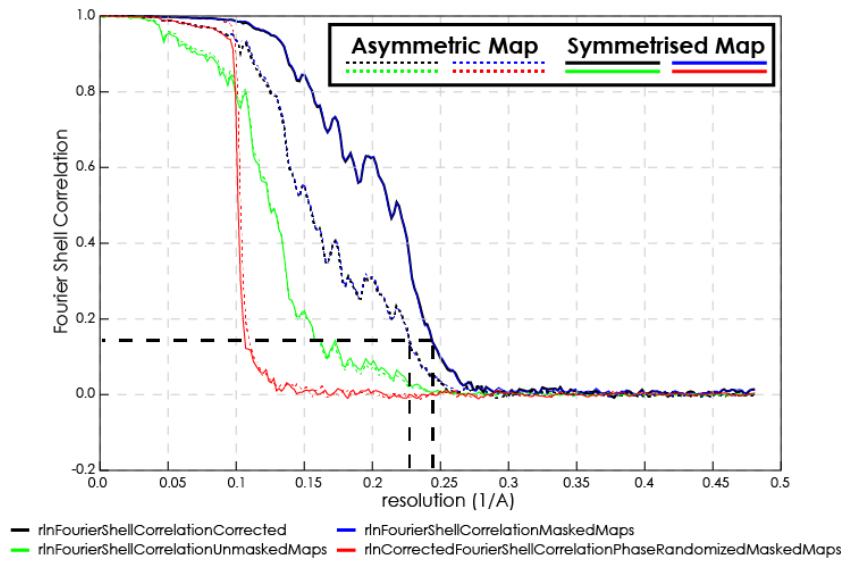


Figure 3.12 - FSC curves for C1 and symmetrised Cyt1-SRS map in Relion

Gold-standard Fourier Shell Correlation of C1 (dotted lines) and symmetrised (continuous line) maps in Relion. Dotted line indicates the 0.143 cutoffs

3.2.9 Maximising resolution through particle expansion and subtraction

I wanted to test whether the resolution of the MTBD could be pushed further. Typically, reconstructions of decorated microtubules have higher resolution in the tubulin density than the decorating protein. The symmetry applied assumes that the MTBD is effectively fixed in relation to the microtubule, where in reality its exact interaction with respect to the microtubule could be more variable. Relion offers an extensive toolkit to optimise the resolution of flexible areas of maps.

The strategies I used involved signal subtraction (**Figure 3.13**). This is where a computed map is projected back onto each particle and the value at each pixel is subtracted. By masking the projected map to only include specific areas to be subtracted, the user can retain density of interest in the particle for further processing. This can uncouple regions that are being co-refined, and has been successful in the past to resolve previously flexible regions.

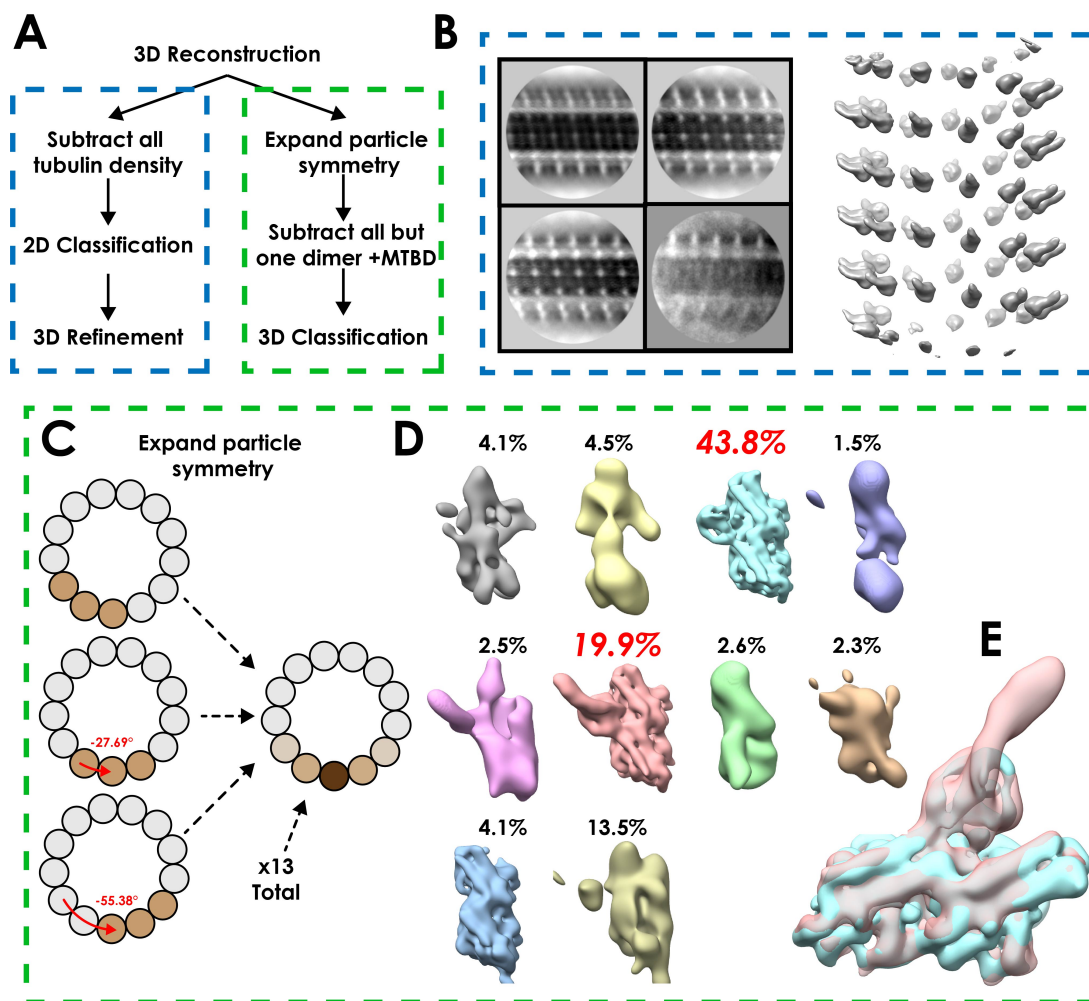


Figure 3.13 - Strategies to specifically improve the resolution of the Cyt1-SRS MTBD

A - Two strategies used to see if Relion could improve the MTBD resolution. **B** - The full microtubule was subtracted from particles, which were used for 2D classification (left) and refinement of a new model (right). **C** - Particle symmetry expansion involves copying each particle thirteen times with new orientations such that each protofilament from the original particle is superimposed on a single position (example show for 3 protofilaments). **D** - All but a single tubulin dimer and MTBD was subtracted from the expanded particles, and 3D classification without an alignment was performed (numbers indicate percentage of particles in each class). **E** - Comparison between the two major classes in D (red, bold).

In the first strategy, I subtracted the microtubule density from each particle, leaving just the MTBD (**Figure 3.13A/B**). 2D classification of these particles showed that the tubulin signal had been removed and only a regular decorating density remained. Local 3D refinement of the resulting particles nominally reached 10\AA resolution, but did not display features indicative of this resolution. Refinement of this dataset likely failed due to the constraints between each of the 13 MTBDs in each particle; an optimal orientation for one MTBD might result in poor alignment for the other MTBDs. However, the failure of the 13 MTBD refinement to reach even intermediate resolution suggests that the size of the particle ($>20\text{kDa}$) is too small for

successful refinement. As such, further strategies involving refinement after subtraction were not pursued.

The second strategy utilized the Relion “particle_symmetry_expand” feature (**Figure 3.13A/C-E**). Each particle is copied in place 13 times. Each of the new particles is rotated and translated by multiples of 27°. If the particles are then subjected to particle signal subtraction for everything except one protofilament, each protofilament in the original particle is represented once in the cohort of subtracted particles. This allows classification of each protofilament simultaneously, rather than being constrained into bulk classification of all 13 protofilaments in a single particle. I performed 3D classification without alignments on these subtracted particles to determine if there is significant variability in the MTBD density. Classification into 10 classes resulted in two well-populated classes and a number of minor classes (**Figure 3.13D**). Some of the minor classes showed good tubulin density without any decorating density, suggesting that undecorated dimers had been identified. However, the two main classes, comprising ~65% of the data, only differed in the strength of the decorating density (**Figure 3.13E**). The tubulin for the two models was identical, and the MTBDs were in the same conformation.

To further verify that all the MTBDs adopt the same conformation on the microtubule, I refined the NCS operators using the “relion_localsym” program. This takes the position of each mask and refines it to find the operators that give the highest quality averaged structure at the end. The masks I refined contained the density for the MTBD only, however the refined symmetry operators had only negligible differences to the original map. This suggests that the MTBD is either too small for any differences to be picked up, or the orientations are already optimal.

3.2.10 Refining a new model

The refined and symmetrised map (**Figure 3.14A**) had an overall resolution of 4.1Å (**Figure 3.12**). Local resolution assessment shows that the tubulin core ranges from 3.6Å to 4.4Å, while the MTBD ranges from 4.4Å to 8Å (**Figure 4.14B/C**). As such the map represents a large improvement on the previous 9.7Å resolution cryo-EM structure.

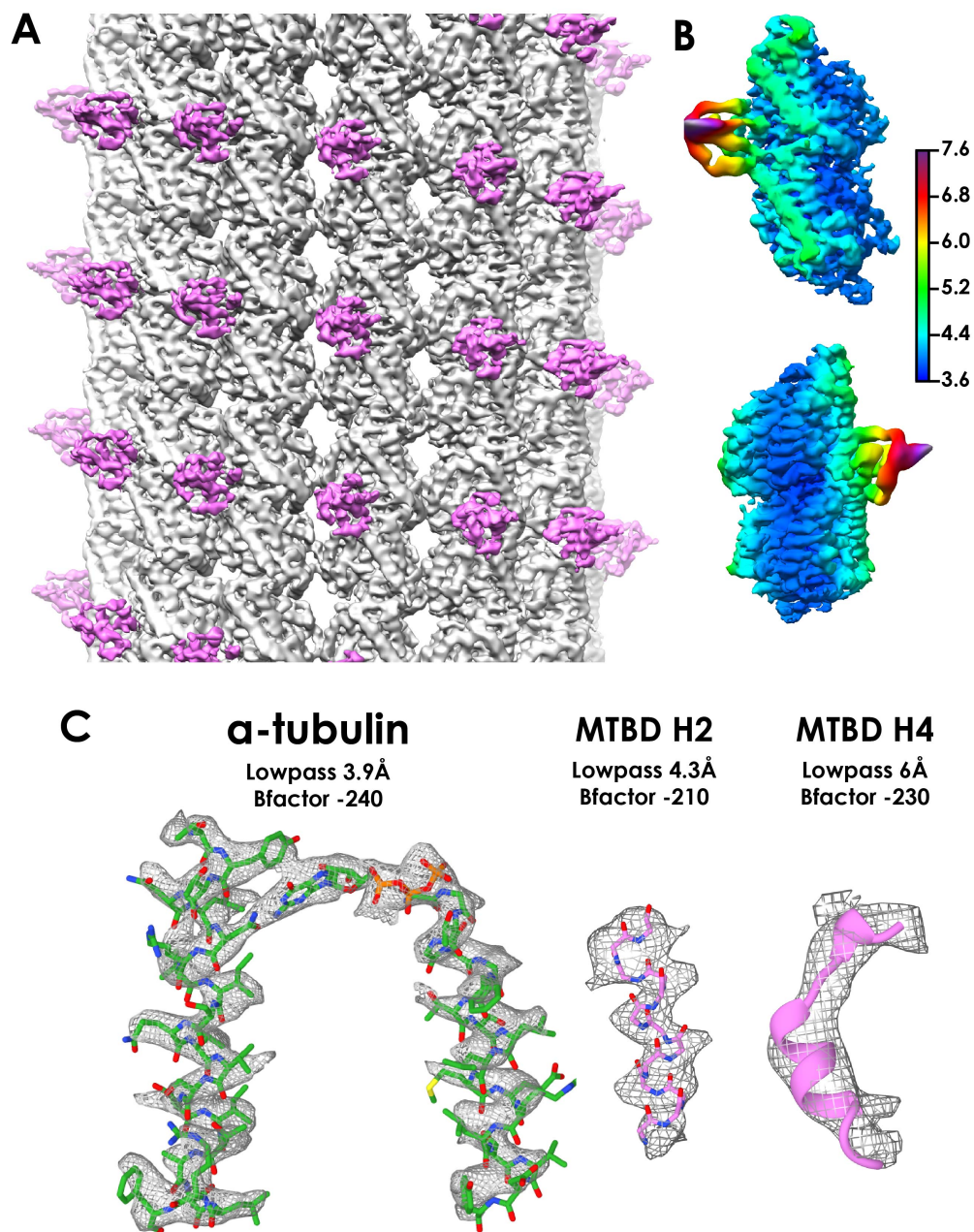


Figure 3.14 - Final Cyt1-SRS map and assessment of local map quality

A - Surface representation of the final symmetrized Cyt1-SRS map, with the Cyt1-SRS density coloured magenta. **B** - Local resolution of the map as assessed in Relion. **C** - Representative density from the core of α -tubulin (H4, H7 and nucleotide), with newly refined model docked **D** - Density for H2 of the MTBD, the highest quality MTBD region, with newly refined model docked. **E** - Density for H4 of the MTBD, representative of the quality in the majority of the MTBD, with newly refined model docked.

It is not possible to build a new atomic model *de novo* into density at this resolution, so I refined the structure of pre-existing models. I fit a model inside its corresponding density and performed manual adjustments using Coot (Emsley and Cowtan, 2004) to improve the fit. This

was followed by automated model refinement in Phenix real-space refine (Adams et al., 2010). Model refinement was done iteratively until the model to map correlation stopped increasing. I initially refined a tubulin dimer in isolation into a 4.0Å filtered map. As a starting model I used a high-resolution cryo-EM model of a taxol-stabilised microtubule (PDB 5SYF, (Kellogg et al., 2017)). This model already fit the density well, and only minor modifications occurred during refinement (C α RMSD between 5SYF and refined model was 1.075Å and 0.897Å for α - and β -tubulin respectively, **Figure 3.15**). For the MTBD, I used a low-affinity crystal structure (PDB 3ERR, (Carter et al., 2008) as the starting model, and refined it into a 5.0Å lowpass filtered map. I then refined the tubulin and MTBD models together into the 5.0Å map to remove any steric clashes.

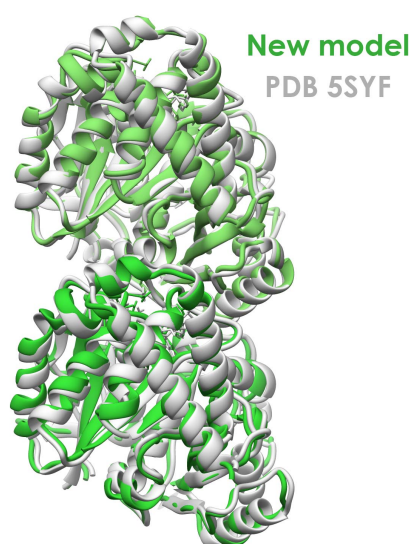


Figure 3.15 - Comparison between newly refined and reference tubulin models

My newly refined tubulin model (green) compared to the reference model used as a starting point for model refinement (PDB 5SYF, grey)

The resulting model performed well in model validation metrics (**Table 1**). The model fit the map well, exemplified by the model to map crossing the FSC_{0.5} criterion at 5.11Å, only slightly less than the limit of 5.0Å resolution of the map.

Map	Cyt1-SRS
Map resolution	5
Map sharpening B factor	-220
Map CC	0.851
Map:Model FSC _{0.5} (Å)	5.11
Model Composition	
Non-hydrogen atoms	8210
Protein residues	1035
Ligands (GTP/GDP)	1/1
R.m.s deviations	
Bond lengths	0.006
Bond angles	1.015
Validation	
MolProbity score	2.09
Clashscore	13.61
Poor rotamers	0.56%
Ramachandran plot	
Favored (%)	93.09
Disallowed (%)	0
CB deviations (%)	0

Table 1 - Model refinement validation statistics for Cyt1-SRS

3.2.11 Structure of the cytoplasmic dynein-1 microtubule-binding domain bound to microtubules

The newly refined high-affinity model fits into the density well (**Figure 3.16A/B**). Comparing this with the low-affinity crystal structure indicates that the two states are surprisingly similar (**Figure 3.16C/D**). The majority of the MTBD undergoes very minor conformational changes in this transition. The only major difference is in H1 and CC1, which move $\sim 5.5\text{\AA}$ together to occupy the intradimer cleft above α - and β -tubulin. This is consistent with CC1 being raised relative to CC2 in the high-affinity α -registry. H6 also moves up to accommodate the tubulin surface, but to a much smaller degree. In contrast, the previous model from the 9.7\AA EM structure suggested that CC1 opens up from CC2. H1 moves $\sim 12\text{\AA}$ away from the intradimer cleft and H2, H3 and H4 all adopted different conformations to bind to the microtubule (**Figure 3.16E/F**).

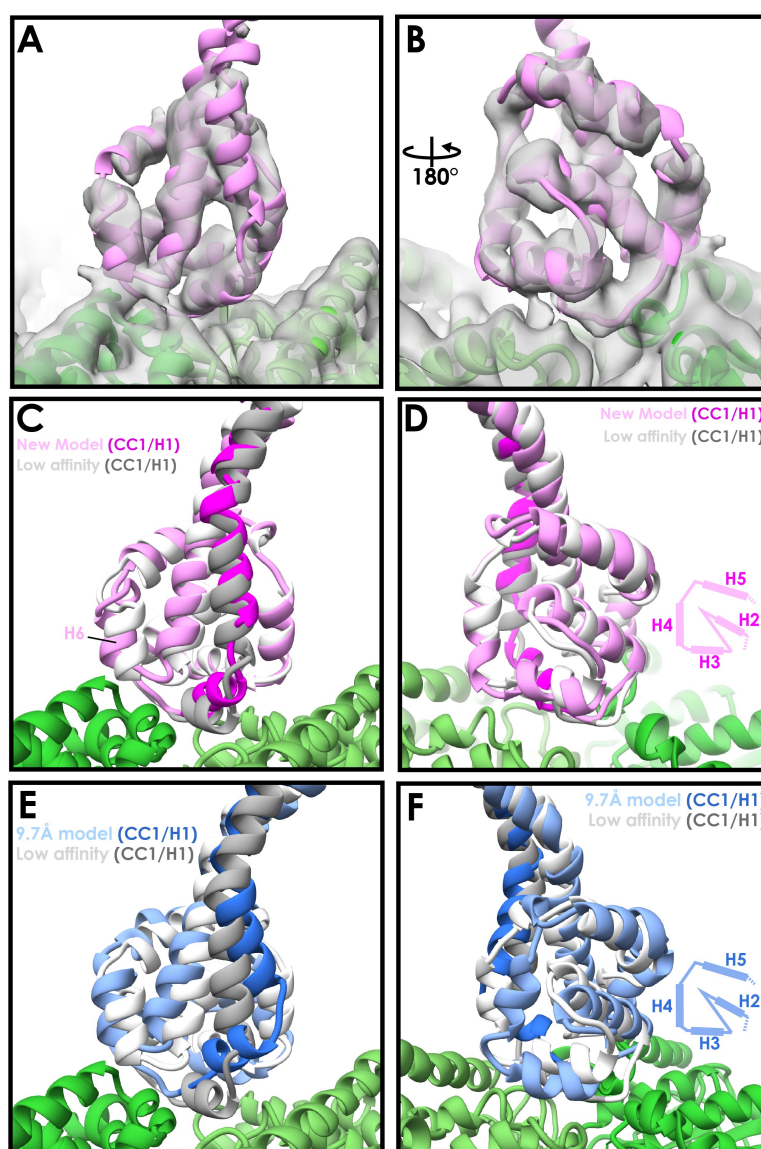


Figure 3.16 - Comparison of the newly refined high-affinity Cyt1-SRS model with previous models

A - The Cyt1-SRS map with the newly refined high-affinity model docked inside (MTBD magenta, α -tubulin dark green, β -tubulin light green). **B** - Orthogonal view of **A**. **C** - Equivalent view to **A**, comparing the newly refined high-affinity model (magenta, CC1/H1 highlighted) with the low-affinity model (PDB 3ERR, white/grey). **D** - Orthogonal view of **C**, with cartoon tracing H2 through to H5. **E** - Equivalent view to **A**, comparing the previous 9.7Å high-affinity model (blue) with the low-affinity model (white). **F** - Orthogonal view of **E**.

The overall fold observed in our new model and the previous 9.7Å model is similar, and the same MTBD residues are positioned to interact with the microtubule. The positions of side-chains are not reliably modelled at the resolution of our MTBD. However, some contacts with the microtubule predicted to occur in the 9.7Å model are now impossible in our structure. At

the boundary between CC1 and H1, K3299 was previously predicted to interact with E420 on the surface of β -tubulin. However, in my structure optimally extended rotamers of these two residues are too far to interact (7.7Å, **Figure 3.17A**). K3299 is now directly proximal to D427 of β -tubulin, making this the more likely interaction. Similarly, R3337 is at least 9.4Å away from its proposed interaction partner β -tubulin E196, while D163 is much closer (**Figure 3.17B**). Other residues are too far from their predicted interaction partners (e.g. R3342, K3298), but new favourable interactions are not as clear. To fully investigate this, molecular dynamics simulations and mutagenesis studies would be required.

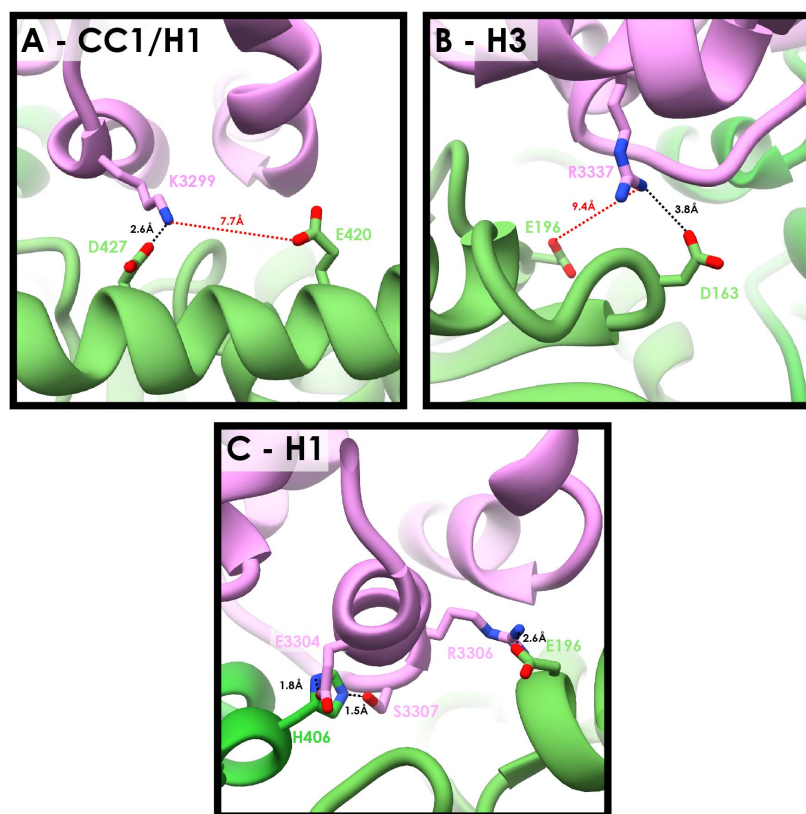


Figure 3.17 - Potential interactions between the MTBD and the microtubule

A - Optimally aligned rotamers of K3299 (dynein) and E420 (β -tubulin), previously predicted to form a salt bridge (Redwine et al., 2012), are too distant to interact now, whereas D427 is directly adjacent to K3299. **B** - Similarly, R3337 is too distant from E196, and D163 seems the more likely partner. **C** - A series of favourable interactions with α - and β -tubulin line up along H1 of the MTBD

The position of H1 in my new model is the biggest structural difference compared to the previous high-affinity model. Its interactions with the microtubule can be predicted despite the lack of side-chain density in the map. The base of H1 contains three charged or polar residues whose side chains are in close proximity to favourable interactors on the microtubule

(Figure 3.17C). These residues are very well conserved throughout different dynein family members (Figure 3.3). These interactions would stabilize the raised H1 conformation, and contribute to the strong attachment of the MTBD to the microtubule. In the previous high-affinity model, many of these residues were raised above the interdimer cleft, and were too distant to interact.

3.2.12 Validating the Cyt1-SRS structure with a dynein motor domain structure

The experimental setup used in this study is slightly different to the previous 9.7Å structure. I used a construct with a longer stalk (12 heptads compared to 3), and imaged it on 13- protofilament microtubules (not 14-PF). To confirm that my 4.1Å structure is the true state of dynein bound to microtubules, I determined the structure of human cytoplasmic dynein-1 motor domain (Dyn1230-4646) (Steinman et al., 2017) bound to microtubules.

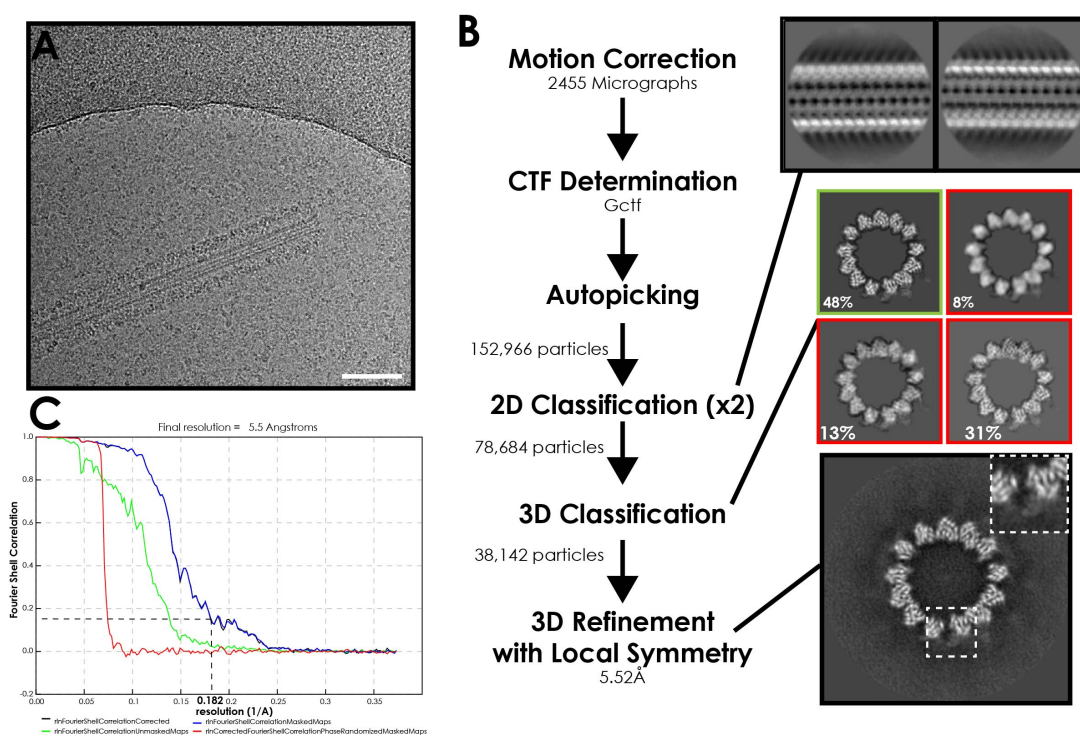


Figure 3.18 - Processing pipeline for Cyt1-MD bound to microtubules

A - Electron micrograph of truncated monomeric dynein motor domains bound to microtubules. Scale bar corresponds to 100nm **B** - Processing for Cyt1-MD followed the same pipeline as Cyt1-SRS. Example 2D classes (top right) show a repeating decorating density. 3D classification (middle) resulted in a single good class (green box) containing 48% of the particles from 2D classification. The final 3D reconstruction (bottom right) only has a weak decorating density (white box, expanded) **C** - FSC curve for the motor domain reconstruction

I purified the insect cell expressed motor domain by its ZZ-tag as described previously (Steinman et al., 2017). The purification and subsequent grid preparation was performed in the absence of nucleotide to create a high-affinity state. I froze grids in the same way as for Cyt1-SRS, and saw a large amount of motor domain binding to microtubules (**Figure 3.18A**). Following the same processing workflow as the Cyt1-SRS sample, 2D classification showed regular decoration on the side of the microtubule (**Figure 3.18B**). The dataset of 2455 micrographs recorded on the Polara refined to 5.5Å resolution (**Figure 3.18B/C**). I

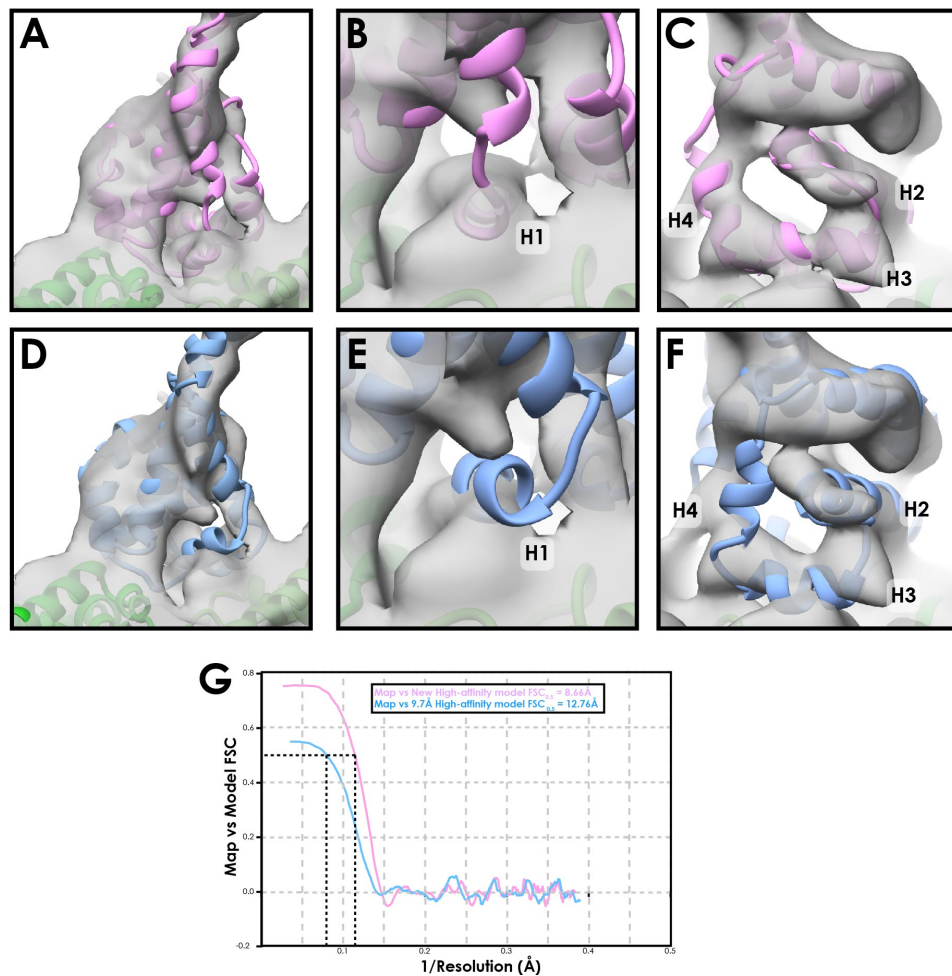


Figure 3.19 - Structure of a dynein motor domain MTBD bound to microtubules
A-C - Images of the motor domain reconstruction with my new high-affinity Cyt1-SRS model docked. **D-E** - Equivalent views of the motor domain reconstruction with the previous 9.7Å high-affinity model docked. **G** - Map to model FSC curves for my new high-affinity model (pink) or the 9.7Å high-affinity model (blue)

In the resulting map, the MTBD density is low (**Figure 3.18B**), most likely due to steric clashes between adjacent motors preventing full decoration. As a result, the resolution of the MTBD is much lower than the overall resolution, and the map was interpreted with an 8Å lowpass filter (**Figure 3.19A**). My high-affinity MTBD model fits inside the motor domain density well (**Figure**

3.19A-C), however in the previous 9.7Å model H1, H2, H3 and H4 all sit outside the model to varying degrees (**Figure 3.19D-F**). Accordingly, the model to map $FSC_{0.5}$ threshold was 8.66Å and 12.76Å for the new model and the previous model respectively (**Figure 3.19G**). I therefore concluded that the 4.1Å resolution map and corresponding model is representative of the native conformation of the dynein MTBD.

3.2.13 Testing the microtubule processing workflow on other data

The new Relion pipeline was successful for these two dynein MTBD structures. However, I wanted to test how it compares to the other methods. I performed the same procedure with a dataset deposited to the publically available EMPIAR EM database (EMPIAR ID 10030). This was submitted by the Nogales lab, and consists of 383 images used to determine the 3.5Å resolution structure of EB3 bound to microtubules. The reconstruction represents one of the highest resolution structures of the microtubule achieved to date, and was made with the ‘super-particle’ reference matching method (Zhang et al., 2015b). It therefore represents a benchmark against which our helical Relion pipeline can be judged.

The EMPIAR deposition consists of unaligned movie stacks. Following motion correction, autopicking picked 105,000 particles, which was reduced to 85,000 after 2D classification. I did not perform 3D classification because the microtubules were polymerized in the presence of EB3, which leads almost exclusively to 13-protofilament architectures (Zhang et al., 2018d). Following 3D refinement and symmetrisation, the map reached 3.5 Å resolution (**Figure 3.20A**), as was reported with the super-particle method (Zhang et al., 2015b). Features in the super-particle map appeared to be equally well resolved in the Relion-refined structure (**Figure 3.20B**), confirming the general ability of the Relion pipeline to reconstruct pseudosymmetrical microtubules to high-resolution.

Inspection of the final asymmetric map from Relion suggested that the seam had not been identified as successfully in the Cyt1-SRS dataset. In protofilaments either side of the seam, the decorating density was weaker than other areas, and compared to the final symmetrised map (**Figure 3.21A**). I noticed that after the first iteration of refinement, the seam was well defined. I stopped a refinement after the first iteration and restarted it with only local refinements. This meant that the position of the seam in each particle was held in the same

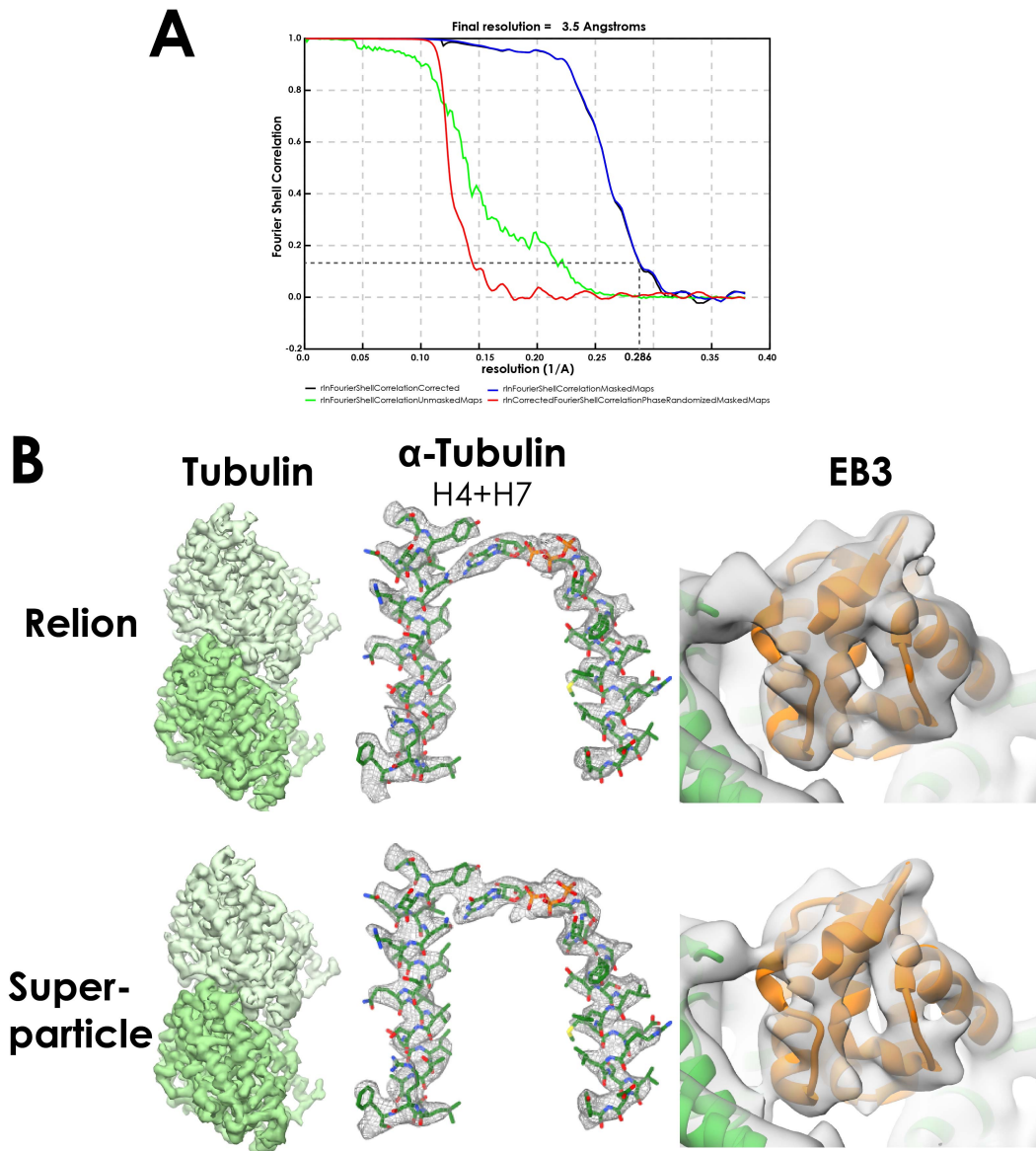


Figure 3.20 - Comparison between symmetrised EB3 maps

A - FSC curve for the EB3 dataset (EMPIAR 10030) processed in the Relion pipeline, determined for the final symmetrised map. **B** - Comparison between maps from Relion and the super-particle approach (EMD 6351) when processing EMPIAR dataset 10030. Left, density for the tubulin dimer B factor sharpened and lowpass filtered to 3.5Å (dark green α -tubulin, light green β -tubulin). Center, density for H4, H7 and GTP of α -tubulin, with pdb model 3JAR docked. Right, the same maps lowpass filtered to 8Å, EB3 density from 3JAR orange.

position as found in the first global iteration. The final map resulted in a much stronger density around the seam, and more closely resembled the asymmetric map produced by the super-particle method (**Figure 3.21B/C**). Therefore, in the case of smaller decorating proteins such as

EB3, it may be necessary to modify the refinement to include only one iteration of global alignments to achieve the best map. In standard refinements the signal from a smaller decorating protein could be overpowered by noise as the resolution of the refinement increases. This means that the first round of global refinement, at lowest resolution, is the most likely to successfully match the seam position as indicated by the decoration pattern.

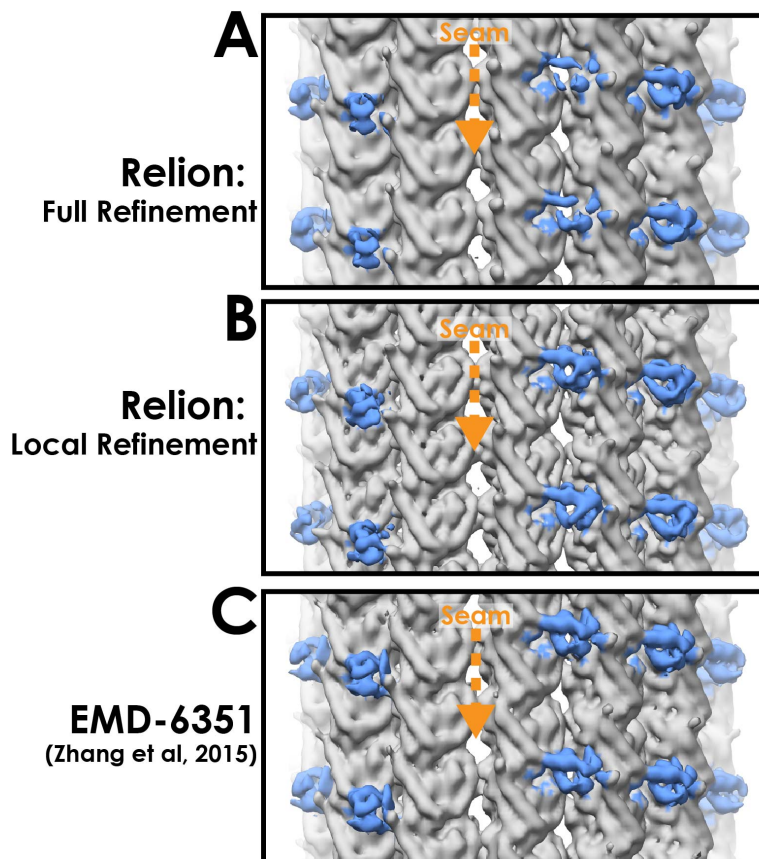


Figure 3.21 - Success of seam finding in refined asymmetric EB3 maps with Relion

Surface representation of maps refined from the EMPIAR 10030 dataset of EB3 decorated microtubules. Density attributed to EB3 is coloured blue, position of the seam indicated with orange arrow. **A** - Refinement according to the same protocol as Cyt1-SRS, following fully automated Relion refinement. **B** - Results when refinement was stopped after one iteration of global refinement and continued with local refinements with the seam position fixed. EB3 density around the seam is stronger, indicating the position of the seam is in better agreement in all the particles. **C** - Results using the “super-particle” reference matching method of (Zhang and Nogales, 2015c)

3.2.14 DNAH7 construct binding to microtubules

After determining the structure of the cytoplasmic dynein-1 MTBD, I wanted to see if distantly related dynein MTBDs bind microtubules in the same way. DNAH7 is a monomeric axonemal inner arm dynein that contains a flap insert in the MTBD (**Figure 3.22A**). It is the human dynein most closely related to *C. reinhardtii* flagellar dynein c, which was the subject of a previous low-affinity NMR structure (Kato et al., 2014). Furthermore, its sequence at the microtubule interaction sites is relatively poorly conserved compared to cytoplasmic dynein-1 (**Figure 3.3**); there is no positive residue equivalent to K3299 at the base of CC1 and there are negative residues in H1 and H3 that are conserved in other axonemal dyneins but not cytoplasmic dynein-1. As such, DNAH7 has one of the most divergent MTBD sequences to cytoplasmic dynein-1, making it a good target to study the universality of dynein binding to microtubules

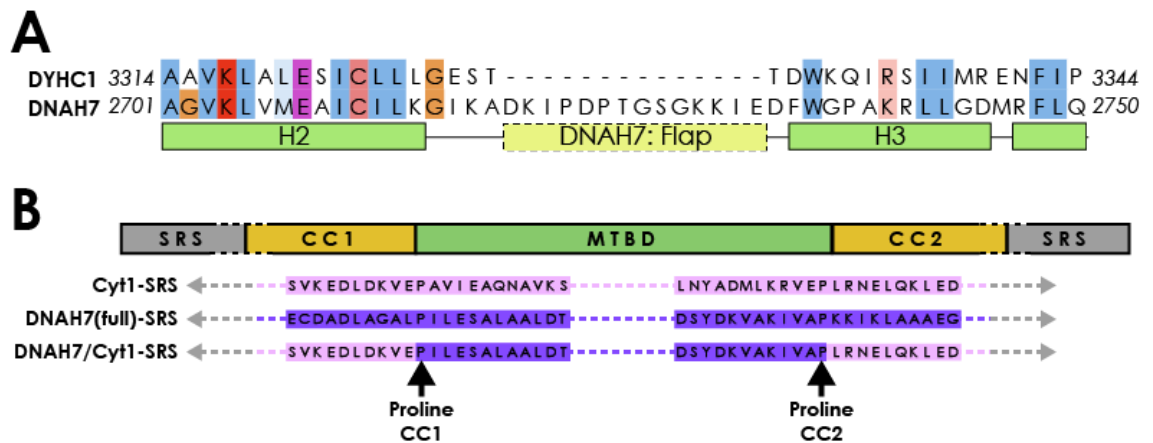


Figure 3.22 - Comparison between Cytoplasmic Dynein-1 and DNAH7 sequences

A - Sequence alignment between cytoplasmic dynein-1 (DYHC1) and DNAH7, in the region between H2 and H3. **B** Schematic showing the stalk sequences of the three SRS fusion constructs.

I ordered a plasmid containing SRS fused to the DNAH7 stalk (85 CC1 residues and 82 CC1 residues for the α -registry). Purification followed the same procedure as Cyt1-SRS, and resulted in a monodisperse peak over gel filtration (**Figure 3.23**). Preparation and screening grids with this construct resulted in no visible decoration (**Figure 3.24A-C**). This is consistent with previous microtubule affinity experiments with SRS constructs (Kato et al., 2014). However, strong binding of full-length flagellar dynein c was observed previously (Sakakibara et al., 1999). Both DNAH7 and flagellar dynein c are among a group of axonemal dyneins that contain a proline residue in CC1 of the stalk (Burgess et al., 2003). As such, the helix sliding

characteristics may be different in DNAH7 such that an SRS fusion cannot capture a high-affinity state.

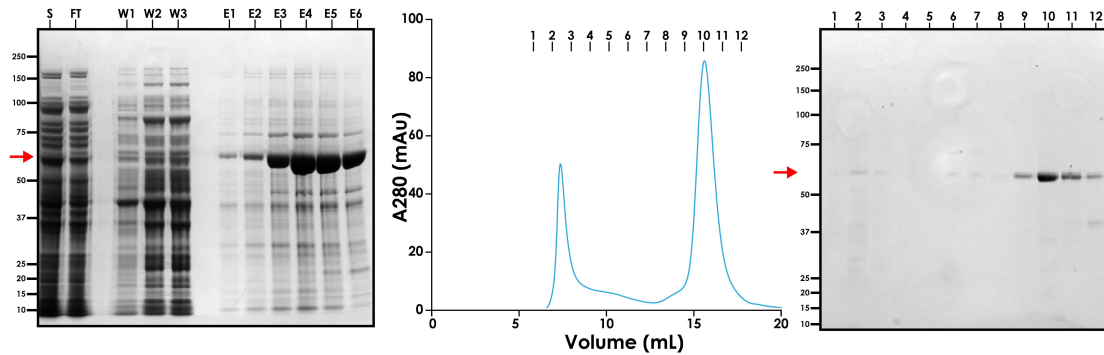


Figure 3.23 - Purification of DNAH7-85:82-SRS

Left - NiNTA affinity gel from purification of DNAH7-85:82-SRS. S=supernatant, FT=Flowthrough, W=wash with 10% elution buffer, E=Elutions. Red arrow corresponds to expected position for DNAH7 85:-82 -SRS
Middle - Gel filtration profile of pooled and concentrated NiNTA elution fractions. **Right** - SDS-PAGE of indicated fractions from gel filtration

To counter this, I made a fusion between the DNAH7 MTBD and the cytoplasmic dynein-1 stalk (Figure 3.22B). The boundary between the two is the universally conserved prolines at the base of each stalk helix (Carter et al., 2008; Gibbons et al., 2005b). This fusion is equivalent to a fusion between the *Dictyostelium discoideum* cytoplasmic dynein-1 motor domain and DNAH7 MTBD used by Imai et al. (Imai et al., 2015). This construct (hereafter DNAH7-SRS) strongly decorated microtubules, as determined by the power spectrum and 2D classes (3.24D-F), and was taken forwards for further data collection.

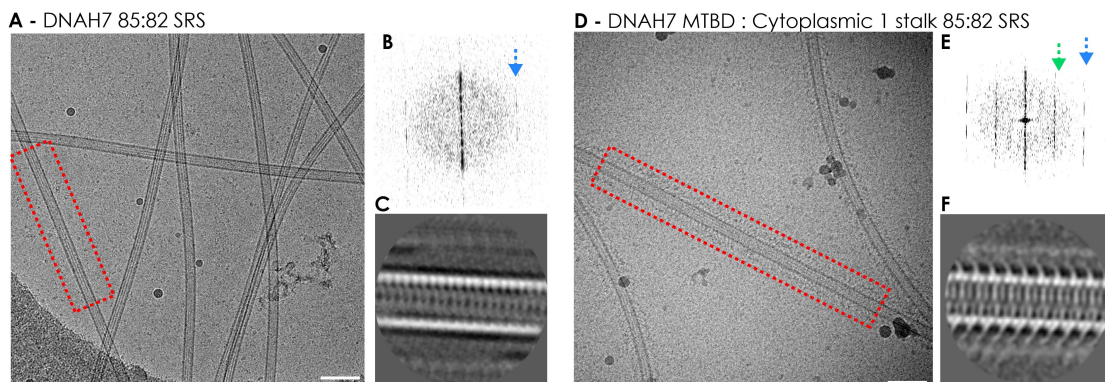


Figure 3.24 - Microtubule decoration of DNAH7 constructs in cryo-EM

A - Cryo-electron micrograph of DNAH7-85:82-SRS incubated with microtubules (left). **B** - The power spectrum of the boxed microtubule only has reflection on the 4nm layer line (blue arrow), and 2D

classification of this microtubule (C) shows no decorating density. D-F Equivalent analyses for DNAH7-SRS, indicating good decoration in the power spectrum (green arrow indicates 8nm layer line) and 2D class. Scale bars correspond to 100nm

3.2.15 Structure of the DNAH7 MTBD bound to microtubules

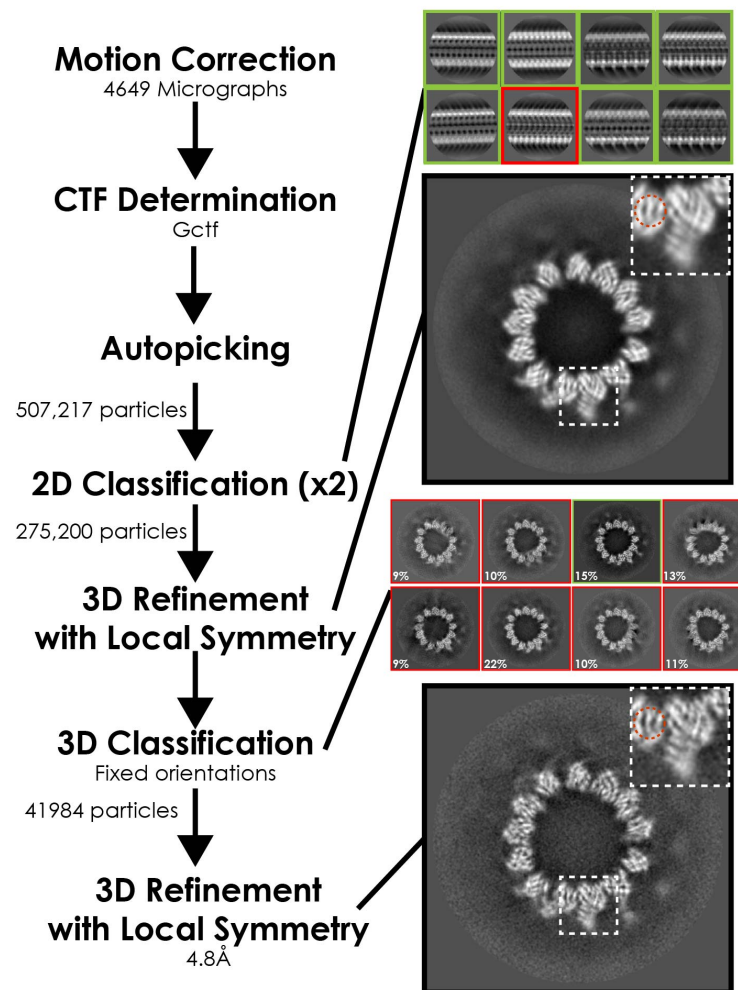


Figure 3.25 - Processing pipeline for DNAH7-SRS

No good classes were formed when 3D classification was performed on the 275,200 particles selected from 2D classification. 3D refinement was performed instead, resulting in a structure with blurry features (note density in red dotted circle). 3D classification was performed with the orientations from the refinement, and one good class was taken forwards for 3D refinement with refined local symmetry

I collected 4649 images of DNAH7-SRS decorated microtubules. When following the same processing regime as Cyt1-SRS I did not obtain any good classes in de novo 3D classification. Instead, I moved straight onto 3D refinement following 2D classification (**Figure 3.25**). This resulted a map with nominally high-resolution ($FSC_{0.143}$ at 4.32\AA), but poorly resolved features

(e.g. blurring between helices in red circle, **Figure 3.25**). To resolve this, I performed 3D classification without alignments into 8 classes to find a good class. This class was then refined to 4.8Å after symmetrisation and postprocessing (**Figure 3.26A**), resulting in an improvement in equivalent features compared to the initial refinement (**Figure 3.25**). However, this was dependent on refinement of local symmetry parameters. The implications of the different behavior of DNAH7-SRS decorated microtubules during processing will be discussed from section 4.2.18 onwards.

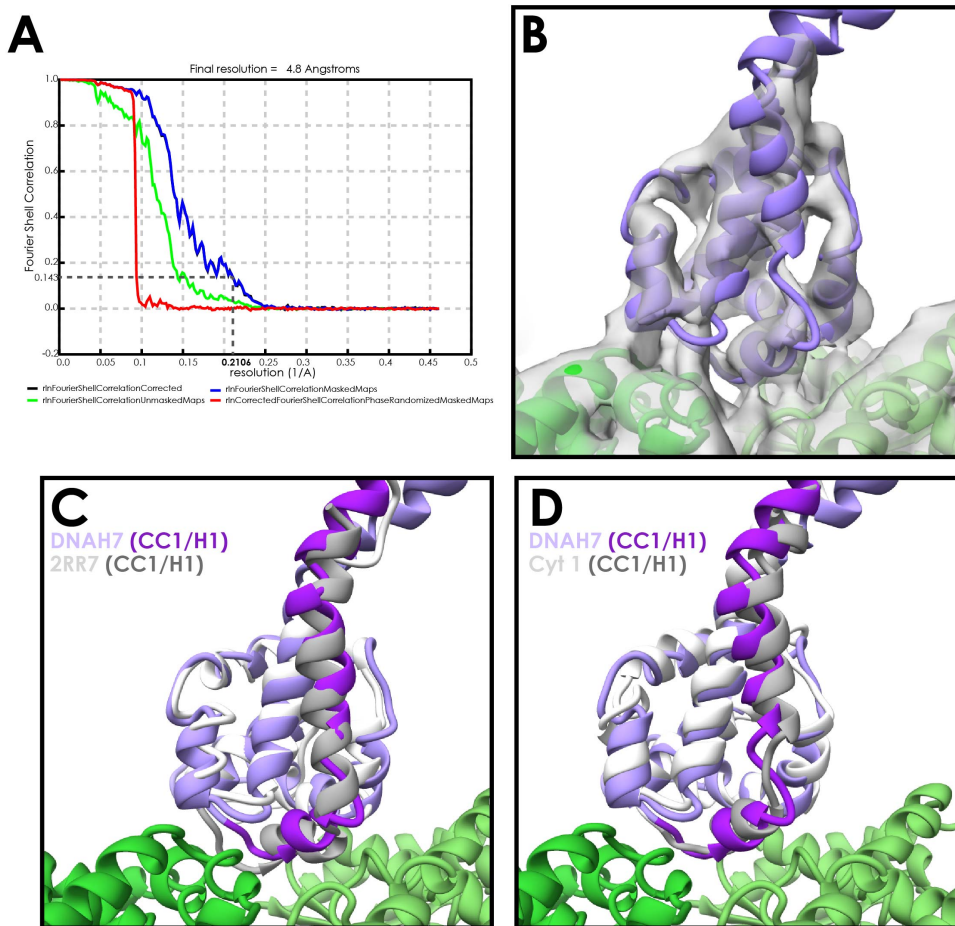


Figure 3.26 - The DNAH7 MTBD structure and refined model

A - FSC curve of the DNAH7 decorated microtubule structure, following symmetrisation with refined local symmetry operators. **B** - Corresponding DNAH7 density with the refined DNAH7 high-affinity model docked in. **C** - Comparison between the newly refined high-affinity DNAH7 model (purple/violet) and the low affinity flagellar dynein c NMR structure (grey/white, PDB 2RR7). **D** - Comparison between my refined high-affinity MTBD structures for Cyt1-SRS and DNAH7-SRS. **E** - Reverse view of the DNAH7 MTBD at a lower threshold, showing density for the flap extending towards the adjacent protofilament. **F** - Close up of the flap and its interaction with the adjacent protofilament.

As a starting reference for DNAH7 model refinement, I made a homology model between the flagellar dynein c NMR structure (PDB 2RR7, (Kato et al., 2014)) and the human DNAH7

sequence. The helices are clearly resolved throughout the MTBD (**Figure 4.26B**), and so the same refinement strategy as for the Cyt1-SRS model was used (**Table 2**). Comparing the low-affinity flagellar dynein c model to the newly refined high-affinity DNAH7-SRS model shows that the transition from low to high affinity occurs in the same way as cytoplasmic dynein-1. Specifically, the majority of the MTBD remains unchanged, but H1 and CC1 move up into a raised position over the intradimer interface (**Figure 3.26C**). Similarly, aligning the Cyt1-SRS and DNAH7-SRS models shows that they adopt almost identical conformations on the microtubule, suggesting that the fundamental basis for microtubule binding is universal (**Figure 3.26D**).

Map	
Map resolution (Å)	5.4
Map sharpening B factor (Å)	-200
Map CC	0.77
Map:Model FSC _{0.5} (Å)	5.54
Model Composition	
Non-hydrogen atoms	15061
Protein residues	1901
Ligands (GTP/GDP)	1/1
R.m.s deviations	
Bond lengths	0.005
Bond angles	0.932
Validation	
MolProbity score	2.49
Clashscore	9.83
Poor rotamers	6.65%
Ramachandran plot	
Favored (%)	95.02
Disallowed (%)	0
CB deviations (%)	0

Table 2 - Model refinement validation statistics for DNAH7-SRS

3.2.16 The DNAH7 flap interacts with a second protofilament

Density for the DNAH7 flap appears at a lower surface threshold compared to the rest of the MTBD, indicating that it is probably somewhat flexible (**Figure 3.27A**). It extends in the same direction as in the NMR structure, and contacts α -tubulin loop H6/7L and β tubulin H10 (**Figure 3.27B**). As such, DNAH7 contacts four tubulin subunits at once. Some residues in the loop are conserved (**Figure 3.3**). In human axonemal dyneins, the 7th or 8th residue is always a negatively charged residue (aspartate or glutamate), and in four out of 5 this is followed by a ionic or polar negative residue two positions later (**Figure 3.3**). These residues would be positioned at furthest extension from the MTBD, suggesting they may be responsible for the interaction with the microtubule.

Aligning the tubulin regions of the Cyt1-SRS and DNAH7-SRS models shows that the DNAH7 MTBD is oriented at a slightly different angle to cytoplasmic dynein-1 (**Figure 3.27C**). This can be described by a 7° rotation around the base of H6. Given that this rotation is in the same direction as the flap, it follows that the flap-microtubule could be responsible for this tilting.

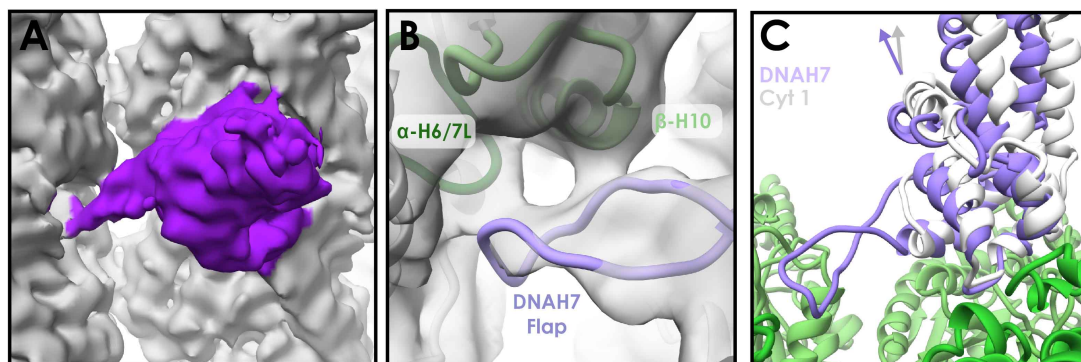


Figure 3.27 - Interaction between the DNAH7 flap and a second protofilament

A - DNAH7 (purple) density at a low surface threshold, showing an extension towards the adjacent protofilament. B - Density of the flap with the modelled DNAH7 residues, and showing an interaction with two tubulin subunits. C - The high-affinity DNAH7-SRS and Cyt1-SRS models aligned by their tubulin, showing a 7° tilt of the DNAH7 MTBD in the same direction as the flap.

3.2.17 A potential link between the DNAH7 MTBD and the β -tubulin E-hook

A second connection between the DNAH7 MTBD and the adjacent protofilament becomes apparent when the map is lowpass filtered to 12Å (**Figure 3.28A**). I tentatively assign it to the normally unstructured β -tubulin C-terminus. In both α - and β -tubulin, the C-terminus is made up of ~20 residues that are almost all acidic. The new density is directly adjacent to the β -tubulin tail, which is the only sequence unaccounted for in the proximity to the MTBD. The MTBD of DNAH7 contains a positively charged pocket near the connecting density, which would favour an interaction with the strongly negative tail (**Figure 3.28B**). Modelling suggests that the β -tubulin tail could reach this pocket. Significantly, the Cyt1-SRS structure shows no such linking density, and the positive patch is not present on the top of the MTBD (**Figure 3.28B/D**). In summary, I propose that in addition to the core microtubule interaction shared with cytoplasmic dynein, DNAH7 binding is bolstered by two separate links to the adjacent protofilament.

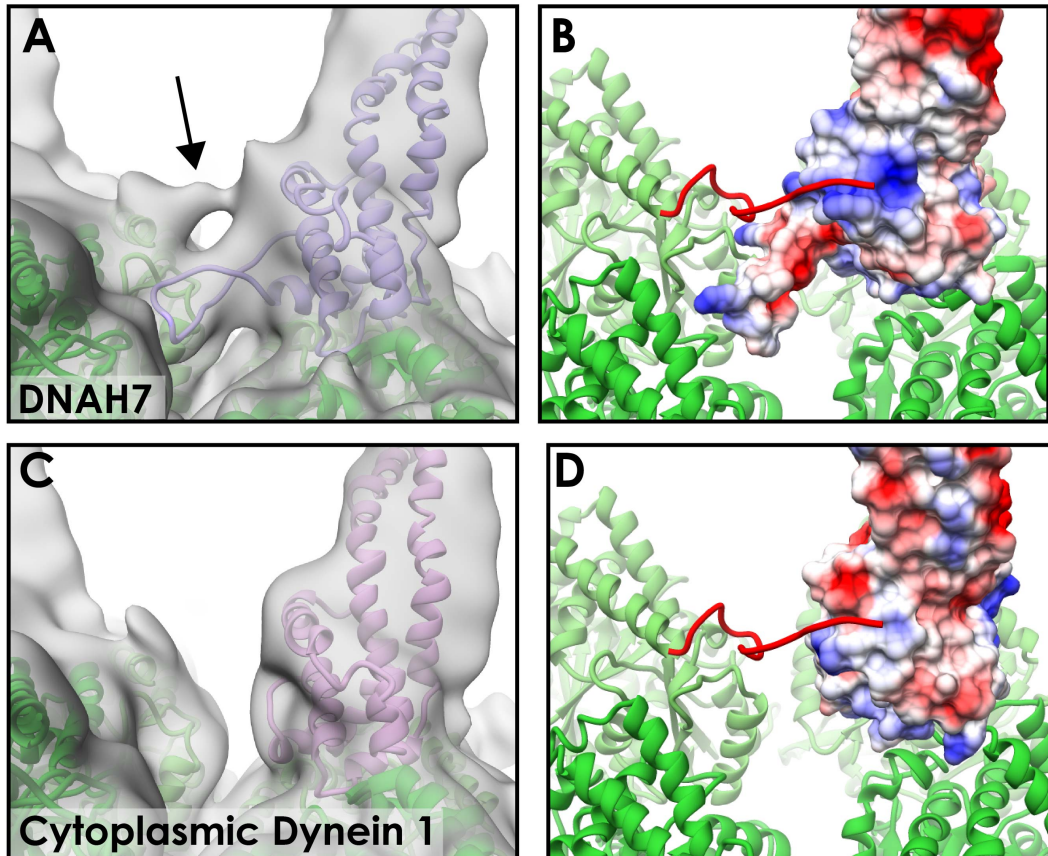


Figure 3.28 - A second link between DNAH7 and the adjacent protofilament

A - The unmasked DNAH7 map lowpass filtered to 12Å and set to a low surface threshold shows a second link unaccounted for by the modelled residues (indicated by black arrow) *B* - The same view with the DNAH7 model coloured by surface charge, and a manual model of the C-terminal tail of β -tubulin (red) showing that it can extend to a positively charged pocket on DNAH7. *C/D* - Equivalent views for Cytoplasmic dynein-1, showing that the positive patch is not conserved, and no connection is observed in the density.

3.2.18 The DNAH7 MTBD changes the cross-sectional curvature of microtubules

As mentioned in section 4.2.15, processing the DNAH7-SRS data required modifications to the standard Relion pipeline. I could not obtain a good 3D class in *de novo* 3D classification, and needed to align all the particles with 3D refinement first (**Figure 3.25**). This was followed by 3D classification without alignments, finding a good class comprising 15% of all particles. Cyt1-SRS resulted in a good class with ~50% of the data in *de novo* classification, suggesting that DNAH7-SRS has greater conformational heterogeneity. In the final DNAH7-SRS map, application of local symmetry with the same operators as Cyt1-SRS decreased the quality of the map. Most notably, the decorating density became significantly weaker (**Figure 3.29A/B**).

The final map was obtained by refining the local symmetry operators relating each protofilament. This highlighted that the relative positions of neighbouring protofilaments is different, and the microtubule is distorted relative to the Cyt1-SRS map.

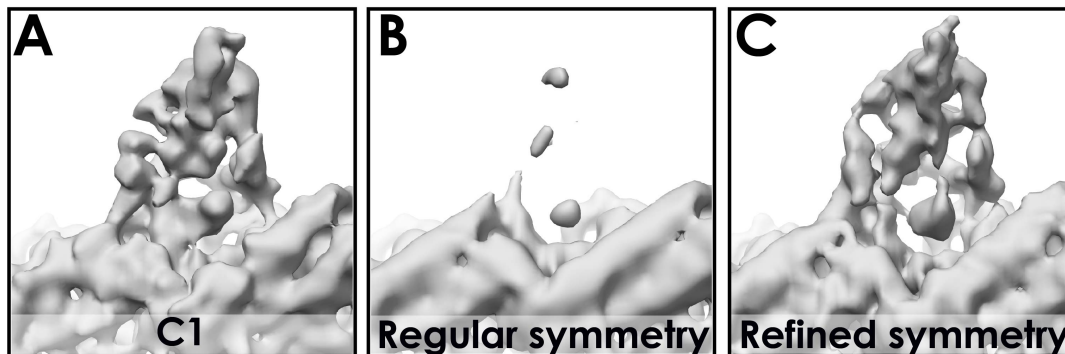


Figure 3.29 - The effect of symmetry on the refined DNAH7 map using regular and refined operators

A - The asymmetric (C1) density of the MTBD in the DNAH7-SRS map. B - Following symmetrisation following regular (circular) symmetry operators, as for Cyt1-SRS, resulted in the MTBD density disappearing. C - Refining the symmetry operators to account for distortions in the cross-sectional curvature of the microtubule resulted in an improvement in the quality of the map.

This distortion can be visualized by plotting the angles between each adjacent pair of protofilaments (**Figure 3.30A**). For a 13-protofilament microtubule, the angle relating each protofilament should be 27.69° ($360^\circ/13$). The angles in the Cyt1-SRS map have only minor deviations from 27.69° (Standard deviation = 0.17° , **Figure 3.30B**). In contrast, the DNAH7-SRS map exhibited protofilament angles ranging from -26.5° to -28.7° , representing a significant distortion in the local curvature of the microtubule (S.D= 0.75° , **Figure 3.30B**). As such, the deterioration in quality observed after regular symmetrisation was a result of incoherent averaging.

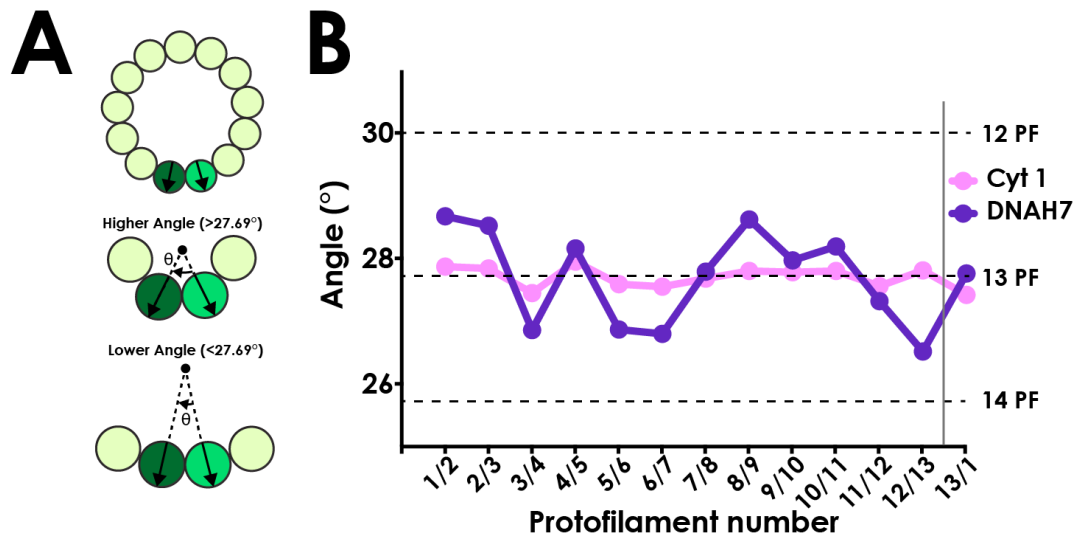


Figure 3.30 - Analysis of protofilament angles in the Cyt1-SRS and DNAH7-SRS maps

A - Schematic of protofilament angle measurements. A tubulin model is docked into two adjacent protofilaments and the relative rotation between the two models is measured. **B** - Plot of protofilaments angles for each pair of protofilaments in Cyt1-SRS and DNAH7-SRS maps

To investigate this distortion further, I reclassified the particles using local refinement and a higher tau value. A higher tau value adjusts the Bayesian weighting in Relion in favour of the data relative to the influence of the prior knowledge (essentially that cryo-EM reconstructions should be smooth). This means that greater deviations from a reference model can in principle be found. This procedure identified two smaller classes (“A” and “B”) with even greater distortions from a regular microtubule (**Figure 3.31A**). Protofilament angles in the two classes ranged from -25.1° to -31.8° (S.D.= 2.1° and 2.2° for class A and B respectively, **Figure 3.31B/C**). This means that curvatures closer to canonical 12 PF microtubules (-25.71°) and 14 PF microtubules (-30°) are induced on the same microtubule by DNAH7 binding.

These distortions change the microtubule cross-section from a circular to an elliptical profile. The ellipticity (the ratio between the long and short diameters of an ellipse) of class A and B is 0.936 and 0.942 respectively (**Figure 3.31D/E**). This is much greater than microtubule ellipticity measured both in the Cyt1-SRS structure (0.995, **Figure 3.31F**) and previous taxol-stabilised microtubule structures (0.98, (Kellogg et al., 2017), indicating that DNAH7 is responsible for this distortion.

To determine how DNAH7 binding affects the curvature of the microtubule, I measured the relationship between the local curvature and local decoration level in the two classes. A clear

correlation is observed in which the decoration is highest at low local protofilament curvatures (Figure 3.31B/C). This suggests that DNAH7 induces a local flattening of the microtubule. It also suggests that the DNAH7 MTBD binds more weakly to higher curvatures and more strongly to flatter curvatures .

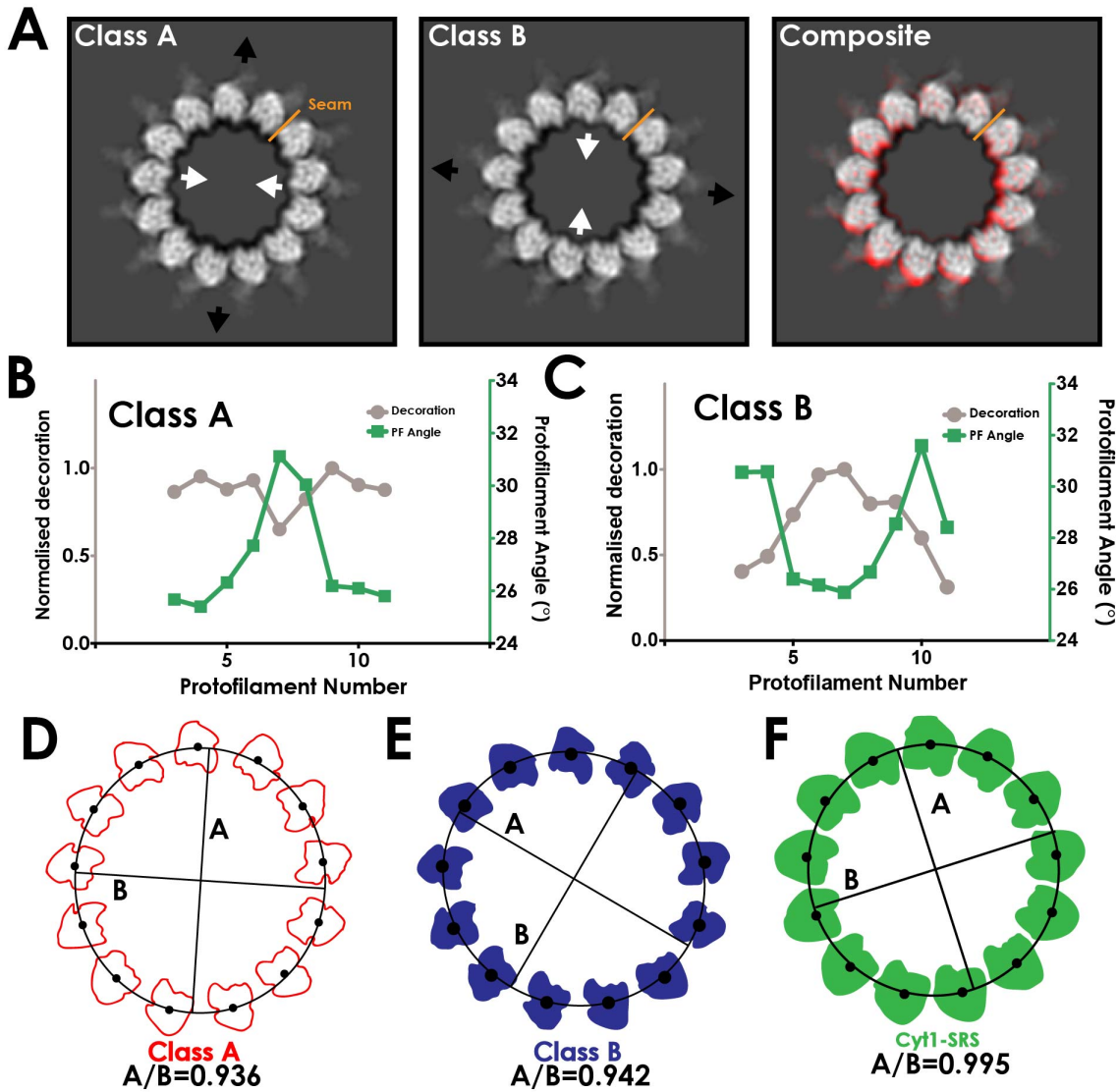


Figure 3.31 - Distortion of microtubules induced by DNAH7-SRS

A - (Left, middle) Projection of Class A and B, with arrows indicating expansion and compression of local curvature compared to a circular microtubule. (Right) Composite of the two classes aligned at the seam, with Class A coloured red. **B** - Plot of local protofilament angle and measured decoration level in class A. **C** - Plot of local protofilament angle and measured decoration level in class B. **D/E/F** - Measured coordinates and fitted ellipse of the indicated map

3.2.19 DNAH7 binding to microtubules is cooperative

To investigate whether the structural differences in microtubule binding of cytoplasmic dynein-1 and DNAH7 affect microtubule affinity, I performed binding measurements with TIRF microscopy. I measured the bound fluorescence intensity of GFP-MTBD constructs on surface-immobilised microtubules at increasing MTBD concentration (**Figure 3.32A/B**). Fitting the saturation curve to the Hill equation (**Figure 3.32C**) shows that the microtubule affinity of Cyt1-SRS ($K_d=171\text{nM}$) is stronger than that of DNAH7-SRS ($K_d=251\text{nM}$). However, DNAH7-SRS has a larger Hill coefficient (1.78, $R^2=0.986$) than Cyt1-SRS (1.37, $R^2=0.995$). These results suggest that DNAH7-SRS binds to microtubules cooperatively. My structural analysis suggests that DNAH7 induces a curvature on the microtubule, and that binding is higher in these flatter areas. The microtubule binding results support a scheme in which one DNAH7 induces a local curvature flattening in the microtubule that makes a more favourable surface for another DNAH7 molecule to bind. However, the difference between cytoplasmic dynein-1 and DNAH7 cooperativity is relatively subtle by these measurements, and so further investigation is needed to validate this model.

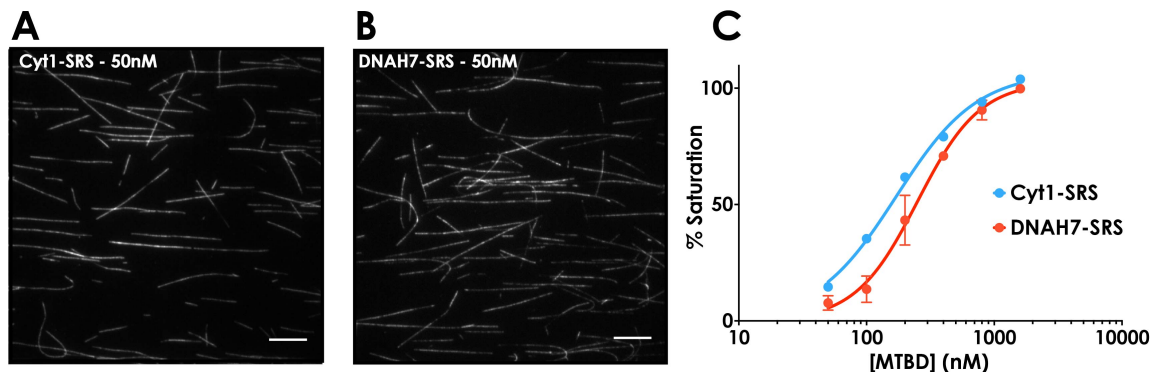


Figure 3.32 - TIRF microscopy measurements of MTBD binding to microtubules

A - Single frame of GFP-tagged Cyt1-SRS bound to microtubules in TIRF microscopy. Scale bar correspond to 10 μm **B** - Single frame of GFP-tagged DNAH7-SRS bound to microtubules. **C** - Saturation curve of MTBD binding to microtubules. Each point is an average of three independent repeats, with the MTBD fluorescence intensity of 20 microtubules from two images measured in each repeat. Average \pm standard deviation plotted.

3.3 Discussion

3.3.1 How does dynein bind to microtubules?

Based on my Cyt1-SRS structure, we can propose a modified model for dynein's interaction with the microtubule. The MTBD is permanently primed for microtubule binding, with a crescent on helices H2, H3 and H6 always in the high-affinity state even in a low-affinity stalk registry. These residues could initiate binding, however when the MTBD is in the low-affinity state the full binding interface cannot form due to a steric clash between H1 of the MTBD and elements of α - and β -tubulin (**Figure 3.33**). When the stalk adopts the α registry, H1 of the MTBD moves up and can form new interactions with tubulin to stabilize this conformation. As in the previous model, these interactions stabilise the α registry fully, which is communicated back to AAA1 to allow the ATPase cycle to continue (Carter et al., 2008; Kon et al., 2009; Redwine et al., 2012). The MTBD releases from the microtubule when CC1 is pushed down again, and the steric clash reforms.

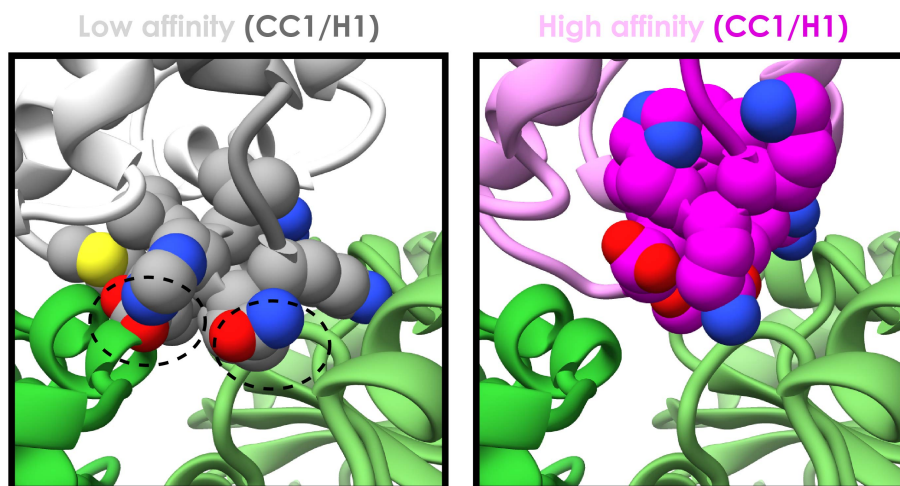


Figure 3.33 - A steric clash prevents dynein binding in the low-affinity state

Low and high affinity dynein MTBD models in the binding pocket. In the low affinity state, H1 residues sterically clash with α - and β -tubulin. These clashes are resolved by raising the helix in the high-affinity state.

Combining the high-affinity, microtubule bound structures with previous studies (Carter et al., 2008; Kato et al., 2014), we now have structures of two distantly related dynein MTBDs both on and off the microtubule. In both cases, the key structural transition going from the low- to high-affinity states is the movement in CC1/H1, whereas the remainder of the MTBD stayed mostly unchanged. Sequence conservation of MTBD residues at the microtubule interface

infers which interactions are most important. There are three well-conserved positions in H1 of the MTBD (3301, 3304 and 3306 according to cytoplasmic dynein-1 numbering, **Figure 3.34**). Two of these (E3304 and R3306) are on the bottom surface of H1, and are well positioned for stabilizing interactions with the microtubule (**Figure 3.17C**). In H3 and H6, positive residues are thought to form salt bridges with the microtubule, however the exact composition (e.g. number and position of these residues) varies. Differences between cytoplasmic dynein-1 and 2 in H6 has previously been predicted to lead to enhanced processivity in the latter (Redwine et al., 2012). It follows that variations in sequence across the microtubule interface can be expected to result in fine-tuning of the binding characteristics. For example, positive residues at the base of CC1 in cytoplasmic dynein-1 are thought to form a salt bridges with β -tubulin (**Figure 3.17**, (Redwine et al., 2012)). DNAH7 lacks these residues (Cytoplasmic dynein-1=KKQ, DNAH7=TAQ), and hence a strong contact on the opposite side to the MTBD as the flap. This may then allow DNAH7 to tilt towards the flap.

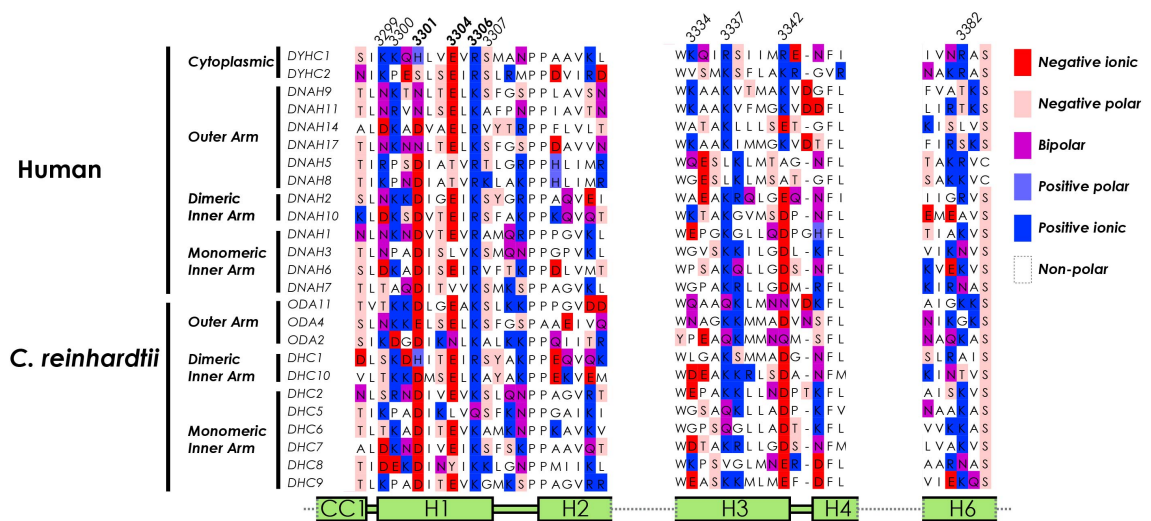


Figure 3.34 - MTBD sequence alignment in regions that interact with the microtubule
Sequences of human and *C. reinhardtii* dynein MTBDs aligned. Residues are coloured by charge (see key) and not conservation.

3.3.2 The structure of the MTBD flap

The DNAH7 MTBD flap contacts α - and β -tubulin on the protofilament adjacent to the core DNAH7 binding site. The regions contacted (α -tubulin loop H6/7 and β -tubulin H10) do not move from their normal conformations, but a local flattening in areas with higher DNAH7 decoration suggest that this interaction pulls on the protofilament as a rigid body. A second

The location of specific human axonemal dynein isoforms within the axonemal repeat is unknown. However these positions are known for *C. reinhardtii*, following cryo-ET studies (Bui et al., 2008; Liu et al., 2008; Nicastro et al., 2006; Song et al., 2018). Flap containing dyneins are spread along the entire 96nm axonemal repeat in both outer and inner arm dyneins (**Figure 3.35A**). The human orthologues of flap containing *C. reinhardtii* dyneins also have a flap, suggesting this pattern will be conserved. Strikingly, the flap containing dyneins bind in a concentrated patch on the adjacent B-tubule (**Figure 3.35B**). This local concentration is in contrast to the unconstrained, near saturation binding around the entire microtubule of DNAH7-SRS in my structure. In this case, local flattening in one area is confounded by the same effect occurring nearby. As such, the local concentration of flap-containing dyneins in the axoneme may result in even greater deformations than seen in my structures. Conversely, axonemal doublets are probably a stiffer and less malleable substrate compared to *in vitro* polymerized microtubules (Ichikawa et al., 2017), making deformation by DNAH7 and other flap-containing dyneins more difficult.

3.3.3 Roles of distortion

A number of microtubule-associated proteins are known to distort the microtubule lattice. Kinesin-1 stabilises GDP-bound microtubules by extending the longitudinal dimer repeat by ~2% and restoring the spacing seen in the GTP-bound lattice (Peet et al., 2018). Interestingly, an optical trap study showed that kinesin 1 binding to microtubules significantly increases the likelihood of more kinesin binding in adjacent areas (Muto et al., 2005). These results suggest that kinesin 1 binding is cooperative. Combining these results suggests that kinesin-1 can also change the microtubule lattice conformation to affect further binding. Conversely, Kinesin-13 walks towards the minus-end of the microtubule, creating longitudinal curvature that results in depolymerisation (Hunter et al., 2003). However, both of these effects relate to longitudinal distortions, and not lateral (cross-sectional) distortions as seen with DNAH7. Kinesin-1 cooperatively therefore works through a different mechanism.

Some non-motile MAPs are able to sense and affect the lateral curvature of microtubules. When Doublecortin or EB-family proteins are incubated with free tubulin and GTP, the microtubules that form all have 13-protofilaments (Moores et al., 2004; Zhang et al., 2018a). Structural work has shown that they bind in the cleft between two protofilaments and contact

four tubulin subunits, thereby constraining lateral interactions to a set curvature during polymerisation (Moore et al., 2006; Zhang et al., 2018d). However, EB3 only binds near the plus-end of mature microtubules, and DCX simply does not bind to mature non-13-prot filament microtubules. As such, to my knowledge DNAH7 is the only protein reported to distort the cross-sectional curvature of microtubules.

The activity of axonemal dyneins is regulated so that only a localised subset are active at once (Lin and Nicastro, 2018). This creates an imbalance in force across the axoneme that leads to the overall ciliary beat. Fundamentally, the nature of this regulation is unknown. My results suggest that the flap could play a role in communication between different dyneins in the axoneme. I show that DNAH7-SRS binding was higher in areas with lower lateral curvature, suggesting that the flap can act as a curvature sensor. In this scheme, the flap-containing dyneins would preferentially bind to the microtubule in different regions of a bent cilium. Furthermore, I show that DNAH7-SRS actively distorted microtubules and binds cooperatively. This could lead to a scheme in which dynein binding in one position increases the affinity of nearby dyneins, helping to spread activity along the cilium. This theory could be tested by modifying the MTBDs of axonemal dyneins in *C. reinhardtii* and seeing the effect it has on the ciliary beat.

3.3.4 Processing microtubules in Relion

My results demonstrate that high-quality reconstructions of pseudosymmetrical microtubules can be achieved in Relion, provided that care is taken during refinement. A key advantage of this workflow is that it does not require specialist scripts or expert knowledge, and is fully integrated in the widely used Relion pipeline. The application of local symmetry requires some command-line expertise beyond the Relion graphical user interface, however the required processes are straightforward and well-documented in the Relion wiki. I show that Relion is less able to find the seam when the decorating density is less prominent (**Figure 3.21**). However, this can be offset if the processing pipeline is modified to include only a single round of global refinements. This could be due to deterioration in the seam after each iteration of global refinement (despite the application of symmetry during refinement). Alternatively, it could be due to higher resolution global refinement iterations being dominated by the tubulin

signal when the 8nm repeat is weaker. The drawback to using a single round of global refinement is the greater potential for model bias to occur.

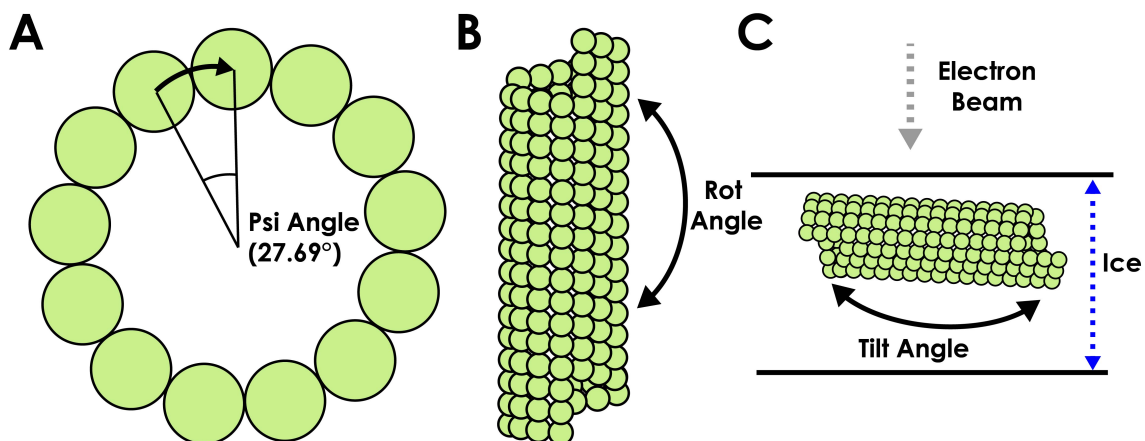


Figure 3.36 - Three Euler angles describe a particle's orientation

A - The Psi angle is a rotation around the helical long axis. B - The Rot angle is perpendicular, and aligns the polarity of each microtubule. C - The Tilt angle is perpendicular again, and describes whether particle was lying flat in the ice or tilted.

Notably, other microtubule reconstruction techniques utilize more information from the restraints that the microtubule lattice imposes than Relion. For each of the three Euler angles describing a particle's orientation (**Figure 3.36A-C**), the difference in consecutive MT segments is only going to change by small amounts. Both Chuff and the Nogales lab's super-particle workflows find consensus orientations for each angle along a microtubule. At present, Relion can perform this local averaging on two of these angles ("Tilt" and "Rot"). However the third angle ("Psi"), which describes rotation around the microtubule long axis and thus determines the position of the seam, is independent in consecutive segments. Accordingly, the orientations of these angles is subject to some variability along a given microtubule in my final refined maps. Introducing restraints along a helical segment for the Psi angle would be a potential source of improvement for future, and could help in refining structures with weaker decorating densities.

Finally, the potential power of Relion in solving microtubule structures may go beyond what is presented here. A recent study imaged kinesin dimers sparsely decorating microtubules, and solved the structure of a two-head bound state using a new technique called FINDKIN (Liu et al., 2017). This uses projection matching against references with one or two kinesin motor domains bound in different positional combinations to identify particles in which two motor

domains are consecutively bound. The asymmetry in the conformation of the two heads provided a structural explanation for why the leading head never releases from the microtubule first. In my results, I show that a combination of symmetry expansion, particle subtraction and 3D classification in Relion is able to distinguish between decorated and undecorated tubulin dimers (**Figure 3.13B**). Extending the area retained after subtraction to include multiple subunits could be used to determine the structure of other dimeric MAPs, or MAPs that bind across multiple tubulin dimers.

Chapter 4. Using cryo-EM to investigate why an engineered dynein walks backwards

4.1 Background

This chapter covers work to resolve the mechanism of dynein directionality. It was not yet understood how dynein walks towards the minus-end of the microtubule. X-ray crystallography resolved the nucleotide-dependent changes in the motor associated with stepping (Schmidt and Carter, 2016). However, these studies were performed on truncated, monomeric dynein motors. As such, they need to be combined with other techniques to understand how the structural transitions operate in the context of a stepping dynein dimer.

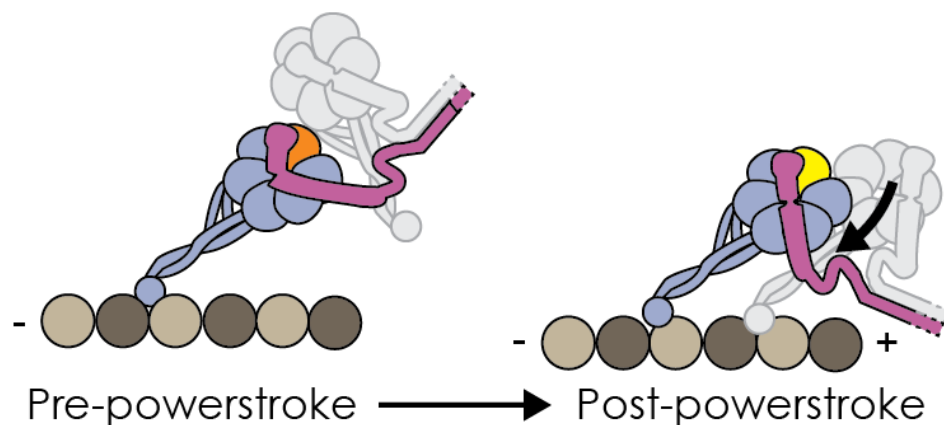


Figure 4.1 - The linker swing during the dynein power stroke points towards the minus-end
Schematic of a dynein motor in the pre- and post-powerstroke states. In the pre-powerstroke conformation, ADP.Pi is in AAA1 (orange) and the linker has a 90° kink. Following phosphate release AAA1 is in the ADP state (yellow), and the linker rearranges to the straight conformation. This linker swing is dynein's power stroke, and is proposed to pull the trailing head (grey) to the minus end.

Structural and biochemical data have provided competing models to explain how dynein walks. Based on the first structural observations of linker movement as part of the nucleotide cycle, Roberts *et al.* proposed a “linker-swing” model for dynein directionality (Roberts *et al.*, 2009). In this model, movement of the linker during the power stroke pulls the trailing head forwards and towards the microtubule minus-end (**Figure 4.1**). Structural data of the movements of the linker during the power stroke (Kon *et al.*, 2012; Schmidt *et al.*, 2015) and the orientation of the motor on the microtubule (Imai *et al.*, 2015) suggest that the linker swing should position the trailing head towards the minus-end.

However, high-resolution single-molecule fluorescence studies of *Saccharomyces cerevisiae* cytoplasmic dynein-1 showed that stepping is highly stochastic, with multiple backwards or sideways steps (Reck-Peterson et al., 2006). Furthermore, imaging the two motor domains simultaneously revealed that the movement of each head is not strongly coordinated with the other (DeWitt et al., 2012). Most significantly, it was possible for the leading head to take multiple forward steps whilst the trailing head remained bound to the microtubule. These observations were hard to reconcile with a linker swing mechanism; how can the linker swing allow the leading head to step forwards?

A competing model for dynein directionality was developed based on optical trap experiments. These showed that when dynein is pulled backwards (towards the plus-end), the motors resist a large amount of force before release. However, when pulled forwards (towards the minus-end) the motors quickly detached from the microtubule (Cleary et al., 2014; Gennerich et al., 2007). These observations led to an “asymmetric release” model for dynein directionality (DeWitt et al., 2012; Qiu et al., 2012). One of the two heads releases from the microtubule and can randomly rebind further from the other. This creates intramolecular strain, essentially meaning that the leading head is pulled backwards and the trailing head is pulled forwards. The trailing head is more likely to release, and relaxation of the intramolecular strain causes it to attach closer to leading head than before.

The structural and biophysical data therefore supported different models. There was also the possibility that both models are correct, with each mechanism influencing dynein stepping and directionality. A project to conclusively solve these problems was conceived by Andrew Carter and Ahmet Yildiz. Based on the available structures, it was predicted that the direction of linker swing (“linker-swing vector”, LSV, **Figure 4.1**) relative to the microtubule could be modified and even reversed by protein engineering of the motor domain. If a reverse-LSV dynein walks in the reverse direction, the linker swing model is shown to be the mechanism determining dynein directionality

Previous structural data showed that the LSV of dynein motors aligns with the microtubule long-axis, and points towards the minus-end (Carter et al., 2008; Imai et al., 2015; Schmidt et al., 2015). The first attempt to reverse the LSV by Ahmet Yildiz and his PhD student Sinan Can was focused around changing the stalk angle. The stalk is the coiled coil extension from AAA4

that links the AAA+ ring to the MTBD. A universally conserved proline residue at the base of each of the stalk helices creates a kink relative to the MTBD (**Figure 4.2A/B**, “Cyt1”). This positions the AAA ring towards the plus-end relative to the MTBD (**Figure 4.2D**). Inserting two residues below each of the prolines was predicted to flip them to the other side of their helices, and thus reverse the angle of the kink (**Figure 4.2A+C**, reverse-kink mutation, “Cyt1^{RK}”). Molecular dynamics simulations performed by a collaborator, Dr Mert Gur, predicted that these modifications would indeed flip the stalk angle (**Figure 4.2E/F**). However, modelling the LSV of Cyt1^{RK} suggested that the main component of the LSV was down, into the microtubule.

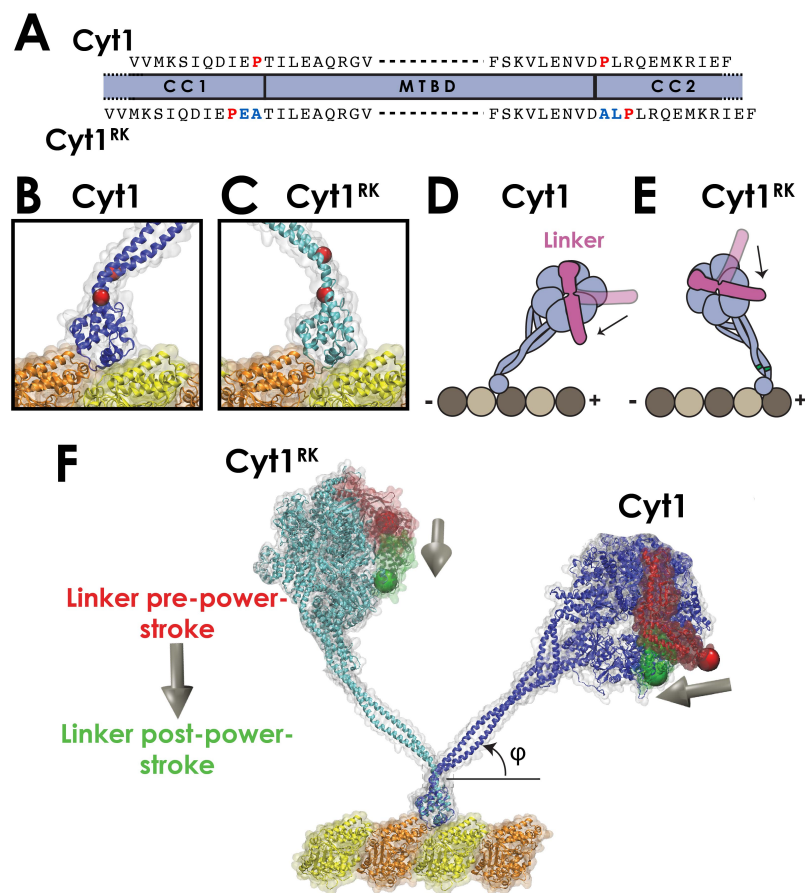


Figure 4.2 - Reversing dynein's stalk angle is predicted to change the LSV

A - Sequence of Cyt1 and Cyt1^{RK} at the base of the stalk. The two universally conserved proline residues (red) are shifted in Cyt1^{RK} by the addition of two extra residues (blue), positioning them on the opposite side of their respective helices (see B/C). **B** - Snapshot from molecular dynamic simulations of cytoplasmic dynein at the junction between the stalk and the MTBD (blue). The two universally conserved proline residues (red) create a kink that point the stalk towards the microtubule (yellow/orange) plus-end. **C** - Equivalent view of Cyt1^{RK}, showing that the reverse-kink insertions are predicted to reverse the stalk angle. **D** - Schematic summarising the MD simulation predicted LSV direction in Cyt1. **E** - The Cyt1^{RK} construct is only predicted to result in a minor plus-end directed LSV. **F** - Snapshot from molecular dynamic simulations of Cyt1 (dark blue) and Cyt1^{RK} (turquoise) bound to

microtubules, with the linker in the pre- (red) and post- (green) power stroke state modelled. The LSV is determined from the two states (grey arrows).

Sinan Can performed gliding assays with dimeric dynein with the Cyt1^{RK} engineered motor domains (**Figure 4.3A**). In this assay the motor is immobilised on a cover slip and polarity-labelled microtubules are free in solution. The motors move the microtubules, and the direction and velocity of movement can be recorded. The gliding speed of the Cyt1^{RK} construct was much slower than wild-type Cyt1 (**Figure 4.3B**), consistent with the LSV pointing off-axis.

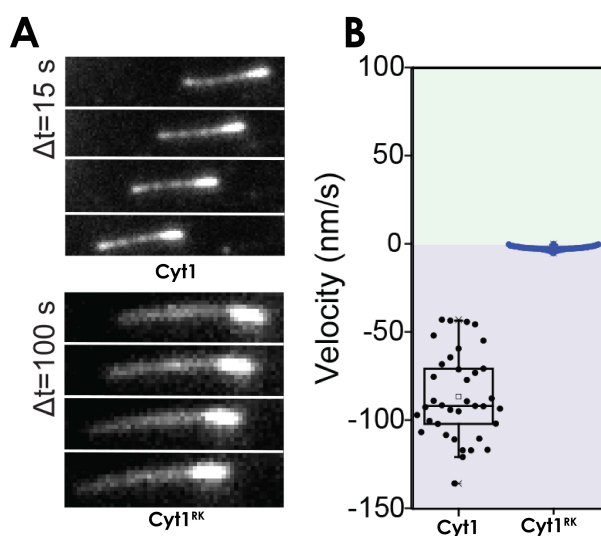


Figure 4.3 gliding activity of Dyn^{RK}

A - Stills from gliding assays performed with Dyn and Dyn^{RK}. Microtubules are polarity labelled with a brighter minus-end. **B** - Quantification of gliding speeds, indicating Dyn^{RK} has been slowed down. **MD simulations performed by Mert Gur, Gliding assays performed by Sinan Can.**

The Cyt1^{RK} modifications had therefore not resulted in a reversal in predicted LSV or the direction of motility. However, the fact that the Cyt1^{RK} construct behaved as predicted in the gliding assay suggested that the modifications were having an effect on dynein directionality. As such, Ahmet Yildiz and Sinan Can started work on finding additional modifications that would result in a robust plus-end directed LSV.

My role in this project was to verify that molecular dynamics simulations predictions were consistent with the conformation of the protein in real life. This will inform us of the real direction of the LSV, and thus allow us to determine whether changes in direction can be attributed to changes in the LSV. I used cryo-EM of Cyt1^{RK}-SRS decorated microtubules to

visualise the stalk angle. However, in my reconstruction the stalk appeared to be mostly disordered. Ahmet and Sinan subsequently developed a plus-end directed dynein motor by combining the reverse-kink mutations with a 7-heptad coiled coil insertion in the stalk. I use 2D cryo-EM of dynein motor domains bound to microtubules to show that the LSV direction of these motors is reversed. We can therefore provide a universal mechanism for dynein directionality, based around the linker-swing model.

4.2 Results

4.2.1 Purification of SRS-Cyt1^{RK} for cryo-EM

To study the stalk angle of engineered Cyt1^{RK} motors, I used a seryl-threonine synthetase (SRS) fusion construct as in chapter 3. The SRS has a coiled coil extension to which the stalk helices are fused. This can fix the stalk in the α -registry, leading to the high-affinity state in the MTBD (Gibbons et al., 2005a). Sinan Can introduced the reverse-kink mutations to an SRS fusion the *Saccharomyces cerevisiae* cytoplasmic dynein-1 stalk (12 heptads), hereafter Cyt1^{RK}-SRS. Sinan expressed Cyt1^{RK}-SRS in *E. coli* and purified it with Ni-NTA affinity, but obtained a low purity and yield. I performed size-exclusion chromatography on the Ni-NTA elutions prior to preparing grids. The elution profile indicated that there was poor separation between Cyt1^{RK}-SRS and a series of contaminating species (**Figure 4.4A-C**). Following concentration (**Figure 4.4D**), the yield was typically ~0.2mg from a 1L cell pellet. Furthermore, Cyt1^{RK}-SRS tended to precipitate from solution when concentrated above 1.5mg/mL, indicating general instability of this construct.

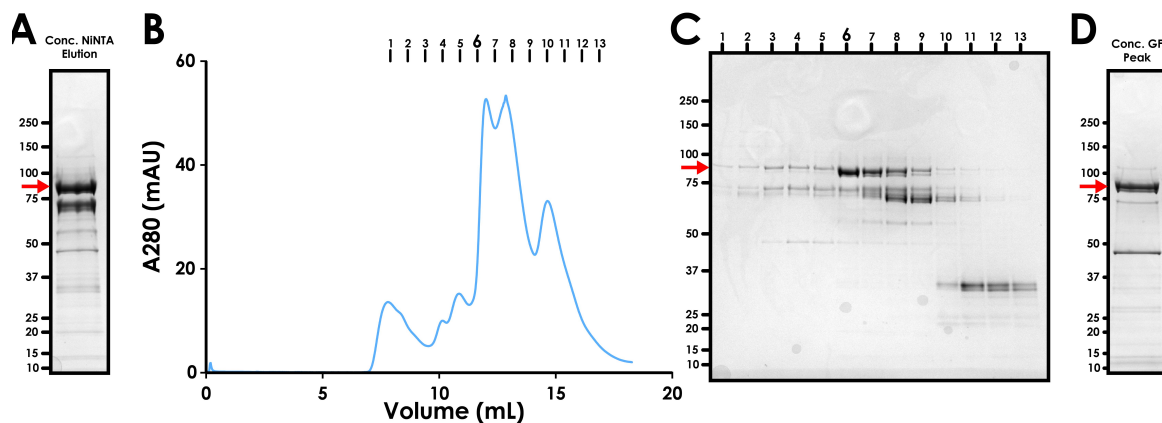


Figure 4.4 - Cyt1^{RK}-SRS preparation

A - Coomassie stained SDS-PAGE of Cyt1^{RK}-SRS following elution from NiNTA affinity. **B** - Gel filtration profile of sample in **A**. **C** - SDS-PAGE of gel filtration fractions indicated in **B**. **D** - Concentrated peak of fractions 6-7 in coomassie stained SDS-PAGE.

4.2.2 SRS-Cyt1^{RK} weakly decorates microtubules in cryo-EM

I prepared Cyt1^{RK}-SRS decorated microtubule grids for cryo-EM, and compared them to wild-type Cyt1-SRS decorated microtubules (**Figure 4.5A/B**). Large areas of aggregated protein were often visible on the Cyt1^{RK}-SRS grids (**Figure 4.5C**). This is consistent with the protein being

unstable during concentration. 2D classification showed that Cyt1^{RK}-SRS decorated microtubules much less than Cyt1-SRS in equivalent conditions (**Figure 4.5D/E**). The low decoration level could be innate lower microtubule affinity as a result of the reverse-kink mutations. However, it could also be due to the effective concentration of MTBD being lower than the measured input concentration as a result of on-grid protein aggregation.

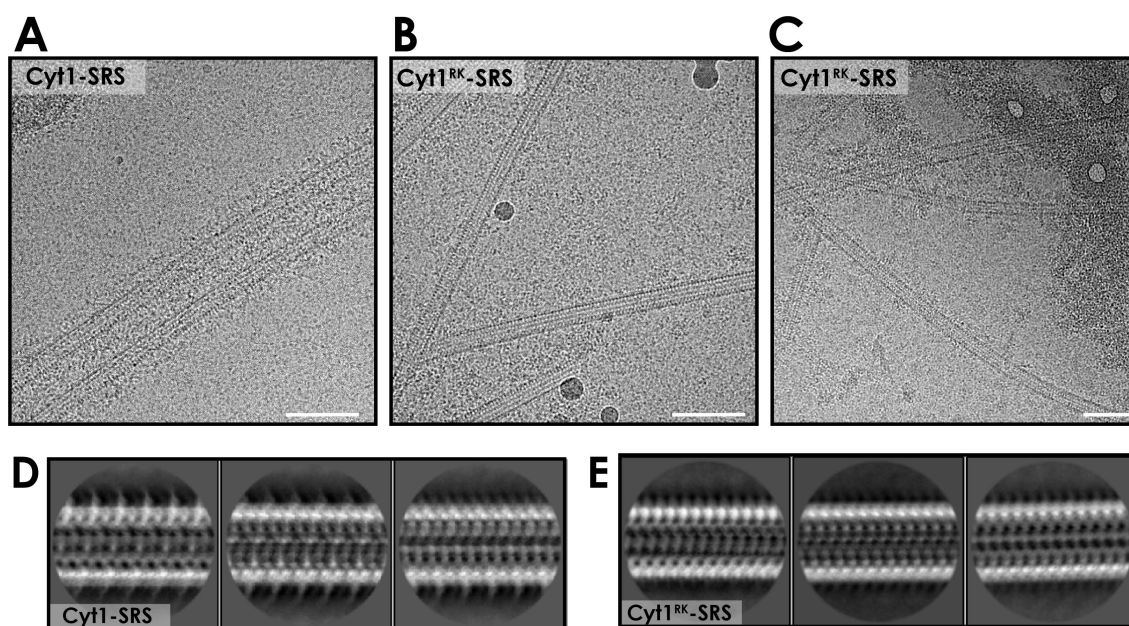


Figure 4.5 - Cyt1^{RK}-SRS microtubule decoration

A - Cryo-electron micrograph of Cyt1-SRS decorated microtubules, showing a regular extra density on the edge of the microtubules. **B** - Cryo-electron micrograph of Cyt1^{RK}-SRS decorated microtubules, with no visible regular decorating density. **C** - Same sample as B in a different area, showing a large area of aggregated protein (top right of image). **D** - 2D class averages of Cyt1-SRS decorated microtubules. **E** - 2D class averages of Cyt1^{RK}-SRS decorated microtubules. All scale bars corresponds to 100nm

4.2.3 Cross-linking MTBD to the microtubule resulted in further protein aggregation

Complexes often fall apart on the grid in the period between blotting and freezing due to interactions with the hydrophobic air-water interface (Glaeser, 2018). Chemical cross-linking is commonly used in cryo-EM to covalently bind more weakly bound protein complex components together (Drulyte et al., 2018). I attempted on-grid glutaraldehyde cross-linking of Cyt1^{RK}-SRS MTBD to the microtubule. Following incubation of MTBD and microtubule on the grid, I side-blotted the excess liquid and replaced it with 0.025% glutaraldehyde in buffer. The grid was incubated for one minute, and then directly plunge-frozen. These grids had much

lower contrast than the normal grids (**Figure 4.6**). This is expected, as glutaraldehyde will scatter the beam more than vitreous ice.

A large amount of protein was bound to the microtubules (**Figure 4.6**), however it was now forming amorphous clumps rather than a regular repeating pattern. Cross-linking was therefore not enriching the native interaction, but was instead keeping more weakly bound aggregated MTBD attached to the microtubule.

0.025% Glutaraldehyde Cross-linking

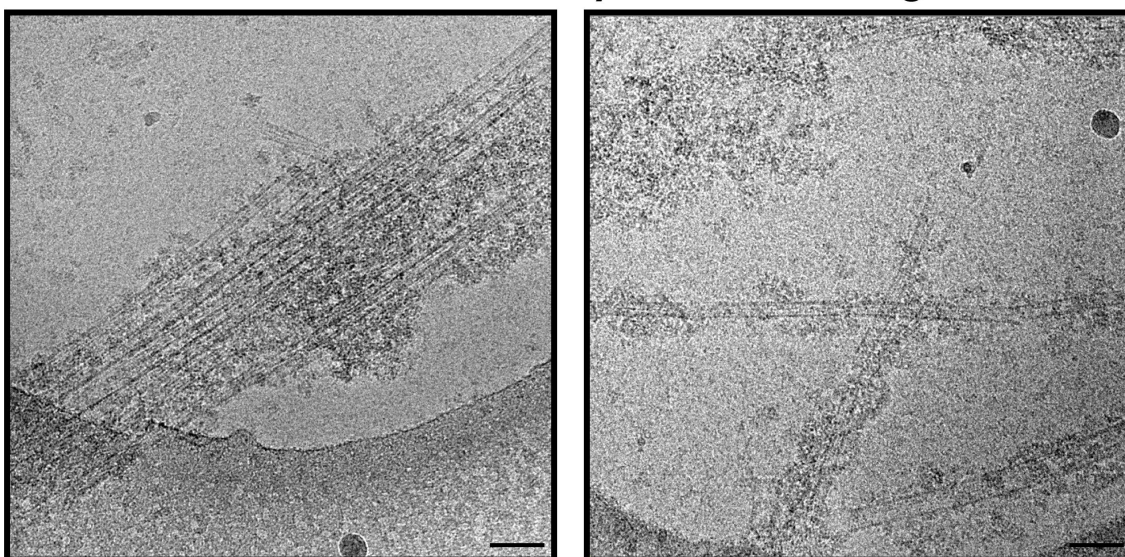


Figure 4.6 - Chemical cross-linking of SRS-Cyt1^{RK} to microtubules

Two cryo-electron micrographs of SRS-Cyt1^{RK} cross-linked on-grid to microtubules with 0.025% glutaraldehyde. Contrast is very low, and aggregated clumps of protein are the only clear microtubule binding densities. Scale bars correspond to 100nm.

4.2.4 The stalk is not visible in a 3D reconstruction of microtubules partially decorated with Cyt1^{RK}-SRS

The partially decorated, uncross-linked Cyt1^{RK}-SRS grids (**Figure 4.5B/C/E**) was the best sample to be taken forwards for further analysis. Over 1000 images were collected on the 300kV Polara microscope, but only 330 were retained after manual inspection of decoration. The most highly decorated 2D classes were selected, and entered for 3D refinement using the Relion pipeline introduced in Chapter 3.2.7 and 3.2.8. The resulting 8Å resolution reconstruction only had a weak decorating density, and was visualised with a 10Å lowpass filter. I compared it to my Cyt1-SRS structure (Chapter 3.2.10), also lowpass filtered to 10Å

(**Figure 4.7A/B**). In the Cyt1-SRS map, the stalk is clearly visible beyond the kink prolines, and points towards the microtubule plus-end as expected. There is no stalk density visible for Cyt1^{RK}-SRS at any threshold. The point at which the density is lost corresponds to the position of the proline residues, suggesting that the reverse-kink modifications have destabilised rather than flipped the stalk.

These observations were in contrast to what Sinan Can had experienced with the reverse-kink insertions in GST-dimerised motor domains expressed in yeast. This construct expressed and purified similar to the wild-type equivalent, and walked on microtubules. I thought that the instability I observed with Cyt1^{RK}-SRS structure could therefore be attributed to the SRS-fusion. The 12-heptad coiled coil in these constructs does not represent the whole length of the stalk, and any disruption at the base of the stalk could potentially be stabilised in the wild-type by a full complement of coiled coil interactions further up.

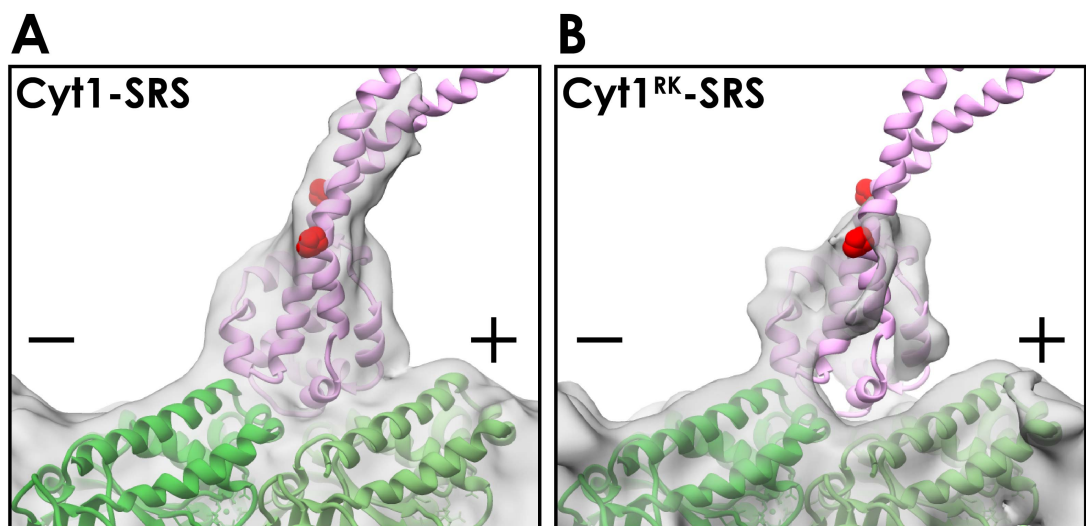


Figure 4.7 - The Cyt1^{RK}-SRS stalk is not resolved in a 3D reconstruction

A - Electron density for my SRS-Cyt1 reconstruction presented in Chapter 4.2.10, lowpass filtered to 10Å and with the refined high-affinity model docked. The two kink prolines are highlighted in red, with sphere representation. **B** - Equivalent view for the Cyt1^{RK}-SRS reconstruction. No density is observed above the kink prolines. The density is thresholded to the lowest level before noise components take over; existing noise in this view has been reduced with the Chimera “hide dust” option. + and - indicate the plus and minus ends of the microtubule

4.2.5 Engineered monomeric dynein motors stably bind to microtubules in cryo-EM

Concurrently with this structural work, our collaborators had designed and tested new constructs. Ahmet and Sinan tried to design a construct with a more robust plus-end directed

LSV (**Figure 4.8**). A previous attempt to reverse the direction of the LSV involved adding 7 heptads of coiled coil to each of the stalk helices (Carter et al., 2008). 7 heptads of coiled coil results in an extra 180° rotation, effectively flipping the AAA+ ring relative to the microtubule. However, this protein still walked towards the minus-end of microtubules (Carter et al., 2008). Ahmet and Sinan noted that the predicted LSV of Cyt1^{RK} pointed down into the microtubule, and that the 180° rotation introduced in a 7-heptad stalk insertion (see dotted line, **Figure 4.8B**) could direct it towards the plus-end (**Figure 4.8C**). Molecular dynamics simulations, again performed by Dr Mert Gur, were consistent with this prediction, and the predicted LSV of the “Cyt1^{RK+7hep}” motor pointed towards the plus-end (**Figure 4.8D**). Sinan showed that Cyt1^{RK+7hep} dynein was plus-end directed in motility assays (see discussion). I needed to show that the conformation that the engineered protein adopts corresponds to the molecular dynamics predictions, and therefore show that the plus-end directed motility is the result of a plus-end directed LSV.

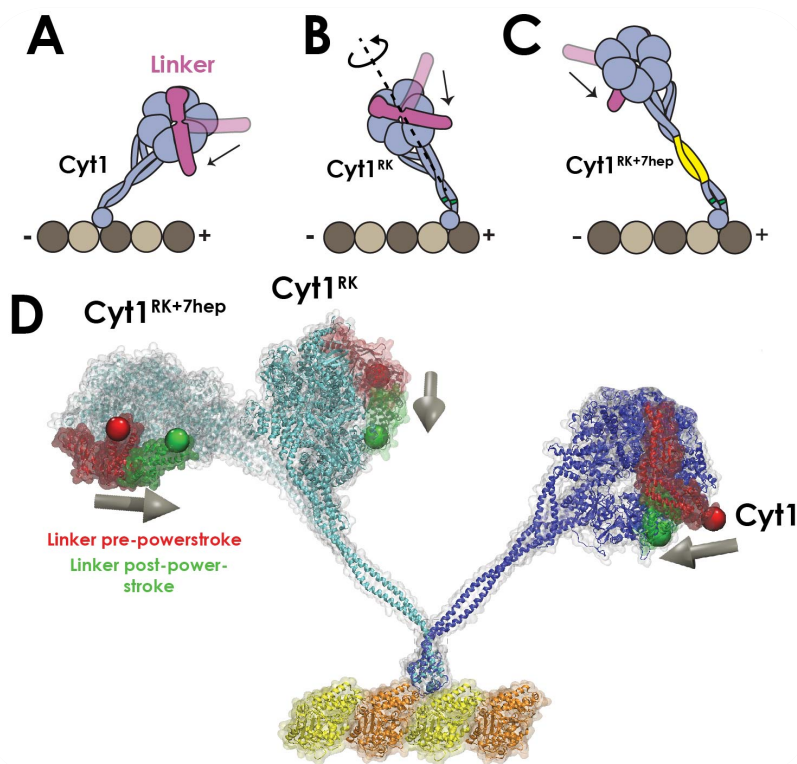


Figure 4.8 - The Cyt1^{RK+7hep} modifications are predicted to reverse the LSV direction

A - Cartoon depicting LSV direction of wild-type Cyt1 dynein predicted by MD simulations. **B** - Predicted LSV direction of Cyt1^{RK}. Dotted line corresponds to rotation axis influenced by the 7-heptad stalk insertion. **C** - Predicted LSV direction of the new Cyt1^{RK+7hep} construct. **D** - Consensus structures following MD simulations of Cyt1, Cyt1^{RK} and Cyt1^{RK+7hep} bound to microtubules. Linker movement pre- and post-powerstroke has been modelled to predict the linker swing vector (LSV), indicating that the LSV of Cyt1^{RK+7hep} points strongly towards the microtubule plus end. **MD simulations performed by Mert Gur, figures put together by Ahmet Yildiz, Sinan Can and Mert Gur.**

We now wanted to know the orientation of the AAA+ ring as well as the stalk angle. I therefore switched to an approach where I imaged engineered monomeric dynein motor domains bound to microtubules. This is a similar approach to a previous study which imaged dynein dimers on microtubules to investigate the flexibility in the angle between the stalk and the MTBD (Imai et al., 2015). The angle between the stalk and the microtubule can be measured directly from these images, and the position of the linker will show if the ring has been flipped 180°. Specifically, in the wild-type motor the linker is positioned below the ring and above the microtubule (**Figure 4.8A**). Simply reversing the stalk angle would position the linker above the ring (**Figure 4.8B**), and so a reversed stalk with the linker below the ring (**Figure 4.8C**) would indicate that the 7-heptad insertion has had the desired effect.

Wild-type monomeric dynein motor domains (Cyt1) and double-engineered dynein motor domains (Cyt1^{RK+7hep}) were expressed in *S. cerevisiae* and purified by Sinan Can. Prior to grid preparation, I exchanged the sample into a low-salt buffer by repeated dilution and concentration in a spin concentrator. Since all processing will be performed in 2D, I only wanted images with side-views of the motor bound to microtubules (i.e. as they appear in **Figure 4.8A-C**). I therefore used a longer blotting time than for the SRS fusion constructs to obtain thinner ice, thus blocking the motor from binding to the top or bottom of the microtubule. To achieve a good distribution of dynein on the microtubules with minimal overlaps between adjacent particles, I used 150 nM of motor domain (nucleotide-free) with 1 μ M microtubules. This is in comparison to 1 μ M microtubules and up to 20 μ M MTBD-SRS construct used for full-decoration. Under these conditions, both Cyt1 and Cyt1^{RK+7hep} specifically bound to microtubules, with the stalk of single particles visible in the raw images (**Figure 4.9**). I collected datasets of ~150 images on the F20 microscope for each construct. I chose the 200kV F20 over a 300kV microscope due to the higher low-frequency contrast at lower voltages. Images were taken at -4 μ m defocus to increase contrast, but ensuring that the 4 nm tubulin repeat was well resolved.

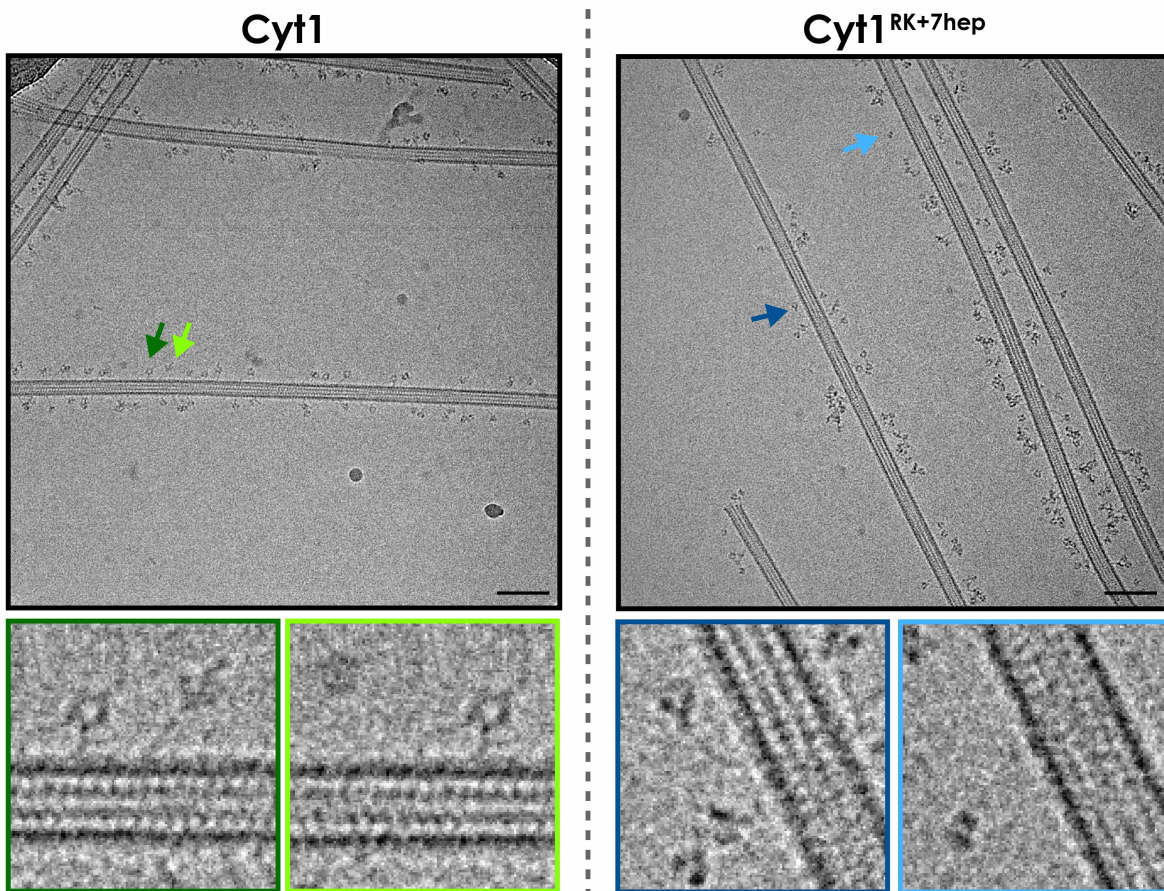


Figure 4.9 - Dynein motors decorating microtubules in cryo-EM

Left - Cryo electron micrograph of wild-type Cyt1-MD particles bound to microtubules, with individual particles enlarged below as indicated. **Right** - Cryo-electron micrograph of engineered Cyt1^{RK+7hep}-MD particles bound to microtubules, with individual particles enlarged below

4.2.6 The polarity of non-13 protofilament microtubules can be determined by cryo-EM

In order to determine whether the stalk angle has been successfully reversed in the engineered motors, the polarity of the microtubule to which they are bound must be determined. A previous study demonstrated how this can be achieved with cryo-EM images (Chrétien et al., 1996). To summarise, transmission cryo-EM creates projection images, which for microtubules means that the signal from the top and bottom surfaces is combined as an interference (Moiré) pattern. 13-PF microtubules are unique, in that their protofilaments run exactly parallel to the microtubule long axis (they have no 'protofilament skew') (**Figure 4.10A/B**). This means that the Moiré pattern does not change along the length of the microtubule (**Figure 4.10C**).

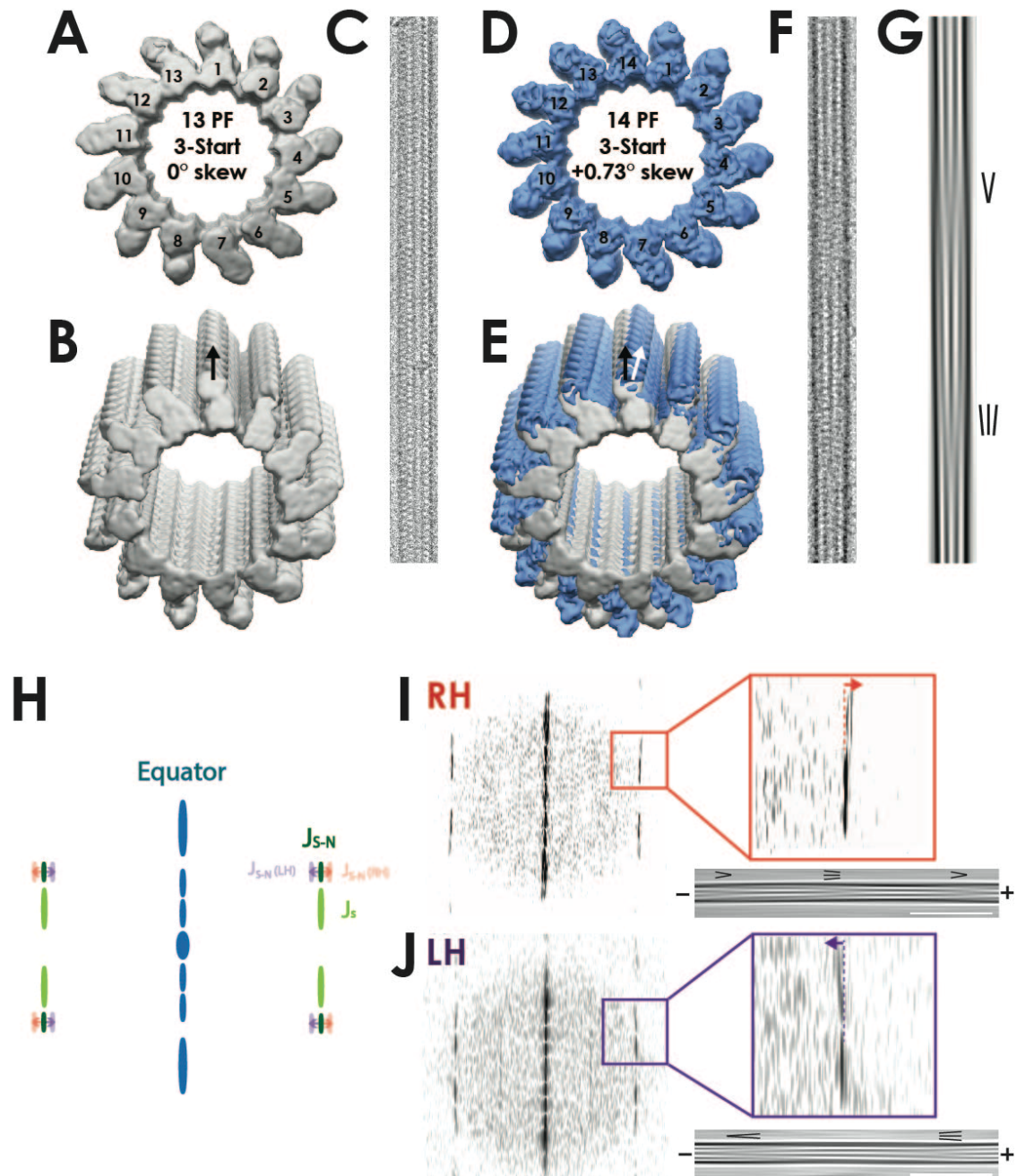


Figure 4.10 - Determining microtubule polarity in cryo-EM images

A - End-on view of a 13-PF, 3-start microtubule decorated with kinesin motor domain (Cryo-EM reconstruction, EMD 6355, (Zhang et al., 2015a)). **B** - Side on view of A; the protofilaments run directly parallel to the long axis of the microtubule (black arrow). **C** - A cryo-EM image of a 13-prot filament microtubule, showing a unchanging regular repeating pattern parallel to the microtubule long axis. **D** - End-on view of a 14-PF, 3-start microtubule decorated with kinesin motor domain (Cryo-EM reconstruction, eMD 6353, (Zhang et al., 2015a)). **E** - Equivalent side-on view to B, showing the 13-PF (grey) and 14-PF (blue) microtubules superposed. The 14-PF microtubule protofilaments twist around the microtubule long-axis (protofilament skew). **F** - A cryo-EM image of a 12-PF microtubule. The protofilament skew means that the Moiré patterns change along the microtubule. **G** - Fourier filtering of F, representing just the equatorial reflections (see H), highlight the repeating arrowhead patterns formed in non-13-PF microtubules a result of the protofilament skew. **H** - Representation of the lower order

reflections of the microtubule lattice. Equatorial reflections (blue) relate to short-axis repeat. Reflections on the 4nm layer line (J_s , J_{s-N}) relate to the 4nm repeat from the top and bottom surfaces of the microtubule long axis. Right-handed helical PF skew results in the J_{s-N} reflection moving further from the equator to J_s and vice versa for left handed skews. **I** - A power spectrum of a microtubule determined to be right-handed due to the position of the J_{s-N} reflection (red arrow, inset). The arrowheads in the Fourier-filtered image point towards the plus-end. **J** - As **I**, but for a left handed helix. Arrowheads now point towards the minus-end.

However, non-13-PF microtubules all exhibit protofilament skew (**Figure 4.10D/E**), which means that the Moiré pattern varies in a regular repeat along the microtubule (**Figure 4.10F**). Chretien *et al.* demonstrated how the polarity of microtubules with skew could be determined from their power spectra. As a regular helix, microtubules produce a characteristic power spectrum relating to the spacing of tubulin in the lattice (**Figure 4.10H**). Equatorial reflections correspond to the periodicity on the short-axis of the microtubule (i.e. the lateral spacing of protofilaments). When signal from only these reflections is included in the image (Fourier filtering), the Moiré interference manifests as a characteristic arrowhead pattern (**Figure 4.10G**). Chretien *et al.* determined through analysis of tilt-pairs that in right-handed microtubule architectures (e.g. 12 protofilament, 3 start) the arrowheads point towards the plus-end, and in left-handed microtubules (e.g. 14-protofilament 3-start) towards the minus-end (Chrétien et al., 1996).

The handedness of the microtubule can in turn be determined from inspection of the microtubule power spectrum. On the 4nm layer line of the power spectrum, relating to the longitudinal tubulin repeats, if the central reflections (J_s) are closer to the equator than the outer reflection (J_{N-s}) then it is a right-handed helix, and vice-versa (**Figure 4.10H**). As such, the polarity of a non-13 protofilament microtubule in a cryo-EM image can be quickly determined by analysis of the microtubule power spectrum and a Fourier-filtered version of the microtubule (**Figure 4.10I/J**).

4.2.7 The stalk angle of Cyt1^{RK+7hep}-MD has been flipped compared to wild-type

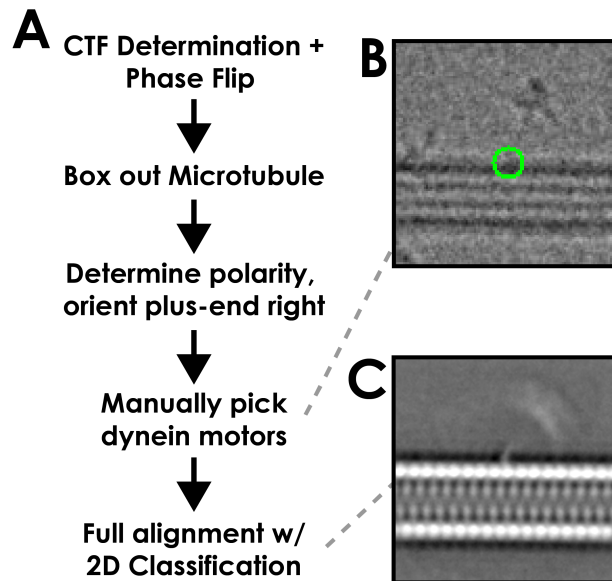


Figure 4.11 - Data processing strategy to determine orientation of motor domains bound to microtubules

Flowchart detailing how the Cyt1 and Cyt1^{RK+7hep} datasets were processed. CTF parameters were determined in Gctf, and negative phases in the CTF were flipped in the whole images. Each microtubule was manually boxed out, the polarity was determined, and the microtubule was orientated with the plus-end to the right of the image. Manual particle picking was used to pick the clearly separated motors, centered at the microtubule junction (green circle). For each dataset, all particles aligned by classification into a single class.

The overall processing workflow used to analyse the motor domains bound to microtubules is given in (Figure 4.11A). Cyt1 and Cyt1^{RK+7hep} datasets were processed separately, but according to the same protocol. To perform 2D classification on the motor domains, the microtubules need to be oriented in the same way. I boxed each microtubule into a new image, determined its polarity, and rotated it to orient it with the plus-end at the right. I then manually picked motor domain particles in Relion, centering on the point where the stalk and microtubule meet (Figure 4.11B). Particles were excluded if they overlapped with other motors, or if the kink at the base of the stalk was not visible (indicating that the particle was not lying flat in the plane of the image). I aligned all the particles from one dataset by performing 2D classification into a single class. This resulted in a blurred average motor domain density above the microtubule (Figure 4.11C)

I performed focussed sub-classification to resolve discrete conformations of the motor domain from the overall average (**Figure 4.12A-C**). This is a common technique in which a 2D mask is applied during 2D classification so that the signal from only a specified subregion is influencing classification. I masked out everything except the blurred motor domain (**Figure 4.12B**). Subsequent 2D classification (with fixed orientations) is therefore not influenced by the microtubule (whose signal dominates the full 2D classification), and can find classes of particles in the same orientation (**Figure 4.12C**).

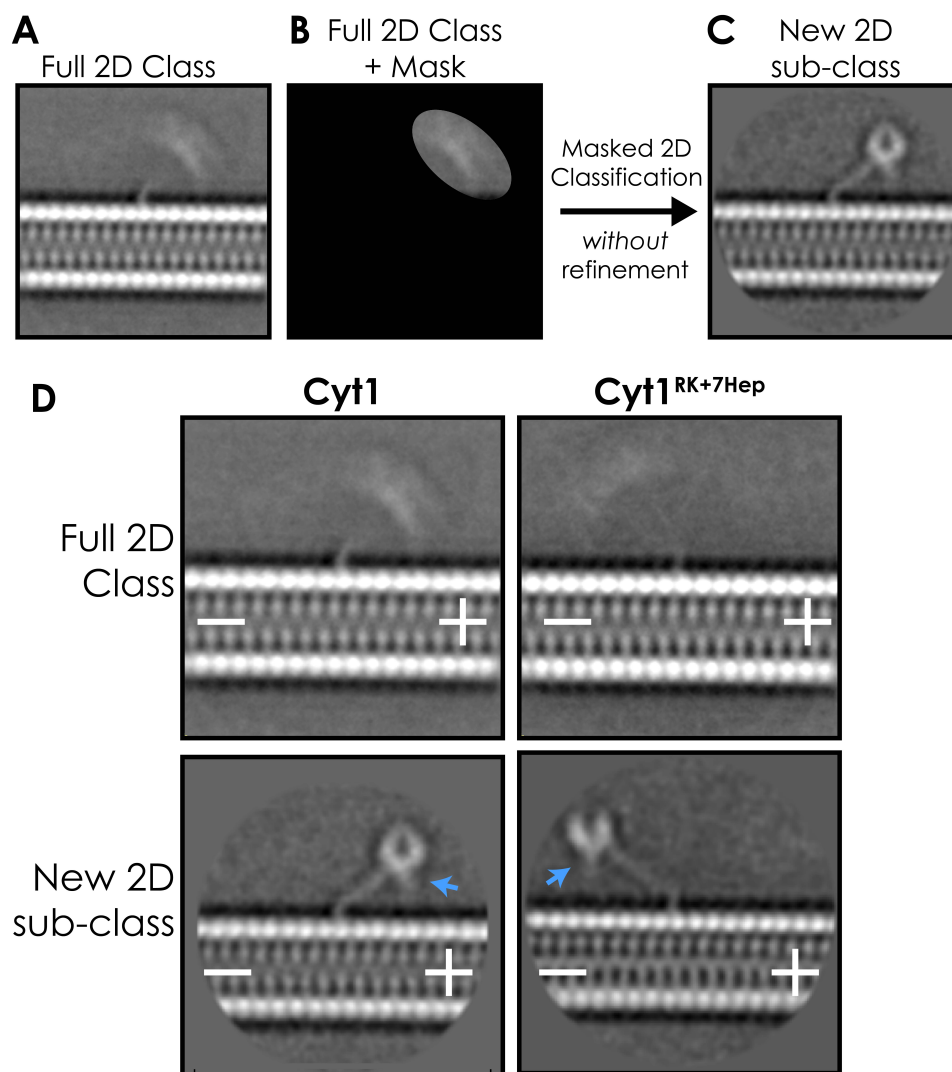


Figure 4.12 - Focussed sub-classification of Cyt1 and Cyt1^{RK+7hep}

A-C Focused sub-classification overview. A 2D mask (**B**) was applied to the full 2D class (**A**) to only include density from the motor domains. Subsequent 2D classification with the mask applied but without refinements (i.e. with fixed orientations) resolves discrete conformations of the motor (**C**). **D** - Full 2D class and new 2D sub-classes following focused sub-classification for Cyt1 and Cyt1^{RK+7hep}. Density attributed to linker domain indicated by blue arrow

As expected, Cyt1 classes had plus-end angled stalks, and density for the linker domain positioned below the ring (**Figure 4.12D**). Only one good class resulted from sub-classification of Cyt1^{RK+7hep} motors (**Figure 4.12D**). This is likely due to the longer stalk length in Cyt1^{RK+7hep}, meaning that an equivalent change in stalk angle results in a greater displacement of the motor, making superposition less likely. The Cyt1^{RK+7hep} class had a minus-end angled stalk, and the linker domain below the ring.

I wanted to confirm that the stalk angle is consistently reversed in Cyt1^{RK+7hep}, and not just in the particles contributing to the resolved sub-class. I measured the stalk angle relative to the microtubule in each particle. Plotting the stalk angle measurements as a histogram (**Figure 4.13A**) shows that 95% of the Cyt1 stalks pointed towards the microtubule plus-end, with an average stalk angle of $55 \pm 26^\circ$, consistent with previous studies (Imai et al., 2015). In comparison, the stalk angle was reversed in 75% of the Cyt1^{RK+7hep} particles, with an average of $111 \pm 35^\circ$. As such, the Cyt1^{RK+7hep} modifications increase the variability in stalk angle, but a clear reversal towards the minus-end is observed in the majority of particles.

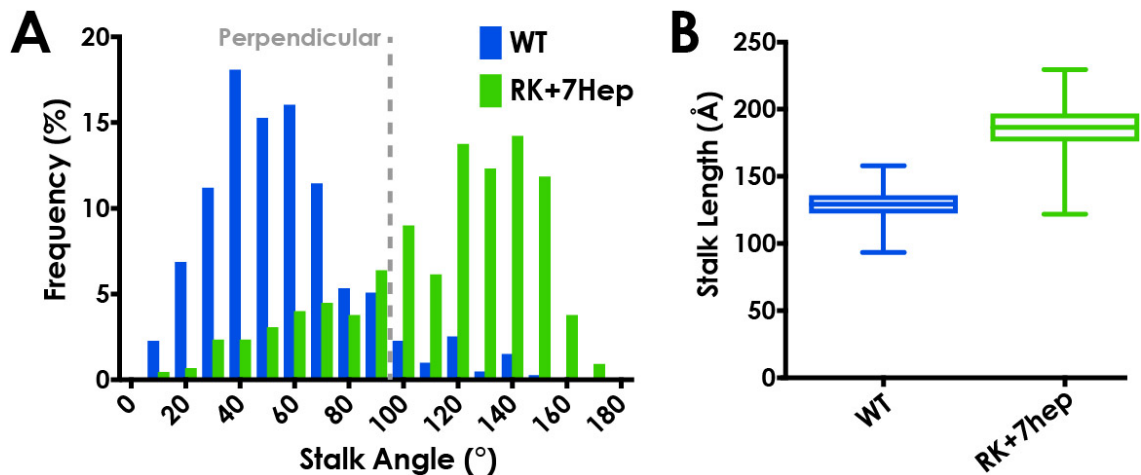


Figure 4.13 - Quantification of motor domain stalk angles and stalk lengths

A - Histogram of Cyt1-MD and Cyt1^{RK+7hep}-MD stalk angles. 95% of Cyt1-MD stalks point towards the microtubule plus-end. 75% of Cyt1^{RK+7hep}-MD points in the opposite direction, indicating that the stalk has been flipped as predicted (0° is pointing fully towards MT plus-end, 90° is perpendicular to MT, 180° is pointing fully towards MT minus-end.) (N= 392 for Cyt1-MD, 421 for Cyt1^{RK+7hep}-MD **B** - Plot of stalk length measurements in Cyt1-MD and Cyt1^{RK+7hep}-MD particles.

The observed stalk angle in 2D projections could be inaccurate if the stalk is not lying in the plane of the image. To verify that the stalks were indeed lying in the plane of the image, I measured length of the stalk for each particle (**Figure 4.13B**). If the stalk length were

significantly shorter than the predicted values, it would suggest that some of the particles were not true side views. In both Cyt1 and Cyt1^{RK+7hep}, the stalk lengths were slightly shorter than the values predicted from crystal structures of molecular dynamics simulations (Cyt1 = 12.7±1.2nm measured, 13.8nm predicted; Cyt1^{RK+7hep} = 18.5±1.9nm measured, 20.9±0.2nm predicted). This meant that Cyt1 and Cyt1^{RK+7hep} were both 9% shorter than predicted. As such, both are being imaged at an equivalent angle.

4.2.8 The AAA+ ring of Cyt1^{RK+7hep}-MD is rotated 180° compared to wild-type

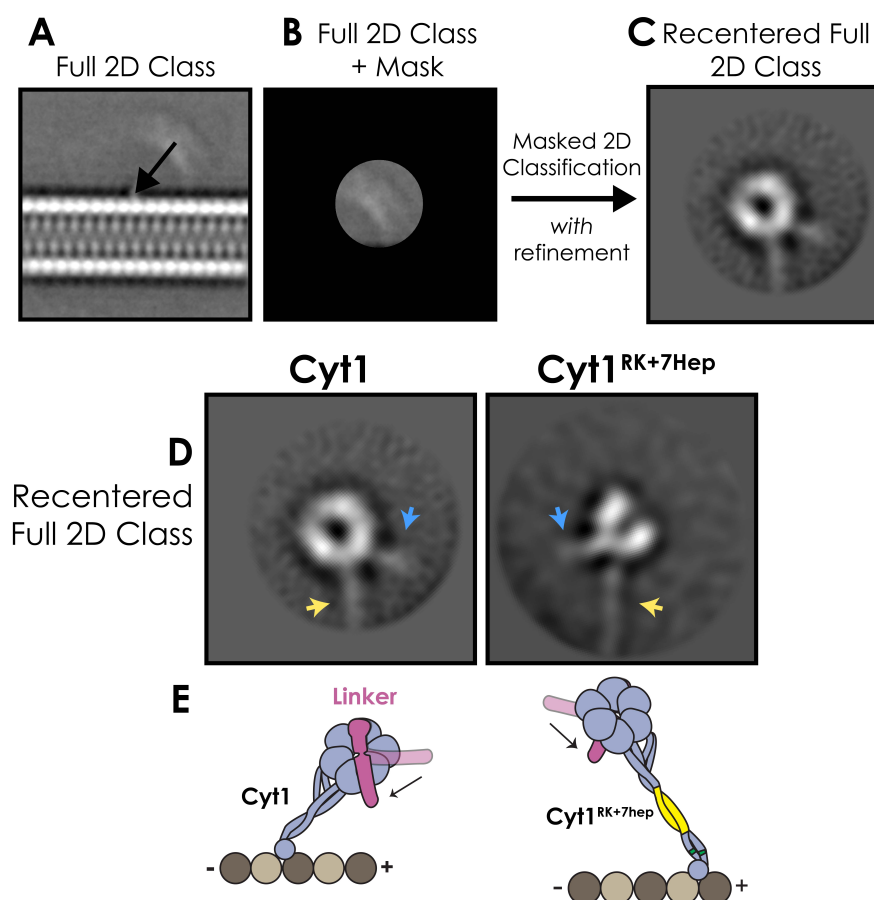


Figure 4.14 - 2D classification of the Cyt1 and Cyt1^{RK+7hep} AAA+ ring

A-C - Classification strategy to average the AAA+ ring in Cyt1 and Cyt1^{RK+7hep}. **A** - The particles in the full 2D class are recentered with the region corresponding to the AAA+ ring at the center. **B** - A tight 2D mask is applied to the center of the image to mask out the microtubule density. **C** - 2D classification with refinements but into a single class aligns the AAA+ ring in each particle. **D** - Results of this procedure for Cyt1 and Cyt1^{RK+7hep}. Linker and stalk density indicated with blue and yellow arrows respectively. **E** - Cartoon depicting the predicted conformation of Cyt1 and Cyt1^{RK+7hep} on the microtubule, according to MD simulation.

I next wanted to confirm that the 7-heptad insertion has the desired effect of flipping the motor ring in every particle and not just in the particles contributing the sub-class. I recentered the particles in the full 2D class such that the blurry density corresponding to the motor domains was now in the centre (**Figure 4.14A**). I then performed focussed classification into a single class, with refinement, to align the motor domain in each of the particles (**Figure 4.14B-C**). In the resulting Cyt1 class the linker is positioned to the right of the stalk, as expected (**Figure 4.14E**). In the equivalent class of Cyt1^{RK+7hep}, the linker is now on the left of the stalk, consistent with a 180° rotation in the stalk (**Figure 4.14E**). As such, the two modifications are both confirmed to have had the desired effect, and dynein constructs with both the reverse-kink and 7-heptad stalk insertions will have a plus-end directed LSV

4.2.9 A crescent shaped AAA+ ring in Cyt1^{RK+7hep}-MD can be explained by a separate rotation

I observed that the ring of the Cyt1^{RK+7hep} motor domain class appeared different to Cyt1 (**Figure 4.14D**). Specifically, it appeared to be a crescent rather than a single continuous ring. I made synthetic projections of a dynein motor in a variety of conformations. The ring appears circular, as in the Cyt1 class, when the stalk is directly perpendicular to the plane of imaging (**Figure 4.15A-C**). A rotation of 32° about the MTBD (i.e. around the microtubule long axis) resulted in a crescent shaped AAA+ ring in projection, directly comparable to the Cyt1^{RK+7hep} class (**Figure 4.15D-F**). A 32° tilt would make the stalk length appear shorter, however I had already shown that the Cyt1^{RK+7hep} stalk length is consistent with molecular dynamics simulations (**Figure 4.13B**). The reason for the crescent shaped appearance is therefore unclear, and could potentially be explained by a bend in the stalk directly proximal to the ring as a result of the engineering. Nevertheless, the LSV will still point towards the plus-end, albeit with a higher off-axis component than initially expected.

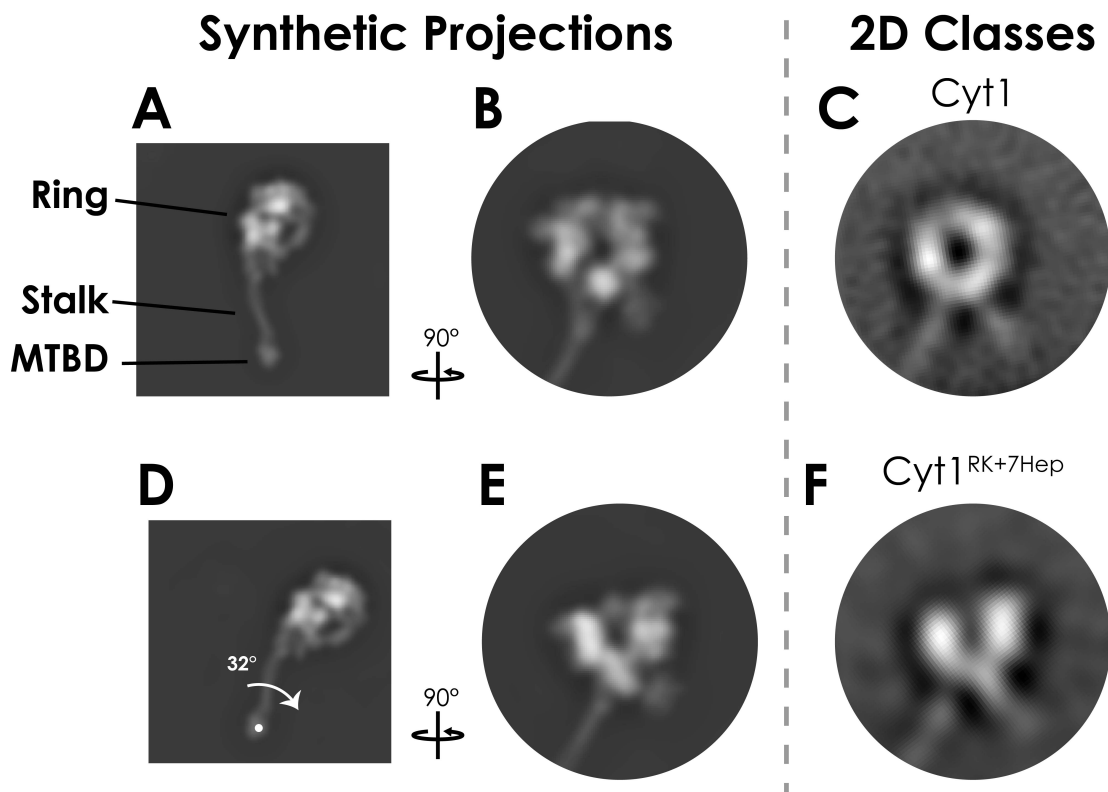


Figure 4.15 - Crescent shaped appearance of Cyt1^{RK+7hep} can be explained by a 32° rotation
A - Synthetic projection of dynein motor in profile, produced from PDB 3VKH **B** - The same view rotated 90°, showing an orientation that represents the Cyt1 motor domain class (**C**). **D** - A synthetic projection of the same motor structure rotated 32° around the MTBD. **E** - The same view rotated 90°, showing a crescent shaped AAA+ ring as in Cyt1^{RK+7hep} (**F**). Note - Cyt1^{RK+7hep} class was flipped around y axis to keep stalk and linker in same orientation as **E**.

4.3 Discussion

4.3.1 Models for directionality

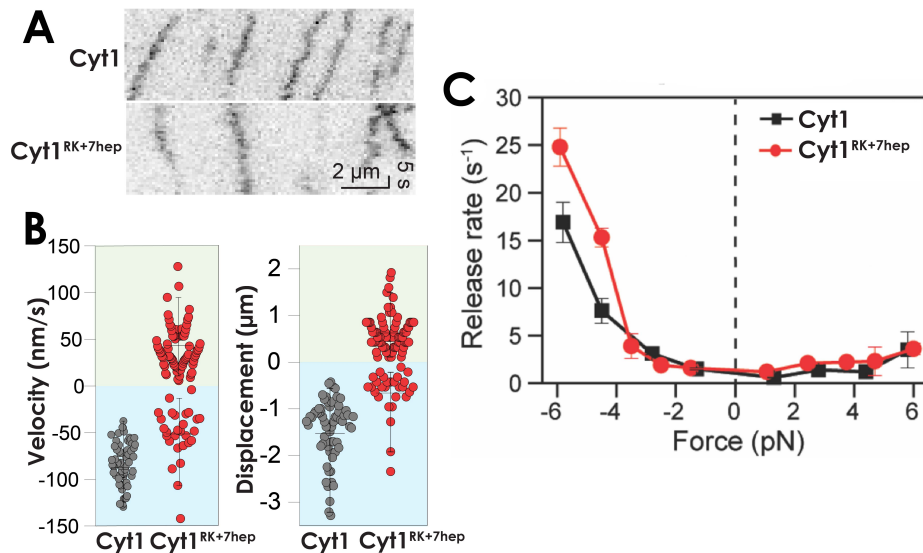


Figure 4.16 - Dyn^{RK+7hep} walks towards the microtubule plus-end

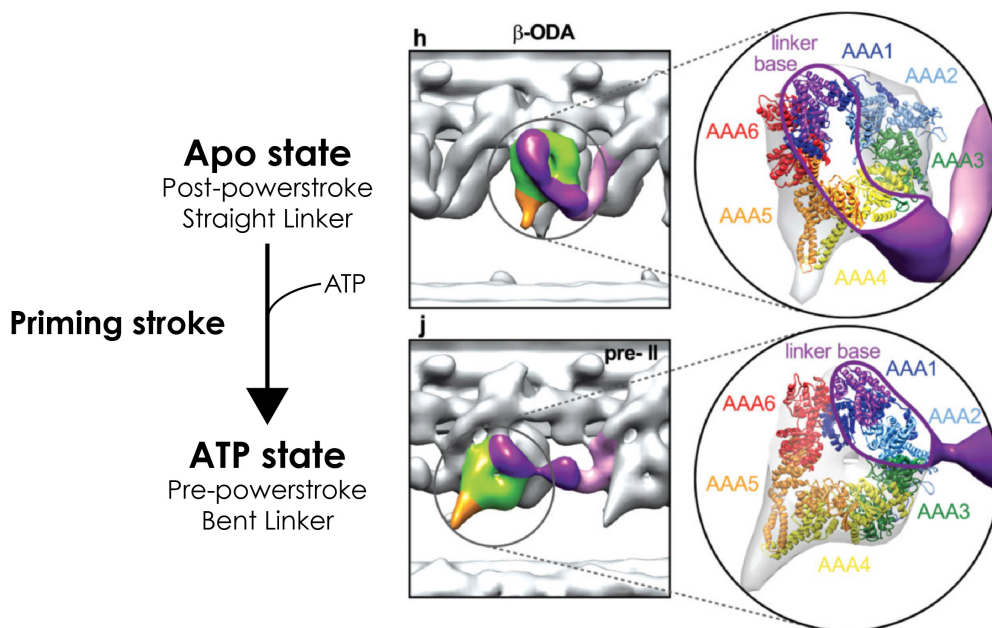
A - Kymograph of single-molecule motility assays of Cyt1 and Cyt1^{RK+7hep} dimers **B** - Quantification of single molecule assays, showing that the majority of Cyt1^{RK+7hep} dimers now walk towards the plus-end of the microtubule. **C** - Response of Cyt1 and Cyt1^{RK+7hep} to forwards and backwards force applied by an optical trap. In both constructs, the motor releases quickly to forwards force (negative values, minus-end directed) and slowly to backwards force (positive values, plus-end directed). As such, the engineered motor walks to the microtubule-plus end despite still preferring minus-end directed release. **Experiments performed and figures made by Sinan Can**

Experiments by Sinan Can showed that single molecules of dimeric Cyt1^{RK+7hep} walk processively towards the plus-end of the microtubule (**Figure 4.16A/B**). 90% of Cyt1^{RK+7hep} dimers showed overall plus-end directed motility in single-molecule motility assays. As such, our data provides a structural and biophysical model for the basis of dynein directionality. The number of dimers with plus-end directed motility is consistent with the probability that both motor domains in the dimer have a plus-end (wild-type) oriented stalk (25% * 25% = 6.25%, **Figure 4.13A**). Further experiments by Sinan Can demonstrated that the Cyt1^{RK+7hep} construct showed no difference to wild-type in asymmetric release characteristics (**Figure 4.16C**). That is, it still withstood force towards the plus-end and released quickly under force towards the minus-end. As such, the LSV and asymmetric release mechanisms have been uncoupled in Cyt1^{RK+7hep}, showing that reversing the LSV direction overrides the asymmetric release. The length of the stalk and the proline residues at the base of the stalk are universally conserved

across cytoplasmic and axonemal dyneins. This suggests that all wild-type dyneins have a minus-end directed LSV, providing a universal model for dyneins directionality.

This is not to say that the asymmetric release characteristics do not contribute to dynein directionality and stepping. Dual-colour labelling of dimer dynein motors shows that the larger the distance between the two heads of a dimer, the more likely it is for the lagging head to step (DeWitt et al., 2012; Qiu et al., 2012). This suggests that there might be two modes of directionality, with the LSV influential at low inter-head distances and asymmetric release at high inter-head distances. Sinan performed high-resolution tracking of quantum dot labelled Cyt1^{RK+7hep}, and showed that it takes backwards steps (towards the minus-end) twice as frequently as wild-type Cyt1 (where backwards steps are towards the plus-end). This could be a result of the dynein preferentially releasing towards the minus-end under intramolecular strain.

It was previously doubted whether the structural elements within dynein were rigid enough to create a bias towards the minus-end. Furthermore, while the linker swing can feasibly explain how a microtubule-attached leading head can pull forwards an unattached trailing head, it is not immediately clear how the leading head can take forward steps on its own. Cryo-electron tomography of axonemal dyneins in different stages of the mechanochemical cycle revealed that the region of the linker domain proximal to the tail is surprisingly rigid (Lin et al., 2014). This meant that during the priming stroke (straight-to-bent transition), the motor domain rotated around the linker as a hinge, positioning the MTBD closer to the minus-end than when bound (**Figure 4.17**). This would mean that both the priming and the power stroke are able to create a net bias towards the minus-end of the microtubule the leading and trailing heads respectively. However, the authors note that the motor and linker domains in the axoneme are contacted by a number of other elements, meaning that the stability observed in the linker domain may not be present in cytoplasmic dynein. Others have suggested that the interaction between AAA2/3 and the linker in the bent conformation will stabilise rotation from the priming stroke (Bhabha et al., 2016).



Lin et al., NCB, 2014

Figure 4.17 - Directionality introduced in the priming stroke

Figure adapted from (Lin et al., 2014). The apo-state of axonemal dynein in cryo-ET shows a straight linker positioned over AAA3/4. Following ATP-binding, the linker bends in the priming stroke. The position of the base of the linker is unchanged, but the whole AAA+ ring rotates, positioning the stalk and MTBD closer to the minus end.

4.3.2 Motor movement

A similar combination of structural and biophysical techniques was previously used to establish the basis of kinesin directionality. Kinesins have a globular motor domain linked to a dimerising tail region by a short flexible element called the neck-linker. Nanogold labelling was used to highlight the position of the neck linker in cryo-EM of monomeric kinesin 1 motor domains bound to microtubules (Rice et al., 1999). When the motor domain was bound to an ATP mimic, the neck-linker adopted an ordered conformation pointing towards the microtubule plus-end. Conversely, similar structural work on a minus-end directed kinesin (Ncd) showed that the neck-linker was docked towards the minus-end in equivalent conditions (Endres et al., 2006). Earlier work had demonstrated that joining a plus-end directed kinesin motor domain to a minus-end directed kinesin neck-linker resulted in minus-end directed motility, and vice versa (Case et al., 1997; Endow and Waligora, 1998).

Taken together, these results indicate that the neck-linker is the key determinant of kinesin directionality. The neck-linker of a microtubule-bound motor domain forms an ordered

conformation to position the unbound head at the next binding site. Therefore, some aspects of the stepping mechanisms of kinesin and dynein are comparable. In each, the trailing head can be pulled forwards by cyclical conformational changes in a flexible element in the bound head. However, the large distance between the linker and the microtubule makes dynein stepping more variable (in terms of length and direction). By comparison, the proximity of the neck-linker to the microtubule, and its highly conserved length, tethers kinesin steps to 8nm (Yildiz et al., 2004). The shorter tether also means that the two head bound state of kinesin always has intra-head tension, creating structural asymmetries that keep the two head in coordinated asynchrony (Liu et al., 2017). Coordination between the two heads of dynein only occurs at high interhead distances (Qiu et al., 2012). It has been suggested that the stochastic nature of dynein stepping, with frequent side and backwards steps, allows it to pass obstacles on the microtubule surface (Can et al., 2014). However it is unclear why kinesin can function without sidestepping if this is the case.

Chapter 5. Investigating the recruitment of Dynein to Herpesviruses

5.1 Background

A small cohort of coiled coil cargo adaptor proteins activate dynein/dynactin into a highly processive motile complex. The best characterised of these have been shown to work in minimal *in vitro* systems (McKenney et al., 2014; Redwine et al., 2017; Schlager et al., 2014a; Urnavicius et al., 2018; Wang et al., 2018b). There are an additional group of putative activating cargo adaptors that interact with dynein and possess stretches of coiled coils, but which have not yet been shown to directly activate dynein/dynactin (Reck-Peterson et al., 2018). The discovery of these verified and candidate “activating cargo-adaptors” suggests that dynein activity is precisely regulated by its recruitment to various cellular cargoes.

Many viruses are dependent of dynein transport for part of their life cycle. Each virus has hijacked an element of the specific dynein transport system. Viruses such as Rabies are moved towards the nucleus inside endosomes (Klingen et al., 2008), utilising the endocytic pathway. Other viruses such as Human Immunodeficiency Virus (HIV), Influenza, and adenovirus are reported to directly recruit dynein from the cytoplasm for transport and uncoating (Carnes et al., 2018; Zhang et al., 2018b; Bremner et al., 2009). Herpesviruses are dependent on long-range dynein transport for delivery to the nucleus, where their DNA genome is replicated and expressed (Döhner et al., 2002b). The alpha-herpesviruses invade neural cells, and so need to be transported on the scale of millimetres down the axon of neurons to reach the nucleus (Steiner et al., 2007). They are therefore dependent on a strong and stable interaction with dynein, the nature of which is investigated in this chapter.

Alpha-herpesviruses include the human pathogens Herpes Simplex 1 and 2 (HSV1/2), Varicella zoster virus (causing chicken pox), and the porcine pathogen Pseudorabies virus (PrV). PrV is commonly used as a model system for HSV1/2 on account of their overall similarity. Disruption of dynein/dynactin by dynamitin overexpression prevents HSV1 from being transported to the nucleus (Döhner et al. 2002). Furthermore, cosedimentation assays showed that dynein is only recruited

by mature detergent purified capsids (which retain their inner tegument) and not nuclear C-capsids (which do not have tegument proteins) (Radtke et al., 2010). Fluorescent tagging and immunogold labelling identified just three tegument proteins, pUL36 (VP1/2), pUL37 and pUS3, which remain associated with the capsid during axonal transport (Granzow et al., 2005; Luxton et al., 2005, 2005)

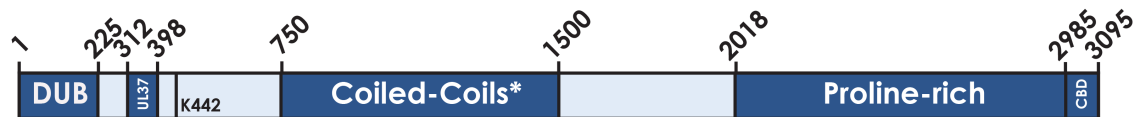


Figure 5.1 - Subdomains of pUL36

Cartoon depicting the domain organisation of PrV pUL36. DUB=Deubiquitinase domain, pUL37=UL37-binding region, K442=Lysine residue important for retrograde transport when ubiquitinated (Huffmaster et al., 2015). Coiled coils are predicted and not fully verified, although the homologous region in HSV1 pUL36 forms thin ~30nm long fibres (Scrima et al., 2015). Proline-rich region contains 28% proline residues. CBD=Capsid-binding domain

pUL36 appears to be the best candidate to recruit dynein to the virus. At 330kDa, it is the largest protein encoded in the HSV1/2 or PrV genomes. It contains multiple defined functional domains with various roles in the viral life cycle (**Figure 5.1**). An N-terminal deubiquitinase (DUB) domain acts on transcription factors to suppress the host innate immune response, and on itself to modulate capsid transport behaviour (Lee et al., 2009; Huffmaster et al., 2015; Ye et al., 2017). A C-terminal capsid-binding domain (CBD) anchors UL36 and its network of interaction partners (e.g UL37, VP16) to the capsid (Coller et al., 2007; Klupp et al., 2002; Owen et al., 2015; Schipke et al., 2012). UL36 is one of the only viral proteins that binds to the capsid, and so is responsible to a large degree for recruiting the tegument during assembly (Owen et al., 2015). Stretches of proline rich regions are present in both HSV1 and PrV UL36, but are the source of the highest variation in sequence between the two species. Their function is unclear, and have been described as both non-essential (Böttcher et al., 2006) and important for retrograde transport (Zaichick et al., 2013). The central regions of UL36 are made up of predicted structural coiled-coils, presumably responsible for projecting the protein away from the core of the capsid (Scrima et al., 2015).

Immunoprecipitation performed with pUL36 expressed in HEK293 cells in the absence of any other viral protein identified an interaction with dynein and dynactin (Zaichick et al., 2013). Truncations of pUL36 reduced the amount of

dynactin pulled down, but a single interaction region could not be identified. Therefore, at the outset of this project the literature strongly suggested that pUL36 recruits dynein/dynactin to Herpesviruses. However, the nature of this interaction was unknown. The presence of a coiled coil rich region led to the possibility that pUL36 acts as an activating cargo adaptor for dynein.

In this chapter, I investigated the interaction between pUL36 and dynein. I purified recombinant pUL36 but showed that it does not activate dynein in the same way as activating cargo adaptors. I concluded that one or more host proteins must mediate the interaction between dynein and pUL36. I therefore moved onto a protein identification strategy, using pull-downs and mass-spectrometry to find proteins that interact with pUL36 in cells. I present preliminary evidence that pUL36 alone and in the context of HSV1 is linked to dynein through the nuclear pore component RanBP2, and discuss future strategies to validate this finding.

5.2 Results

5.2.1 Full-length pUL36 is insoluble

One way to demonstrate that a protein is an activating cargo adaptor is a single-molecule motility assay. Dynein alone or in the presence of dynactin is diffusive and non-processive on microtubules. The activating cargo adaptors interact with dynein and dynactin, and activate them into a unidirectional highly processive motile complex. If a purified protein is sufficient to activate dynein motility on its own, it can be considered an activating cargo adaptor. Therefore, my first aim was to purify pUL36 and assess its ability to activate motility in single-molecule motility TIRF assay.

In the past, short fragments of pUL36 have been recombinantly expressed and purified (Schlieker et al., 2007; Scrima et al., 2015). However, there are no reports of purified full-length pUL36. I chose to express pUL36 using the baculovirus Sf9 (*Spodoptera frugiperda*) insect cell system due to its strength in the soluble expression of large multi-domain proteins. I obtained the full-length PrV (Becker strain) UL36 sequence as a synthetic gene product in the pACEBac1 vector. This vector places UL36 under the control of the baculovirus polyhedron (polh) promoter. The pACEBac1 vector is transformed into EmBacY *E. coli* cells, which transfer the expression cassette (including the UL36 ORF and its promoter) into a bacmid at Tn7 transposition sites. As well as the UL36 expression cassette, the bacmid contains the genome of baculovirus, a *Spodoptera frugiperda* pathogen (Bieniossek et al., 2012). The modified baculovirus infects Sf9 cells and expresses the inserted protein. Cells are typically recovered 72 hours after infection, when the protein of interest is highly expressed but before most of the cells are lysed by the virus (Bieniossek et al., 2012).

For full-length pUL36 (pUL36^{FL}), I infected a 50mL Sf9 culture with the UL36^{FL} baculovirus stock, and harvested the cells after 72 hours. To test the level of expression and solubility of pUL36^{FL} I performed a small-scale purification from the cells. I resuspended the cell pellet in lysis buffer, and mechanically lysed the cells with dounce homogenisation. Next, I centrifuged the lysate to separate the soluble and insoluble fractions of the cytosol, and applied the supernatant to Strep-tactin

beads. The plasmid encodes a tandem Strep-tag at the N-terminus of UL36 for affinity purification. Strep-tactin is a modified version of streptavidin to which the Strep-tag (mimicking biotin) binds with high-affinity.

Following a 1 hour of incubation with the Strep-tactin resin, I performed desthiobiotin elution and ran samples from each stage of the purification in SDS-PAGE. A strong 330kDa band attributable to pUL36^{FL} is in the insoluble pellet fraction, and only a small amount is retained in the supernatant (**Figure 5.2**). No corresponding band is present in the elutions. These results indicate that pUL36^{FL} is mostly insoluble either in the cell or following lysis. Previously, an equivalent construct expressed in mammalian cells was inactive and diffuse (Zaichick et al., 2013). In this case, removal of the C-terminal 110 residues, corresponding to the capsid-binding domain, resulted in extensive cytoplasmic motility. I therefore set out to make this construct (UL36 residues 1-2985, hereafter UL36^{ΔCBD}), rather than attempt to optimise expression of pUL36^{FL} further.

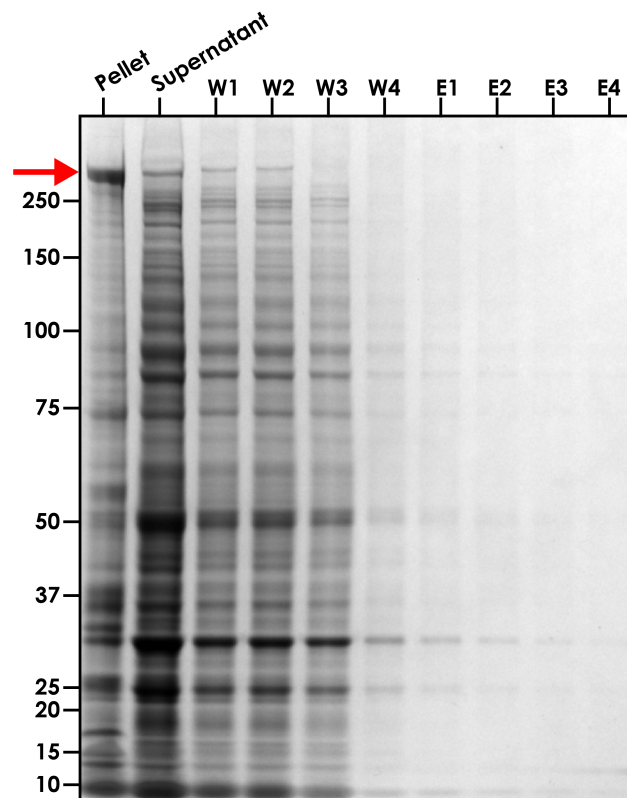


Figure 5.2 - pUL36^{FL} is almost completely insoluble following Sf9 expression
Coomassie stained SDS-PAGE of indicated fractions from small-scale pUL36^{FL} purification.
W=Wash (washing unbound protein from Strep-tactin), E=desthiobiotin Elution.

5.2.2 A modified PCR protocol used to clone UL36

To make UL36^{ACBD}, and all other UL36 constructs in this chapter, I used Gibson assembly. This is a scar free cloning technique that can join multiple DNA fragments together in a one-step reaction.

To start, PCR is used to introduce ~30 base overlaps in the ends of two fragments to be joined (**Figure 5.3A**). The user can exactly engineer the sequence of the new fusion site, potentially including point mutations, by design of the primer overlaps. The PCR fragments are mixed with a Gibson reaction mixture, which contains three enzymes. A 5' to 3' exonuclease exposes sticky ends in the fragments (**Figure 5.3B**), allowing the now exposed overlaps to anneal to each other (**Figure 5.3C**). A DNA polymerase then fills in the degraded area up to the overlap, and a ligase joins the backbone (**Figure 5.3D**).

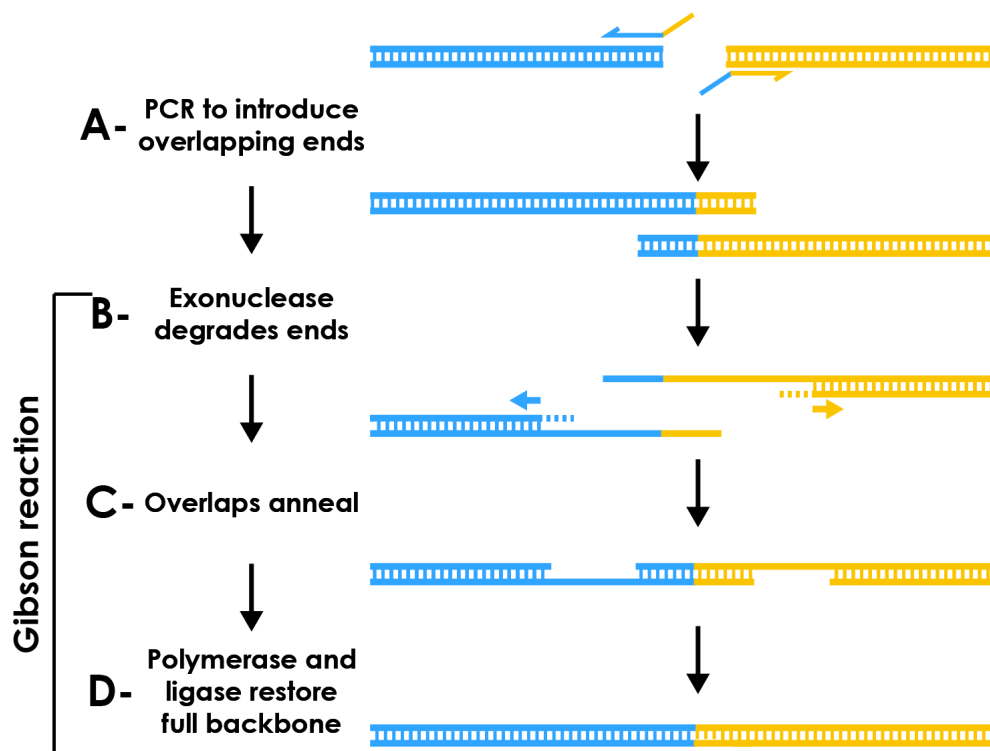


Figure 5.3 - Schematic of Gibson Cloning Protocol

A - Two fragments are PCR amplified with primers that insert sequence overlaps to the end of the other fragment. B - The first step in the Gibson reaction is a 5' exonuclease degrading the 5' end of the dsDNA, revealing sticky ends. C - The sticky ends of the two fragments are complementary due to the overlap introduced in the PCR reaction, and so they anneal. D - A DNA polymerase is primed by the new overlaps and repolymerises the degraded section, and a DNA ligase rejoins the backbone.

Gibson assembly is now established as a robust and efficient cloning technique, however it depends on the sequence of interest to be PCR amplified. The UL36 ORF contains over 9000 base pairs and is GC rich. The GC content is particularly high and repetitive in the proline rich region (**Figure 5.1**), since the four proline codons are CCX (where X is any DNA base). A long, GC-rich sequence with low-complexity regions is typically problematic in PCR due to the higher melting temperature of G/C pairs, formation of secondary structures, and complications in proofreading.

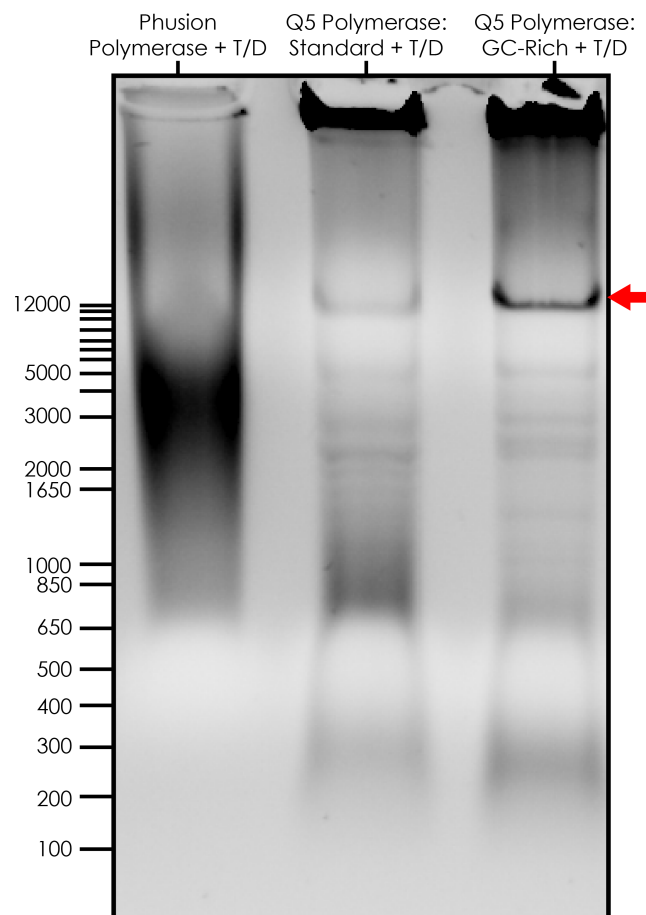


Figure 5.4 - A modified PCR protocol for UL36

*A Sybrsafe-stained agarose gel of PCR amplification of UL36 and the plasmid it is in, representative for results from all UL36 cloning, comparing different PCR protocols. **Left**, using phusion polymerase with standard buffer, **Center**, using Q5 polymerase with standard buffer, **Right**, using Q5 polymerase with its GC-rich optimised buffer. Note that all reactions were run according to the same touchdown PCR protocol.*

Accordingly, PCR amplification of the UL36 ORF using the high-fidelity Phusion polymerase failed. To improve the reaction, I utilised a modified PCR protocol called “touch-down” PCR. This involves applying a higher annealing temperature in the early iterations, and then gradually decreasing it in the later iterations. The early

iterations therefore have high stringency, preventing the build-up of shorter misprimed sequences and so creating a better platform for amplification in the later iterations. When this was performed with Phusion polymerase the reaction still failed (**Figure 5.4, left**). However, I attained a band of the correct size when I switched to Q5 polymerase, which has higher processivity than Phusion making it more capable to amplify long sequences (**Figure 5.4, centre**). The Q5 polymerase reaction buffer optimised for GC-rich sequences resulted in a more intense band (**Figure 5.4, right**). These modifications yielded consistent results for PCR amplification of UL36.

5.2.3 UL36^{ΔCBD} is soluble during affinity purification

The new UL36 construct, UL36^{ΔCBD}, consists of residues 1-2985. I also added a SNAP tag for covalent labelling with fluorescent dye when desired. I expressed it in Sf9 insect cells in a scaled up 500mL culture. Following the same purification protocol as pUL36^{FL}, some of the ~330kDa protein attributable to pUL36^{ΔCBD} still pelleted in the insoluble fraction following lysate centrifugation (**Figure 5.5A**). However, a much larger amount of protein was retained in the supernatant, indicating that pUL36^{ΔCBD} is mostly soluble (**Figure 5.5A**). Strikingly, a large proportion of pUL36^{ΔCBD} did not bind to the affinity resin and was lost in the flowthrough. The amount of protein in the elutions is much lower than would be expected if the affinity resin was saturated. This was observed in all repeats of pUL36^{ΔCBD} purification, and was invariant to the use of more strep-tactin resin, longer incubation times and lower salt concentrations. This suggests that there is a proportion of the soluble protein in which the Strep-tag is occluded. A crystal structure of the N-terminal DUB domain of pUL36 shows that the N-terminus is exposed to the surface (Schlieker et al., 2007), so the Strep-tag should also be exposed on the surface. Results presented below suggest that occlusion could potentially be mediated by an interaction between the N- and C-terminus.

The pooled elution of pUL36^{ΔCBD} typically yielded ~0.4mg from a 500mL culture. To assess the solubility of the protein, remove any impurities, and obtain a monodisperse population of pUL36 for the TIRF assays, I performed size exclusion chromatography on the concentrated eluate (**Figure 5.5B**). In the resulting elution

profile, a void peak (at 7.8mL) and a second, soluble peak (at 8.7mL) were only poorly resolved from each other. SDS-PAGE showed that both of the peaks contained the same ~330kDa protein (**Figure 5.5C**). The Superose 6 resin can separate globular proteins up to 6MDa, so for the soluble peak of pUL36^{ΔCBD} to elute so close to the void suggests that it is either highly elongated or oligomeric.

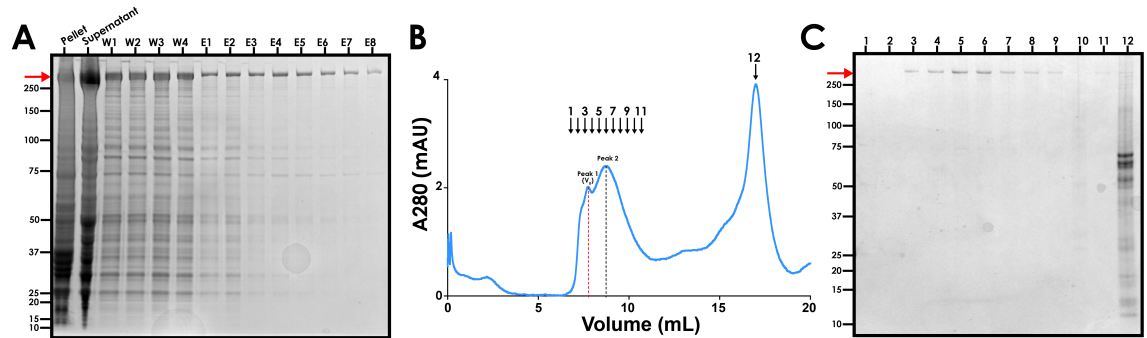


Figure 5.5 - Affinity purification and gel filtration of pUL36^{ΔCBD}

A - Coomassie stained SDS-PAGE gel of pUL36^{ΔCBD} during affinity purification (W=Wash, E=Elution). **B** - Size exclusion chromatography of pUL36^{ΔCBD} following affinity purification. Red and black dotted lines indicate the centre of the void and soluble peak respectively **C** - SDS-PAGE following gel filtration, according to the fractions as indicated in **B**.

The void peak is made by species that are too large to enter the porous resin, and can be formed by disordered aggregates of unstable protein or monodisperse species too large to be resolved. I attempted to run the sample on a G4000_{SWXL} column, which is able to resolve larger proteins than the Superose 6, but no protein was recovered. Therefore, I could not verify if the void peak was formed of a stable oligomer of pUL36^{ΔCBD} or if it was simply aggregated protein. As such, for subsequent use in the single molecule motility assay, I concentrated and froze the fractions of the second peak that did not overlap with the extrapolated void peak (Fractions 6-11, **Figure 6.5B/C**). I typically recovered 10% of the input to gel filtration (0.04mg/500mL culture)

The behaviour of pUL36^{ΔCBD} at each stage of purification suggests that it is not a very stable construct. A significant fraction is not retained on the affinity resin and the elution from size-exclusion chromatography contains a large void peak. For functional assays and structural work, it is desirable to work with a single stable homogeneous sample. As such, my next aim was to find a pUL36 construct that meets these criteria better than pUL36^{ΔCBD}.

5.2.4 N- and C-terminal truncations improve the stability of pUL36

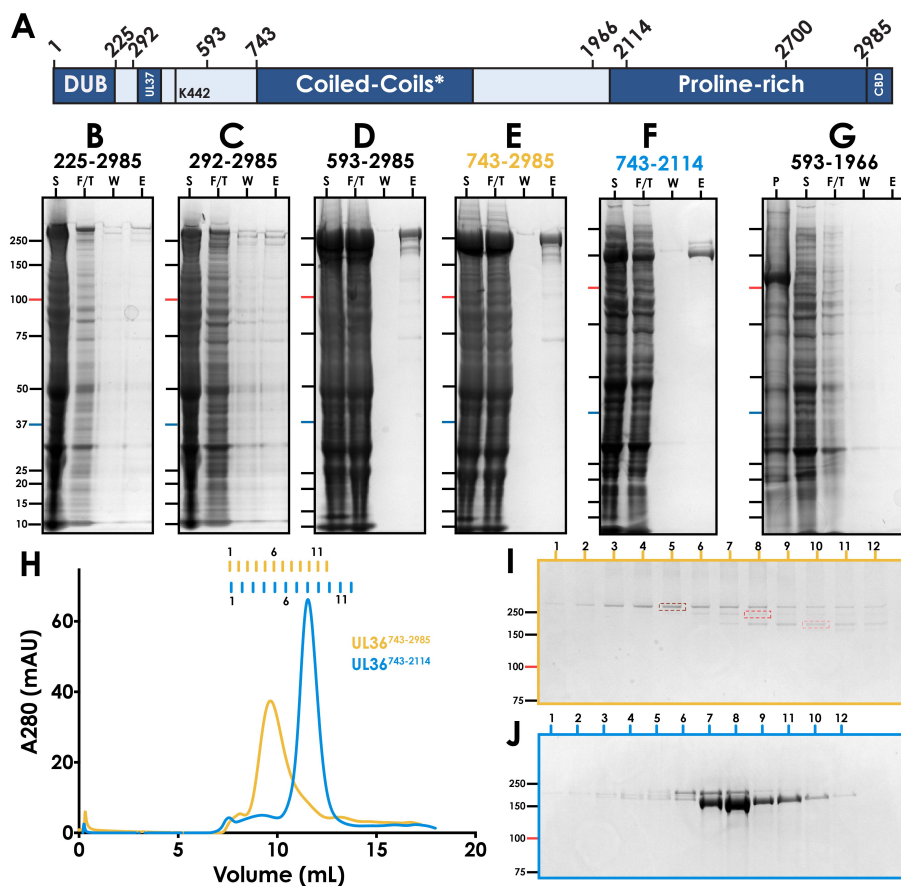


Figure 5.6 - Purification of N- and C-terminal truncations of pUL36

A - Schematic of pUL36, indicating the positions of each truncation site. **B-G** - SDS-PAGE following affinity purification of the indicated truncation construct (P=Pellet, S=Supernatant, F/T=Flowthrough, W=Wash, E=Elution). **H** - Size-exclusion chromatography traces for pUL36⁷⁴³⁻²⁹⁸⁵ (yellow) and pUL36⁷⁴³⁻²¹¹⁴ (blue). **I** - SDS-PAGE of pUL36⁷⁴³⁻²⁹⁸⁵ fractions indicated in **I**. **J** - SDS-PAGE of pUL36⁷⁴³⁻²¹¹⁴ fractions indicated in **I**.

Every activating cargo adaptor of dynein identified to date contains a coiled coil that lies at the extended interface between dynein and dynactin. Sequence analysis of UL36 has previously predicted that the central region between position 750 and 1500 (HSV1 pUL36 numbering) is likely to contain mostly coiled coils (Figure 5.1, (Scrima et al., 2015)). This region is therefore the prime candidate to interact with dynein and dynactin as an activating cargo adaptor. I made a series of N- and C-terminal truncations to remove the regions potentially introducing instability whilst retaining the central coiled coil regions (Figure 5.6A). The positions of these truncations was based on similar constructs made previously (Zaichick et al., 2013)

or in regions not predicted to have secondary structure (based on the JPred server(Drozdetskiy et al., 2015)) .

pUL36²²⁵⁻²⁹⁸⁵ and pUL36²⁹²⁻²⁹⁸⁵, both of which were used by Zaichick *et al*, were soluble but no protein eluted of the strp-tactin (**Figure 5.6B/C**). This suggests that an even greater population of these constructs has an occluded affinity tag and is unable to bind. However, further truncations from the N-terminus increased the yield of pUL36. Both pUL36⁵⁹³⁻²⁹⁸⁵ and pUL36⁷⁴³⁻²⁹⁸⁵ still lost a significant proportion of protein in the flow through, but resulted in a ~2-fold higher like-for-like yield in the elution than pUL36^{ΔCBD} (~1mg from 500mL cell pellet following affinity elution) (**Figure 5.6D/E**). I did not make truncations C-terminal to position 743 since this would start to remove the predicted coiled coil region.

Following the identification of a more stable N-terminus at positions 593 and 743, I next wanted to see if a C-terminal truncation could improve the yield further. Affinity purification of pUL36⁷⁴³⁻²¹¹⁴ resulted in a yield around 2-fold higher than pUL36⁷⁴³⁻²⁹⁸⁵ (~2m from 500mL cell pellet) (**Figure 5.6F**, less sample loaded on gel than pUL36⁷⁴³⁻²⁹⁸⁵). None of the truncation sites I tried N-terminal to position 2114 (e.g. pUL36⁵⁹³⁻¹⁹⁶⁶, **Figure 5.6G**) was stable.

Size-exclusion chromatography of pUL36⁷⁴³⁻²⁹⁸⁵ resulted in a negligible void peak, with a main soluble peak eluting at 9.7mL (**Figure 5.6H, yellow**). This is 1mL later than pUL36^{ΔCBD}, consistent with pUL36⁷⁴³⁻²⁹⁸⁵ being smaller. The main pUL36⁷⁴³⁻²⁹⁸⁵ peak had a shoulder however, and SDS-PAGE showed that this right-handed tail consists of multiple species up to 100kDa smaller than the expected 258kDa band (**Figure 5.6I**). I extracted the separated bands (**Figure 5.6I, boxes**) and sent them for identification by mass-spectrometry. For each of the species, the sequence identified closest to the N-terminus started at position 832. However, the sequence identified closest to the C-terminus got progressively earlier in the smaller molecular weight species (from 2961 in the highest band to 2634 in the lowest band). This indicates that the C-terminus is being degraded in pUL36⁷⁴³⁻²⁹⁸⁵. The C-terminal truncation site is identical in pUL36^{ΔCBD} and pUL36⁷⁴³⁻²⁹⁸⁵, however this C-terminal degradation is only observed in pUL36⁷⁴³⁻²⁹⁸⁵. This raises the intriguing

possibility that some of the N-terminal 743 residues of pUL36 interact with and stabilise the C-terminus.

pUL36⁷⁴³⁻²¹¹⁴ also lacked a void peak in gel filtration, and resulted in large soluble peak with an elution volume of 11.5mL. (Figure 5.6H, blue). SDS-PAGE showed that there were two protein bands present, however the main peak at 150kDa was significantly in excess.

Following concentration of the peak gel filtration fractions, pUL36⁷⁴³⁻²⁹⁸⁵ and pUL36⁷⁴³⁻²¹¹⁴ typically resulted in final yields of 0.2mg and 0.4mg per 500mL culture respectively. This represents a 5-10 fold increase compared to pUL36^{ACBD}. Despite the presence of impurities, they represent a more stable sample than pUL36^{ACBD} given that their soluble peaks are much larger and separated from the void peak in gel filtration.

5.2.5 pUL36⁷⁴³⁻²⁹⁸⁵ is monomeric

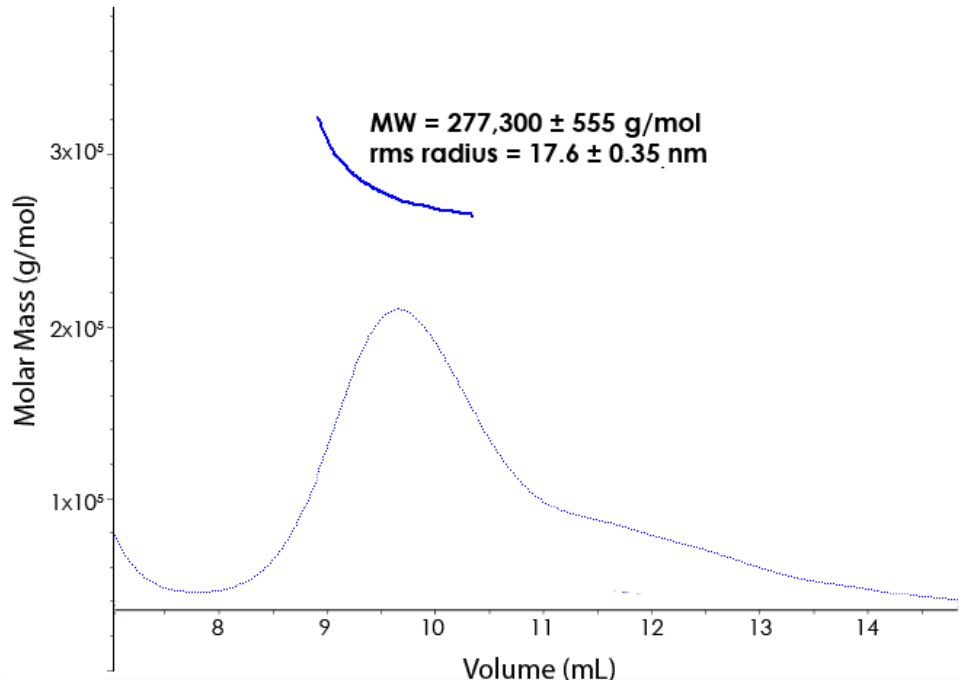


Figure 5.7 - SEC-MALS of pUL36⁷⁴³⁻²⁹⁸⁵

SEC-MALS curve of pUL36⁷⁴³⁻²⁹⁸⁵, showing continuous UV (A280) trace of pUL36⁷⁴³⁻²⁹⁸⁵ SEC elution and MALS calculated molar mass of the main pUL36⁷⁴³⁻²⁹⁸⁵ peaks (thick blue line). Molecular weight (MW) and rms radius ± calibration error of the instrument of this peak annotated.

Manufacturer calibration curves of the Superose 6 10/300 size-exclusion chromatography column suggest that a 440kDa globular protein (Ferritin) should elute at ~14mL. All pUL36 constructs I tested, which are expected to be smaller than Ferritin by molecular weight (pUL36^{ΔCBD} = 330kDa, pUL36⁷⁴³⁻²⁹⁸⁵ = 258kDa, pUL36⁷⁴³⁻²¹¹⁴ = 170kDa), elute much earlier than this (**Figure 5.5B, 5.6I**). Earlier elution in size-exclusion chromatography can be explained by oligomerisation into larger molecular weight species, or the formation of elongated conformations. I investigated the molecular weight of the pUL36⁷⁴³⁻²⁹⁸⁵ peak by Size-Exclusion Chromatography coupled to Multi-Angle Light Scattering (SEC-MALS). MALS measures the absolute molecular weight of a soluble sample by illuminating it with a collimated laser. The oscillating electromagnetic wave of the laser induces an oscillating dipole in the macromolecule, which re-radiates light at a magnitude proportional to the size of the molecule. The MALS detectors measure the amplitude of the re-radiated light to determine the molecular weight of the sample.

SEC-MALS demonstrated that the pUL36⁷⁴³⁻²⁹⁸⁵ peak is heterogeneous, given that the molecular weight is higher in the earlier sections of the peak (**Figure 5.7**). However, an average MW across the peak of 277kDa is only slightly larger than the expected monomer size of 258kDa. This indicates that pUL36⁷⁴³⁻²⁹⁸⁵ is predominantly monomeric, with only low levels of oligomerisation or aggregation occurring. A root mean square (rms) radius of 17.7nm indicates that the early SEC elution volume of pUL36⁷⁴³⁻²⁹⁸⁵, and probably pUL36^{ΔCBD}, can be explained by them being elongated particles that are less able to enter the size-exclusion resin than a compact, globular protein of the same molecular weight. I did not perform SEC-MALS on pUL36^{ΔCBD} as the overlap between the main and void peaks would convolute the results.

5.2.6 TIRF Microscopy of pUL36

I now had three constructs (pUL36^{ΔCBD}, pUL36⁷⁴³⁻²⁹⁸⁵ and pUL36⁷⁴³⁻²¹¹⁴) that I could test in the single molecule motility assay. I purified recombinant SNAP-tagged full-length dynein complexes (including accessory chains) from Sf9 cells and native dynactin from pig brains as previously described (Schlager et al., 2014a; Urnavicius et al., 2015). During the purification I fluorescently labelled the SNAP-tag of dynein

with TMR-Star. For a positive control, I also purified the well-established activating cargo adaptor BICD2N from Sf9 cells as previously described (Schlager et al., 2014a).

The assay records the movement of single dynein molecules on surface-immobilised microtubules. When dynein and dynactin are added to the TIRF chamber in the absence of an activating cargo adaptor, the dynein remains static or diffusive (**Figure 5.8A**). In kymographs (a representation of distance along microtubules vs time), the dynein molecules are mostly static, or undergo small diffusive events. When BICD2N is added (in a stoichiometric ratio of 1 Dynein : 2 Dynactin : 20 BICD2N) robust unidirectional motility is observed, as shown by diagonal lines in the kymograph (**Figure 5.8B**).

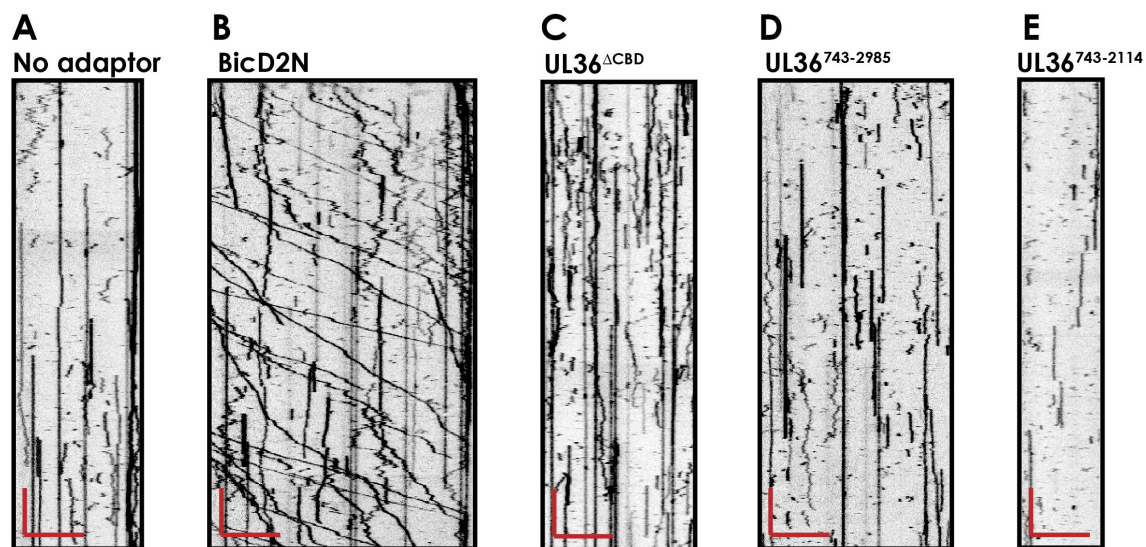


Figure 5.8 - Single Molecule motility assay of pUL36 constructs

A-E - Representative kymograph from the single molecule motility assay, using an assay mix of Dynein, Dynactin and the indicated protein. Scale bars correspond to 5 seconds (vertical) and 10 μ m (horizontal)

None of the pUL36 constructs I tested activated dynein motility in the single molecule TIRF assay. Chambers in which pUL36 ^{Δ CBD}, pUL36⁷⁴³⁻²⁹⁸⁵ or pUL36⁷⁴³⁻²¹¹⁴ had been incubated with dynein and dynactin showed no difference in motility to dynein and dynactin alone (**Figure 5.8C/D/E**). This was still the case when the concentration of each pUL36 construct was raised as high as possible during complex formation. Therefore, despite the reported interaction between pUL36 ^{Δ CBD} and dynein/dynactin when expressed in mammalian cells (Zaichick et al., 2013), these results suggest that pUL36 is not an activating cargo adaptor.

5.2.7 Colocalisation of pUL36 and activated dynein complexes

There are a wide-range of cellular mechanisms that would potentially allow pUL36 to undergo dynein-dependent transport in cells without directly activating dynein itself. The simplest of these is a “hitchhiking” model, in which pUL36 directly binds to dynein and/or dynactin away from the activating cargo adaptor binding regions. When an activating cargo adaptor activates dynein motility pUL36 would then be pulled along. I tested this model in the single-molecule motility assay by adding a fluorescent label, Alexa647, to the SNAP tag of pUL36⁷⁴³⁻²⁹⁸⁵ during purification.

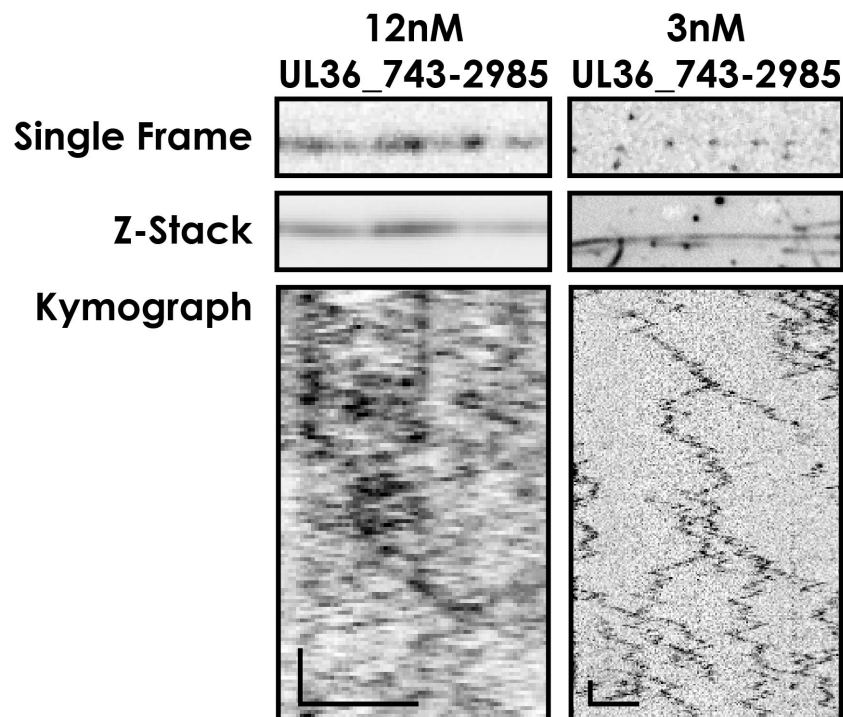


Figure 5.9 - pUL36⁷⁴³⁻²⁹⁸⁵ binds to and diffuses on microtubules

Images from single molecule TIRF assay when Alexa647-pUL36⁷⁴³⁻²⁹⁸⁵ is added to surface-immobilised microtubules. Left - 12nM pUL36 coats microtubules in single frames (20ms/frame), and single-particles are not distinguishable in the kymograph. Right - Reducing the concentration to 3nM results in distinction between single particles. Kymographs show Alexa647-pUL36⁷⁴³⁻²⁹⁸⁵ is diffuses rapidly on microtubules. Scale bars correspond to 5µm (horizontal) and 0.2 seconds (vertical)

Unexpectedly, when Alexa647-pUL36⁷⁴³⁻²⁹⁸⁵ was added to the TIRF chambers it coated the microtubules (**Figure 5.9, left**). Reducing the concentration to 3nM showed that the Alexa647-pUL36⁷⁴³⁻²⁹⁸⁵ was binding to microtubules as distinct highly diffusive particles (**Figure 5.9, right**). By comparison, the concentration of dynein used in the single-molecule assays, which leads to a comparable level of

binding as seen here (**Figure 5.8A**), is 2nM. The diffusiveness of pUL36 movement seen here (covering >10um in a matter of seconds) indicates that it is not tightly binding to the microtubule like dynein, but is instead probably “surfing” on the acidic C-terminal tails of the tubulin. An interaction between pUL36 and microtubules has not been previously reported, and it is unclear what region of pUL36 could be mediating this.

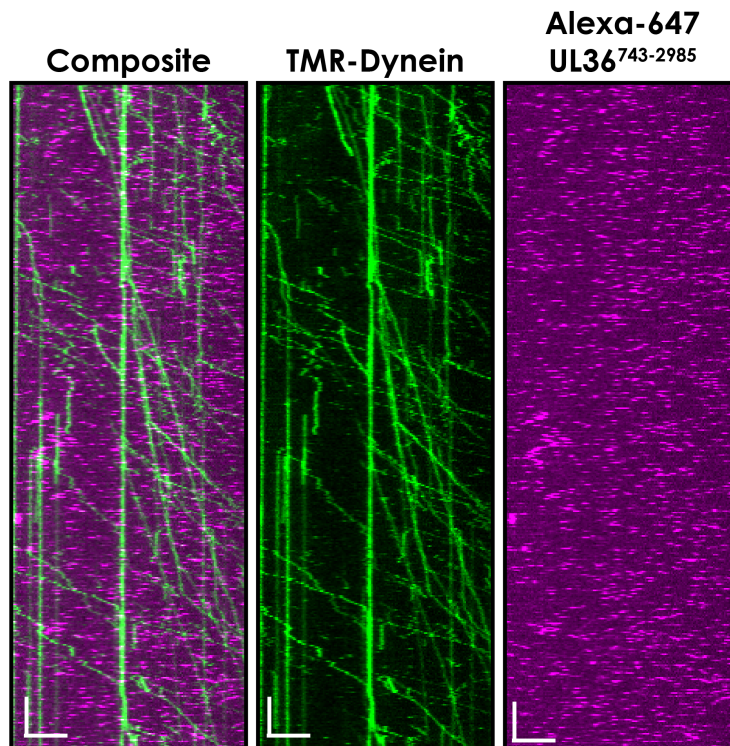


Figure 5.10 - Two-colour motility assay of TMR-Dynein and Alexa647-UL36⁷⁴³⁻²⁹⁸⁵
A representative kymograph of the TIRF motility assay in which TMR-Dynein, Dynactin, BICD2N and Alexa647-UL36⁷⁴³⁻²⁹⁸⁵ were incubated together. Dynein motility is activated by Dynactin and BICD2N, but pUL36⁷⁴³⁻²⁹⁸⁵ does not colocalise with motile complexes. Scale bars correspond to 5 seconds (vertical) and 15um (horizontal)

To test the hijacking model, I assayed a mixture of TMR- dynein, dynactin, BICD2N and Alexa647-pUL36⁷⁴³⁻²⁹⁸⁵ in the single-molecule TIRF assay. The high level of intrinsic microtubule binding of Alexa647-pUL36⁷⁴³⁻²⁹⁸⁵ made it impossible to differentiate particles colocalising with dynein at high Alexa647-pUL36⁷⁴³⁻²⁹⁸⁵ concentrations. As such, Alexa647-pUL36⁷⁴³⁻²⁹⁸⁵ was 5-fold more dilute than dynein in the complex. However, over multiple of repeat experiments, no colocalisation was observed between the dynein and pUL36 signal (**Figure 5.10**). These results suggest that pUL36 is not able to hitchhike on dynein/dynactin complexes, and is instead linked through one or many additional factors

5.2.8 $pUL36^{\Delta CBD}$ motility can be recapitulated in Vero cells

Based on these results, I concluded that pUL36 and dynein are not directly linked, and probably require additional cellular factors to mediate their interaction. Therefore, in order to continue with the reconstitution of a motile complex, I needed to switch strategies to identify these factors. As a starting point, Zaichick et al. reported that pUL36^{ΔCBD} moves with dynein in the cytoplasm of Vero cells (Zaichick et al., 2013), an adherent cell line from green African monkey (*Chlorocebus aethiops*) kidney epithelial cells. The interaction between pUL36 and dynein is therefore functional in this system. I decided to perform a pull-down of pUL36 in Vero cells followed by mass-spectrometry to identify the proteins interacting with pUL36.

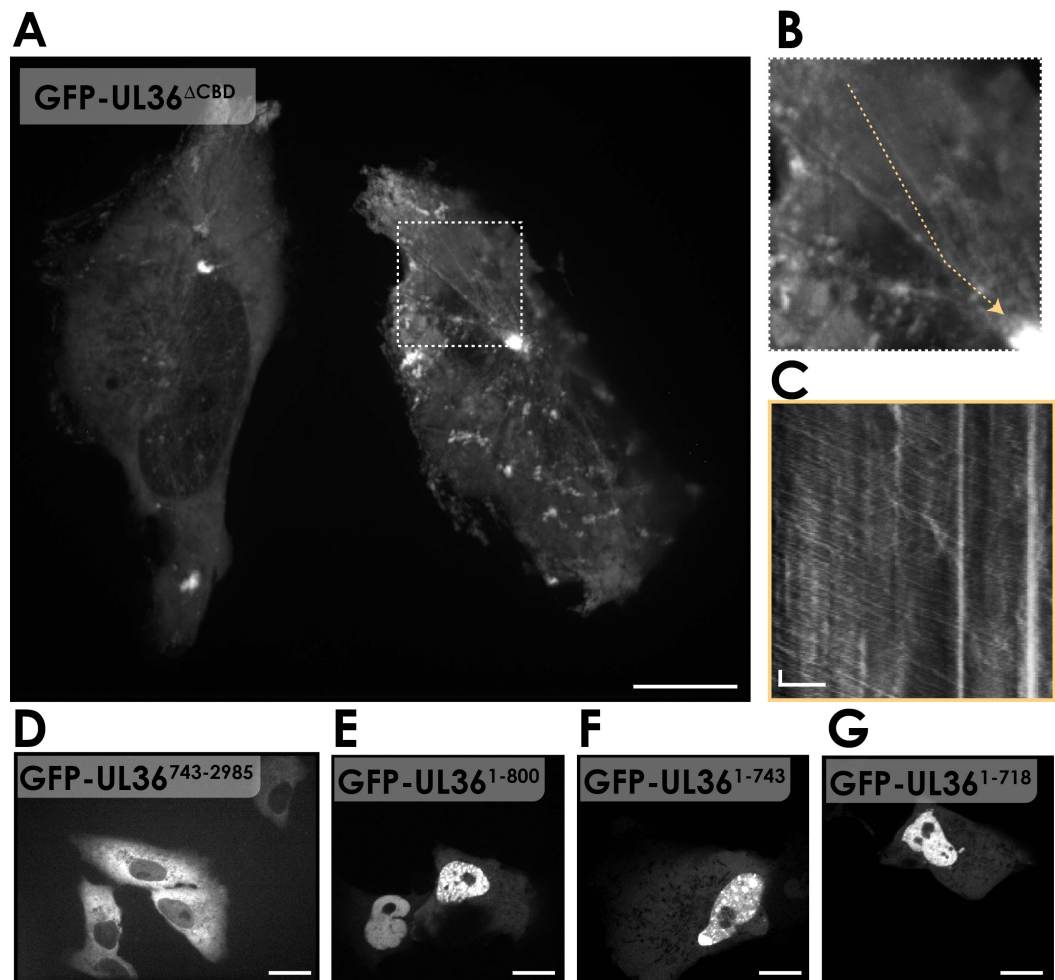


Figure 5.11 - Motility of pUL36 in Vero cells

A - Two Vero cells transfected with GFP-pUL36^{ΔCBD}, displaying cytoplasmic motility of the pUL36, imaged in spinning disk microscope. This still is the average of 30 seconds (30 frames total), and shows long filaments in the cytoplasmic corresponding to the pUL36 moving on

microtubules. Scale bar=2.5um **B** - Close up of dotted box in A, depicting these cytoplasmic filaments more clearly. **C** - Kymograph of the line drawn in B, showing unidirectional motility. (Vertical scale bar=10 seconds, horizontal scale bar=0.5um) **D-G** - Still images of pUL36 truncation constructs as indicated, displaying diffuse cytoplasmic or nuclear localisation (Scale bars=5um)

I made a construct equivalent to that used by Zaichick *et al*, containing the sequence for GFP-tagged pUL36^{ΔCBD} in the mammalian expression plasmid pcDNA4 (GFP-pUL36^{ΔCBD}). This vector places the pUL36 ORF downstream of a CMV (Cytomegalovirus) promoter for expression in mammalian cells. I imaged the transfected cells on a spinning disk microscope and assayed for cytoplasmic movement of the fluorescent protein.

Consistent with previous observations, pUL36 was highly motile in the cytoplasm of many transfected cells. A typical example is given in (**Figure 5.11A-C**). A radial array of fluorescence located on cellular filaments is visible in the cells (**Figure 5.11A-B**). Kymograph analysis shows multiple particles moving on each microtubule (**Figure 5.11C**). Movement occurs in a single direction on each microtubule, typically towards the centre of the cell. A large cluster of the GFP-pUL36^{ΔCBD} forms in the centre of these cells, suggesting that the movement was dynein-dependent.

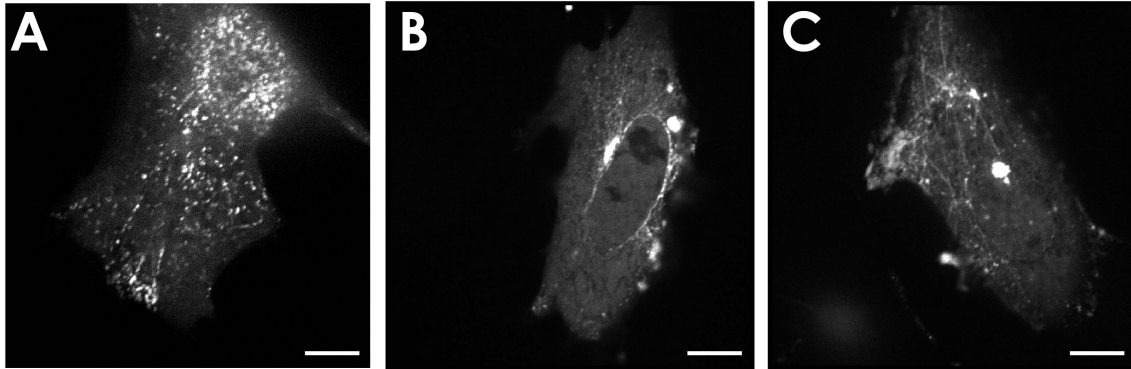
GFP-pUL36⁷⁴³⁻²⁹⁸⁵ displayed a completely diffusive distribution in the cytoplasm of Vero cells (**Figure 5.11D**). This would suggest that the region of pUL36 that recruits dynein is in the N-terminal 743 residues. However, GFP-pUL36¹⁻⁷⁴³ and other N-terminal fragments mostly localised to the nucleus, with any fluorescence in the cytoplasm being diffuse and immotile (**Figure 5.11E-G**). This could be consistent with the previous observation that pUL36 does not contain a single motif responsible for its interaction with dynein (Zaichick *et al.*, 2013). Instead, it requires sequences in both the N- and C-terminus, which potentially interact with each other based on my previous results (**Figure 5.6I**).

5.2.9 GFP-pUL36^{ΔCBD} is only motile in a subset of cells

A caveat to these results is that motility of GFP-pUL36^{ΔCBD} was highly variable in neighbouring cells. Robust microtubule motility only occurred in ~10-20% of cells, varying day-to-day (**Figure 5.12A-C**). The remaining cells displayed a number of

phenotypes. In some cells, GFP-pUL36^{ΔCBD} was distributed diffusely in the cytoplasm (**Figure 5.12D**), and occasionally in the (**Figure 5.12E**). Other cells showed the same distribution as observed in cells with motile GFP-pUL36^{ΔCBD} (bright central cluster, more fluorescence localised to cytoplasmic filaments), but did not contain any moving particles (**Figure 5.12F**). Still others were diffuse with a ring of fluorescence around the nuclear rim (**Figure 5.12G**), or only had large aggregates in the cytoplasm (**Figure 5.12H**). Finally, a common observation in both motile and non-motile cells was blebbing of the nucleus, a general sign of unhappy or dying cells (**Figure 5.12I**). The cause of this cell-to-cell variation is unknown.

GFP-UL36^{ΔCBD} Motile



GFP-UL36^{ΔCBD} Non-motile

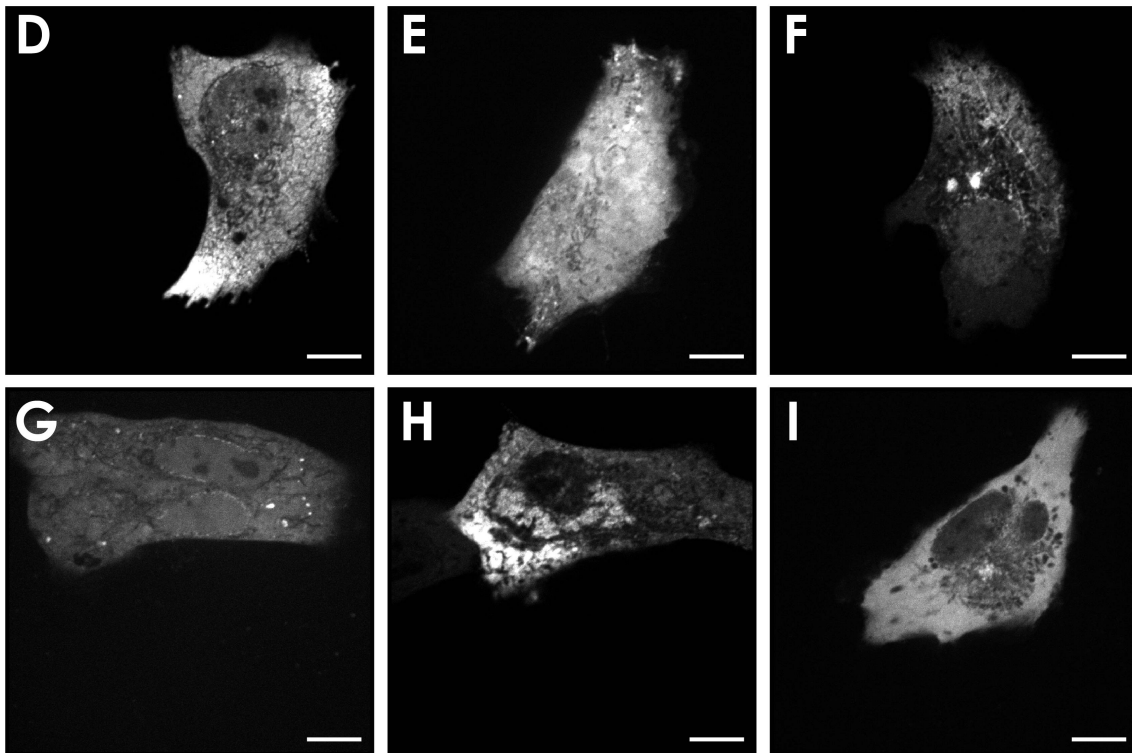


Figure 5.12 - Variability of GFP-UL36^{ΔCBD} motility in Vero cells

A-C - Single frames of Vero cells transfected with GFP-UL36^{ΔCBD} showing robust cytoplasmic motility of pUL36. D-I - Cells from the same population of transfected cells without pUL36 motility in the cytoplasm

5.2.10 Exploring methods to increase pUL36 motility in cells

As such, only a relatively small proportion of transfected cells contained GFP-pUL36^{ΔCBD} in an active motile complex. I next looked for ways to reduce the cell-to-

cell variation, in order to obtain a stronger signal in the subsequent pull-down assays.

A previous paper had highlighted a role for the N-terminal DUB domain of pUL36 in viral motility (Huffmaster et al., 2015). Retrograde transport was dependent on ubiquitination of pUL36 K442, and the DUB domain removed ubiquitin at K442. Therefore, mutation of the catalytic cysteine in the DUB active site (C26) to alanine could result in more pUL36 being ubiquitinated, and therefore more robust motility. I made a GFP-pUL36^{ΔCBD_C26A} construct and expressed it in Vero cells as before. Movement was still observed in cells transfected with GFP-pUL36^{ΔCBD_C26A} (Figure 5.13A), but the vast majority of cells showed the same non-motile phenotypes as in GFP-pUL36^{ΔCBD}. Huffmaster *et al.* showed that viruses with a K442R point mutation in pUL36, such that ubiquitin can no longer be added to this position, were unable to undergo long-range retrograde transport. Consistent with this, GFP-pUL36^{ΔCBD_K442R} bound microtubules but did not move on them (Figure 5.13B), with the exception of isolated events of bright probably aggregated punctae. This is a distinct phenotype to GFP-pUL36⁷⁴³⁻²⁹⁸⁵, which was completely diffuse (Figure 5.11D). This is an interesting result to pursue in the future, however the K442R mutation reduced rather than strengthened the interaction with dynein, and was therefore not useful for my immediate aims.

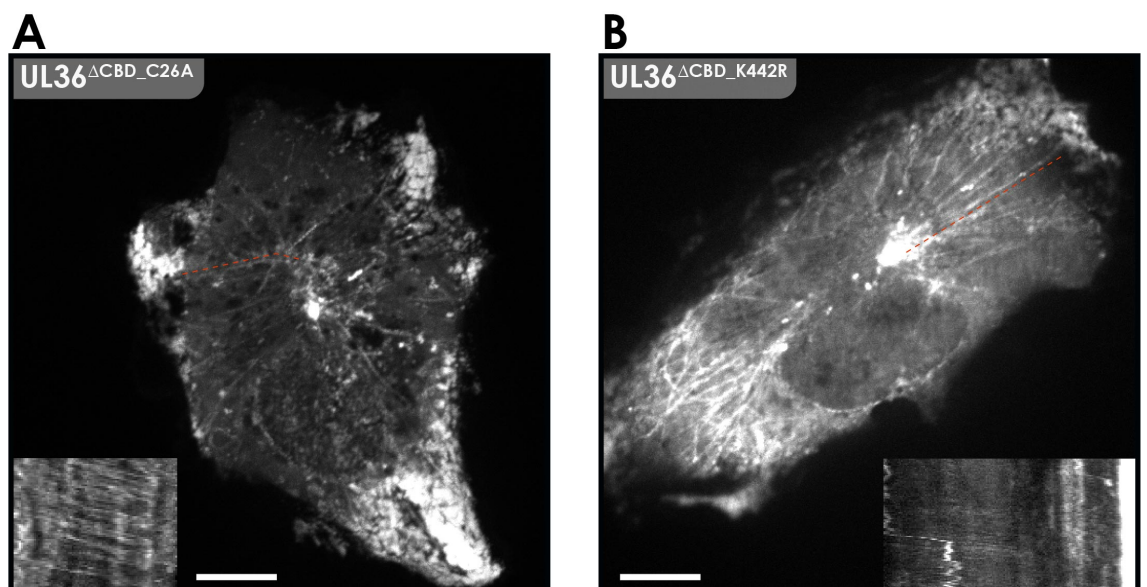


Figure 5.13 - Effect of K442 ubiquitination on pUL36 motility

A - An example of a cell transfected with pUL36^{ΔCBD_C26A} displaying cytoplasmic motility, with kymograph of microtubule indicated by red dotted line inset. **B** - No cells transfected with

pUL36^{ΔCBD_K442R} displayed cytoplasmic motility, and instead bound to microtubules without moving (kymograph of microtubule indicated by red dotted line inset).

My next strategy was to co-express pUL36 with pUL37. pUL37 is another inner tegument protein that remains attached to the capsid in the cytoplasm via its interaction with pUL36 (Luxton et al., 2005). When pUL37 is deleted, viral transport to the nucleus is slowed down or, in axons, is effectively abolished (Buch et al., 2017; Krautwald et al., 2009). Furthermore, the virus forms large aggregates within the cytoplasm in the absence of pUL37 (Klupp et al., 2002), suggesting that exposure to solvent of the pUL37-binding region in pUL36 (pUL36 residues aa312-398, **Figure 5.1**) destabilises pUL36. When I cotransfected cells with mCherry-pUL37 and GFP-pUL36^{ΔCBD}, the motility of pUL36 was abolished and only diffuse localisation was observed (**Figure 5.14**). mCherry-pUL37 was also mostly diffuse, with a small number of diffusive punctae moving in the cytoplasm as well. Given the stronger viral motility when pUL37 is present, this result was unexpected. pUL36 and pUL37 colocalised most clearly in central clusters, however how these clusters formed without cytoplasmic motility is unclear.

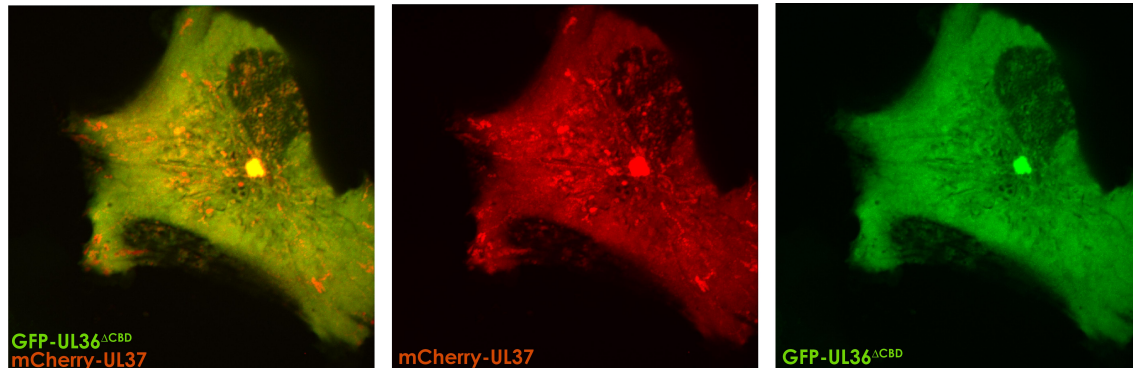


Figure 5.5.14 - pUL36^{ΔCBD} is not motile when co-expressed with pUL37

A representative cell cotransfected with GFP-pUL36^{ΔCBD} and mCherry-pUL37 (Left, composite; Centre, pUL37; Right, pUL36). Image is a maximum-intensity Z-stack of 30 frames (2 second frame interval), showing small diffusive tracks of mCherry-pUL37 movement.

I next tried a strategy employed in (Zaichick et al., 2013), where they added a hydrophobic mitochondrial targeting sequence (MTS) to the C-terminus of pUL36. The MTS is a short peptide that is recruited to the outer mitochondrial membrane, which means that the GFP-pUL36^{ΔCBD-MTS} fusion will be immobilised on mitochondria. Consistent with Zaichick *et al.*, I observed a clustering near the cell centre of both pUL36 and the mitochondria in 38.5 ± 4.0 % (of transfected cells (mean \pm standard

deviation, N=3 independent transfections, **Figure 5.15A-C**). Interestingly, in cells co-expressing GFP-pUL36^{ΔCBD-MTS} and mCherry-pUL37, a new mitochondrial morphology was observed. Mitochondria were still limited to the center of the cell, but formed an extended tubular network rather than a dense cluster (**Figure 5.15D-F**). These tubes were constantly being remodelled, undergoing phases of extension and retraction within 30 seconds (**Figure 5.15G**). This bidirectional motility suggests that pUL37 was helping recruit plus-end directed motors in addition to dynein. Whereas this is an interesting interaction in the context of the virus, the reduced dynein activity made this unsuitable for my purposes. Nevertheless, the large proportion of cells expressing GFP-pUL36^{ΔCBD-MTS} that had clustered mitochondria makes this construct highly suitable for the pull-down assays.

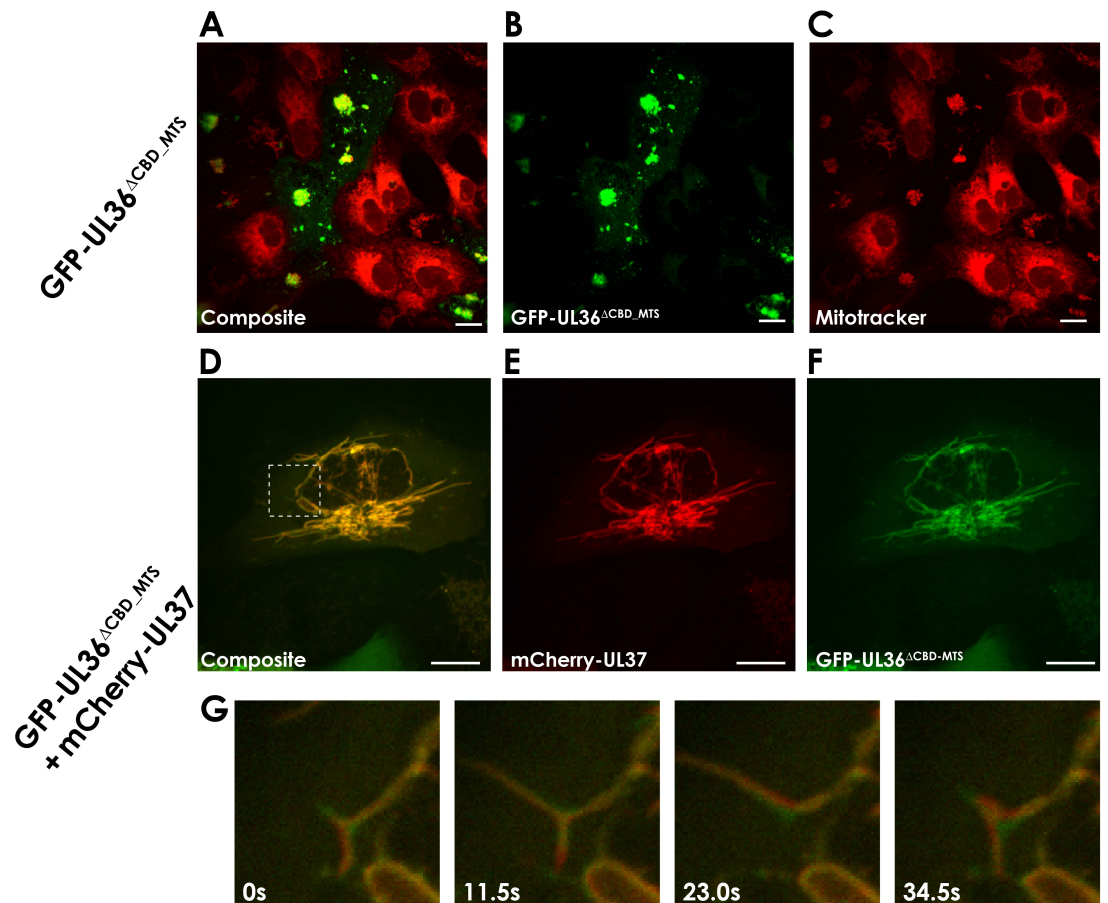


Figure 5.15 - pUL36^{ΔCBD-MTS} clusters mitochondria

A-C - Mitochondrial clustering in Vero cells transfected with GFP-pUL36^{ΔCBD-MTS} (Left, composite; Centre, GFP-pUL36; Right, Mitotracker-647, a specific live-cell dye for mitochondria), single frames. Scale=5um **D-E** - Mitochondria cluster when mCherry-pUL37 is coexpressed with GFP-pUL36^{ΔCBD-MTS}, but long dynamic tubular extensions from the central cluster form. Scale=2.5um **G** - A time series of the area indicated in D, showing the extension and retraction of one of the mitochondrial tubes

5.2.11 pUL36 constructs used for pull-downs

I took GFP-pUL36^{ΔCBD} and GFP-pUL36^{ΔCBD-MTS} forward for pulldown assays as these constructs exhibited the most promising behaviour consistent with dynein activity. I performed repeat pull-downs with the two constructs in order to validate hits between the two systems.

My transfections of pUL36 into Vero cells generally achieved a transfection efficiency of only ~20%, probably due to the large size of the plasmid (15kb). Low transfection efficiency leads to a weaker pull-down, since less of the protein of interest is expressed. For GFP-pUL36^{ΔCBD-MTS} I increased the transfection efficiency by switching to HeLa cells, in which the same transfection protocol resulted in 60-70% efficiency. The GFP-pUL36^{ΔCBD-MTS} construct is equally active in human cell lines, however pUL36^{ΔCBD} was inactive (diffuse) in all human cell lines I tested (**Figure 5.16**). The reason for this discrepancy is unclear. For pulldowns with GFP-pUL36^{ΔCBD} I used the Neon electroporation system to increase the transfection efficiency into Vero cells.

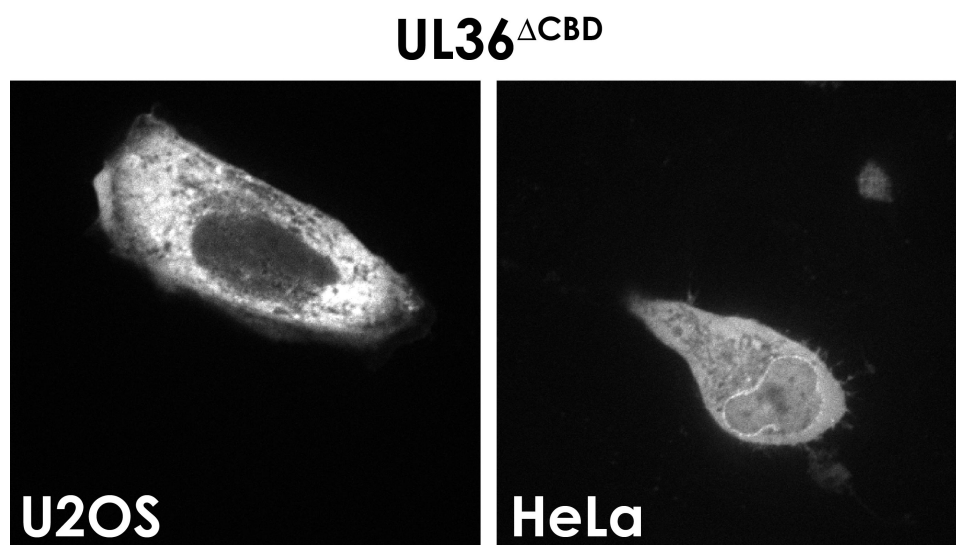


Figure 5.16 - pUL36^{ΔCBD} is immotile in human cell lines

Human cell lines (as indicated) transfected with pUL36^{ΔCBD} show only a diffuse distribution, with no cytoplasmic motility

5.2.12 Optimisation of GFP-trap pull-downs to reduce background binding

I first optimised conditions for the pull-down for GFP-pUL36^{ΔCBD-MTS} in HeLa cells. I wanted to use a low-salt buffer in order to retain as many interactions as possible,

however this could result in a higher background signal. As a negative control, I transfected cells with the same plasmid expressing GFP^{MTS} only. I harvested cells with a cell scraper 18 hours after transfection. I washed the cells in PBS, and detergent lysed them in a buffer containing 0.1% NP-40 and 50mM KCl. The lysate was cleared by centrifugation, and I normalised the total protein concentration of each sample by dilution with lysis buffer in order to maintain equivalency between repeats. I then incubated the supernatants with magnetic GFP-trap resin for three hours. GFP-trap is an anti-GFP nanobody that will bind GFP-tagged proteins, conjugated to magnetic resin for quick and consistent separation. Next, I washed the resin three times in lysis buffer and added SDS-PAGE loading buffer. As SDS is an ionic detergent it denatures any proteins attached to the beads, effectively making this the elution. I ran the samples on SDS-PAGE and analysed by Western blot for the dynactin subunit p150.

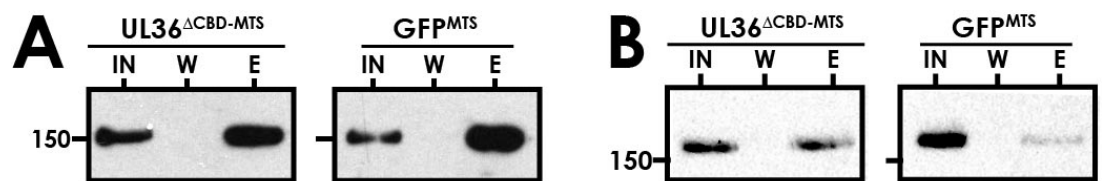


Figure 5.17 - Optimisation of pUL36^{ΔCBD-MTS} pull-down assay

A - Western blot for p150 of the pull-down according to the initial protocol (IN=Input (normalised supernatant), W = Final wash, E= elution). **B** - Equivalent Western blot following optimisation of the pull-down protocol to remove background binding.

Initially using this protocol the amount of p150 pulled down was the same for GFP-pUL36^{ΔCBD-MTS} as for GFP^{MTS} (**Figure 5.17A**). This is not surprising given that the salt concentration is so low. Through trial and error, I reduced the amount of background binding with some modifications to the above protocol. The most important was blocking the GFP-trap resin with a 1% Bovine Serum Albumin (BSA) solution for 1 hour. The BSA binds non-specifically to the resin, effectively saturating the surfaces to which the proteins in the lysate were binding non-specifically. Furthermore, reducing the resin incubation time to 1 hour (from 3) and performing a 4th wash reduce the amount of background binding further. With these modifications, I observe 6-fold stronger pull-down efficiency of p150 with GFP-pUL36^{ΔCBD-MTS} compared to GFP^{MTS}, as measured by band intensity in FIJI (**Figure 5.17B**).

5.2.13 pUL36^{ΔCBD-MTS} pull-down and mass-spectrometry

I performed the pUL36^{ΔCBD-MTS} (and GFP^{MTS} control) pulldown in triplicate. I transfected HeLa cells and performed the pulldowns after 18 hours in parallel. Following SDS-PAGE and coomassie blue staining (**Figure 5.18**), I cut each of the lanes into 20 segments and sent them to Farida Begum in the LMB mass-spectrometry facility for protein identification. She trypsinised the samples, and identified the sequence of the resulting fragments by tandem mass-spectrometry. The fragments were then cross-referenced against a human library of protein sequences and matched to a specific protein.

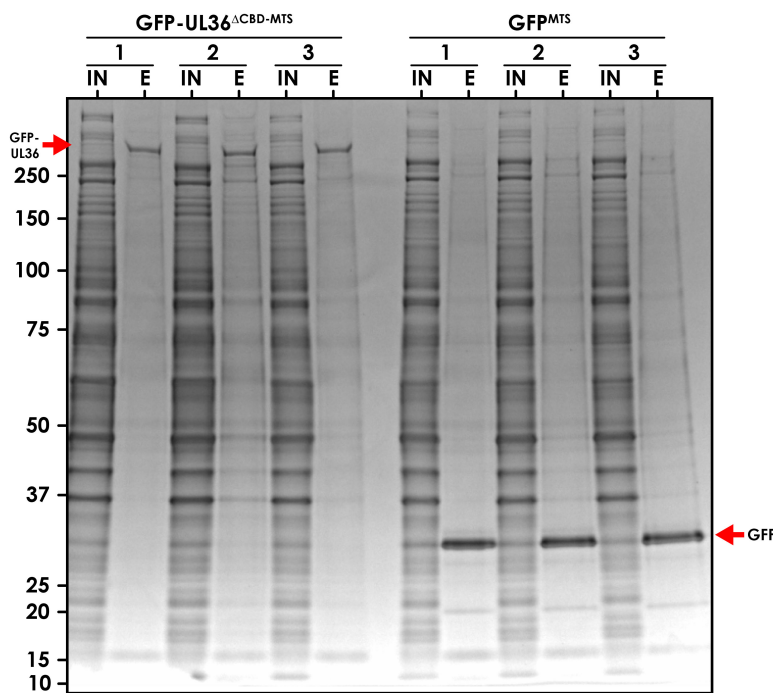


Figure 5.18 - Triplicate pull-down of pUL36^{ΔCBD-MTS} in HeLa cells

Coomassie stained SDS-PAGE gel showing the input (IN, normalised supernatant) and Elution (E, boiled beads) of the three repeat pull-downs of pUL36^{ΔCBD-MTS} and GFP^{MTS} from HeLa cells. Elution lanes cut cut out and sent for mass-spectrometry

The results from this analysis are semi-quantitative, in that the more of a protein there is present the more fragments you are likely to recover. However, each protein will result in different numbers and sizes of trypsin fragments, some of which may not be amenable to the electrospray ionisation at the start of the MS process. For each protein identified, I took the average normalised spectral

abundance factor (NSAF) over each of the three repeats. The NSAF is calculated as the number of identified fragments divided by the length of the protein, and then divided by the sum of this value for every protein (Zhu et al., 2010). It therefore corrects for the fact that longer proteins are more likely to have more fragments identified, and is the most reliable metric to measure protein abundance with this experimental set-up. Proteins were sorted by fold-enrichment compared to GFP^{MTS} (Figure 5.19). The proteins with no equivalents found in the GFP^{MTS} pull-down were separately ranked by average NSAF.

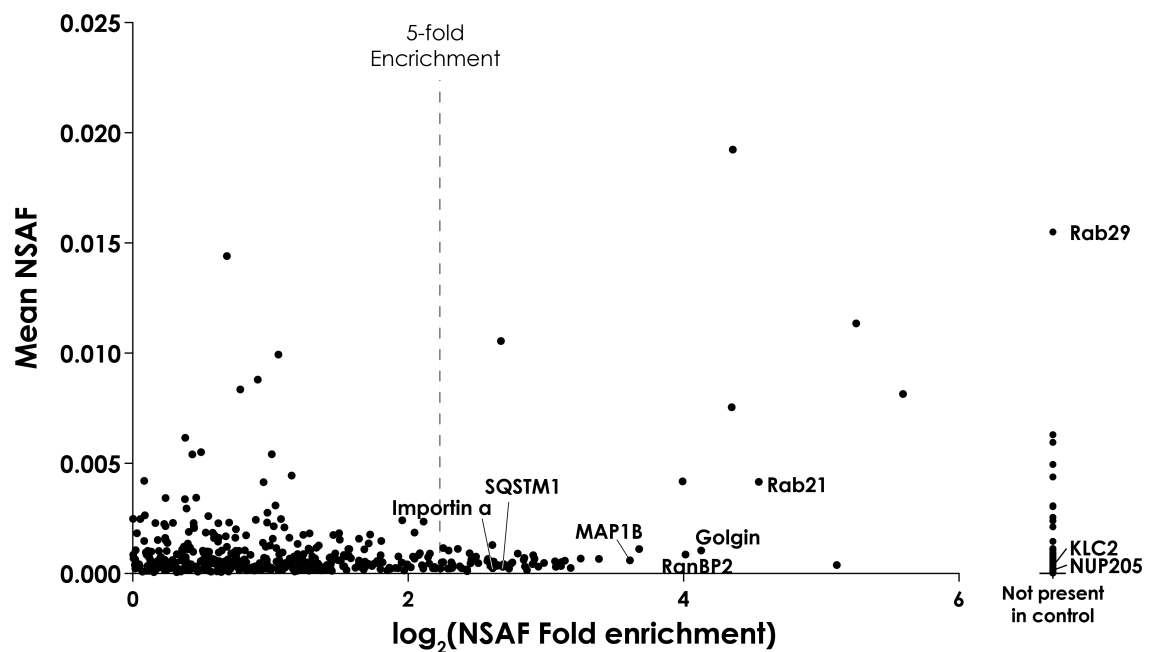


Figure 5.19 - Proteins enriched in pUL36^{ACBD-MTS} pull-down mass-spectrometry

A plot of mean NSAF value against NSAF fold-enrichment compared to negative control for the pUL36^{ACBD-MTS} HeLa pull-down. Each identified protein is represented by a single point, with cytoskeleton- or dynein-related proteins annotated

57 proteins were enriched more than 5-fold compared to the negative control (Figure 5.19). A further 395 proteins were identified in the pUL36^{ACBD-MTS} sample that were not identified in the negative control (Figure 5.19). The majority of enriched targets were ribosomal, mitochondrial, and metabolic proteins. I therefore selected the enriched targets for further analysis based on their association with the cytoskeleton, or if they are thought to interact with dynein.

Two Rab GTPases were identified in the screen. Rab21 was enriched 23-fold, and Rab29 was the most abundant protein sample identified for pUL36^{ACBD-MTS} but not

GFP^{MTS} (**Figure 5.19**). Rab proteins often link activating dynein cargo adaptors to the membranes of cellular compartments (Reck-Peterson et al., 2018). Rab21 is primarily associated with endosomal trafficking when internalising activated integrin receptors, however it has not been shown to interact with the dynein machinery (Simpson et al., 2004). Rab29 is involved in trafficking from the endosome to the trans-Golgi network (Wang et al., 2014b).

Another group of potentially significant hits are based around the nuclear pore complex. RanBP2 (NUP358), Nup205 and Importin subunit α were all enriched in the GFP-pUL36^{MTS} sample. Herpesviruses are known to dock at the nuclear pore through an interaction with pUL36 before injecting the genome into the nucleus (Copeland et al., 2009; Padeloup et al., 2009). However, RanBP2 has been shown to interact with BICD2 during G2 phase, recruiting dynein to ensure the nucleus is in the correct position prior to mitosis (Splinter et al., 2010b). Furthermore, importins can form retrograde complexes with damage signalling and dynein/dynactin in neurons (Hanz et al., 2003).

Another dynein-associated protein identified by mass-spectrometry is Sequestosome-1 (SQSTM1/p62). This protein is thought to bind to aggregated proteins as well as dynein, in order to move the protein to the cell centre as part of the aggresome pathway to degraded misfolded proteins (Calderilla-Barbosa et al., 2014). A few kinesin-associated proteins (KLC2, ensconsin) were also found.

A small cohort of dynein or dynactin subunits was identified in the pull-downs. DLIC2, DLIC1 and DCTN2 (dynactin subunit p50) were all found in the pUL36^{ACBD_MTS} pull-down, with no dynein/dynactin subunits found in the negative control. However, they all ranked below the top 150 in terms of 'abundance'. DCTN1 (dynactin subunit p150) was 2.7-fold enriched compared to GFP, and DYNC1H1 (dynein heavy chain 1) was 2.3-fold enriched.

5.2.14 pUL36^{ACBD} pull-down and mass-spectrometry

I repeated the pull-down assay in Vero cells using GFP-pUL36^{ACBD} and GFP alone as a control, again in triplicate (**Figure 5.20**). As discussed above, the variability in Vero

cells means that the amount of moving pUL36 in cells before lysis is lower than for pUL36^{ΔCBD-MTS}. Perhaps as a result of this, fewer proteins were enriched in this experiment (**Figure 5.21**). RanBP2 was the only protein identified in both screens. The only other cytoskeleton-associated protein identified in this assay was tubulin α 1b. The remaining proteins were almost all ribosomal.

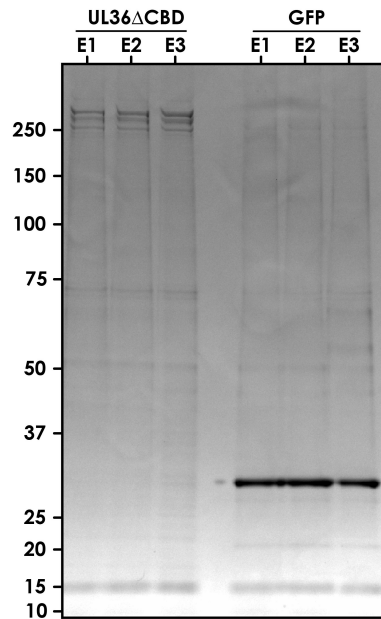


Figure 5.20 - Triplicate pull-down of pUL36^{ΔCBD} in Vero cells
Coomassie stained SDS-PAGE gel showing the Elution (E, boiled beads) of the three repeat pull-downs of pUL36^{ΔCBD} and GFP from Vero cells. Lanes were cut out and sent for mass-spectrometry

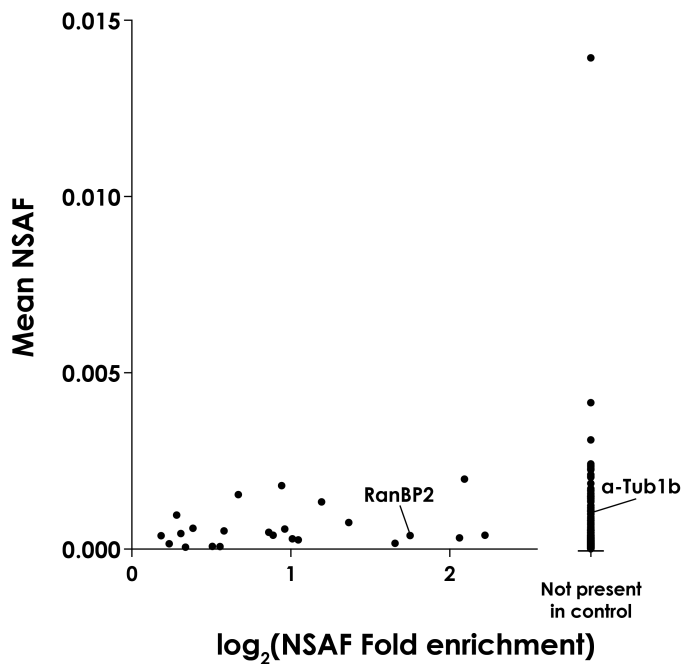


Figure 5.21 - Proteins enriched in pUL36^{ΔCBD} pull-down mass-spectrometry from Vero cells

A plot of mean NSAF value against NSAF fold-enrichment compared to negative control for the pUL36^{ΔCBD} Vero cell pull-down. Each identified protein is represented by a single point, with the two proteins of interest annotated

5.2.15 Validation of mass-spectrometry hits with immunofluorescence colocalisation

I used immunofluorescence as the first step in validating the hits identified in the pull-downs. This excludes some targets in the first instance, such as Rab29, which do not have commercially available antibodies recommended for immunofluorescence. I transfected cells with GFP-pUL36^{ΔCBD} or GFP-pUL36^{ΔCBD-MTS} as normal. After 18 hours, I fixed them in formaldehyde, blocked and permeabilised the wells, and performed consecutive incubations with protein-specific primary and fluorescent secondary antibodies. GFP retains its fluorescence after formaldehyde fixation, so the localisation of pUL36 could be visualised as normal.

I inferred whether GFP-pUL36^{ΔCBD} was moving prior to fixation based on the presence of a central cluster of fluorescence near the center of the cell, with signs of microtubule localisation radiating from this point. However, given that this is a subjective measure and not 100% correlated with pUL36 motility, most targets were cross-referenced with GFP-pUL36^{ΔCBD-MTS} where the clustering of mitochondria

provides a direct readout of activity prior to fixation. Immunofluorescence was only performed in Vero cells.

Rab21 displayed bright punctate staining throughout the cell, however there was no colocalisation visible with pUL36 in any cells (**Figure 5.22A**), and I therefore concluded it was not interacting with pUL36. p62 (SQSTM1) expression was variable in different cells, but it was always more highly expressed in cells expressing GFP-pUL36^{ΔCBD} (**Figure 5.22B/C**). In some transfected cells it was diffuse, with intense cytoplasmic clusters not correlated with pUL36 (**Figure 5.22B**). However, in other cells there was a clear correlation between p62 and GFP-pUL36^{ΔCBD} (**Figure 5.22C**). The fact that this was not the case in all the cells would suggest that this interaction is not necessary for pUL36 mobility, and is a secondary effect. MAP1B had a mostly nuclear localisation (**Figure 5.22D**), suggesting that the antibody is unsuitable for immunostaining.

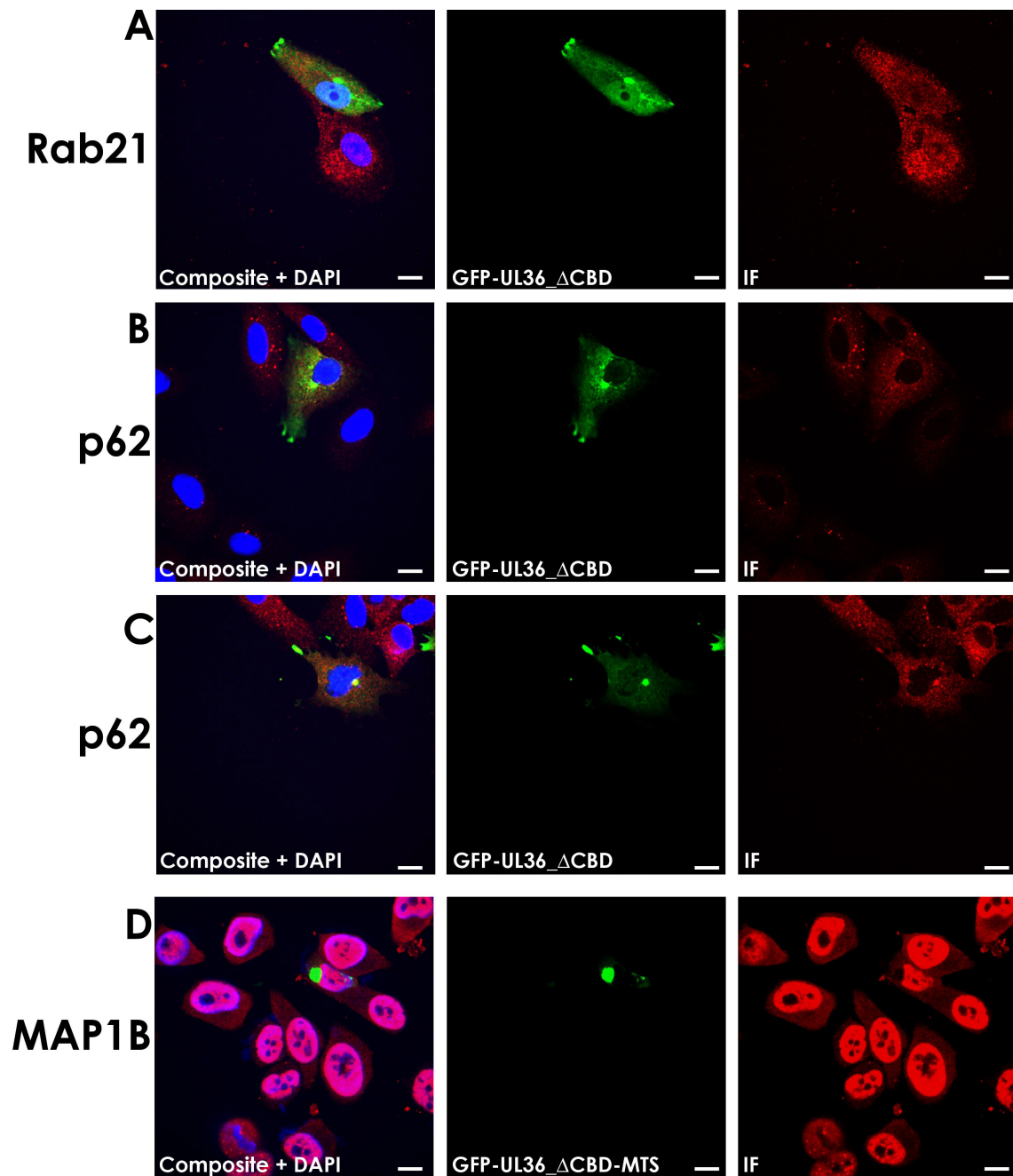


Figure 5.22 - Assessing colocalisation between pUL36 and pull-down hits with immunofluorescence

Immunofluorescence of target indicated (red) and pUL36 (as indicated, green), with composite image also staining DNA with DAPI (blue). Scale bars=2.5um

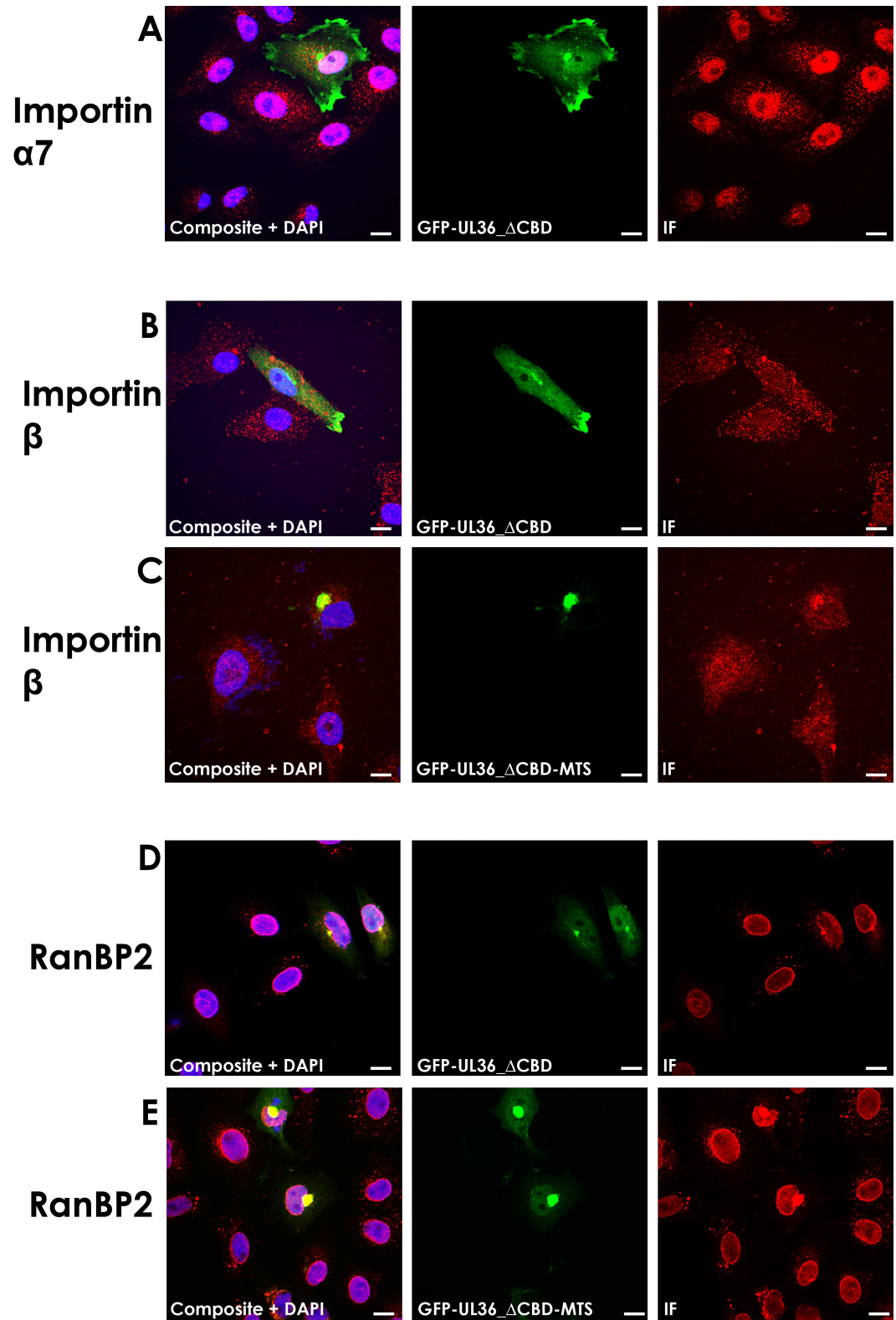


Figure 5.23 - Nuclear pore associated proteins colocalise with pUL36 in the cytoplasm

Immunofluorescence of target indicated (red) and pUL36 (as indicated, green), with composite image also staining DNA with DAPI (blue). Scale bars=2.5um

Importin α 7 did not colocalise with pUL36 clusters (**Figure 5.23A**), although other importin- α family members were not tested. Importin β had a similar pattern to p62, in that it colocalised in some cells but not in others (**Figure 5.23B/C**). The most striking effect was observed with RanBP2. In every cell imaged, RanBP2 strongly colocalised with pUL36 clusters (**Figure 5.23D/E**). It suggested previously that RanBP2 and pUL36 interact at the nucleus (Copeland et al., 2009). However, this result is significant because pUL36 is interacting with a cytoplasmic pool of RanBP2. RanBP2 is found in cytoplasmic stacks of nuclear pores called annulate lamellae (Raghunayakula et al., 2015), which are able to recruit dynein in the same way as regular nuclear pore complexes (Splinter et al., 2010b).

5.2.16 pUL36 ^{Δ CBD} colocalises with Cyclin B1

Previous work has shown that RanBP2 recruits BICD2 to the nuclear pore during G2 phase, in turn recruiting dynein to position the nucleus in the center of the cell prior to mitosis (Splinter et al., 2010b). In the Splinter study a cell was determined to be in G2 phase if it was expressing cyclin B1, as determined by immunofluorescence. I wanted to determine whether a similar mechanism occurs for pUL36 movement. I transfected Vero cells with pUL36 ^{Δ CBD} or pUL36 ^{Δ CBD-MTS} and performed immunofluorescent staining with a cyclin B1 antibody. Strikingly, cyclin B1 was often strongly colocalised with GFP-pUL36 ^{Δ CBD} and GFP-pUL36 ^{Δ CBD-MTS} (**Figure 5.24A/B**). The average cyclin fluorescence intensity was measured within each cell. In cells with a cluster of pUL36 ^{Δ CBD} at the cell center, the whole-cell cyclin B1 expression was significantly higher (**Figure 5.25** 1929 ± 1684 au against 779 ± 428 au, Number of cells=36 vs 22, $p=0.0023$, unpaired t-test). As before, whether or not the pUL36 is moving in these cells can only be inferred from static images, so this is still a preliminary result. In cells expressing GFP-pUL36 ^{Δ CBD-MTS} the clustered mitochondria often cluster with cyclin B1 (**5.24B**), but similar quantification has not yet been performed.

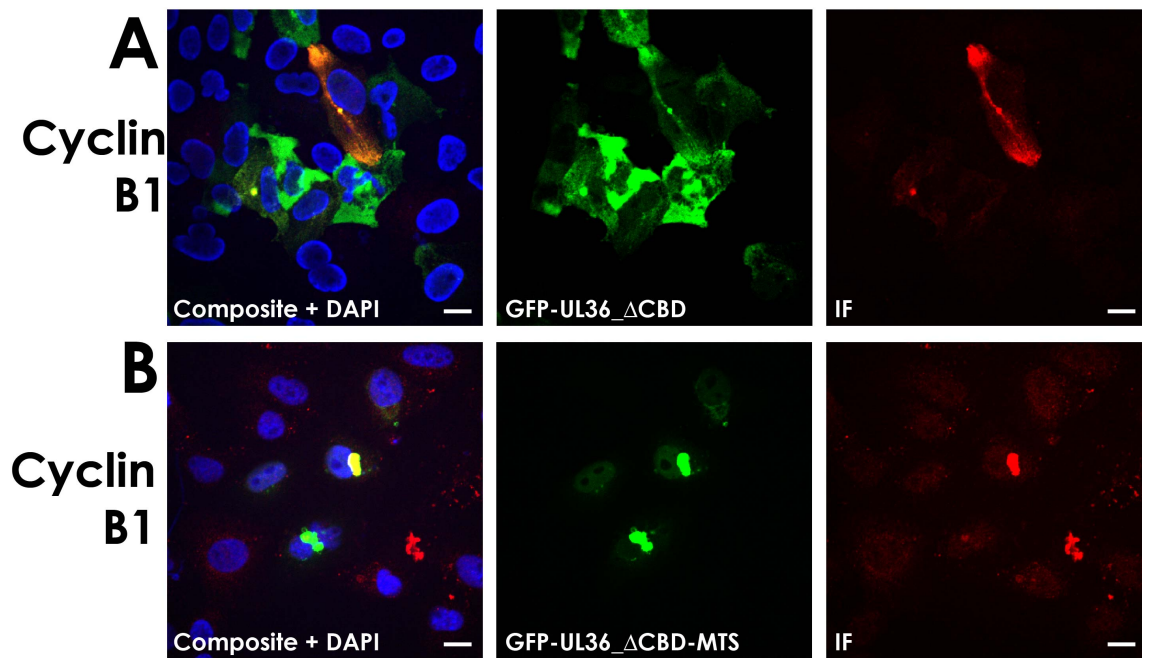


Figure 5.24 - Colocalisation between pUL36 and Cyclin B1

IF between GFP-pUL36 (as indicated, green) and Cyclin B1, along with composite image stained with DNA by DAPI (blue).

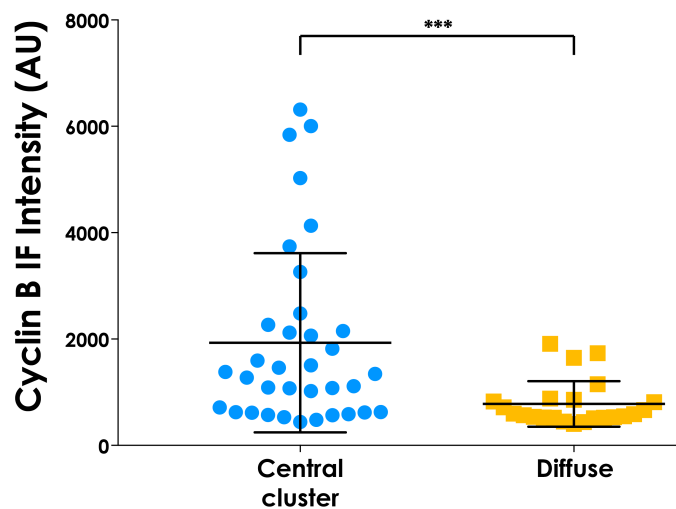


Figure 5.25 - Cyclin B1 expression is associated with pUL36^{ΔCBD} activity

Quantification of the Cyclin B1 IF intensity in cells expressing pUL36^{ΔCBD} with either diffuse pUL36 fluorescence or a central cluster of pUL36

5.2.17 Testing the importance of RanBP2 for pUL36 motility with knock-downs

To assess whether an interaction with RanBP2 was necessary for movement of pUL36, I attempted to knock down RanBP2 and see if pUL36 was still actively transported or clustered. RanBP2 is an essential protein (Hamada et al., 2011), so a

genomic knockout would not be viable. Instead I tested two transient knockdown techniques to remove RanBP2 protein from the cytoplasm.

I first used TRIM-Away to reduce levels of RanBP2 in the cytoplasm. This is a new protein knockdown technique based on the activity of the E3 ubiquitin ligase TRIM21 (Clift et al., 2017). TRIM21 forms part of the cells innate immune response by binding to the Fc domain of antibodies, and ubiquitinating the antibody and its target to trigger its degradation by the cell. TRIM21 and an antibody specific to a protein of interest are electroporated into cells, and full degradation is typically achieved within three hours. TRIM-Away has the advantage of being fast, so cells will not be disrupted by lack of RanBP2 over a long period. Purified TRIM21 (kindly supplied by Dr Dean Clift) was electroporated into Vero cells along with RanBP2 antibody. After 5 hours, I probed for RanBP2 by Western blot of whole cell lysate. The amount of RanBP2 in the cells had only decreased by ~50% compared to the negative control (**Figure 5.26A**), indicating that only a partial knock-down had been achieved.

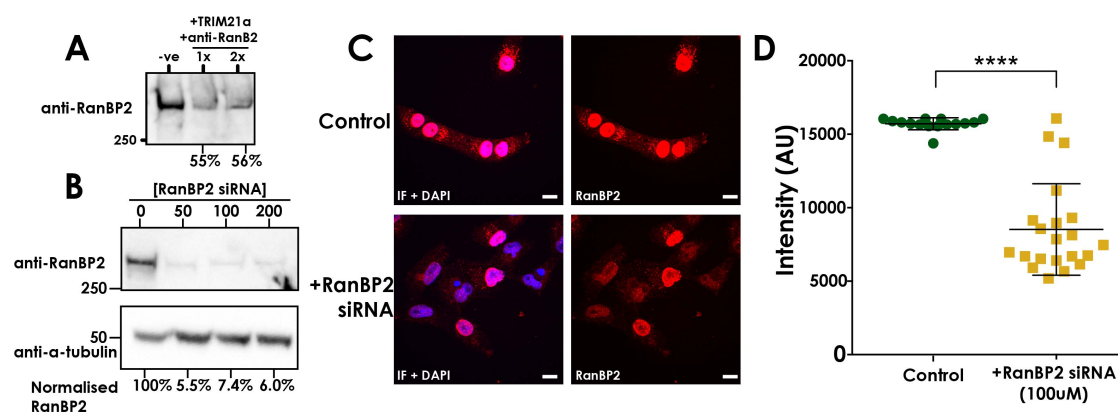


Figure 5.26 - Two different knockdown strategies for RanBP2

A - Western blot for RanBP2 in whole Vero cell lysate in control cells and cells electroporated with TRIM21 and anti_RANBP2 antibody (TRIM-Away). RanBP2 levels calculated from RanBP2 band intensity. **B** - Western blots for RanBP2 and α-tubulin in whole Vero cell lysate in control cells and cells transfected with RanBP2 siRNA at given concentration. RanBP2 levels calculated from RanBP2 band intensity normalised to tubulin band intensity. **C** - Immunofluorescence of control Vero cells or Vero cells transfected with RanBP2 siRNA, showing cell-to-cell variability in the level of the knockdown. **D** - Whole cell intensity measurements of a dataset of images represented by **C**. Unpaired t-test, $p < 0.0001$, $n = 15$ cells (control), 21 cells (siRNA)

To achieve a stronger knockdown of RanBP2, I switched to siRNA silencing. I used a commercial pool of 4 siRNAs (Dharmacon smart-pool) specific to RanBP2. In the

past, others have performed siRNA knockdown of RanBP2 over the course of 2 days, indicating that the protein has a long half-life (Kim et al., 2016). I transfected the siRNA into Vero cells with RNAiMax transfection reagent, and incubated the cells for 3 days. Quantification of Western blot bands showed that the siRNA had efficiently silenced the RanBP2 down to ~5% of its endogenous level (**Figure 5.26B**). However, immunofluorescence of cells transfected in parallel showed a reduction in whole-cell IF intensity of only 45% compared to the control (**Figure 5.26C/D**). Furthermore, some cells had the same level as expression as cells transfected with scrambled siRNA. The reason for the discrepancy in the two quantification techniques is unclear. The only difference between the two transfections was the wells in which they were plated (i.e. 6-well plate for Western blot and small 4-well imaging chambers for IF). It is possible the lower surface area to volume ratio in the imaging chambers may have resulted in a lower transfection efficiency.

Despite being only a partial knock-down, I quantified the number of cells with clustered mitochondria following transfection with GFP-pUL36^{ΔCBD_MTS} and RanBP2 siRNA to see if there is a dose-dependent reduction in clustering in the absence of RanBP2. In the RanBP2 siRNA treated cells, there was still a significant amount of RanBP2 colocalising with GFP-pUL36^{ΔCBD_MTS} (**Figure 5.27A/B**). Consistent with this observation, the amount of cells with clustered mitochondria was only slightly reduced in the RanBP2 siRNA treated cells (**Figure 5.27C**).

In the past, HSV-1 has been inhibited from docking at the nuclear pore by the addition of anti-RanBP2 antibody into the cytoplasm of Vero cells (Copeland et al., 2009). Copeland et al. suggested that the antibody binding to RanBP2 prevented it from interacting with other proteins as normal. I therefore electroporated anti-RanBP2 antibody into Vero cells at the same time as transfection with the GFP-pUL36^{ΔCBD_MTS} plasmid and incubated overnight. These cells displayed normal expression of GFP-pUL36^{ΔCBD_MTS}, but the number of cells with clustered mitochondria had dropped to 10% (**Figure 5.27C**). This result suggests that GFP-pUL36^{ΔCBD_MTS} requires its interaction with RanBP2 for normal motility, however further controls must be performed to verify this result. Most importantly, cells electroporated with RanBP2 antibody should be assayed for normal dynein activity.

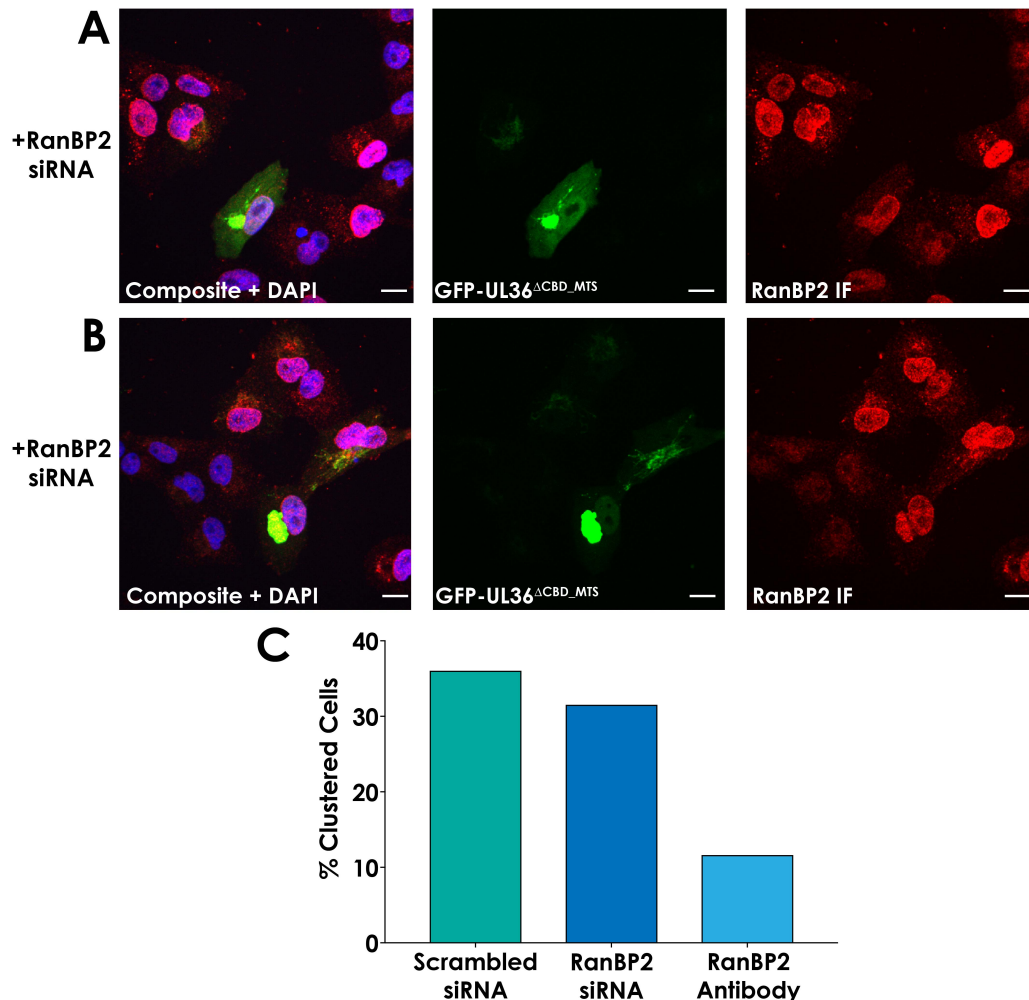


Figure 5.27 - Colocalisation between RanBP2 and pUL36^{ΔCBD-MTS} after RanBP2 knockdown

A/B - Representative images depicting residual RanBP2 following siRNA-mediated knockdown still colocalising with clustered pUL36^{ΔCBD-MTS}. Scale bars=2.5um *C* - Percentage of cells with clustered mitochondria when expressing pUL36^{ΔCBD-MTS} in the indicated conditions. "RanBP2 antibody" cells were not treated with siRNA, and instead were electroporated to introduce RanBP2 at the same time as the pUL36^{ΔCBD-MTS} plasmid. Each condition is an average of 50-100 cells from a single experiment.

5.2.18 pUL36 interacts more strongly with Dynactin in the presence of RanBP2

I next tested whether silencing RanBP2 disrupts the interaction between pUL36 and dynactin. I performed siRNA knockdown on Vero cells in 6-well plates (i.e. where it appears to have a stronger effect), and transformed them with GFP-pUL36^{ΔCBD} after 72 hours. After 18 hours I lysed the cells and performed a GFP pull-down as before. As controls, this was done in parallel with cells transfected with scrambled siRNA, and cells transfected with GFP^{MTS}. The level of pUL36 expression in the

mock-silenced and RanBP2 silenced cells was directly comparable, as assessed by Sypro Ruby staining (**Figure 5.28A**). RanBP2 was not visible in the Western blot of the input (**Figure 5.28B**). This is likely to be because the lysate was more dilute in this experiment compared to the knockdown optimisation (**Figure 5.26**). However, the knockdown was confirmed by the presence of a strong RanBP2 band in the elution of the mock-transfected pUL36 control, and nothing in the siRNA transfected pUL36 experiment (**Figure 5.28B**). There was a band present for dynactin subunit p150 in each of the three elutions. Quantification of band intensity was performed in FIJI by measuring the area under the intensity plot of each peak (**Figure 5.28B**). In absolute terms, pUL36 pulled down 57% as much p150 when RanBP2 is absent. If the intensity from the GFP control is taken as background and subtracted from each of the pUL36 bands, pUL36 pulls down 31% as much p150 when RanBP2 is absent. Further repeats for this experiment are needed, however these results indicate that pUL36 is at least partially dependent on RanBP2 for an interaction with dynactin.

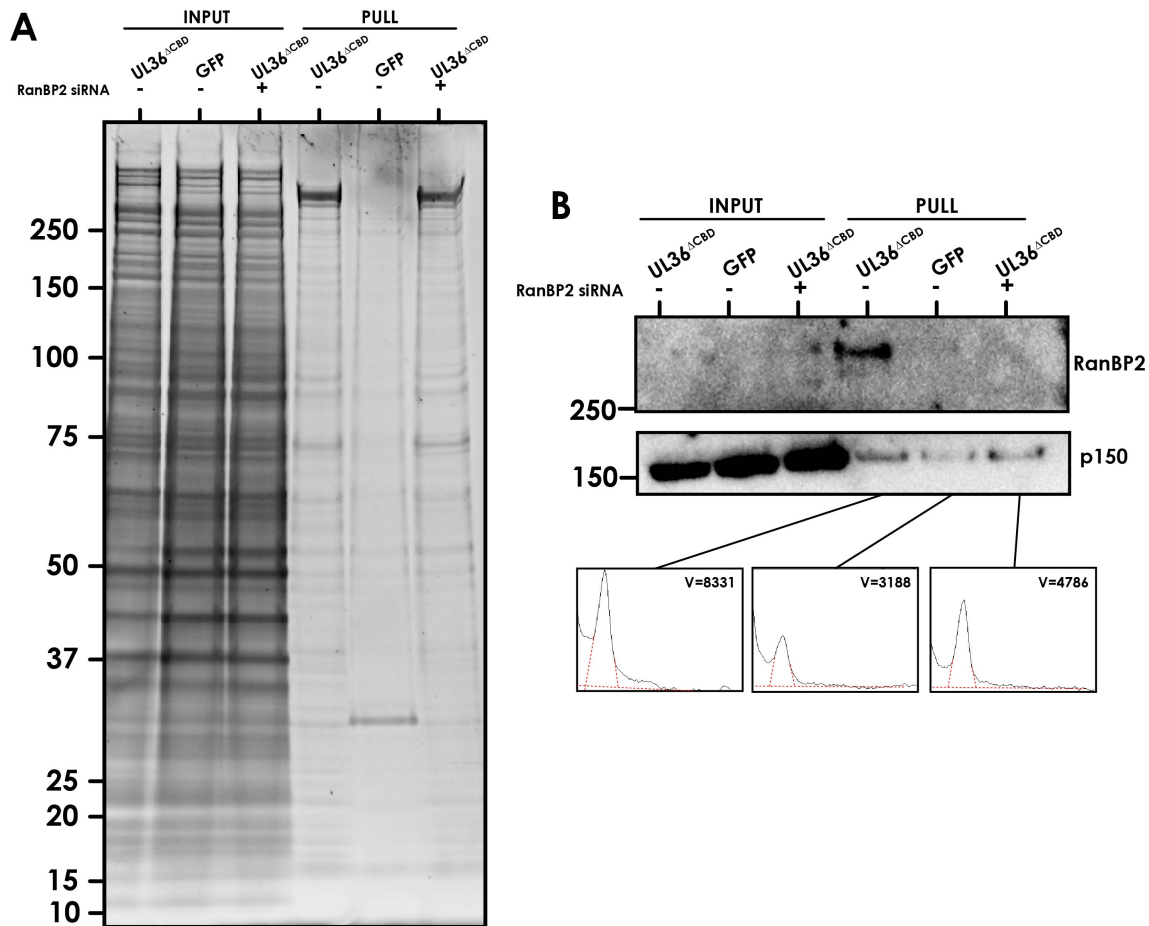


Figure 5.28 - pUL36^{ΔCBD} interacts more strongly with dynein when RanBP2 is present

A - Sypro Ruby stained SDS-PAGE gel of the input and elutions from the GFP-pUL36^{ΔCBD} pull-downs with and without RanBP2 siRNA treatment. **B** - Western blots for RanBP2 and p150 of the same pull-down, with band intensity profiles and area measurement (V) inset.

5.2.19 HSV1 capsids colocalise with RanBP2 in the cytoplasm

As the first step to determine whether any interaction between RanBP2 and pUL36 is physiologically relevant for dynein-based microtubule motility, I performed colocalisation experiments in Vero cells infected with HSV1. This was performed with Dr Colin Crump, who performed all virus handling. The virus was fluorescently labelled with YFP on the capsid protein VP26. We infected the cells with a high multiplicity of infection (MOI, 20), incubated the cells for three hours and then fixed them with formaldehyde. In this time, we expected the virus to have been transported by dynein to the perinuclear rim as in previous studies (Copeland et al., 2009)

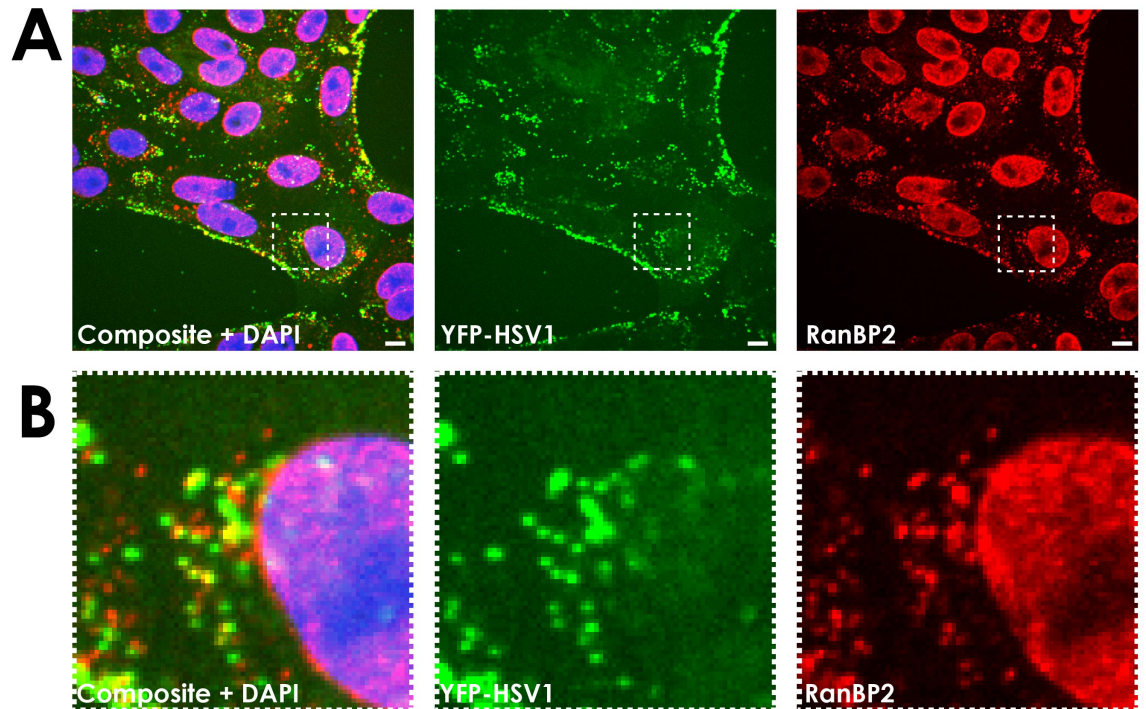


Figure 5.29 - Colocalisation between HSV1 and RanBP2

A - Vero cells were infected with YFP-VP26 HSV1 (green) at an MOI of 20, and fixed after 3 hours. The cells were then immunostained for RanBP2 (red); composite image stained for DNA with DAPI. Scale bars=2um **B** - Enlargement of area indicated in A.

Immunofluorescence staining was performed as before for RanBP2. However, we observed that viruses had not reached the nuclear envelope *en masse* as predicted (**Figure 5.29A-C**). This could be because the infectivity of the viral stock might have decreased after being frozen for a long time. However, RanBP2 had relocated to the cell periphery, where the majority of the virus remained (**Figure 5.29A**). There was further colocalisation between cytoplasmic virus and RanBP2 (**Figure 5.29B**). These results, again preliminary, support a role for RanBP2 in HSV1 transport. However, further experiments are needed to validate these results on account of cross-reactivity between rabbit IgG and HSV-1 encoded Fc receptors. This was mitigated by the use of donkey serum to block the HSV-1 Fc receptors. To validate that this block was successful, further experiments should be performed with endogenously tagged fluorescent RanBP2 rather than antibody-based detection.

5.3 Discussion

5.3.1 What conformation does pUL36 adopt?

The organisation of pUL36 away from the capsid-binding domain remains unknown. A cryo-EM structure of HSV-2 shows that there are ten pUL36 molecules arranged around each penton (Dai and Zhou, 2018)(Wang et al., 2018a). pUL36 was previously thought to project from the pentons into the tegument. However, super-resolution microscopy using a labelled antibody for an epitope between residues 1564-1876 of HSV1 pUL36 showed that this section remains close to the capsid (Laine et al., 2015). Furthermore, targeted proteolysis has showed that the N-terminus of PrV pUL36 remains attached to the capsid after cleavage at residue 482 (Daniel et al., 2018). These results suggest that the native state of pUL36 probably involves extensive intra- and inter-molecular interactions. This are consistent with my observation of instability of the pUL36 C-terminus when the N-terminus is removed (**Figure 5.6**), which I suggest is due to interactions between the N- and C-termini.

The central ~1000 residues of HSV1 pUL36 are predicted to form coiled coils, and folds into a filamentous particle over 30nm in length when expressed in *E. coli* (Scrima et al., 2015). A crystal structure of a 130 residue fragment (1600-1733) suggests it forms an unusual monomeric five-helix bundle (Scrima et al., 2015). The central region of pUL36 was therefore suggested to form a modular series of helical bundles, rather than a traditional coiled coil. In agreement, my results show that pUL36 forms monomers in solution (**Figure 5.7**), unlike all activating dynein cargo adaptors structurally characterised to date, which are homodimeric parallel coiled coils (Reck-Peterson et al., 2018). Accordingly, pUL36 does not appear to act as an activating cargo adaptor for dynein (**Figure 5.8**).

5.3.2 Variability in pUL36 motility

A consistent observation I made of pUL36^{ΔCBD} transfected cells was the cell-to-cell variability in the observed phenotype. Around 10-20% of cells displayed cytoplasmic motility of pUL36^{ΔCBD}, although this varied day-to-day and was a difficult

phenomenon to properly quantify. The variability could be due to the amount of plasmid DNA received by each cell, but motility occurred in cells with both low and high levels of pUL36 expression. My later results suggested that pUL36^{ΔCBD} motility is potentially correlated with cyclin B1 expression (**Figure 5.24 + 5.25**). I attempted a thymidine block to synchronise the cell cycle of transfected cells. This technique involves incubating cells in minimal media to starve them of the bases needed for DNA synthesis, and thus blocking the cell cycle at the G1/S boundary. The cells are then released synchronously by the addition of complete media. I monitored pUL36^{ΔCBD} motility in the released cells, however the cells rapidly started to bleb and die. This is an avenue to pursue in the future however, because pUL36 only being motile at a certain stage of the cell cycle would support the theory that it is dependent on RanBP2 for transport.

Another source of variability in pUL36 motility is the different effects observed in different cell types and with or without the MTS tag. pUL36^{ΔCBD} is only motile in Vero cells, but pUL36^{ΔCBD_MTS} clustered by dynein in both Vero and Human cells. In Vero cells, a greater proportion of cells have clustered pUL36^{ΔCBD_MTS} compared to motile pUL36^{ΔCBD}. The MTS system is probably less sensitive to the variability observed in pUL36^{ΔCBD}, since the mitochondria are coated with multiple copies of pUL36 and only a small proportion of them need to be “active” to cluster the mitochondria. Furthermore, Pseudorabies virus infects HeLa cells 10-fold less productively than Vero cells (Petrovskis et al., 1988), suggesting that pUL36 motility may be expected to be higher in Vero cells.

5.3.3 A model for RanBP2-dependent motility of pUL36 in cells

RanBP2 is a component of the nuclear pore, and is the main component of the cytoplasmic filaments that initiate the nuclear import process (Wu et al., 1995; Yokoyama et al., 1995). During G2 phase RanBP2 recruits BICD2 to the nuclear pore in order to keep the nucleus close to the centrosome prior to mitosis (Splinter et al., 2010). The same 100 amino acid region that interacts with BICD2 also binds to the kinesin-1 family members KIF5B and KIF5C, and disruption of the interaction with kinesin results in clustering of mitochondria near the nucleus (Cho et al., 2007). As

such, RanBP2 is known to recruit both plus- and minus-end directed microtubule motors, providing a strong rationale for its role in pUL36 motility.

pUL36 interacts with nuclear pore components in order to dock at the nuclear pore prior to injection of genomic DNA into the nucleus (Copeland et al., 2009; Padeloup et al., 2009). This was thought to be mediated by RanBP2 and Nup214, both of which were identified in my screens, although Copeland *et al.* saw normal behaviour when the interaction with Nup214 was inhibited. Copeland *et al.* also observed that inhibiting the interaction between virus and RanBP2 prevented virus docking at the nuclear rim. However, in the representative image they show, the virus is located almost entirely at the cell periphery, indicating that microtubule-based transport is inhibited as well.

These studies did not establish whether or not RanBP2 and pUL36 form a direct interaction. The large proline-rich regions of pUL36 are probably intrinsically disordered, given that the limited dihedral angles of proline mean it cannot form conventional alpha-helices or beta-strands. The disordered, hydrophobic proline-rich region of pUL36 could potentially interact with the hydrophobic FG repeats that RanBP2 uses to form a diffusion barrier in the nuclear pore (Knockenbauer and Schwartz, 2016). Removal of the proline-rich region reduced the co-IP efficiency of pUL36 for p150 10-fold (Zaichick et al., 2013). Alternatively, pUL36 contains a nuclear localisation signal, which may mediate recruitment to RanBP2 and the nuclear pore (Abaitua et al., 2012).

A potential weakness in the model that RanBP2 links dynein to viruses is that herpesviruses initiate transport in the periphery of the cell, so the dynein adaptor needs to be present there as well. Consistent with previous results, I saw a large amount of RanBP2 in the cytoplasm of untransfected cells (**Figure 5.22, 5.25**). This cytoplasmic RanBP2 is probably located in annulate lamellae (AL), which are a cytoplasmic pool of nuclear pores that can be inserted into the nuclear membrane during cell growth (Hampoelz et al., 2016), and thus could interact with herpesviruses near the cell periphery. It is unknown if there is a population of RanBP2 in the cytoplasm not associated with annulate lamellae or nuclear pores. A previous study saw a large-scale relocalisation of RanBP2 from the nucleus to the

cytoplasm of epithelial cells following infection by Human immunodeficiency virus (HIV) (Dharan et al., 2016). This is consistent with what I observed in HSV1 infection of Vero cells (**Figure 5.29**), and shows that a cytoplasmic pool of RanBP2 can be mobilised in response to viral infection.

Alpha Herpesviruses are neurotropic, and retrograde transport needs to be initiated at the distal ends of the axons. In retinal neurons, RanBP2 is present in the mitochondria rich ellipsoid compartment of the inner segment, a distinct subcellular compartment distal from the cell body (Mavlyutov et al., 2002). However, there is no information regarding the localisation of RanBP2 in other neuronal cells. However, virus is being transported in the axons of cultured neurons within 30 minutes of infection (Koyuncu et al., 2015), which is probably too quick for a pool of RanBP2 in the cell body to relocate in time. Furthermore, RanBP2 is only thought to recruit dynein in G2 phase of the cell cycle (Splinter et al., 2010), and it is unknown whether it still interacts in cell cycle quiescent cells like neurons. Finally, contrary to a model in which RanBP2 recruits dynein to the pUL36, it could be argued that the interaction I observe between RanBP2 and pUL36 is reflective of their interaction at the nuclear pore. A tight interaction is likely to be required to keep the capsid docked when DNA is being ejected. This interaction could therefore be strong enough to recruit RanBP2 from annulate lamellae or the cytoplasm to pUL36.

To address these points, I intend to investigate any colocalisation between RanBP2 and pUL36 or HSV1 in cultured primary hippocampal neuron. Furthermore, a CRISPR knock-in to fluorescently label RanBP2 in Vero cells would show if pUL36 and RanBP2 are actively co-transported in these cells. Finally, RanBP2 is not an activating cargo adaptor for dynein, and is thought to recruit BICD2 for this purpose (Splinter et al., 2010). I therefore intend to investigate whether silencing of BICD2 disrupts pUL36 or HSV1 transport.

5.3.4 Separate models for pUL36 transport

Retrograde transport of PrV was previously shown to be strongly dependent on pUL36 K442 being ubiquitinated (Huffmaster et al., 2015). My results were consistent with this, in that a pUL36 point mutant incapable of being ubiquitinated

at this position was immotile in cells (**Figure 5.13**). RanBP2 contains an E3 SUMO (Small Ubiquitin-like Modifier) ligase domain, however pUL36 was specifically shown to be ubiquitinated and not SUMOylated by Huffmaster *et al.*

Dynein is known to transport ubiquitinated proteins as part of the aggresome pathway, where aggregated proteins are ubiquitinated, transported to the centre of the cell, and degraded (Johnston *et al.*, 1998, 2002). Dynein interacts with two proteins, Histone Deacetylase 6 (HDAC6) and SQSTM1/p62, which in turn bind to polyubiquitylated aggregated proteins (Calderilla-Barbosa *et al.*, 2014; Kawaguchi *et al.*, 2003). HDAC6 was not identified as a potential interactor in my pull-downs, however p62 was. I showed that p62 occasionally but not exclusively colocalised with pUL36^{ΔCBD_MTS} clusters (**Figure 5.22**). This colocalisation could be due to p62 treating pUL36^{ΔCBD_MTS} as a ubiquitinated protein and linking it to dynein for transport, or it could be a secondary effect where a high local concentration of unstable or ubiquitinated protein recruits p62. In the future, I intend to investigate colocalisation between RanBP2 and pUL36^{ΔCBD_K442R}, and it may be of interest to repeat the pull-down/mass-spec protocol with pUL36^{ΔCBD_K442R} to see if any interactors are lost.

It is possible that the motility of ectopically expressed pUL36 occurs in a different mechanism to whole herpesviruses. Herpesvirus transport in cultured cells and axons has been variously shown to depend on; CLIP170-mediated initiation (Jovasevic *et al.*, 2015), local synthesis of proteins including Lis1 in the axon (Koyuncu *et al.*, 2013), the presence of a large amount of virus infecting the cell at once (Koyuncu *et al.*, 2015) and wild-type pUL37 (Richards *et al.*, 2017). It is possible, but not guaranteed, that pUL36 mediates these effects and interactions for the virus. Future experiments should therefore focus on validating results with relevant viral models.

A number of untested hits from my pull-downs remain to be explored. Rab29 was strongly enriched, and when it is silenced in cells the trans-Golgi network disperses (Wang *et al.*, 2014). The same phenotype occurs when dynein is inhibited (Harada *et al.*, 1998), suggesting that the two are linked directly or indirectly. I did not investigate this hit in the first instance due to the absence of a good antibody for

immunofluorescence. Its role in pUL36 transport could be tested with an siRNA knock-down in the future.

Chapter 6. References

- Abaitua, F., Hollinshead, M., Bolstad, M., Crump, C.M., and O'Hare, P. (2012). A Nuclear Localization Signal in Herpesvirus Protein VP1-2 Is Essential for Infection via Capsid Routing to the Nuclear Pore. *Journal of Virology* *86*, 8998–9014.
- Adams, P.D., Afonine, P.V., Bunkóczi, G., Chen, V.B., Davis, I.W., Echols, N., Headd, J.J., Hung, L.-W., Kapral, G.J., Grosse-Kunstleve, R.W., et al. (2010). PHENIX: a comprehensive Python-based system for macromolecular structure solution. *Acta Cryst D* *66*, 213–221.
- Adrian, M., Dubochet, J., Lepault, J., and McDowell, A.W. (1984). Cryo-electron microscopy of viruses. *Nature* *308*, 32.
- Aggarwal, A., Miranda-Saksena, M., Boadle, R.A., Kelly, B.J., Diefenbach, R.J., Alam, W., and Cunningham, A.L. (2012). Ultrastructural Visualization of Individual Tegument Protein Dissociation during Entry of Herpes Simplex Virus 1 into Human and Rat Dorsal Root Ganglion Neurons. *Journal of Virology* *86*, 6123–6137.
- Aitken, C.E., Marshall, R.A., and Puglisi, J.D. (2008). An Oxygen Scavenging System for Improvement of Dye Stability in Single-Molecule Fluorescence Experiments. *Biophys J* *94*, 1826–1835.
- Albecka, A., Laine, R.F., Janssen, A.F.J., Kaminski, C.F., and Crump, C.M. (2016). HSV-1 Glycoproteins Are Delivered to Virus Assembly Sites Through Dynamin-Dependent Endocytosis. *Traffic* *17*, 21–39.
- Amos, L.A., and Hirose, K. (1997). The structure of microtubule-motor complexes. *Current Opinion in Cell Biology* *9*, 4–11.
- Amos, L.A., and Klug, A. (1974a). ARRANGEMENT OF SUBUNITS IN FLAGELLAR MICROTUBULES. 28.
- Amos, L.A., and Klug, A. (1974b). Arrangement of Subunits in Flagellar Microtubules. *Journal of Cell Science* *14*, 523–549.
- Andreasson, J.O., Milic, B., Chen, G.-Y., Guydosh, N.R., Hancock, W.O., and Block, S.M. (2015). Examining kinesin processivity within a general gating framework. *ELife* *4*.
- Aniento, F., Emans, N., Griffiths, G., and Gruenberg, J. (1993). Cytoplasmic dynein-dependent vesicular transport from early to late endosomes. *The Journal of Cell Biology* *123*, 1373–1387.
- Antonone, S.E., and Smith, G.A. (2010). Retrograde Axon Transport of Herpes Simplex Virus and Pseudorabies Virus: a Live-Cell Comparative Analysis. *J. Virol.* *84*, 1504–1512.
- Antonone, S.E., Zaichick, S.V., and Smith, G.A. (2010). Resolving the Assembly State of Herpes Simplex Virus during Axon Transport by Live-Cell Imaging. *Journal of Virology* *84*, 13019–13030.
- Arii, J., Goto, H., Suenaga, T., Oyama, M., Kozuka-Hata, H., Imai, T., Minowa, A., Akashi, H., Arase, H., Kawaoka, Y., et al. (2010). Non-muscle myosin IIA is a functional entry receptor for herpes simplex virus-1. *Nature* *467*, 859–862.
- Arnal, I., and Wade, R.H. (1995). How does taxol stabilize microtubules? *Current Biology* *5*, 900–908.
- Asante, D., Stevenson, N.L., and Stephens, D.J. (2014). Subunit composition of the human cytoplasmic dynein-2 complex. *J Cell Sci* *127*, 4774–4787.
- Asbury, C.L., Fehr, A.N., and Block, S.M. (2003). Kinesin Moves by an Asymmetric Hand-Over-Hand Mechanism. *Science* *302*, 2130–2134.
- Atherton, J., Farabella, I., Yu, I.-M., Rosenfeld, S.S., Houdusse, A., Topf, M., and Moores, C.A. (2014). Conserved mechanisms of microtubule-stimulated ADP release, ATP binding, and force generation in transport kinesins. *ELife* *3*, e03680.
- Atherton, J., Jiang, K., Stangier, M.M., Luo, Y., Hua, S., Houben, K., van Hooff, J.J.E., Joseph, A.-P., Scarabelli, G., Grant, B.J., et al. (2017). A structural model for microtubule minus-end recognition and protection by CAMSAP proteins. *Nat. Struct. Mol. Biol.* *24*, 931–943.
- Atherton, J., Stouffer, M., Francis, F., and Moores, C.A. (2018). Microtubule architecture *in vitro* and in cells revealed by cryo-electron tomography. *Acta Crystallographica Section D Structural Biology* *74*, 572–584.
- Aumeier, C., Schaedel, L., Gaillard, J., John, K., Blanchoin, L., and Théry, M. (2016). Self-repair promotes microtubule rescue. *Nature Cell Biology* *18*, 1054–1064.
- Baker, L.A., and Rubinstein, J.L. (2010). Chapter Fifteen - Radiation Damage in Electron Cryomicroscopy. In *Methods in Enzymology*, G.J. Jensen, ed. (Academic Press), pp. 371–388.
- Baker, T.S., and Amos, L.A. (1978). Structure of the tubulin dimer in zinc-induced sheets. *Journal of Molecular Biology* *123*, 89–106.
- Barisic, M., and Geley, S. (2011). Spindly switch controls anaphase: Spindly and RZZ functions in chromosome attachment and mitotic checkpoint control. *Cell Cycle* *10*, 449–456.
- Bauer, D.W., Huffman, J.B., Homa, F.L., and Evilevitch, A. (2013). Herpes virus genome, the pressure is on. *J. Am. Chem. Soc.* *135*, 11216–11221.
- Bearer, E.L., Breakefield, X.O., Schuback, D., Reese, T.S., and LaVail, J.H. (2000). Retrograde axonal transport of herpes simplex virus: Evidence for a single mechanism and a role for tegument. *PNAS* *97*, 8146–8150.

- Belyy, V., Schlager, M.A., Foster, H., Reimer, A.E., Carter, A.P., and Yildiz, A. (2016). The mammalian dynein-dynactin complex is a strong opponent to kinesin in a tug-of-war competition. *Nat Cell Biol* *18*, 1018–1024.
- Beranger, F., Paterson, H., Powers, S., de Gunzburg, J., and Hancock, J.F. (1994). The effector domain of Rab6, plus a highly hydrophobic C terminus, is required for Golgi apparatus localization. *Molecular and Cellular Biology* *14*, 744–758.
- Bhabha, G., Johnson, G.T., Schroeder, C.M., and Vale, R.D. (2016). How dynein moves along microtubules. *Trends Biochem Sci* *41*, 94–105.
- Bhogaraju, S., Cajanek, L., Fort, C., Blisnick, T., Weber, K., Taschner, M., Mizuno, N., Lamla, S., Bastin, P., Nigg, E.A., et al. (2013). Molecular Basis of Tubulin Transport Within the Cilium by IFT74 and IFT81. *Science* *341*, 1009–1012.
- Bieniossek, C., Imasaki, T., Takagi, Y., and Berger, I. (2012). MultiBac: expanding the research toolbox for multiprotein complexes. *Trends in Biochemical Sciences* *37*, 49–57.
- Bigalke, J.M., and Heldwein, E.E. (2015). The Great (Nuclear) Escape: New Insights into the Role of the Nuclear Egress Complex of Herpesviruses. *Journal of Virology* *89*, 9150–9153.
- Bonnet, C., Boucher, D., Lazereg, S., Pedrotti, B., Islam, K., Denoulet, P., and Larcher, J.C. (2001). Differential Binding Regulation of Microtubule-associated Proteins MAP1A, MAP1B, and MAP2 by Tubulin Polyglutamylation. *J. Biol. Chem.* *276*, 12839–12848.
- Böttcher, S., Klupp, B.G., Granzow, H., Fuchs, W., Michael, K., and Mettenleiter, T.C. (2006). Identification of a 709-Amino-Acid Internal Nonessential Region within the Essential Conserved Tegument Protein (p)UL36 of Pseudorabies Virus. *Journal of Virology* *80*, 9910–9915.
- Bremner, K.H., Scherer, J., Yi, J., Verzhinin, M., Gross, S.P., and Vallee, R.B. (2009). Adenovirus transport via direct interaction of cytoplasmic dynein with the viral capsid hexon subunit. *Cell Host Microbe* *6*, 523–535.
- Brilot, A.F., Chen, J.Z., Cheng, A., Pan, J., Harrison, S.C., Potter, C.S., Carragher, B., Henderson, R., and Grigorieff, N. (2012). Beam-induced motion of vitrified specimen on holey carbon film. *Journal of Structural Biology* *177*, 630–637.
- Brokaw, C.J., and Kamiya, R. (1987). Bending patterns of *Chlamydomonas* flagella: IV. Mutants with defects in inner and outer dynein arms indicate differences in dynein arm function. *Cell Motility and the Cytoskeleton* *8*, 68–75.
- Brouhard, G.J., and Rice, L.M. (2014). The contribution of $\alpha\beta$ -tubulin curvature to microtubule dynamics. *J Cell Biol* *207*, 323–334.
- Brouhard, G.J., and Rice, L.M. (2018). Microtubule dynamics: an interplay of biochemistry and mechanics. *Nature Reviews Molecular Cell Biology* *19*, 451.
- Brown, J.C., and Newcomb, W.W. (2011). Herpesvirus capsid assembly: insights from structural analysis. *Curr Opin Virol* *1*, 142–149.
- Buch, A., Müller, O., Ivanova, L., Döhner, K., Bialy, D., Bosse, J.B., Pohlmann, A., Binz, A., Hegemann, M., Nagel, C.-H., et al. (2017). Inner tegument proteins of Herpes Simplex Virus are sufficient for intracellular capsid motility in neurons but not for axonal targeting. *PLoS Pathog.* *13*, e1006813.
- Bucks, M.A., O'Regan, K.J., Murphy, M.A., Wills, J.W., and Courtney, R.J. (2007). Herpes simplex virus type 1 tegument proteins VP1/2 and UL37 are associated with intranuclear capsids. *Virology* *361*, 316–324.
- Bui, K.H., Sakakibara, H., Movassagh, T., Oiwa, K., and Ishikawa, T. (2008). Molecular architecture of inner dynein arms in situ in *Chlamydomonas reinhardtii* flagella. *The Journal of Cell Biology* *183*, 923–932.
- Burgess, S.A., Walker, M.L., Sakakibara, H., Knight, P.J., and Oiwa, K. (2003). Dynein structure and power stroke. *Nature* *421*, 715–718.
- Burkhardt, J.K., Echeverri, C.J., Nilsson, T., and Vallee, R.B. (1997). Overexpression of the Dynamitin (p50) Subunit of the Dynactin Complex Disrupts Dynein-dependent Maintenance of Membrane Organelle Distribution. *J Cell Biol* *139*, 469–484.
- Burns, R.G. (1991). Alpha-, beta-, and gamma-tubulins: sequence comparisons and structural constraints. *Cell Motil. Cytoskeleton* *20*, 181–189.
- Calderilla-Barbosa, L., Seibenhener, M.L., Du, Y., Diaz-Meco, M.-T., Moscat, J., Yan, J., Wooten, M.W., and Wooten, M.C. (2014). Interaction of SQSTM1 with the motor protein dynein – SQSTM1 is required for normal dynein function and trafficking. *J Cell Sci* *127*, 4052–4063.
- Calero, M., Chen, C.Z., Zhu, W., Winand, N., Havas, K.A., Gilbert, P.M., Burd, C.G., and Collins, R.N. (2003). Dual Prenylation Is Required for Rab Protein Localization and Function. *MBoC* *14*, 1852–1867.
- Can, S., Dewitt, M.A., and Yildiz, A. (2014). Bidirectional helical motility of cytoplasmic dynein around microtubules. *ELife* *3*, e03205.
- Carnes, S.K., Zhou, J., and Aiken, C. (2018). HIV-1 Engages a Dynein-Dynactin-BICD2 Complex for Infection and Transport to the Nucleus. *J. Virol.* *JVI.00358-18*.
- Carter, A.P., Garbarino, J.E., Wilson-Kubalek, E.M., Shipley, W.E., Cho, C., Milligan, R.A., Vale, R.D., and Gibbons, I.R. (2008). Structure and functional role of dynein's microtubule-binding domain. *Science* *322*, 1691–1695.

- Carter, A.P., Cho, C., Jin, L., and Vale, R.D. (2011). Crystal structure of the dynein motor domain. *Science* *331*, 1159–1165.
- Case, R.B., Pierce, D.W., Hom-Booher, N., Hart, C.L., and Vale, R.D. (1997). The Directional Preference of Kinesin Motors Is Specified by an Element outside of the Motor Catalytic Domain. *Cell* *90*, 959–966.
- Celestino, R., Henen, M.A., Gama, J.B., Carvalho, C., McCabe, M., Barbosa, D.J., Born, A., Nichols, P.J., Carvalho, A.X., Gassmann, R., et al. (2019). A transient helix in the disordered region of dynein light intermediate chain links the motor to structurally diverse adaptors for cargo transport. *PLOS Biology* *17*, e3000100.
- Chen, Z., Suzuki, H., Kobayashi, Y., Wang, A.C., DiMaio, F., Kawashima, S.A., Walz, T., and Kapoor, T.M. (2018). Structural Insights into Mdn1, an Essential AAA Protein Required for Ribosome Biogenesis. *Cell* *175*, 822–834.e18.
- Cho, K., Cai, Y., Yi, H., Yeh, A., Aslanukov, A., and Ferreira, P.A. (2007). Association of the kinesin-binding domain of RanBP2 to KIF5B and KIF5C determines mitochondria localization and function. *Traffic* *8*, 1722–1735.
- Chrétien, D., Kenney, J.M., Fuller, S.D., and Wade, R.H. (1996). Determination of microtubule polarity by cryo-electron microscopy. *Structure* *4*, 1031–1040.
- Cleary, F.B., Dewitt, M.A., Bilyard, T., Htet, Z.M., Belyy, V., Chan, D.D., Chang, A.Y., and Yildiz, A. (2014). Tension on the linker gates the ATP-dependent release of dynein from microtubules. *Nature Communications* *5*, 4587.
- Clement, C., Tiwari, V., Scanlan, P.M., Valyi-Nagy, T., Yue, B.Y.J.T., and Shukla, D. (2006). A novel role for phagocytosis-like uptake in herpes simplex virus entry. *The Journal of Cell Biology* *174*, 1009–1021.
- Clift, D., McEwan, W.A., Labzin, L.I., Konieczny, V., Mogessie, B., James, L.C., and Schuh, M. (2017). A Method for the Acute and Rapid Degradation of Endogenous Proteins. *Cell* *171*, 1692–1706.e18.
- Coller, K.E., Lee, J.I.-H., Ueda, A., and Smith, G.A. (2007). The Capsid and Tegument of the Alphaherpesviruses Are Linked by an Interaction between the UL25 and VP1/2 Proteins. *J Virol* *81*, 11790–11797.
- Cooper, R.S., and Heldwein, E.E. (2015). Herpesvirus gB: A Finely Tuned Fusion Machine. *Viruses* *7*, 6552–6569.
- Copeland, A.M., Newcomb, W.W., and Brown, J.C. (2009). Herpes Simplex Virus Replication: Roles of Viral Proteins and Nucleoporins in Capsid-Nucleus Attachment. *J Virol* *83*, 1660–1668.
- Crump, C. (2018). Virus Assembly and Egress of HSV. In *Human Herpesviruses*, Y. Kawaguchi, Y. Mori, and H. Kimura, eds. (Singapore: Springer Singapore), pp. 23–44.
- Dai, X., and Zhou, Z.H. (2018). Structure of the herpes simplex virus 1 capsid with associated tegument protein complexes. *Science* *360*, eaao7298.
- Danev, R., and Baumeister, W. (2016). Cryo-EM single particle analysis with the Volta phase plate. *ELife* *5*, e13046.
- Daniel, G.R., Pegg, C.E., and Smith, G.A. (2018). Dissecting the Herpesvirus Architecture by Targeted Proteolysis. *Journal of Virology* *92*, e00738-18.
- De Rosier, D.J., and Klug, A. (1968). Reconstruction of Three Dimensional Structures from Electron Micrographs. *Nature* *217*, 130–134.
- DeRosier, D.J. (2000). Correction of high-resolution data for curvature of the Ewald sphere. *Ultramicroscopy* *81*, 83–98.
- Desai, P.J. (2000). A null mutation in the UL36 gene of herpes simplex virus type 1 results in accumulation of unenveloped DNA-filled capsids in the cytoplasm of infected cells. *J. Virol.* *74*, 11608–11618.
- Desai, A., and Mitchison, T.J. (1997). Microtubule Polymerization Dynamics. *Annual Review of Cell and Developmental Biology* *13*, 83–117.
- Desai, A., Verma, S., Mitchison, T.J., and Walczak, C.E. (1999). Kin I Kinesins Are Microtubule-Destabilizing Enzymes. *Cell* *96*, 69–78.
- Devadas, D., Koithan, T., Diestel, R., Prank, U., Sodeik, B., and Döhner, K. (2014). Herpes simplex virus internalization into epithelial cells requires Na⁺/H⁺ exchangers and p21-activated kinases but neither clathrin- nor caveolin-mediated endocytosis. *J. Virol.* *88*, 13378–13395.
- DeWitt, M.A., Chang, A.Y., Combs, P.A., and Yildiz, A. (2012). Cytoplasmic Dynein Moves Through Uncoordinated Stepping of the AAA+ Ring Domains. *Science* *335*, 221–225.
- DeWitt, M.A., Cypranowska, C.A., Cleary, F.B., Belyy, V., and Yildiz, A. (2015). The AAA3 domain of cytoplasmic dynein acts as a switch to facilitate microtubule release. *Nature Structural & Molecular Biology* *22*, 73–80.
- Dharan, A., Talley, S., Tripathi, A., Mamede, J.I., Majetschak, M., Hope, T.J., and Campbell, E.M. (2016). KIF5B and Nup358 Cooperatively Mediate the Nuclear Import of HIV-1 during Infection. *PLOS Pathogens* *12*, e1005700.
- Diefenbach, R.J. (2015). Conserved tegument protein complexes: Essential components in the assembly of herpesviruses. *Virus Res* *210*, 308–317.
- Diefenbach, R.J., Davis, A., Miranda-Saksena, M., Fernandez, M.A., Kelly, B.J., Jones, C.A., LaVail, J.H., Xue, J., Lai, J., and Cunningham, A.L. (2016). The Basic Domain of Herpes Simplex Virus 1 pUS9 Recruits Kinesin-1 To Facilitate Egress from Neurons. *Journal of Virology* *90*, 2102–2111.
- Dobro, M.J., Melanson, L.A., Jensen, G.J., and McDowell, A.W. (2010). Chapter Three - Plunge Freezing for Electron Cryomicroscopy. In *Methods in Enzymology*, G.J. Jensen, ed. (Academic Press), pp. 63–82.
- Dodding, M.P., and Way, M. (2011). Coupling viruses to dynein and kinesin-1. *EMBO J* *30*, 3527–3539.

- Döhner, K., Wolfstein, A., Prank, U., Echeverri, C., Dujardin, D., Vallee, R., and Sodeik, B. (2002a). Function of Dynein and Dynactin in Herpes Simplex Virus Capsid Transport. *Mol Biol Cell* *13*, 2795–2809.
- Döhner, K., Wolfstein, A., Prank, U., Echeverri, C., Dujardin, D., Vallee, R., and Sodeik, B. (2002b). Function of Dynein and Dynactin in Herpes Simplex Virus Capsid Transport. *MBoC* *13*, 2795–2809.
- Döhner, K., Ramos-Nascimento, A., Bialy, D., Anderson, F., Hickford-Martinez, A., Rother, F., Koithan, T., Rudolph, K., Buch, A., Prank, U., et al. (2018). Importin α 1 is required for nuclear import of herpes simplex virus proteins and capsid assembly in fibroblasts and neurons. *PLOS Pathogens* *14*, e1006823.
- Dougherty, G.W., Loges, N.T., Klinkenbusch, J.A., Olbrich, H., Pennekamp, P., Menchen, T., Raidt, J., Wallmeier, J., Werner, C., Westermann, C., et al. (2016). DNAH11 Localization in the Proximal Region of Respiratory Cilia Defines Distinct Outer Dynein Arm Complexes. *Am J Respir Cell Mol Biol* *55*, 213–224.
- Drozdetskiy, A., Cole, C., Procter, J., and Barton, G.J. (2015). JPred4: a protein secondary structure prediction server. *Nucleic Acids Res* *43*, W389–W394.
- Drulyte, I., Johnson, R.M., Hesketh, E.L., Hurdiss, D.L., Scarff, C.A., Porav, S.A., Ranson, N.A., Muench, S.P., and Thompson, R.F. (2018). Approaches to altering particle distributions in cryo-electron microscopy sample preparation. *Acta Crystallogr D Struct Biol* *74*, 560–571.
- Dubochet, J., Adrian, M., Chang, J.-J., Homo, J.-C., Lepault, J., McDowell, A.W., and Schultz, P. (1988). Cryo-electron microscopy of vitrified specimens. 100.
- Duellberg, C., Cade, N.I., Holmes, D., and Surrey, T. (2016). The size of the EB cap determines instantaneous microtubule stability. *ELife* *5*.
- Eckley, D.M., Gill, S.R., Melkonian, K.A., Bingham, J.B., Goodson, H.V., Heuser, J.E., and Schroer, T.A. (1999). Analysis of Dynactin Subcomplexes Reveals a Novel Actin-Related Protein Associated with the Arp1 Minifilament Pointed End. *J Cell Biol* *147*, 307–320.
- Egerton, R.F. (2005). *Physical Principles of Electron Microscopy: An Introduction to TEM, SEM, and AEM* (Springer US).
- Eisenberg, R.J., Atanasiu, D., Cairns, T.M., Gallagher, J.R., Krummenacher, C., and Cohen, G.H. (2012). Herpes virus fusion and entry: a story with many characters. *Viruses* *4*, 800–832.
- Elie-Caille, C., Severin, F., Helenius, J., Howard, J., Muller, D.J., and Hyman, A.A. (2007). Straight GDP-Tubulin Protofilaments Form in the Presence of Taxol. *Current Biology* *17*, 1765–1770.
- Emsley, P., and Cowtan, K. (2004). Coot: model-building tools for molecular graphics. *Acta Crystallogr. D Biol. Crystallogr.* *60*, 2126–2132.
- Endow, S.A., and Waligora, K.W. (1998). Determinants of Kinesin Motor Polarity. *Science* *281*, 1200–1202.
- Endow, S.A., Kull, F.J., and Liu, H. (2010). Kinesins at a glance. *J Cell Sci* *123*, 3420–3424.
- Endres, N.F., Yoshioka, C., Milligan, R.A., and Vale, R.D. (2006). A lever-arm rotation drives motility of the minus-end-directed kinesin Ncd. *Nature* *439*, 875–878.
- Engel, B.D., Ishikawa, H., Wemmer, K.A., Geimer, S., Wakabayashi, K., Hirono, M., Craige, B., Pazour, G.J., Witman, G.B., Kamiya, R., et al. (2012). The role of retrograde intraflagellar transport in flagellar assembly, maintenance, and function. *J. Cell Biol.* *199*, 151–167.
- Erickson, H.P., and Klug, A. (1971). Measurement and Compensation of Defocusing and Aberrations by Fourier Processing of Electron Micrographs. *Philosophical Transactions of the Royal Society B: Biological Sciences* *261*, 105–118.
- Eshun-Wilson, L., Zhang, R., Portran, D., Nachury, M., Toso, D., Lohr, T., Vendruscolo, M., Bonomi, M., Fraser, J., and Nogales, E. (2019). Effects of α -tubulin acetylation on microtubule structure and stability. *BioRxiv* 516591.
- Farnsworth, A., Wisner, T.W., Webb, M., Roller, R., Cohen, G., Eisenberg, R., and Johnson, D.C. (2007). Herpes simplex virus glycoproteins gB and gH function in fusion between the virion envelope and the outer nuclear membrane. *PNAS* *104*, 10187–10192.
- Fink, G., Hajdo, L., Skowronek, K.J., Reuther, C., Kasprzak, A.A., and Diez, S. (2009). The mitotic kinesin-14 Ncd drives directional microtubule–microtubule sliding. *Nature Cell Biology* *11*, 717–723.
- Franker, M.A.M., and Hoogenraad, C.C. (2013). Microtubule-based transport – basic mechanisms, traffic rules and role in neurological pathogenesis. *J Cell Sci* *126*, 2319–2329.
- Fuchs, W., Klupp, B.G., Granzow, H., and Mettenleiter, T.C. (2004a). Essential Function of the Pseudorabies Virus UL36 Gene Product Is Independent of Its Interaction with the UL37 Protein. *J Virol* *78*, 11879–11889.
- Fuchs, W., Klupp, B.G., Granzow, H., and Mettenleiter, T.C. (2004b). Essential Function of the Pseudorabies Virus UL36 Gene Product Is Independent of Its Interaction with the UL37 Protein. *J Virol* *78*, 11879–11889.
- Fygenson, null, Braun, null, and Libchaber, null (1994). Phase diagram of microtubules. *Phys Rev E Stat Phys Plasmas Fluids Relat Interdiscip Topics* *50*, 1579–1588.
- Gama, J.B., Pereira, C., Simões, P.A., Celestino, R., Reis, R.M., Barbosa, D.J., Pires, H.R., Carvalho, C., Amorim, J., Carvalho, A.X., et al. (2017). Molecular mechanism of dynein recruitment to kinetochores by the Rod–Zw10–Zwlich complex and Spindly. *J Cell Biol* *216*, 943–960.
- Gee, M.A., Heuser, J.E., and Vallee, R.B. (1997). An extended microtubule-binding structure within the dynein motor domain. *Nature* *390*, 636–639.
- Gennerich, A., Carter, A.P., Reck-Peterson, S.L., and Vale, R.D. (2007). Force-Induced Bidirectional Stepping of Cytoplasmic Dynein. *Cell* *131*, 952–965.

- Geraghty, R.J., Krummenacher, C., Cohen, G.H., Eisenberg, R.J., and Spear, P.G. (1998). Entry of Alphaherpesviruses Mediated by Poliovirus Receptor-Related Protein 1 and Poliovirus Receptor. *Science* **280**, 1618–1620.
- Gibbons, I.R., Garbarino, J.E., Tan, C.E., Reck-Peterson, S.L., Vale, R.D., and Carter, A.P. (2005a). The Affinity of the Dynein Microtubule-Binding Domain is Modulated by the Conformation of its Coiled-Coil Stalk. *J Biol Chem* **280**, 23960–23965.
- Gibbons, I.R., Garbarino, J.E., Tan, C.E., Reck-Peterson, S.L., Vale, R.D., and Carter, A.P. (2005b). The Affinity of the Dynein Microtubule-binding Domain Is Modulated by the Conformation of Its Coiled-coil Stalk. *J. Biol. Chem.* **280**, 23960–23965.
- Gindhart, J.G., Desai, C.J., Beushausen, S., Zinn, K., and Goldstein, L.S.B. (1998). Kinesin Light Chains Are Essential for Axonal Transport in *Drosophila*. *The Journal of Cell Biology* **141**, 443–454.
- Glaeser, R.M. (2018). Proteins, interfaces, and cryo-EM grids. *Current Opinion in Colloid & Interface Science* **34**, 1–8.
- Glaeser, R.M., and Han, B.-G. (2017). Opinion: hazards faced by macromolecules when confined to thin aqueous films. *Biophysics Reports* **3**, 1–7.
- Gleave, E.S., Schmidt, H., and Carter, A.P. (2014). A structural analysis of the AAA+ domains in *Saccharomyces cerevisiae* cytoplasmic dynein. *J Struct Biol* **186**, 367–375.
- Grant, T., Rohou, A., and Grigorieff, N. (2018). cisTEM, user-friendly software for single-particle image processing. *ELife* **7**, e35383.
- Granzow, H., Klupp, B.G., and Mettenleiter, T.C. (2005). Entry of Pseudorabies Virus: an Immunogold-Labeling Study. *Journal of Virology* **79**, 3200–3205.
- Grotjahn, D.A., Chowdhury, S., Xu, Y., McKenney, R.J., Schroer, T.A., and Lander, G.C. (2018). Cryo-electron tomography reveals that dynactin recruits a team of dyneins for processive motility. *Nat Struct Mol Biol* **25**, 203–207.
- Grünewald, K., Desai, P., Winkler, D.C., Heymann, J.B., Belnap, D.M., Baumeister, W., and Steven, A.C. (2003). Three-Dimensional Structure of Herpes Simplex Virus from Cryo-Electron Tomography. *Science* **302**, 1396–1398.
- Hafezi, W., Lorentzen, E.U., Eing, B.R., Müller, M., King, N.J.C., Klupp, B., Mettenleiter, T.C., and Kühn, J.E. (2012). Entry of Herpes Simplex Virus Type 1 (HSV-1) into the Distal Axons of Trigeminal Neurons Favors the Onset of Nonproductive, Silent Infection. *PLOS Pathogens* **8**, e1002679.
- Hagen, C., Dent, K.C., Zeev-Ben-Mordehai, T., Grange, M., Bosse, J.B., Whittle, C., Klupp, B.G., Siebert, C.A., Vasishtan, D., Bäuerlein, F.J.B., et al. (2015). Structural Basis of Vesicle Formation at the Inner Nuclear Membrane. *Cell* **163**, 1692–1701.
- Hamada, M., Haeger, A., Jeganathan, K.B., Ree, J.H. van, Malureanu, L., Wälde, S., Joseph, J., Kehlenbach, R.H., and Deursen, J.M. van (2011). Ran-dependent docking of importin- β to RanBP2/Nup358 filaments is essential for protein import and cell viability. *The Journal of Cell Biology* **194**, 597–612.
- Hampoelz, B., Mackmull, M.-T., Machado, P., Ronchi, P., Bui, K.H., Schieber, N., Santarella-Mellwig, R., Necakov, A., Andrés-Pons, A., Philippe, J.M., et al. (2016). Pre-assembled Nuclear Pores Insert into the Nuclear Envelope during Early Development. *Cell* **166**, 664–678.
- Hanz, S., Perlson, E., Willis, D., Zheng, J.-Q., Massarwa, R., Huerta, J.J., Koltzenburg, M., Kohler, M., van-Minnen, J., Twiss, J.L., et al. (2003). Axoplasmic Importins Enable Retrograde Injury Signaling in Lesioned Nerve. *Neuron* **40**, 1095–1104.
- Hao, L., and Scholey, J.M. (2009). Intraflagellar transport at a glance. *Journal of Cell Science* **122**, 889–892.
- Harada, A., Takei, Y., Kanai, Y., Tanaka, Y., Nonaka, S., and Hirokawa, N. (1998). Golgi vesiculation and lysosome dispersion in cells lacking cytoplasmic dynein. *J. Cell Biol.* **141**, 51–59.
- Hartman, M.A., and Spudich, J.A. (2012). The myosin superfamily at a glance. *J Cell Sci* **125**, 1627–1632.
- He, S., and Scheres, S.H.W. (2017). Helical reconstruction in RELION. *Journal of Structural Biology* **198**, 163–176.
- Heerssen, H.M., Pazyra, M.F., and Segal, R.A. (2004). Dynein motors transport activated Trks to promote survival of target-dependent neurons. *Nature Neuroscience* **7**, 596.
- Heming, J.D., Conway, J.F., and Homa, F.L. (2017). Herpesvirus capsid assembly and DNA packaging. *Adv Anat Embryol Cell Biol* **223**, 119–142.
- Henderson, R. (1995). The potential and limitations of neutrons, electrons and X-rays for atomic resolution microscopy of unstained biological molecules. *Quarterly Reviews of Biophysics* **28**, 171.
- Heymann, J.B., Cheng, N., Newcomb, W.W., Trus, B.L., Brown, J.C., and Steven, A.C. (2003). Dynamics of herpes simplex virus capsid maturation visualized by time-lapse cryo-electron microscopy. *Nature Structural & Molecular Biology* **10**, 334–341.
- Hirokawa, N., Noda, Y., Tanaka, Y., and Niwa, S. (2009). Kinesin superfamily motor proteins and intracellular transport. *Nature Reviews Molecular Cell Biology* **10**, 682–696.
- Höing, S., Yeh, T.-Y., Baumann, M., Martinez, N.E., Habenberger, P., Kremer, L., Drexler, H.C.A., Küchler, P., Reinhardt, P., Choidas, A., et al. (2018). Dynarrestin, a Novel Inhibitor of Cytoplasmic Dynein. *Cell Chemical Biology* **25**, 357-369.e6.
- Hom, E.F.Y., Witman, G.B., Harris, E.H., Dutcher, S.K., Kamiya, R., Mitchell, D.R., Pazour, G.J., Porter, M.E., Sale, W.S., Wirschell, M., et al. (2011). A unified taxonomy for ciliary dyneins. *Cytoskeleton* **68**, 555–565.

- Hoogenraad, C.C., Akhmanova, A., Howell, S.A., Dortland, B.R., De Zeeuw, C.I., Willemsen, R., Visser, P., Grosveld, F., and Galjart, N. (2001). Mammalian Golgi-associated Bicaudal-D2 functions in the dynein-dynactin pathway by interacting with these complexes. *EMBO J.* *20*, 4041–4054.
- Hoogenraad, C.C., Wulf, P., Schiefermeier, N., Stepanova, T., Galjart, N., Small, J.V., Grosveld, F., Zeeuw, C.I. de, and Akhmanova, A. (2003). Bicaudal D induces selective dynein - mediated microtubule minus end - directed transport. *The EMBO Journal* *22*, 6004–6015.
- Horgan, C.P., Hanscom, S.R., Jolly, R.S., Futter, C.E., and McCaffrey, M.W. (2010). Rab11-FIP3 links the Rab11 GTPase and cytoplasmic dynein to mediate transport to the endosomal-recycling compartment. *J Cell Sci* *123*, 181–191.
- Horio, T., and Hotani, H. (1986). Visualization of the dynamic instability of individual microtubules by dark-field microscopy. *Nature* *321*, 605–607.
- Howard, P.W., Howard, T.L., and Johnson, D.C. (2013). Herpes Simplex Virus Membrane Proteins gE/gI and US9 Act Cooperatively To Promote Transport of Capsids and Glycoproteins from Neuron Cell Bodies into Initial Axon Segments. *Journal of Virology* *87*, 403–414.
- Howell, B.J., McEwen, B.F., Canman, J.C., Hoffman, D.B., Farrar, E.M., Rieder, C.L., and Salmon, E.D. (2001). Cytoplasmic dynein/dynactin drives kinetochore protein transport to the spindle poles and has a role in mitotic spindle checkpoint inactivation. *J. Cell Biol.* *155*, 1159–1172.
- Hueschen, C.L., Kenny, S.J., Xu, K., and Dumont, S. (2017). NuMA recruits dynein activity to microtubule minus-ends at mitosis. *Elife* *6*.
- Huet, A., Makhov, A.M., Huffman, J.B., Vos, M., Homa, F.L., and Conway, J.F. (2016). Extensive subunit contacts underpin herpesvirus capsid stability and interior-to-exterior allostery. *Nature Structural & Molecular Biology* *23*, 531–539.
- Huffmaster, N.J., Sollars, P.J., Richards, A.L., Pickard, G.E., and Smith, G.A. (2015). Dynamic ubiquitination drives herpesvirus neuroinvasion. *PNAS* *112*, 12818–12823.
- Hunter, A.W., Caplow, M., Coy, D.L., Hancock, W.O., Diez, S., Wordeman, L., and Howard, J. (2003). The Kinesin-Related Protein MCAK Is a Microtubule Depolymerase that Forms an ATP-Hydrolyzing Complex at Microtubule Ends. *Molecular Cell* *11*, 445–457.
- Hutchinson, I., Whiteley, A., Browne, H., and Elliott, G. (2002). Sequential Localization of Two Herpes Simplex Virus Tegument Proteins to Punctate Nuclear Dots Adjacent to ICP0 Domains. *J Virol* *76*, 10365–10373.
- Ibiricu, I., Huiskonen, J.T., Döhner, K., Bradke, F., Sodeik, B., and Grünewald, K. (2011). Cryo Electron Tomography of Herpes Simplex Virus during Axonal Transport and Secondary Envelopment in Primary Neurons. *PLOS Pathogens* *7*, e1002406.
- Ichikawa, M., Liu, D., Kastiris, P.L., Basu, K., Hsu, T.C., Yang, S., and Bui, K.H. (2017). Subnanometre-resolution structure of the doublet microtubule reveals new classes of microtubule-associated proteins. *Nature Communications* *8*, 15035.
- Imai, H., Shima, T., Sutoh, K., Walker, M.L., Knight, P.J., Kon, T., and Burgess, S.A. (2015). Direct observation shows superposition and large scale flexibility within cytoplasmic dynein motors moving along microtubules. *Nature Communications* *6*, 8179.
- Imamula, K., Kon, T., Ohkura, R., and Sutoh, K. (2007). The coordination of cyclic microtubule association/dissociation and tail swing of cytoplasmic dynein. *PNAS* *104*, 16134–16139.
- Ishikawa, T. (2016). Axoneme Structure from Motile Cilia. *Cold Spring Harb Perspect Biol* a028076.
- Ishikawa, H., and Marshall, W.F. (2017). Intraflagellar Transport and Ciliary Dynamics. *Cold Spring Harb Perspect Biol* *9*, a021998.
- Ishikawa, T., Sakakibara, H., and Oiwa, K. (2007). The Architecture of Outer Dynein Arms in Situ. *Journal of Molecular Biology* *368*, 1249–1258.
- Jambunathan, N., Chouljenko, D., Desai, P., Charles, A.-S., Subramanian, R., Chouljenko, V.N., and Kousoulas, K.G. (2014). Herpes Simplex Virus 1 Protein UL37 Interacts with Viral Glycoprotein gK and Membrane Protein UL20 and Functions in Cytoplasmic Virion Envelopment. *Journal of Virology* *88*, 5927–5935.
- Johnson, D.C., and Baines, J.D. (2011). Herpesviruses remodel host membranes for virus egress. *Nature Reviews Microbiology* *9*, 382–394.
- Johnston, J.A., Ward, C.L., and Kopito, R.R. (1998). Aggresomes: A Cellular Response to Misfolded Proteins. *J Cell Biol* *143*, 1883–1898.
- Johnston, J.A., Illing, M.E., and Kopito, R.R. (2002). Cytoplasmic dynein/dynactin mediates the assembly of aggresomes. *Cell Motil. Cytoskeleton* *53*, 26–38.
- Jordan, M.A., Diener, D.R., Stepanek, L., and Pigino, G. (2018). The cryo-EM structure of intraflagellar transport trains reveals how dynein is inactivated to ensure unidirectional anterograde movement in cilia. *Nature Cell Biology* *20*, 1250.
- Jovasevic, V., Liang, L., and Roizman, B. (2008). Proteolytic Cleavage of VP1-2 Is Required for Release of Herpes Simplex Virus 1 DNA into the Nucleus. *Journal of Virology* *82*, 3311–3319.
- Jovasevic, V., Naghavi, M.H., and Walsh, D. (2015). Microtubule plus end-associated CLIP-170 initiates HSV-1 retrograde transport in primary human cells. *J Cell Biol* *211*, 323–337.

- Kadavath, H., Hofele, R.V., Biernat, J., Kumar, S., Tepper, K., Urlaub, H., Mandelkow, E., and Zweckstetter, M. (2015). Tau stabilizes microtubules by binding at the interface between tubulin heterodimers. *Proc. Natl. Acad. Sci. U.S.A.* *112*, 7501–7506.
- Kamiya, R., and Okamoto, M. (1985). A mutant of *Chlamydomonas reinhardtii* that lacks the flagellar outer dynein arm but can swim. *Journal of Cell Science* *74*, 181–191.
- Kamiya, R., and Yagi, T. (2014). Functional diversity of axonemal dyneins as assessed by in vitro and in vivo motility assays of *Chlamydomonas* mutants. *Zool. Sci.* *31*, 633–644.
- Kamiya, R., Kurimoto, E., and Muto, E. (1991). Two types of *Chlamydomonas* flagellar mutants missing different components of inner-arm dynein. *J. Cell Biol.* *112*, 441–447.
- Kapitein, L.C., Peterman, E.J.G., Kwok, B.H., Kim, J.H., Kapoor, T.M., and Schmidt, C.F. (2005). The bipolar mitotic kinesin Eg5 moves on both microtubules that it crosslinks. *Nature* *435*, 114.
- Kapoor, T.M., Mayer, T.U., Coughlin, M.L., and Mitchison, T.J. (2000). Probing Spindle Assembly Mechanisms with Monastrol, a Small Molecule Inhibitor of the Mitotic Kinesin, Eg5. *The Journal of Cell Biology* *150*, 975–988.
- Kashlana, A.S., Baskin, R.J., Cole, D.G., Wedaman, K.P., Saxton, W.M., and Scholey, J.M. (1996). A bipolar kinesin. *Nature* *379*, 270.
- Kato, Y.S., Yagi, T., Harris, S.A., Ohki, S., Yura, K., Shimizu, Y., Honda, S., Kamiya, R., Burgess, S.A., and Tanokura, M. (2014). Structure of the Microtubule-Binding Domain of Flagellar Dynein. *Structure* *22*, 1628–1638.
- Kawaguchi, Y., Kovacs, J.J., McLaurin, A., Vance, J.M., Ito, A., and Yao, T.-P. (2003). The Deacetylase HDAC6 Regulates Aggresome Formation and Cell Viability in Response to Misfolded Protein Stress. *Cell* *115*, 727–738.
- Kellogg, E.H., Hejab, N.M.A., Howes, S., Northcote, P., Miller, J.H., Díaz, J.F., Downing, K.H., and Nogales, E. (2017). Insights into the Distinct Mechanisms of Action of Taxane and Non-Taxane Microtubule Stabilizers from Cryo-EM Structures. *Journal of Molecular Biology* *429*, 633–646.
- Kellogg, E.H., Hejab, N.M.A., Poepsel, S., Downing, K.H., DiMaio, F., and Nogales, E. (2018). Near-atomic model of microtubule-tau interactions. *Science* *360*, 1242–1246.
- Kim, D.-H., Kwon, S., Byun, S., Xiao, Z., Park, S., Wu, S.-Y., Chiang, C.-M., Kemper, B., and Kemper, J.K. (2016). Critical role of RanBP2-mediated SUMOylation of Small Heterodimer Partner in maintaining bile acid homeostasis. *Nature Communications* *7*.
- Kimura, S., Noda, T., and Yoshimori, T. (2008). Dynein-dependent Movement of Autophagosomes Mediates Efficient Encounters with Lysosomes. *Cell Struct. Funct.* *33*, 109–122.
- King, S.M. (2000). AAA domains and organization of the dynein motor unit. *J Cell Sci* *113*, 2521–2526.
- King, S.M. (2016). Axonemal Dynein Arms. *Cold Spring Harb Perspect Biol* *8*, a028100.
- King, S.J., Brown, C.L., Maier, K.C., Quintyne, N.J., and Schroer, T.A. (2003). Analysis of the Dynein-Dynactin Interaction In Vitro and In Vivo. *Mol Biol Cell* *14*, 5089–5097.
- Klingen, Y., Conzelmann, K.-K., and Finke, S. (2008). Double-Labeled Rabies Virus: Live Tracking of Enveloped Virus Transport. *Journal of Virology* *82*, 237–245.
- Klupp, B., Altenschmidt, J., Granzow, H., Fuchs, W., and Mettenleiter, T.C. (2008). Glycoproteins Required for Entry Are Not Necessary for Egress of Pseudorabies Virus. *J Virol* *82*, 6299–6309.
- Klupp, B.G., Fuchs, W., Granzow, H., Nixdorf, R., and Mettenleiter, T.C. (2002). Pseudorabies Virus UL36 Tegument Protein Physically Interacts with the UL37 Protein. *Journal of Virology* *76*, 3065–3071.
- Knipe, D.M., and Howley, P.M. (2007). *Fields' Virology* (Lippincott Williams & Wilkins).
- Knockenauer, K.E., and Schwartz, T.U. (2016). The Nuclear Pore Complex as a Flexible and Dynamic Gate. *Cell* *164*, 1162–1171.
- Kollman, J.M., Greenberg, C.H., Li, S., Moritz, M., Zelter, A., Fong, K.K., Fernandez, J.-J., Sali, A., Kilmartin, J., Davis, T.N., et al. (2015). Ring closure activates yeast γ TuRC for species-specific microtubule nucleation. *Nature Structural & Molecular Biology* *22*, 132–137.
- Kollmar, M. (2016). Fine-Tuning Motile Cilia and Flagella: Evolution of the Dynein Motor Proteins from Plants to Humans at High Resolution. *Mol Biol Evol* *33*, 3249–3267.
- Kon, T., Nishiura, M., Ohkura, R., Toyoshima, Y.Y., and Sutoh, K. (2004). Distinct Functions of Nucleotide-Binding/Hydrolysis Sites in the Four AAA Modules of Cytoplasmic Dynein[†]. *Biochemistry* *43*, 11266–11274.
- Kon, T., Imamula, K., Roberts, A.J., Ohkura, R., Knight, P.J., Gibbons, I.R., Burgess, S.A., and Sutoh, K. (2009). Helix sliding in the stalk coiled coil of dynein couples ATPase and microtubule binding. *Nature Structural & Molecular Biology* *16*, 325–333.
- Kon, T., Sutoh, K., and Kurisu, G. (2011). X-ray structure of a functional full-length dynein motor domain. *Nat. Struct. Mol. Biol.* *18*, 638–642.
- Kon, T., Oyama, T., Shimo-Kon, R., Imamula, K., Shima, T., Sutoh, K., and Kurisu, G. (2012). The 2.8 Å crystal structure of the dynein motor domain. *Nature* *484*, 345–350.
- Koonce, M.P., Tikhonenko, I., and McIntosh, J.R. (2000). Functional Elements within the Dynein Microtubule-binding Domain. *MBoC* *11*, 523–529.
- Koyuncu, O.O., Perlman, D.H., and Enquist, L.W. (2013). Efficient Retrograde Transport of Pseudorabies Virus within Neurons Requires Local Protein Synthesis in Axons. *Cell Host & Microbe* *13*, 54–66.

- Koyuncu, O.O., Song, R., Greco, T.M., Cristea, I.M., and Enquist, L.W. (2015). The Number of Alphaherpesvirus Particles Infecting Axons and the Axonal Protein Repertoire Determines the Outcome of Neuronal Infection. *MBio* 6, e00276-15.
- Koyuncu, O.O., MacGibeny, M.A., and Enquist, L.W. (2018). Latent versus productive infection: the alpha herpesvirus switch.
- Kramer, T., Greco, T.M., Enquist, L.W., and Cristea, I.M. (2011). Proteomic characterization of pseudorabies virus extracellular virions. *J. Virol.* 85, 6427–6441.
- Kramer, T., Greco, T.M., Taylor, M.P., Ambrosini, A.E., Cristea, I.M., and Enquist, L.W. (2012). Kinesin-3 Mediates Axonal Sorting and Directional Transport of Alphaherpesvirus Particles in Neurons. *Cell Host & Microbe* 12, 806–814.
- Krautwald, M., Fuchs, W., Klupp, B.G., and Mettenleiter, T.C. (2009). Translocation of Incoming Pseudorabies Virus Capsids to the Cell Nucleus Is Delayed in the Absence of Tegument Protein pUL37. *J Virol* 83, 3389–3396.
- Kull, F.J., Sablin, E.P., Lau, R., Fletterick, R.J., and Vale, R.D. (1996). Crystal structure of the kinesin motor domain reveals a structural similarity to myosin. *Nature* 380, 550–555.
- Laine, R.F., Albecka, A., van de Linde, S., Rees, E.J., Crump, C.M., and Kaminski, C.F. (2015). Structural analysis of herpes simplex virus by optical super-resolution imaging. *Nature Communications* 6, 5980.
- Law, B.M.H., Spain, V.A., Leinster, V.H.L., Chia, R., Beilina, A., Cho, H.J., Taymans, J.-M., Urban, M.K., Sancho, R.M., Ramírez, M.B., et al. (2014). A Direct Interaction between Leucine-rich Repeat Kinase 2 and Specific β -Tubulin Isoforms Regulates Tubulin Acetylation. *J. Biol. Chem.* 289, 895–908.
- Lawrence, C.J., Morris, N.R., Meagher, R.B., and Dawe, R.K. (2001). Dyneins Have Run Their Course in Plant Lineage. *Traffic* 2, 362–363.
- Lawrence, C.J., Dawe, R.K., Christie, K.R., Cleveland, D.W., Dawson, S.C., Endow, S.A., Goldstein, L.S.B., Goodson, H.V., Hirokawa, N., Howard, J., et al. (2004). A standardized kinesin nomenclature. *The Journal of Cell Biology* 167, 19–22.
- Lee, J.H., and Gleeson, J.G. (2010). The role of primary cilia in neuronal function. *Neurobiol. Dis.* 38, 167–172.
- Lee, I.-G., Olenick, M.A., Boczkowska, M., Franzini-Armstrong, C., Holzbaur, E.L.F., and Dominguez, R. (2018). A conserved interaction of the dynein light intermediate chain with dynein-dynactin effectors necessary for processivity. *Nature Communications* 9.
- Lee, J.H., Vittone, V., Diefenbach, E., Cunningham, A.L., and Diefenbach, R.J. (2008). Identification of structural protein–protein interactions of herpes simplex virus type 1. *Virology* 378, 347–354.
- Lee, J.I., Sollars, P.J., Baver, S.B., Pickard, G.E., Leelawong, M., and Smith, G.A. (2009). A Herpesvirus Encoded Deubiquitinase Is a Novel Neuroinvasive Determinant. *PLOS Pathogens* 5, e1000387.
- Lewis, S.A., Lee, M.G., and Cowan, N.J. (1985). Five mouse tubulin isotypes and their regulated expression during development. *The Journal of Cell Biology* 101, 852–861.
- L’Hernault, S.W. (1983). Chlamydomonas alpha-tubulin is posttranslationally modified in the flagella during flagellar assembly. *The Journal of Cell Biology* 97, 258–263.
- Lieberman, P.M. (2016). Epigenetics and Genetics of Viral Latency. *Cell Host & Microbe* 19, 619–628.
- Lin, J., and Nicastro, D. (2018). Asymmetric distribution and spatial switching of dynein activity generates ciliary motility. *Science* 360, eaar1968.
- Lin, J., Okada, K., Raytchev, M., Smith, M.C., and Nicastro, D. (2014). Structural mechanism of the dynein powerstroke. *Nat Cell Biol* 16, 479–485.
- Liu, D., Liu, X., Shang, Z., and Sindelar, C.V. (2017). Structural basis of cooperativity in kinesin revealed by 3D reconstruction of a two-head-bound state on microtubules. *ELife* 6, e24490.
- Liu, Y., Salter, H.K., Holding, A.N., Johnson, C.M., Stephens, E., Lukavsky, P.J., Walshaw, J., and Bullock, S.L. (2013). Bicaudal-D uses a parallel, homodimeric coiled coil with heterotypic registry to coordinate recruitment of cargos to dynein. *Genes Dev.*
- Liu, Z., Takazaki, H., Nakazawa, Y., Sakato, M., Yagi, T., Yasunaga, T., King, S.M., and Kamiya, R. (2008). Partially Functional Outer-Arm Dynein in a Novel Chlamydomonas Mutant Expressing a Truncated γ Heavy Chain. *Eukaryotic Cell* 7, 1136–1145.
- Loret, S., Guay, G., and Lippé, R. (2008). Comprehensive Characterization of Extracellular Herpes Simplex Virus Type 1 Virions. *Journal of Virology* 82, 8605–8618.
- Löwe, J., Li, H., Downing, K.H., and Nogales, E. (2001). Refined structure of $\alpha\beta$ -tubulin at 3.5 Å resolution 1 1Edited by I. A. Wilson. *Journal of Molecular Biology* 313, 1045–1057.
- Ludueña, R.F. (1993). Are tubulin isotypes functionally significant. *Mol Biol Cell* 4, 445–457.
- Luxton, G.W.G., Haverlock, S., Coller, K.E., Antinone, S.E., Pincetic, A., and Smith, G.A. (2005). Targeting of herpesvirus capsid transport in axons is coupled to association with specific sets of tegument proteins. *Proceedings of the National Academy of Sciences* 102, 5832–5837.
- Lyman, M.G., and Enquist, L.W. (2009). Herpesvirus Interactions with the Host Cytoskeleton. *J Virol* 83, 2058–2066.
- Manka, S.W., and Moores, C.A. (2018). The role of tubulin–tubulin lattice contacts in the mechanism of microtubule dynamic instability. *Nature Structural & Molecular Biology* 25, 607.

- Matanis, T., Akhmanova, A., Wulf, P., Del Nery, E., Weide, T., Stepanova, T., Galjart, N., Grosveld, F., Goud, B., De Zeeuw, C.I., et al. (2002). Bicaudal-D regulates COPI-independent Golgi-ER transport by recruiting the dynein-dynactin motor complex. *Nature Cell Biology* 4, 986–992.
- Maurer, U.E., Sodeik, B., and Grunewald, K. (2008). Native 3D intermediates of membrane fusion in herpes simplex virus 1 entry. *PNAS* 105, 10559–10564.
- Mavlyutov, T.A., Cai, Y., and Ferreira, P.A. (2002). Identification of RanBP2- and Kinesin-Mediated Transport Pathways with Restricted Neuronal and Subcellular Localization. *Traffic* 3, 630–640.
- McElwee, M., Beilstein, F., Labetoulle, M., Rixon, F.J., and Padeloup, D. (2013). Dystonin/BPAG1 Promotes Plus-End-Directed Transport of Herpes Simplex Virus 1 Capsids on Microtubules during Entry. *J Virol* 87, 11008–11018.
- McElwee, M., Vijayakrishnan, S., Rixon, F., and Bhella, D. (2018). Structure of the herpes simplex virus portal-vertex. *PLOS Biology* 16, e2006191.
- McKenney, R.J., Huynh, W., Tanenbaum, M.E., Bhabha, G., and Vale, R.D. (2014). Activation of cytoplasmic dynein motility by dynactin-cargo adapter complexes. *Science* 345, 337–341.
- McKenney, R.J., Huynh, W., Vale, R.D., and Sirajuddin, M. (2016). Tyrosination of α -tubulin controls the initiation of processive dynein-dynactin motility. *The EMBO Journal* 35, 1175–1185.
- McMullan, G., Faruqi, A.R., Clare, D., and Henderson, R. (2014). Comparison of optimal performance at 300 keV of three direct electron detectors for use in low dose electron microscopy. *Ultramicroscopy* 147, 156–163.
- McNally, F.J. (2013). Mechanisms of spindle positioning. *J Cell Biol* 200, 131–140.
- McNaughton, L., Tikhonenko, I., Banavali, N.K., LeMaster, D.M., and Koonce, M.P. (2010). A low affinity ground state conformation for the Dynein microtubule binding domain. *J. Biol. Chem.* 285, 15994–16002.
- Meads, T., and Schroer, T.A. (1995). Polarity and nucleation of microtubules in polarized epithelial cells. *Cell Motility and the Cytoskeleton* 32, 273–288.
- Merdes, A., Ramyar, K., Vechio, J.D., and Cleveland, D.W. (1996). A Complex of NuMA and Cytoplasmic Dynein Is Essential for Mitotic Spindle Assembly. *Cell* 87, 447–458.
- Mettenleiter, T.C., Müller, F., Granzow, H., and Klupp, B.G. (2013). The way out: what we know and do not know about herpesvirus nuclear egress. *Cellular Microbiology* 15, 170–178.
- Meunier, S., and Vernos, I. (2012). Microtubule assembly during mitosis – from distinct origins to distinct functions? *J Cell Sci* 125, 2805–2814.
- Miki, H., Setou, M., Kaneshiro, K., and Hirokawa, N. (2001). All kinesin superfamily protein, KIF, genes in mouse and human. *PNAS* 98, 7004–7011.
- Miller, J.M., and Enemark, E.J. (2016). Fundamental Characteristics of AAA+ Protein Family Structure and Function. *Archaea* 2016.
- Miranda-Saksena, M., Boadle, R.A., Aggarwal, A., Tijono, B., Rixon, F.J., Diefenbach, R.J., and Cunningham, A.L. (2009). Herpes Simplex Virus Utilizes the Large Secretory Vesicle Pathway for Anterograde Transport of Tegument and Envelope Proteins and for Viral Exocytosis from Growth Cones of Human Fetal Axons. *Journal of Virology* 83, 3187–3199.
- Miranda-Saksena, M., Denes, C.E., Diefenbach, R.J., and Cunningham, A.L. (2018). Infection and Transport of Herpes Simplex Virus Type 1 in Neurons: Role of the Cytoskeleton. *Viruses* 10.
- Mitchell, D.R., and Rosenbaum, J.L. (1985). A motile Chlamydomonas flagellar mutant that lacks outer dynein arms. *J. Cell Biol.* 100, 1228–1234.
- Mitchison, H.M., and Valente, E.M. (2017). Motile and non-motile cilia in human pathology: from function to phenotypes. *The Journal of Pathology* 241, 294–309.
- Mitchison, T., and Kirschner, M. (1984). Dynamic instability of microtubule growth. *Nature* 312, 237–242.
- Montgomery, R.I., Warner, M.S., Lum, B.J., and Spear, P.G. (1996). Herpes Simplex Virus-1 Entry into Cells Mediated by a Novel Member of the TNF/NGF Receptor Family. *Cell* 87, 427–436.
- Moores, C.A., Perderiset, M., Francis, F., Chelly, J., Houdusse, A., and Milligan, R.A. (2004). Mechanism of Microtubule Stabilization by Doublecortin. *Molecular Cell* 14, 833–839.
- Moores, C.A., Perderiset, M., Kappeler, C., Kain, S., Drummond, D., Perkins, S.J., Chelly, J., Cross, R., Houdusse, A., and Francis, F. (2006). Distinct roles of doublecortin modulating the microtubule cytoskeleton. *EMBO J.* 25, 4448–4457.
- Muto, E., Sakai, H., and Kaseda, K. (2005). Long-range cooperative binding of kinesin to a microtubule in the presence of ATP. *J. Cell Biol.* 168, 691–696.
- Neuwald, A.F., Aravind, L., Spouge, J.L., and Koonin, E.V. (1999). AAA+: A Class of Chaperone-Like ATPases Associated with the Assembly, Operation, and Disassembly of Protein Complexes. *Genome Res.* 9, 27–43.
- Newcomb, W.W., Homa, F.L., Thomsen, D.R., Booy, F.P., Trus, B.L., Steven, A.C., Spencer, J.V., and Brown, J.C. (1996). Assembly of the Herpes Simplex Virus Capsid: Characterization of Intermediates Observed During Cell-free Capsid Formation. *Journal of Molecular Biology* 263, 432–446.
- Newcomb, W.W., Trus, B.L., Cheng, N., Steven, A.C., Sheaffer, A.K., Tenney, D.J., Weller, S.K., and Brown, J.C. (2000). Isolation of Herpes Simplex Virus Procapsids from Cells Infected with a Protease-Deficient Mutant Virus. *Journal of Virology* 74, 1663–1673.

- Newcomb, W.W., Booy, F.P., and Brown, J.C. (2007). Uncoating the Herpes Simplex Virus Genome. *Journal of Molecular Biology* 370, 633–642.
- Nicastro, D., Schwartz, C., Pierson, J., Gaudette, R., Porter, M.E., and McIntosh, J.R. (2006). The molecular architecture of axonemes revealed by cryoelectron tomography. *Science* 313, 944–948.
- Nicholas, M.P., Höök, P., Brenner, S., Wynne, C.L., Vallee, R.B., and Gennerich, A. (2015a). Control of cytoplasmic dynein force production and processivity by its C-terminal domain. *Nature Communications* 6, 6206.
- Nicholas, M.P., Berger, F., Rao, L., Brenner, S., Cho, C., and Gennerich, A. (2015b). Cytoplasmic dynein regulates its attachment to microtubules via nucleotide state-switched mechanosensing at multiple AAA domains. *Proc Natl Acad Sci U S A* 112, 6371–6376.
- Nicola, A.V., and Straus, S.E. (2004). Cellular and Viral Requirements for Rapid Endocytic Entry of Herpes Simplex Virus. *Journal of Virology* 78, 7508–7517.
- Nicola, A.V., McEvoy, A.M., and Straus, S.E. (2003). Roles for endocytosis and low pH in herpes simplex virus entry into HeLa and Chinese hamster ovary cells. *J. Virol.* 77, 5324–5332.
- Nicoll, M.P., Proença, J.T., and Efstathiou, S. (2012). The molecular basis of herpes simplex virus latency. *FEMS Microbiol Rev* 36, 684–705.
- Niekamp, S., Coudray, N., Zhang, N., Vale, R.D., and Bhabha, G. (2019). Coupling of ATPase activity, microtubule binding and mechanics in the dynein motor domain. *BioRxiv*.
- Nishikawa, Y., Inatomi, M., Iwasaki, H., and Kurisu, G. (2016a). Structural Change in the Dynein Stalk Region Associated with Two Different Affinities for the Microtubule. *Journal of Molecular Biology* 428, 1886–1896.
- Nishikawa, Y., Inatomi, M., Iwasaki, H., and Kurisu, G. (2016b). Structural Change in the Dynein Stalk Region Associated with Two Different Affinities for the Microtubule. *Journal of Molecular Biology* 428, 1886–1896.
- Nithianantham, S., Cook, B.D., Beans, M., Guo, F., Chang, F., and Al-Bassam, J. (2018). Structural basis of tubulin recruitment and assembly by microtubule polymerases with tumor overexpressed gene (TOG) domain arrays. *ELife* 7, e38922.
- Niwa, H., Miyauchi-Nanri, Y., Okumoto, K., Mukai, S., Noi, K., Ogura, T., and Fujiki, Y. (2018). A newly isolated Pex7-binding, atypical PTS2 protein P7BP2 is a novel dynein-type AAA+ protein. *J. Biochem.* 164, 437–447.
- Noble, A.J., Dandey, V.P., Wei, H., Brasch, J., Chase, J., Acharya, P., Tan, Y.Z., Zhang, Z., Kim, L.Y., Scapin, G., et al. (2018). Routine single particle CryoEM sample and grid characterization by tomography. *Elife* 7.
- Nogales, E., Wolf, S.G., and Downing, K.H. (1998a). Structure of the $\alpha\beta$ tubulin dimer by electron crystallography. *Nature* 391, 199–203.
- Nogales, E., Wolf, S.G., and Downing, K.H. (1998b). Structure of the $\alpha\beta$ tubulin dimer by electron crystallography. *391*, 6.
- Nogales, E., Whittaker, M., Milligan, R.A., and Downing, K.H. (1999). High-Resolution Model of the Microtubule. *Cell* 96, 79–88.
- Oh, M.-J., Akhtar, J., Desai, P., and Shukla, D. (2010). A role for heparan sulfate in viral surfing. *Biochemical and Biophysical Research Communications* 391, 176–181.
- Ojala, P.M., Sodeik, B., Ebersold, M.W., Kutay, U., and Helenius, A. (2000). Herpes Simplex Virus Type 1 Entry into Host Cells: Reconstitution of Capsid Binding and Uncoating at the Nuclear Pore Complex In Vitro. *Molecular and Cellular Biology* 20, 4922–4931.
- Olenick, M.A., Dominguez, R., and Holzbaur, E.L.F. (2019). Dynein activator Hook1 is required for trafficking of BDNF-signaling endosomes in neurons. *J Cell Biol* 218, 220–233.
- Orlova, E.V., and Saibil, H.R. (2011). Structural Analysis of Macromolecular Assemblies by Electron Microscopy. *Chem. Rev.* 111, 7710–7748.
- Owen, D.J., Crump, C.M., and Graham, S.C. (2015). Tegument Assembly and Secondary Envelopment of Alphaherpesviruses. *Viruses* 7, 5084–5114.
- Pasdeloup, D., Blondel, D., Isidro, A.L., and Rixon, F.J. (2009). Herpesvirus Capsid Association with the Nuclear Pore Complex and Viral DNA Release Involve the Nucleoporin CAN/Nup214 and the Capsid Protein pUL25. *Journal of Virology* 83, 6610–6623.
- Pasdeloup, D., McElwee, M., Beilstein, F., Labetoulle, M., and Rixon, F.J. (2013). Herpesvirus tegument protein pUL37 interacts with dystonin/BPAG1 to promote capsid transport on microtubules during egress. *J. Virol.* 87, 2857–2867.
- Peet, D.R., Burroughs, N.J., and Cross, R.A. (2018). Kinesin expands and stabilizes the GDP-microtubule lattice. *Nature Nanotechnology* 13, 386.
- Petrovskis, E.A., Meyer, A.L., and Post, L.E. (1988). Reduced Yield of Infectious Pseudorabies Virus and Herpes Simplex Virus from Cell Lines Producing Viral Glycoprotein gp50. *62*, 4.
- Pettersen, E.F., Goddard, T.D., Huang, C.C., Couch, G.S., Greenblatt, D.M., Meng, E.C., and Ferrin, T.E. (2004). UCSF Chimera—a visualization system for exploratory research and analysis. *J Comput Chem* 25, 1605–1612.
- Pfister, K.K., Shah, P.R., Hummerich, H., Russ, A., Cotton, J., Annuar, A.A., King, S.M., and Fisher, E.M.C. (2006). Genetic Analysis of the Cytoplasmic Dynein Subunit Families. *PLOS Genetics* 2, e1.

- Pierson, G.B., Burton, P.R., and Himes, R.H. (1978). Alterations in number of protofilaments in microtubules assembled in vitro. *The Journal of Cell Biology* *76*, 223–228.
- Prevo, B., Scholey, J.M., and Peterman, E.J.G. (2017). Intraflagellar transport: mechanisms of motor action, cooperation, and cargo delivery. *The FEBS Journal* *284*, 2905–2931.
- Pronobis, M.I., Deutch, N., and Peifer, M. (2016). The Miraprep: A Protocol that Uses a Miniprep Kit and Provides Maxiprep Yields. *PLOS ONE* *11*, e0160509.
- Punjani, A., Rubinstein, J.L., Fleet, D.J., and Brubaker, M.A. (2017). cryoSPARC: algorithms for rapid unsupervised cryo-EM structure determination. *Nature Methods* *14*, 290–296.
- Qin, H., Diener, D.R., Geimer, S., Cole, D.G., and Rosenbaum, J.L. (2004). Intraflagellar transport (IFT) cargo: IFT transports flagellar precursors to the tip and turnover products to the cell body. *The Journal of Cell Biology* *164*, 255–266.
- Qiu, W., Derr, N.D., Goodman, B.S., Villa, E., Wu, D., Shih, W., and Reck-Peterson, S.L. (2012). Dynein achieves processive motion using both stochastic and coordinated stepping. *Nature Structural & Molecular Biology* *19*, 193–200.
- Radtke, K., Kienek, D., Wolfstein, A., Michael, K., Steffen, W., Scholz, T., Karger, A., and Sodeik, B. (2010). Plus- and Minus-End Directed Microtubule Motors Bind Simultaneously to Herpes Simplex Virus Capsids Using Different Inner Tegument Structures. *PLOS Pathogens* *6*, e1000991.
- Raff, E.C., Hoyle, H.D., Popodi, E.M., and Turner, F.R. (2008). Axoneme β -Tubulin Sequence Determines Attachment of Outer Dynein Arms. *Current Biology* *18*, 911–914.
- Raghunayakula, S., Subramonian, D., Dasso, M., Kumar, R., and Zhang, X.-D. (2015). Molecular Characterization and Functional Analysis of Annulate Lamellae Pore Complexes in Nuclear Transport in Mammalian Cells. *PLOS ONE* *10*, e0144508.
- Ray, S., Meyhöfer, E., Milligan, R.A., and Howard, J. (1993). Kinesin follows the microtubule's protofilament axis. *J. Cell Biol.* *121*, 1083–1093.
- Rayment, I. (1996). Kinesin and myosin: molecular motors with similar engines. *Structure* *4*, 501–504.
- Reck-Peterson, S.L., Yildiz, A., Carter, A.P., Gennerich, A., Zhang, N., and Vale, R.D. (2006). Single-Molecule Analysis of Dynein Processivity and Stepping Behavior. *Cell* *126*, 335–348.
- Reck-Peterson, S.L., Redwine, W.B., Vale, R.D., and Carter, A.P. (2018). The cytoplasmic dynein transport machinery and its many cargoes. *Nature Reviews Molecular Cell Biology* *19*, 382.
- Redwine, W.B., Hernandez-Lopez, R., Zou, S., Huang, J., Reck-Peterson, S.L., and Leschziner, A.E. (2012). Structural basis for microtubule binding and release by dynein. *Science* *337*, 1532–1536.
- Redwine, W.B., DeSantis, M.E., Hollyer, I., Htet, Z.M., Tran, P.T., Swanson, S.K., Florens, L., Washburn, M.P., and Reck-Peterson, S.L. (2017). The human cytoplasmic dynein interactome reveals novel activators of motility. *ELife* *6*, e28257.
- Reimer, L. (2013). *Transmission Electron Microscopy: Physics of Image Formation and Microanalysis* (Springer).
- Rice, S., Lin, A.W., Safer, D., Hart, C.L., Naber, N., Carragher, B.O., Cain, S.M., Pechatnikova, E., Wilson-Kubalek, E.M., Whittaker, M., et al. (1999). A structural change in the kinesin motor protein that drives motility. *Nature* *402*, 778–784.
- Richards, A.L., Sollars, P.J., Pitts, J.D., Stults, A.M., Heldwein, E.E., Pickard, G.E., and Smith, G.A. (2017). The pUL37 tegument protein guides alpha-herpesvirus retrograde axonal transport to promote neuroinvasion. *PLOS Pathogens* *13*, e1006741.
- Roberts, A.J., Numata, N., Walker, M.L., Kato, Y.S., Malkova, B., Kon, T., Ohkura, R., Arisaka, F., Knight, P.J., Sutoh, K., et al. (2009). AAA+ Ring and Linker Swing Mechanism in the Dynein Motor. *Cell* *136*, 485–495.
- Roberts, A.J., Kon, T., Knight, P.J., Sutoh, K., and Burgess, S.A. (2013). Functions and mechanics of dynein motor proteins. *Nat. Rev. Mol. Cell Biol.* *14*, 713–726.
- Roberts, A.J., Goodman, B.S., and Reck-Peterson, S.L. (2014). Reconstitution of dynein transport to the microtubule plus end by kinesin. *ELife* *3*, e02641.
- Roostalu, J., and Surrey, T. (2017). Microtubule nucleation: beyond the template. *Nature Reviews Molecular Cell Biology* *18*, 702–710.
- Rosenthal, P.B., and Henderson, R. (2003). Optimal Determination of Particle Orientation, Absolute Hand, and Contrast Loss in Single-particle Electron Cryomicroscopy. *Journal of Molecular Biology* *333*, 721–745.
- Sakakibara, H., Kojima, H., Sakai, Y., Katayama, E., and Oiwa, K. (1999). Inner-arm dynein c of *Chlamydomonas* flagella is a single-headed processive motor. *Nature* *400*, 586–590.
- Sali, A., and Blundell, T.L. (1993). Comparative protein modelling by satisfaction of spatial restraints. *J. Mol. Biol.* *234*, 779–815.
- Sánchez-Huertas, C., Freixo, F., Viais, R., Lacasa, C., Soriano, E., and Lüders, J. (2016). Non-centrosomal nucleation mediated by augmin organizes microtubules in post-mitotic neurons and controls axonal microtubule polarity. *Nature Communications* *7*, 12187.
- Satir, P., Pedersen, L.B., and Christensen, S.T. (2010). The primary cilium at a glance. *J Cell Sci* *123*, 499–503.
- Satir, P., Heuser, T., and Sale, W.S. (2014). A Structural Basis for How Motile Cilia Beat. *Bioscience* *64*, 1073–1083.
- Scherer, J., Yaffe, Z.A., Vershinin, M., and Enquist, L.W. (2016). Dual-Color Herpesvirus Capsids Discriminate Inoculum from Progeny and Reveal Axonal Transport Dynamics. *Journal of Virology* *90*, 9997–10006.

- Scheres, S.H.W. (2012). RELION: Implementation of a Bayesian approach to cryo-EM structure determination. *Journal of Structural Biology* 180, 519–530.
- Scheres, S.H.W., and Chen, S. (2012). Prevention of overfitting in cryo-EM structure determination. *Nature Methods* 9, 853.
- Schindelin, J., Arganda-Carreras, I., Frise, E., Kaynig, V., Longair, M., Pietzsch, T., Preibisch, S., Rueden, C., Saalfeld, S., Schmid, B., et al. (2012). Fiji: an open-source platform for biological-image analysis. *Nature Methods* 9, 676–682.
- Schipke, J., Pohlmann, A., Diestel, R., Binz, A., Rudolph, K., Nagel, C.-H., Bauerfeind, R., and Sodeik, B. (2012). The C Terminus of the Large Tegument Protein pUL36 Contains Multiple Capsid Binding Sites That Function Differently during Assembly and Cell Entry of Herpes Simplex Virus. *J Virol* 86, 3682–3700.
- Schlager, M.A., Hoang, H.T., Urnavicius, L., Bullock, S.L., and Carter, A.P. (2014a). In vitro reconstitution of a highly processive recombinant human dynein complex. *EMBO J.* 33, 1855–1868.
- Schlager, M.A., Serra-Marques, A., Grigoriev, I., Gumy, L.F., Esteves da Silva, M., Wulf, P.S., Akhmanova, A., and Hoogenraad, C.C. (2014b). Bicaudal D Family Adaptor Proteins Control the Velocity of Dynein-Based Movements. *Cell Reports* 8, 1248–1256.
- Schlieker, C., Weihofen, W.A., Frijns, E., Kattenhorn, L.M., Gaudet, R., and Ploegh, H.L. (2007). Structure of a Herpesvirus-Encoded Cysteine Protease Reveals a Unique Class of Deubiquitinating Enzymes. *Molecular Cell* 25, 677–687.
- Schmidt, H., and Carter, A.P. (2016). Review: Structure and mechanism of the dynein motor ATPase. *Biopolymers* 105, 557–567.
- Schmidt, H., Gleave, E.S., and Carter, A.P. (2012). Insights into dynein motor domain function from a 3.3-Å crystal structure. *Nature Structural & Molecular Biology* 19, 492–497.
- Schmidt, H., Zalyte, R., Urnavicius, L., and Carter, A.P. (2015). Structure of human cytoplasmic dynein-2 primed for its power stroke. *Nature* 518, 435–438.
- Scholey, J.M. (2013). Kinesin-2: a family of heterotrimeric and homodimeric motors with diverse intracellular transport functions. *Annu. Rev. Cell Dev. Biol.* 29, 443–469.
- Scholey, J.E., Nithianantham, S., Scholey, J.M., and Al-Bassam, J. (2014). Structural basis for the assembly of the mitotic motor Kinesin-5 into bipolar tetramers. *ELife* 3, e02217.
- Schroer, T.A. (2004). Dynactin. *Annual Review of Cell and Developmental Biology* 20, 759–779.
- Scrima, N., Lepault, J., Boulard, Y., Padeloup, D., Bressanelli, S., and Roche, S. (2015). Insights into Herpesvirus Tegument Organization from Structural Analyses of HSV-1 UL36 Central 970 Residues. *J. Biol. Chem.* jbc.M114.612838.
- Shang, Z., Zhou, K., Xu, C., Csencsits, R., Cochran, J.C., and Sindelar, C.V. (2014). High-resolution structures of kinesin on microtubules provide a basis for nucleotide-gated force-generation. *ELife* 3, e04686.
- Shieh, M.T., WuDunn, D., Montgomery, R.I., Esko, J.D., and Spear, P.G. (1992). Cell surface receptors for herpes simplex virus are heparan sulfate proteoglycans. *J. Cell Biol.* 116, 1273–1281.
- Shimizu, Y., Sakakibara, H., Kojima, H., and Oiwa, K. (2014). Slow Axonemal Dynein e Facilitates the Motility of Faster Dynein c. *Biophys J* 106, 2157–2165.
- Shukla, D., Liu, J., Blaiklock, P., Shworak, N.W., Bai, X., Esko, J.D., Cohen, G.H., Eisenberg, R.J., Rosenberg, R.D., and Spear, P.G. (1999). A Novel Role for 3-O-Sulfated Heparan Sulfate in Herpes Simplex Virus 1 Entry. *Cell* 99, 13–22.
- Sigworth, F.J. (2016). Principles of cryo-EM single-particle image processing. *Microscopy (Oxf)* 65, 57–67.
- Simpson, J.C., Griffiths, G., Wessling-Resnick, M., Fransen, J.A.M., Bennett, H., and Jones, A.T. (2004). A role for the small GTPase Rab21 in the early endocytic pathway. *Journal of Cell Science* 117, 6297–6311.
- Sindelar, C.V., and Downing, K.H. (2007). The beginning of kinesin's force-generating cycle visualized at 9-Å resolution. *J Cell Biol* 177, 377–385.
- Smith, G. (2012). Herpesvirus Transport to the Nervous System and Back Again. *Annu Rev Microbiol* 66.
- Sodeik, B. (2000). Mechanisms of viral transport in the cytoplasm. *Trends in Microbiology* 8, 465–472.
- Sodeik, B., Ebersold, M.W., and Helenius, A. (1997). Microtubule-mediated transport of incoming herpes simplex virus 1 capsids to the nucleus. *J. Cell Biol.* 136, 1007–1021.
- Song, K., Shang, Z., Fu, X., Lou, X., Grigorieff, N., and Nicastro, D. (2018). Structure of the ciliary axoneme at nanometer resolution reconstructed by TYGRESS. *BioRxiv* 363317.
- Sosa, H., Dias, D.P., Hoenger, A., Whittaker, M., Wilson-Kubalek, E., Sablin, E., Fletterick, R.J., Vale, R.D., and Milligan, R.A. (1997). A Model for the Microtubule-Ncd Motor Protein Complex Obtained by Cryo-Electron Microscopy and Image Analysis. *Cell* 90, 217–224.
- Spear, P.G., and Longnecker, R. (2003). Herpesvirus Entry: an Update. *Journal of Virology* 77, 10179–10185.
- Splinter, D., Tanenbaum, M.E., Lindqvist, A., Jaarsma, D., Flotho, A., Yu, K.L., Grigoriev, I., Engelsma, D., Haasdijk, E.D., Keijzer, N., et al. (2010a). Bicaudal D2, Dynein, and Kinesin-1 Associate with Nuclear Pore Complexes and Regulate Centrosome and Nuclear Positioning during Mitotic Entry. *PLOS Biology* 8, e1000350.
- Splinter, D., Tanenbaum, M.E., Lindqvist, A., Jaarsma, D., Flotho, A., Yu, K.L., Grigoriev, I., Engelsma, D., Haasdijk, E.D., Keijzer, N., et al. (2010b). Bicaudal D2, Dynein, and Kinesin-1 Associate with Nuclear Pore

- Complexes and Regulate Centrosome and Nuclear Positioning during Mitotic Entry. *PLOS Biology* 8, e1000350.
- Splinter, D., Razafsky, D.S., Schlager, M.A., Serra-Marques, A., Grigoriev, I., Demmers, J., Keijzer, N., Jiang, K., Poser, I., Hyman, A.A., et al. (2012). BICD2, dynactin, and LIS1 cooperate in regulating dynein recruitment to cellular structures. *MBoC* 23, 4226–4241.
- Steiner, I., Kennedy, P.G., and Pachner, A.R. (2007). The neurotropic herpes viruses: herpes simplex and varicella-zoster. *The Lancet Neurology* 6, 1015–1028.
- Steinman, J.B., Santarossa, C.C., Miller, R.M., Yu, L.S., Serpinskaya, A.S., Furukawa, H., Morimoto, S., Tanaka, Y., Nishitani, M., Asano, M., et al. (2017). Chemical structure-guided design of dynapyrazoles, cell-permeable dynein inhibitors with a unique mode of action. *ELife* 6.
- Tang, G., Peng, L., Baldwin, P.R., Mann, D.S., Jiang, W., Rees, I., and Ludtke, S.J. (2007). EMAN2: an extensible image processing suite for electron microscopy. *J. Struct. Biol.* 157, 38–46.
- Tas, R.P., Chazeau, A., Cloin, B.M.C., Lambers, M.L.A., Hoogenraad, C.C., and Kapitein, L.C. (2017). Differentiation between Oppositely Oriented Microtubules Controls Polarized Neuronal Transport. *Neuron* 96, 1264–1271.e5.
- Teixidó-Travesa, N., Roig, J., and Lüders, J. (2012). The where, when and how of microtubule nucleation – one ring to rule them all. *J Cell Sci* 125, 4445–4456.
- Thellman, N.M., and Triezenberg, S.J. (2017). Herpes Simplex Virus Establishment, Maintenance, and Reactivation: In Vitro Modeling of Latency. *Pathogens* 6.
- Thompson, R.L., Preston, C.M., and Sawtell, N.M. (2009). De Novo Synthesis of VP16 Coordinates the Exit from HSV Latency In Vivo. *PLoS Pathog* 5.
- Ti, S.-C., Pamula, M.C., Howes, S.C., Duellberg, C., Cade, N.I., Kleiner, R.E., Forth, S., Surrey, T., Nogales, E., and Kapoor, T.M. (2016). Mutations in Human Tubulin Proximal to the Kinesin-Binding Site Alter Dynamic Instability at Microtubule Plus- and Minus-Ends. *Developmental Cell* 37, 72–84.
- Tilney, L.G., Bryan, J., Bush, D.J., Fujiwara, K., Mooseker, M.S., Murphy, D.B., and Snyder, D.H. (1973). Microtubules: Evidence for 13 Protofilaments. *The Journal of Cell Biology* 59, 267–275.
- Toropova, K., Mladenov, M., and Roberts, A.J. (2017). Intraflagellar Transport Dynein is Autoinhibited by Trapping of its Mechanical and Track-Binding Elements. *Nat Struct Mol Biol* 24, 461–468.
- Trocter, M., Mücke, N., and Surrey, T. (2012). Reconstitution of the human cytoplasmic dynein complex. *PNAS* 109, 20895–20900.
- Urnavicius, L., Zhang, K., Diamant, A.G., Motz, C., Schlager, M.A., Yu, M., Patel, N.A., Robinson, C.V., and Carter, A.P. (2015). The structure of the dynactin complex and its interaction with dynein. *Science* 347, 1441–1446.
- Urnavicius, L., Lau, C.K., Elshenawy, M.M., Morales-Rios, E., Motz, C., Yildiz, A., and Carter, A.P. (2018). Cryo-EM shows how dynactin recruits two dyneins for faster movement. *Nature* 554, 202–206.
- Vale, R.D., and Toyoshima, Y.Y. (1988). Rotation and translocation of microtubules in vitro induced by dyneins from *Tetrahymena* cilia. *Cell* 52, 459–469.
- Vaughan, K.T., and Vallee, R.B. (1995). Cytoplasmic dynein binds dynactin through a direct interaction between the intermediate chains and p150Glued. *The Journal of Cell Biology* 131, 1507–1516.
- Vemu, A., Atherton, J., Spector, J.O., Moores, C.A., and Roll-Mecak, A. (2017). Tubulin isoform composition tunes microtubule dynamics. *MBoC* 28, 3564–3572.
- Vemu, A., Szczesna, E., Zehr, E.A., Spector, J.O., Grigorieff, N., Deaconescu, A.M., and Roll-Mecak, A. (2018). Severing enzymes amplify microtubule arrays through lattice GTP-tubulin incorporation. *Science* 361, eaau1504.
- Verhey, K.J., Kaul, N., and Soppina, V. (2011). Kinesin Assembly and Movement in Cells. *Annual Review of Biophysics* 40, 267–288.
- Vittone, V., Diefenbach, E., Triffett, D., Douglas, M.W., Cunningham, A.L., and Diefenbach, R.J. (2005). Determination of Interactions between Tegument Proteins of Herpes Simplex Virus Type 1. *Journal of Virology* 79, 9566–9571.
- Wang, J., Yuan, S., Zhu, D., Tang, H., Wang, N., Chen, W., Gao, Q., Li, Y., Wang, J., Liu, H., et al. (2018a). Structure of the herpes simplex virus type 2 C-capsid with capsid-vertex-specific component. *Nature Communications* 9, 3668.
- Wang, Q., Crevenna, A.H., Kunze, I., and Mizuno, N. (2014a). Structural basis for the extended CAP-Gly domains of p150glued binding to microtubules and the implication for tubulin dynamics. *Proceedings of the National Academy of Sciences* 111, 11347–11352.
- Wang, S., Ma, Z., Xu, X., Wang, Z., Sun, L., Zhou, Y., Lin, X., Hong, W., and Wang, T. (2014b). A Role of Rab29 in the Integrity of the Trans-Golgi Network and Retrograde Trafficking of Mannose-6-Phosphate Receptor. *PLoS ONE* 9, e96242.
- Wang, Y., Huynh, W., Skokan, T., and Vale, R. (2018b). A new calcium-activated dynein adaptor protein, CRACR2a, regulates clathrin-independent endocytic traffic in T cells. *BioRxiv*.
- Weisenberg, R.C., Broisy, G.G., and Taylor, E.William. (1968). Colchicine-binding protein of mammalian brain and its relation to microtubules. *Biochemistry* 7, 4466–4479.

- Werner, S., Pimenta-Marques, A., and Bettencourt-Dias, M. (2017). Maintaining centrosomes and cilia. *J Cell Sci* *130*, 3789–3800.
- Wickstead, B., and Gull, K. (2006). A “Holistic” Kinesin Phylogeny Reveals New Kinesin Families and Predicts Protein Functions. *Mol Biol Cell* *17*, 1734–1743.
- Wickstead, B., and Gull, K. (2007). Dyneins Across Eukaryotes: A Comparative Genomic Analysis. *Traffic* *8*, 1708–1721.
- Wisner, T.W., Sugimoto, K., Howard, P.W., Kawaguchi, Y., and Johnson, D.C. (2011). Anterograde Transport of Herpes Simplex Virus Capsids in Neurons by both Separate and Married Mechanisms. *J Virol* *85*, 5919–5928.
- Woodruff, J.B., Gomes, B.F., Widlund, P.O., Mahamid, J., Honigsmann, A., and Hyman, A.A. (2017). The Centrosome Is a Selective Condensate that Nucleates Microtubules by Concentrating Tubulin. *Cell* *169*, 1066–1077.e10.
- Woźniak, M.J., Bola, B., Brownhill, K., Yang, Y.-C., Levakova, V., and Allan, V.J. (2009). Role of kinesin-1 and cytoplasmic dynein in endoplasmic reticulum movement in VERO cells. *J. Cell. Sci.* *122*, 1979–1989.
- Wu, J., Matunis, M.J., Kraemer, D., Blobel, G., and Coutavas, E. (1995). Nup358, a Cytoplasmically Exposed Nucleoporin with Peptide Repeats, Ran-GTP Binding Sites, Zinc Fingers, a Cyclophilin A Homologous Domain, and a Leucine-rich Region. *J. Biol. Chem.* *270*, 14209–14213.
- Xu, Z., Schaedel, L., Portran, D., Aguilar, A., Gaillard, J., Marinkovich, M.P., Théry, M., and Nachury, M.V. (2017). Microtubules acquire resistance from mechanical breakage through intraluminal acetylation. *Science* *356*, 328–332.
- Yagi, T., Uematsu, K., Liu, Z., and Kamiya, R. (2009). Identification of dyneins that localize exclusively to the proximal portion of Chlamydomonas flagella. *J Cell Sci* *122*, 1306–1314.
- Yamada, M., Tanaka-Takiguchi, Y., Hayashi, M., Nishina, M., and Goshima, G. (2017). Multiple kinesin-14 family members drive microtubule minus end-directed transport in plant cells. *J Cell Biol* *216*, 1705–1714.
- Yau, K.W., Schätzle, P., Tortosa, E., Pagès, S., Holtmaat, A., Kapitein, L.C., and Hoogenraad, C.C. (2016). Dendrites In Vitro and In Vivo Contain Microtubules of Opposite Polarity and Axon Formation Correlates with Uniform Plus-End-Out Microtubule Orientation. *J. Neurosci.* *36*, 1071–1085.
- Ye, R., Su, C., Xu, H., and Zheng, C. (2017). Herpes Simplex Virus 1 Ubiquitin-Specific Protease UL36 Abrogates NF- κ B Activation in DNA Sensing Signal Pathway. *J. Virol.* *91*.
- Yildiz, A., Tomishige, M., Vale, R.D., and Selvin, P.R. (2004). Kinesin Walks Hand-Over-Hand. *Science* *303*, 676–678.
- Yokoyama, N., Hayashi, N., Seki, T., Panté, N., Ohba, T., Nishii, K., Kuma, K., Hayashida, T., Miyata, T., Aebi, U., et al. (1995). A giant nucleopore protein that binds Ran/TC4. *Nature* *376*, 184–188.
- Yuan, S., Wang, J., Zhu, D., Wang, N., Gao, Q., Chen, W., Tang, H., Wang, J., Zhang, X., Liu, H., et al. (2018). Cryo-EM structure of a herpesvirus capsid at 3.1 Å. *Science* *360*, eaao7283.
- Zaichick, S.V., Bohannon, K.P., Hughes, A., Sollars, P.J., Pickard, G.E., and Smith, G.A. (2013). The herpesvirus VP1/2 protein is an effector of dynein-mediated capsid transport and neuroinvasion. *Cell Host Microbe* *13*, 193–203.
- Zhang, K. (2016). Gctf: Real-time CTF determination and correction. *J Struct Biol* *193*, 1–12.
- Zhang, R., and Nogales, E. (2015a). A New Protocol to Accurately Determine Microtubule Lattice Seam Location. *J Struct Biol* *192*, 245–254.
- Zhang, R., and Nogales, E. (2015b). A new protocol to accurately determine microtubule lattice seam location. *Journal of Structural Biology* *192*, 245–254.
- Zhang, R., and Nogales, E. (2015c). A new protocol to accurately determine microtubule lattice seam location. *Journal of Structural Biology* *192*, 245–254.
- Zhang, K., Foster, H.E., Rondelet, A., Lacey, S.E., Bahi-Buisson, N., Bird, A.W., and Carter, A.P. (2017a). Cryo-EM Reveals How Human Cytoplasmic Dynein Is Auto-inhibited and Activated. *Cell* *169*, 1303–1314.e18.
- Zhang, L.-J., Xia, L., Liu, S.-L., Sun, E.-Z., Wu, Q.-M., Wen, L., Zhang, Z.-L., and Pang, D.-W. (2018a). A “Driver Switchover” Mechanism of Influenza Virus Transport from Microfilaments to Microtubules. *ACS Nano* *12*, 474–484.
- Zhang, L.-J., Xia, L., Liu, S.-L., Sun, E.-Z., Wu, Q.-M., Wen, L., Zhang, Z.-L., and Pang, D.-W. (2018b). A “Driver Switchover” Mechanism of Influenza Virus Transport from Microfilaments to Microtubules. *ACS Nano* *12*, 474–484.
- Zhang, R., Alushin, G.M., Brown, A., and Nogales, E. (2015a). Mechanistic Origin of Microtubule Dynamic Instability and Its Modulation by EB Proteins. *Cell* *162*, 849–859.
- Zhang, R., Alushin, G.M., Brown, A., and Nogales, E. (2015b). Mechanistic Origin of Microtubule Dynamic Instability and Its Modulation by EB Proteins. *Cell* *162*, 849–859.
- Zhang, R., Roostalu, J., Surrey, T., and Nogales, E. (2017b). Structural insight into TPX2-stimulated microtubule assembly. *ELife* *6*, e30959.
- Zhang, R., LaFrance, B., and Nogales, E. (2018c). Separating the effects of nucleotide and EB binding on microtubule structure. *PNAS* *115*, E6191–E6200.
- Zhang, R., LaFrance, B., and Nogales, E. (2018d). Separating the effects of nucleotide and EB binding on microtubule structure. *PNAS* *115*, E6191–E6200.

- Zheng, S.Q., Palovcak, E., Armache, J.-P., Verba, K.A., Cheng, Y., and Agard, D.A. (2017). MotionCor2: anisotropic correction of beam-induced motion for improved cryo-electron microscopy. *Nature Methods* 14, 331–332.
- Zhu, W., Smith, J.W., and Huang, C.-M. (2010). Mass Spectrometry-Based Label-Free Quantitative Proteomics.
- Zivanov, J., Nakane, T., Forsberg, B., Kimanius, D., Hagen, W.J.H., Lindahl, E., and Scheres, S.H.W. (2018). RELION-3: new tools for automated high-resolution cryo-EM structure determination. *BioRxiv*.